Assessment of the potentials and limitations of cortical-based analysis for the integration of structure and function in normal and pathological brains using MRI

Mahsa Shokouhi

BSc, MSc

Submitted in fulfilment of the requirements for the degree of Doctor of Philosophy

Department of Clinical Physics

College of Medical, Veterinary and Life Sciences

University of Glasgow

February 2012

Abstract

The software package Brainvisa (www.brainvisa.tnfo) offers a wide range of possibilities for cortical analysis using its automatic sulci recognition feature. Automated sulci identification is an attractive feature as the manual labelling of the cortical sulci is often challenging even for the experienced neuro-radiologists. This can also be of interest in fMRI studies of individual subjects where activated regions of the cortex can simply be identified using sulcal labels without the need for normalization to an atlas. As it will be explained later in this thesis, normalization to atlas can especially be problematic for pathologic brains.

In addition, Brainvisa allows for sulcal morphometry from structural MR images by estimating a wide range of sulcal properties such as size, coordinates, direction, and pattern. Morphometry of abnormal brains has gained huge interest and has been widely used in finding the biomarkers of several neurological diseases or psychiatric disorders. However mainly because of its complexity, only a limited use of sulcal morphometry has been reported so far. With a wide range of possibilities for sulcal morphometry offered by Brainvisa, it is possible to thoroughly investigate the sulcal changes due to the abnormality.

However, as any other automated method, Brainvisa can be susceptible to limitations associated with image quality. Factors such as noise, spatial resolution, and so on, can have an impact on the detection of the cortical folds and estimation of their attributes. Hence the robustness of Brainvisa needs to be assessed. This can be done by estimating the reliability and reproducibility of results as well as exploring the changes in results caused by other factors.

This thesis is an attempt to investigate the possible benefits of sulci identification and sulcal morphometry for functional and structural MRI studies as well as the limitations of Brainvisa. In addition, the possibility of improvement of activation localization with functional MRI studies is further investigated. This investigation was motivated by a review of other cortical-based analysis methods, namely the cortical surface-based methods, which are discussed in the literature review chapter of this thesis. The application of these approaches in functional MRI data analysis and their potential benefits is used in this investigation.

Table of Contents

List of Tables

List of Figures

List of Equations

Acknowledgement

I wish to thank my supervisor Prof Barrie Condon for all his guidance, support, and patience throughout the course of this work. I am also grateful to Dr. Bill Moorhead for his help and invaluable pieces of advice and Dr. Dave Brennan for all his help.

I gratefully acknowledge the funding I received from the SINAPSE for this three year studentship.

I would also like to thank Prof. Donald Hadley, Drs Jim Patterson, John McLean, and Rosario Gonzalez, Mr. Abdul Mumuni, and other friendly staff at the Institute of Neurological Sciences, Southern General Hospital, who made my PhD experience a memorable journey.

My special thanks go to my parents for all their continuing support and encouragement in all my endeavours.

Author’s Declaration

This thesis has been composed by the undersigned. The work contained in this thesis was carried out during my three year studentship in the University of Glasgow, Department of Clinical Physics (October 2008 – October 2011).

All data analysis reported in this thesis was undertaken by me, unless otherwise indicated in the text.

Mahsa Shokouhi

List of Abbreviations

2D	Two Dimensional
3D	Three Dimensional
AC	Anterior Commissure
ANOVA	Analysis of Variance
ASD	Autism Spectrum Disorder
ASP	Anatomic Segmentation using Proximity
ASW	Automated Spherical Warping
AVM	ArterioVenous Malformation
BOLD	Blood Oxygenation Level Dependant
CADASIL	Cerebral Autosomal Dominant Arteriolopathy with Subcortical Infarcts and Leukoencephalopathy
CLASP	Constrained Laplacian Anatomic Segmentation using Proximity
CN	Centre-of-Normal
CSF	Cerebro-Spinal Fluid
EPI	Echo Planar Imaging
FEM	Finite Element Method
fMRI	Functional Magnetic Resonance Imaging

FN	False Negative
FP	False Positive
FPF	False Positive Fraction
FWE	Family-Wise Error
FWHM	Full Width at Half Maximum
GMB	GlioBlastoma Multiform
GE	General Electric
GLM	General Linear Model
GM	Grey Matter
GRE	Gradient Echo
GSI	Global Sulcal Index
ICBM	International Consortium of Brain Imaging
INU	Intensity Non-uniformity
IRFSPGR	Inversion Recovery Fast Spoiled Gradient Recalled
LBW	Landmark Based Warping
MAP	Maximum A Posteriori
MNI	Montreal Neurological Institute
MRI	Magnetic Resonance Imaging
NEX	Number of Excitations

PALS	Population Average, Landmark and Surface based atlas
PC	Posterior Commissure
PEF	Probabilistic Extra Fraction
POF	Probabilistic Overlap Fraction
PPV	Positive Predictive Value
PSI	Probabilistic Similarity Index
QA	Quality Assurance
RD	Dispersion Radius
RF	Radiofrequency
ROI	Region Of Interest
SFLASH	Spoiled Fast Low Angel Shot
SNR	Signal to Noise Ratio
SPAM	Statistical Parametric Anatomy Map
SPGR	Spoiled Gradient Recalled
SVM	Support Vector Machine
TE	Echo Time
TI	Inversion Time
TN	True Negative
TP	True Positive

TR	Repetition Time
TS	Two-Surface
WM	White Matter

Chapter 1. Introduction

1.1 Overview of the thesis

The aim of this project is to assess the potential of the automated labelling of the cortex and sulcal morphometry using Brainvisa for both structural and functional Magnetic Resonance Imaging (MRI) studies of abnormal brains as well as the robustness of this software package and the reproducibility and reliability of the analysis.

The assessment for abnormal brains considered in this project include identifying the abnormality-related structural changes in the cortex for subjects with autism using cortical morphometry as well as using the automatic identification of eloquent cortical regions for evaluation of the cerebral plasticity in patients with epilepsy, brain tumour, or vascular malformation.

To assess different aspects of robustness of this package, healthy brains from real data as well as simulated data have been used.

In addition, the possibility of improvement in activation localization and whether functional MRI (fMRI) analysis can benefit from cortical surface-based methods has also been investigated.

This thesis consists of eight chapters. Chapter one is an introduction to the software package Brainvisa (www.brainvisa.info) which is the tool for cortical analysis used throughout this thesis. In this chapter some of the possible benefits of using Brainvisa and what can be achieved by this package are reviewed, and the procedure for data analysis with Brainvisa is explained. The possible benefit of

its sulci recognition facility in fMRI studies is also discussed. The chapter ends by a brief discussion.

Chapter two begins with a detailed description of the cortical surface-based approaches. The success of such methods and how cortical analysis using structural and functional MRI can benefit from these methods are explored. The chapter finishes by a discussion on how such methods can be used in this project.

In chapter three the reproducibility and reliability of the morphometry analysis using Brainvisa is assessed using data from two groups of multi-centre studies acquired using 1.5 T and 3 T. The aim of this chapter is twofold: Firstly, to investigate the suitability of Brainvisa for multi-centre and longitudinal studies which have been of growing interest and secondly, to identify some possible ways in which Brainvisa can be improved in order to produce more reliable and reproducible morphometry results and become more robust.

Chapter four estimates the effect of noise, slice thickness and magnetic field inhomogeneity on brain morphometry using simulated data and how the results change with these factors. The purpose of this chapter is to identify the main factors affecting brain and sulcal morphometry using Brainvisa. The advantage of simulated data over real data is that they enable a direct manipulation of changes in the above-mentioned factors whereas with real data these factors may not be directly changed.

Chapter five is an attempt to investigate the utility of sulcal morphometry in identifying novel aspects of cortical changes in autism. This was motivated by previous studies confirming the increased local gyrification in subjects with autism. This chapter investigates whether such local changes have some correlations with sulcal size. The cortical gyrification as well as sulcal parameters such as length, surface, and the mean geodesic depth, are therefore calculated for adolescents with autism and compared to those for healthy subjects.

Chapters six and seven look into the possible benefit of using automated cortical labelling with Brainvisa for pre-surgical planning and assessment of the cerebral plasticity in patients with brain tumour, vascular malformations, and epilepsy. Based on the type of the pathology or the location of the lesion, the motor and/or

the language function is mapped to the labelled cortex of these patients and the variations in the activation location across patients are assessed.

Due to the importance of the accuracy of activation localization in pre-surgical planning using fMRI, and since the conventional methods of smoothing the functional images are prone to the extension of activation across different cortical region, novel approaches to address this issue have also been considered in chapter eight. In this chapter, two new smoothing filters are developed to investigate whether localization of brain activation with fMRI studies can benefit from using the cortical surface-based smoothing. The development of these alternative algorithms is driven by the results of previous studies reviewed in chapter two. The resulting activation maps are then compared to those obtained with conventional Gaussian methods to verify whether these methods can improve the activation localization.

Chapter nine summarizes the findings in all chapters and includes a discussion on the possibilities for future work.

1.2 Background

A considerable number of brain imaging studies using MRI have focused on cortex because of its key role in several brain functions such as cognition. In addition numerous studies have indicated the correlation between neurological diseases or psychiatric disorders and changes in the structural or functional properties of cortex (e.g. Hardan et al., 2006; Kim et al., 2008; Kates et al., 2009; Jouvent et al., 2008; Cachia et al., 2008; Chung et al., 2005; Cycowski et al., 2008; Ecker et al. 2010; Levitt et al., 2003; Nordahl et al., 2007; Penttila et al., 2009 a,b). Hence, reliable estimation of the cortical properties is of paramount importance.

The estimation of the cortical properties has been hugely facilitated since the inception of cortical surface-based approaches which extract the cortical sheet and reconstruct the cortical surface to overcome the complexity of its folded structure (Dale et al., 1999; Fischl et al., 1999a,b; Saad et al., 2004; Van Essen et al., 2005). Such methods were developed to address the shortcomings of the three-dimensional (3D) space for studies concerning cortex which essentially has a

sheet-like structure. A detailed description of some of these methods is presented in chapter two.

Brainvisa is one of the software packages with versatile features from automatic sulci recognition to brain and sulcal morphometry. Unlike the cortical surface-based algorithms, Brainvisa is not limited to cortical analysis and hence is not based on the cortical surface reconstruction. Instead, cortical folds are automatically detected and labelled as cerebral sulci. Its automatic sulci recognition facility is attractive for several reasons. Firstly, manual identification of the cerebral sulci is often challenging even for experienced neuro-radiologists. Therefore, automatic methods can be a useful tool for addressing such difficulties. Secondly, by automatic calculation of different parameters (such as length, volume, depth, coordinates, pattern, etc.) for each sulcus, sulcal morphometry can be used in cross-sectional studies (comparison between different groups of subjects) to estimate the cortical changes due to abnormality. Another attractive feature of Brainvisa is that the analysis is performed in the native space; obviating the need for normalisation to an atlas and therefore avoiding the potential problems with normalisation (see section 1.4).

In the following section of this chapter, the procedure of image analysis using Brainvisa is described. Section 1.4 discusses the potential advantages of using Brainvisa for identifying the eloquent areas with fMRI studies, compared to the conventional approaches.

1.3 MR image analysis using Brainvisa

The automatic analysis of high resolution, 3D, T1-wighted images is achieved within the segmentation pipeline of Brainvisa. The advantage of using 3D images is due to the fact that, as will be seen in chapter four, image resolution plays an important role on the morphometry results. Figure 1-1 shows an example of a 3D T1-weighted image. Grey matter (GM), white matter (WM), and cerebrospinal fluid (CSF) are also shown on this figure.

Different steps of image analysis with Brainvisa are explained in the following sections.

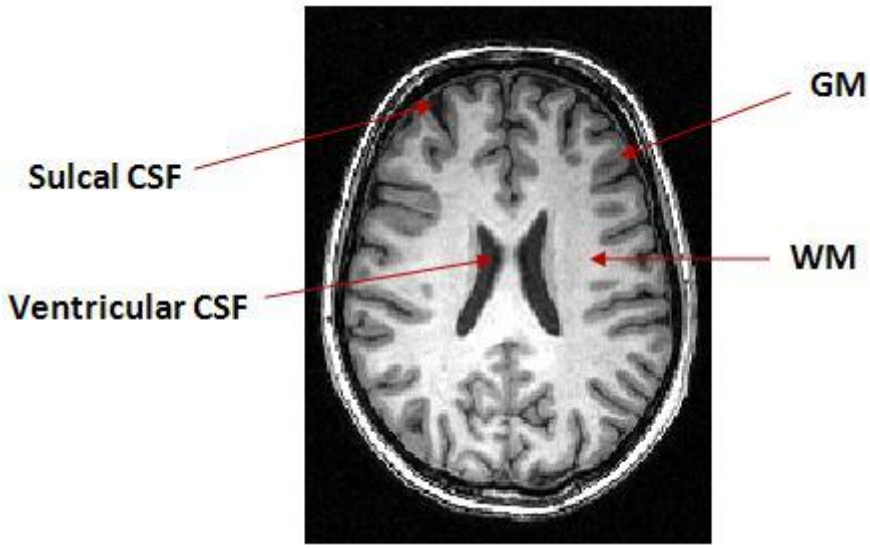

Figure 1-1 An example of a T1-weighted image (shown in axial cross section) GM, WM, sulcal CSF (CSF inside the sulci), and ventricular CSF (CSF inside the ventricles) are shown on this figure.

1.3.1 Bias field correction

The first step includes correction for magnetic field inhomogeneity throughout the image. The magnetic field inhomogeneity (or bias field) causes the signal intensities of a tissue type to vary at different spatial locations (Simmons et al., 1994; Condon et al., 1987). In other words within each tissue, some voxels can be brighter than others, resulting in merging the peaks of different tissues in the image histogram. Thus, to achieve more robust segmentation (which works based on grey-level values), bias field correction is essential prior to segmentation. Field inhomogeneity may mainly arise from the radiofrequency (RF) coils and the imperfect gradient fields or the eddy currents induced by switching the gradient fields. In addition, imperfections in magnet manufacturing as well as the susceptibility artefact especially in the border of tissues with considerably different magnetic susceptibilities can be other sources contributing to the bias field.

The method of bias field correction adopted by Brainvisa makes use of the entropy of signal intensity distribution (Mangin et al., 2000) and is based on the assumption that without the bias field, each tissue type should appear as a sharp peak on the image histogram. In the presence of the bias field however, the histogram peaks are blurred and the image entropy is increased. Hence, applying

a correcting field that minimizes the entropy of the image which is a measure of information contained in the image (or randomness of the values) should lead to the minimization of the bias field. Mangin et al. defined the bias field, F(x), as a smooth multiplicative function for each location x of the image and formulated the output (observed) image, O(x), as:

$$O(x) = I(x)\,F(x) + N(x)$$

1-1

Where I(x) is the original, input image that would have been obtained if the bias field did not exist, and N(x) refers to the white noise (noise with the same power at all frequencies). Bias correction was then achieved by finding the correcting field, F_c, which after multiplication with the observed image (O), would restore the input image (I). The optimum estimation for F_c was chosen as trade-off between minimum entropy of the restored image, minimum difference between the observed (O) and restored image (I), and the smoothness of the correcting field (F_c). Therefore bias correction was driven by finding the function F_c which minimized the function $U(F_c)$ defined by:

$$U(F_c) = K_s S(F_c O) + K_R R(F_c) + K_M M(F_c O)$$

1-2

Where $S(F_cO)$ refers to the entropy of the restored image, $R(F_c)$ is the term which enforces the smoothness of the correcting field, $M(F_cO)$ refers to the difference between the observed and restored images, and K_s, K_R, and K_M are the corresponding constants for each term. Figure 1-2 shows a colour-coded presentation of the signal intensities before and after bias correction. As can be seen, following bias correction the distribution of the signal intensities of each tissue type is more uniform.

Figure 1-3 demonstrates the effect of bias correction on the image histogram and shows that bias correction has separated the GM and WM peaks which had been mingled together before bias correction.

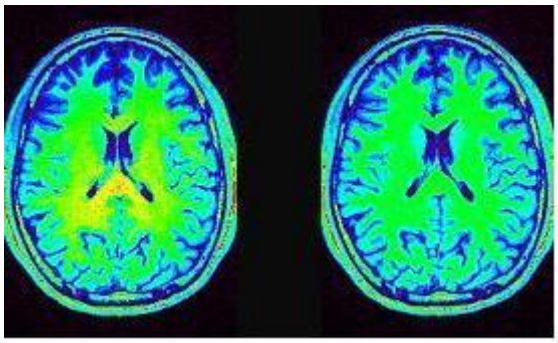

Figure 1-2 The effect of bias correction on 3D T1 image
(left) raw and (right) bias corrected images are colour-coded to clarify the effect of bias correction

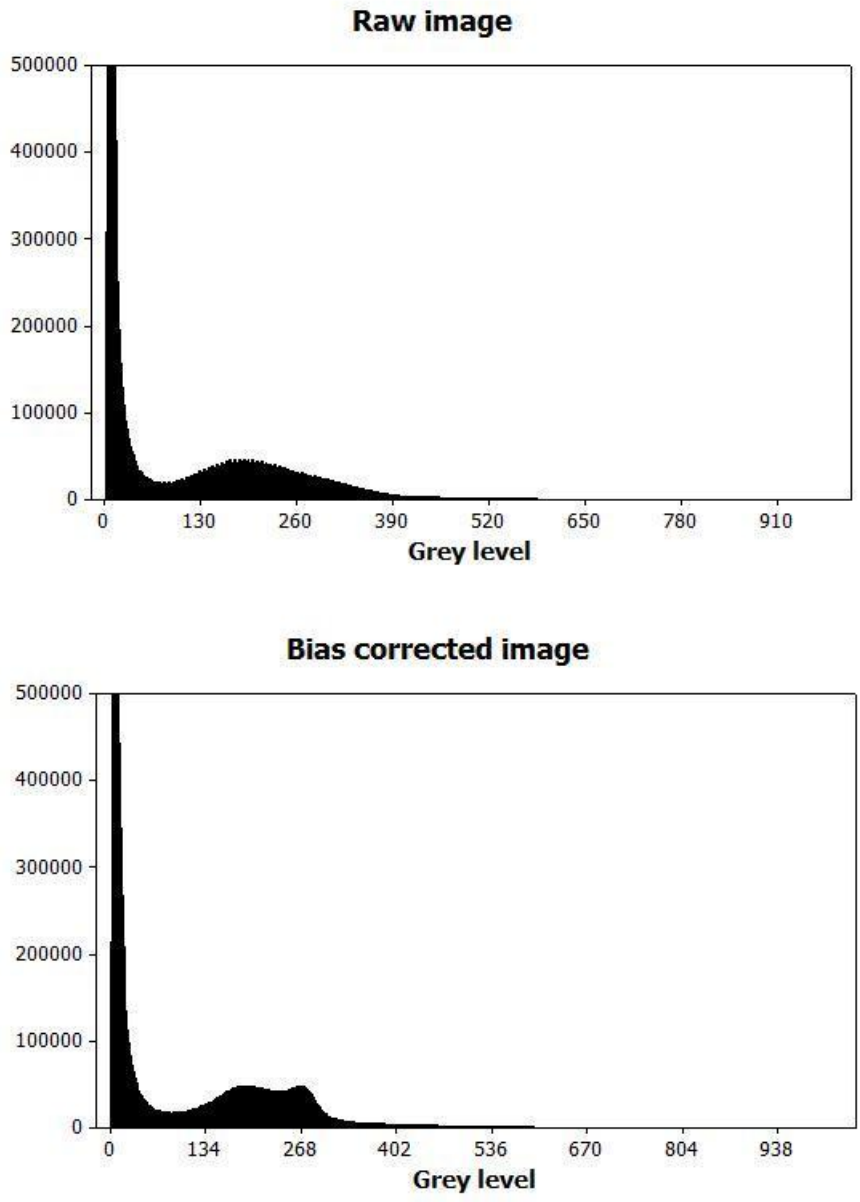

Figure 1-3 The effect of bias correction on the image histogram
(top) the histogram of the raw image, and (bottom) the histogram of the bias corrected image

1.3.2 Histogram analysis

The aim of this step is to estimate the means and standard deviations of the grey-levels for the peaks corresponding to the GM, WM, and CSF from the histogram of the bias corrected image. To increase the peak detection power the derivatives of the histogram were used (Mangin et al., 1998). This can be explained by approximating each peak with a one-dimensional Gaussian function and analyzing its derivatives as demonstrated by figure 1-4. As can be seen the Gaussian function and its first three derivatives have one, two, three, and four extrema (minima or maxima: http://mathworld.wolfram.com/Extremum.html), respectively.

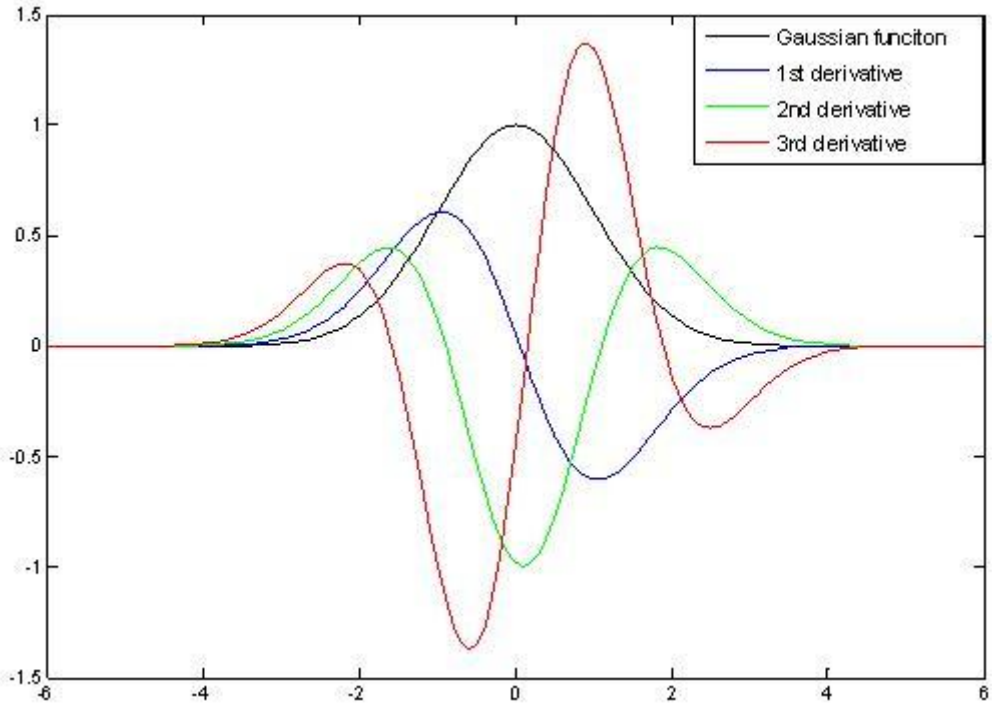

Figure 1-4 The one dimensional Gaussian function and its first three derivatives

When the Gaussian function is smoothed by increasing its standard deviation, its width increases and the extrema of its derivatives move further away from the peak centre. Figure 1-5 shows the trajectory of each extremum (minimum or maximum) when applying a scale-space smoothing (which involves varying filter width) where the higher the scales correspond to the larger filter widths.

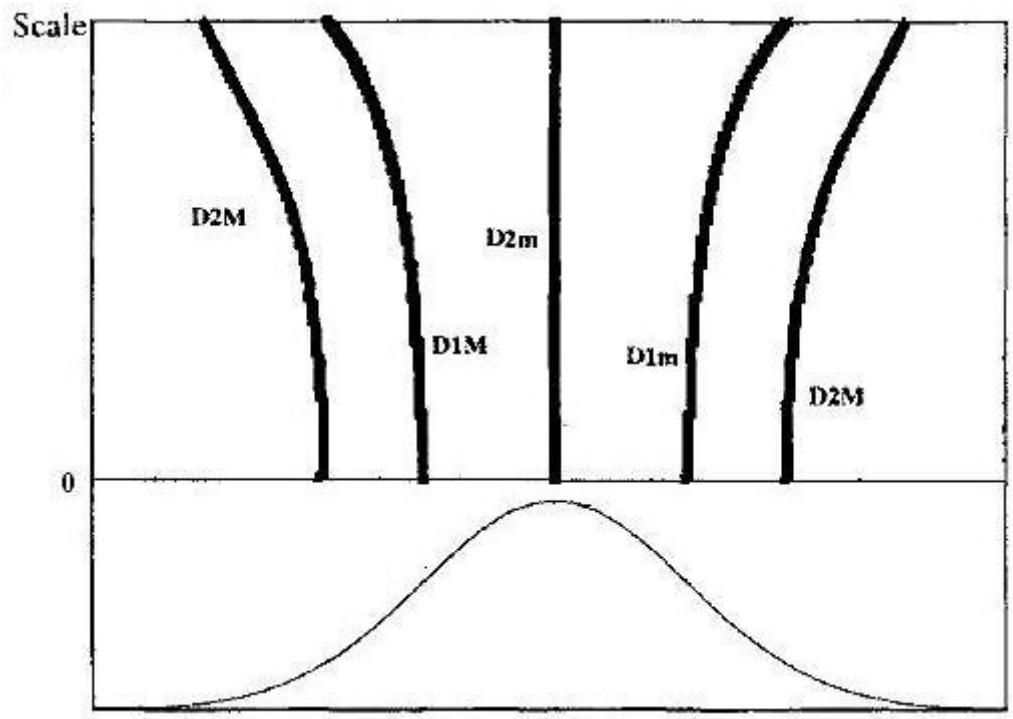

Figure 1-5 The Gaussian function and the trajectories of its first two extrema in the scale space
D1 and D2 represent first and second extremum while M and m correspond to maximum and minimum, respectively.

If the histogram consists of two peaks, defined by Gaussian functions G1 and G2, each derivative of the histogram will be equal to the sum of the derivatives of G1 and G2. Smoothing brings the two peaks closer to each other, making them indistinguishable. Hence increasing the smoothing scale will lead to gradual extinction of their derivatives (singularities) such that the lower order derivatives disappear first. When the smoothing scale is large enough, the extrema pattern will only be distinguishable for higher derivative extrema. This is shown in figure 1-6 which illustrates that the first extrema (green and dark blue trajectories) extinct before second extrema (bright blue and purple trajectories). The order i singularities happen at the same location in the scale space where the trajectories of two i^{th} extrema and one $(i+1)^{th}$ extremum intersect as shown by figure 1-6. The singularities were also shown to correspond to minima of the drift velocity. This pattern of singularities is independent of their relative positions and other parameters.

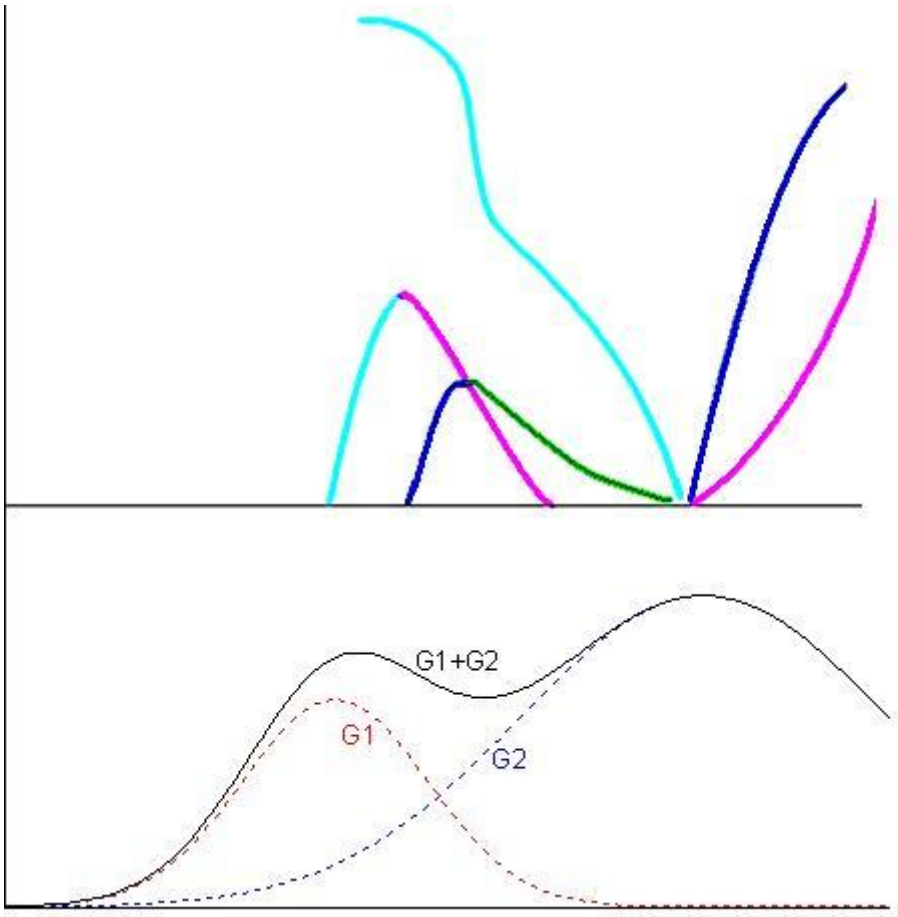

Figure 1-6 The histogram containing two peaks and schematic presentation of the trajectories of its first two derivatives in scale space
The dark blue and green trajectories represent the first derivative extrema and bright blue and purple trajectories correspond to second derivative extrema.

Intuitively the singularities at the highest scales result from merging peaks of different tissues thus represent a combination of different tissues (the whole brain for example), while singularities at the lowest scales should represent minor modes or noise. Extremum trajectories are composed of periods of high drift velocities as well as stable intervals. The stability periods correspond to ranges of smoothing scales where some underlying event is captured. If a peak is relatively symmetric then the location of the minimum of the second order derivative provides a good estimation of the peak mean value (figure 1-4). Moreover, its neighbouring first derivative extrema can be used to estimate the standard deviation, as also shown by figure 1-5.

Briefly, the whole procedure of histogram analysis consists of applying a scale-based smoothing to the first and second derivatives of the histogram until only one second derivative minimum trajectory survives. Then starting from the highest

scales, the locations of the main peaks are found as the locations where the second derivative minimum trajectories show highest minima of drift velocities.

1.3.3 Brain extraction

Using morphological operations the brain was extracted from all other structures e.g. skull, meninges, eyes, etc (Mangin et al., 1998). For this purpose, Mangin et al. first produced a binary mask of the T1-wighetd image and eroded the binary image to remove all the non-brain structures. The largest connected component was then chosen as the seed of the brain and the brain mask was constructed through dilation of the seed conditionally to the initial binary image.

If the sizes of the structuring elements for erosion and dilation are not optimum, the morphological operations may lead to including the non-brain structures in the final brain mask (under-opening) or eliminating some part of the brain, e.g. part of a gyrus, from the mask (over-opening). Thus to reduce the risk of under-opening, a regularized approach was adopted for the initial binarization. The regularization involved setting the low threshold (for binarization) to m_G-$2\sigma_{G,}$ where m_G and σ_G represent the mean and standard deviation of the GM peak and were obtained from the histogram analysis. To reduce the over-opening effect, two morphological openings with two different sizes (large and small) of structuring element were carried out. The large-scaled opening aimed to disconnect brain from non-brain structures while the small-scale opening defined the final brain shape (removing the meninges for example). Figure 1-7 shows an example of the brain mask overlaid on the T1-weighted image.

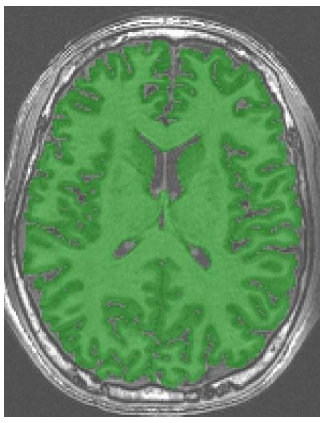

Figure 1-7 Brain mask extraction
The picture shows the overlay of the brain mask (green) on the T1 image.

1.3.4 Split brain

In this step the brain mask obtained in the previous section is split into the two cerebral hemispheres and cerebellum (Mangin et al., 2004). For this purpose the WM mask was first reconstructed through another regularized binarization, using the information about mean and standard deviation of WM (gained from the histogram analysis step). The WM binary image was then eroded until at least one connected component was found in each of the three parts (the two hemispheres and the cerebellum) and was used as the seed point for that region. The erosion process was controlled by a virtual transformation to the Talairach space (Talairach and Tournoux, 1988) and by using a template image (also normalized to the Talairach space) already segmented in the three regions. Then region growing was applied to the seed points to restore the three regions. Figure 1-8 shows the result of this step in dividing the brain into two hemispheres and cerebellum.

Figure 1-8 The brain partitioned in two hemispheres and cerebellum

1.3.5 Brain segmentation

Using information about peaks for each tissue type obtained from histogram analysis, each cerebral hemisphere were segmented into GM, WM, and CSF as shown by figure 1-9

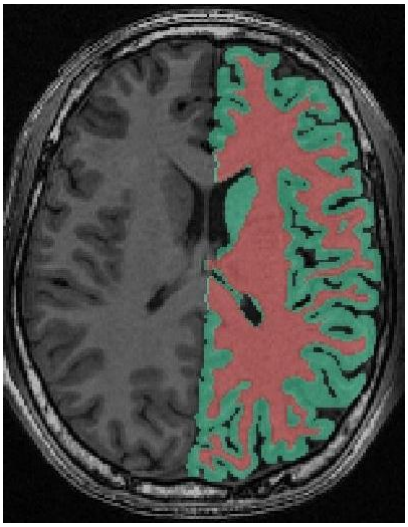

Figure 1-9 A colour-coded representation of segmentation of one cerebral hemisphere

1.3.6 Cortical folds extraction

To extract the cortical folds, Mangin used the idea that if the union of GM and CSF (GM-CSF) is skeletonised the remaining object would define the folds (Mangin et al., 1995). For this purpose, a multi-stage technique was adopted first to produce a representation of GM-CSF with the spherical topology as illustrated by figure 1-10. Figure 1-10a shows an empty parallelepipedic bounding box (O) of GM-CSF as the deformable region, with O_{int} and O_{ext} as its inner and outer surfaces, respectively. To reconstruct the object GM-CSF with spherical topology, the object O was first dilated conditionally to the complement of GM-CSF (figure 1-10b). Then O_{ext} was eroded conditionally to O in such a way that avoids any intersection between O_{int} and O_{ext} (figure 1-10c). At this stage O has been deformed to a thin object representing the brain hull. Afterwards O was dilated to reach the GM-WM interface (figure 1-10 d).

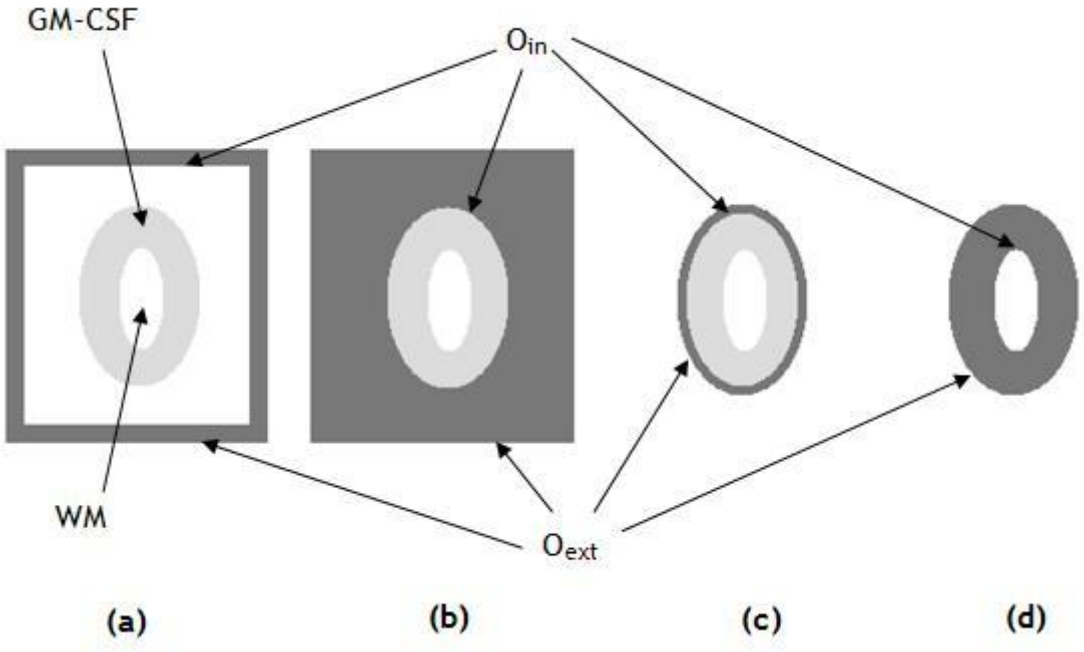

Figure 1-10 Creating a presentation of GM-CSF whilst also enforcing topological constraints

The GM-CSF object (figure 1-11 left) was then skeletonised using topology preserving erosion (figure 1-11 middle). The skeleton points connected to the outside representing the brain hull were removed and the remaining skeleton points were divided into simple surfaces, i.e. pieces of surfaces that do not contain any junctions. Each simple surface represents a cortical fold. Each simple surface was then split further to represent situations where a gyrus had been buried in the bottom of the fold (Mangin et al., 2004). Figure 1-11 (right) shows the cortical folds on a T1-weighted image. The red points represent the fold bottom.

1.3.7 Relational graph reconstruction

The folds and their mutual relationships were gathered in a graph (Mangin et al., 1995). Figure 1-12 shows a schematic explanation of the possible relationships between the related folds and how this information is summarized in the graph. Three kinds of relations exist: topological junction (ρ_T), split induced by a buried gyrus, called a “pli de passage”, (ρ_P), and neighbour geodesic to the brain hull (ρ_C). Each node of the graph (fold) is specified by certain attributes including its links with other nodes. Figure 1-12 also exemplifies how the graph nodes (shown as SS for Simple Surface) can be linked through any of the three possible relationships.

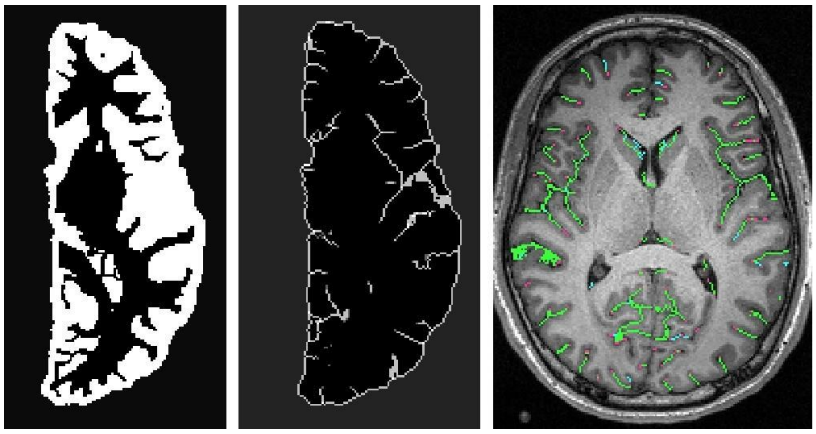

Figure 1-11 Extraction of the cortical folds
(left) the union of GM and CSF, (middle) skeletonisation of the union of GM and CSF, and (right) cortical folds (green) on T1 image

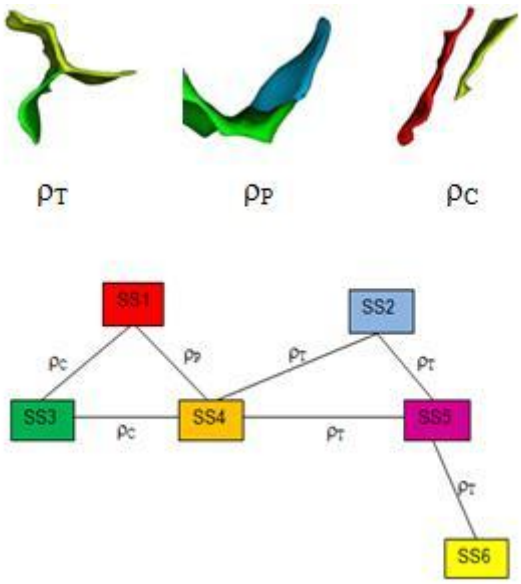

Figure 1-12 Fold graph and their possible relationship
(top) three kinds of relationships between neighbouring folds, (bottom) the folds and their relationships gathered in graph

The graph contains all the information about the folds which will later be used for sulci labelling and morphometry. The folds attributes gathered in the graph also include attributes such as size, minimum/maximum depth, gravity centre coordinates, mean direction, mean normal direction, and the coordinates of the end points.

1.3.8 Sulci recognition

The folds gathered in the relational graph structure are grouped together to form the sulci. The sulci recognition algorithm uses prior knowledge to group several folds forming each sulcus (Perrot et al., 2008; Perrot et al., 2009).

Cortical topography (folds and their junctions) and the folding pattern are highly variable across individuals. For example a sulcus that appears as a continuous fold in one brain may be composed of several, seemingly independent folds in another brain. For this reason, Le Goualher et al. generated a probabilistic model of the sulci, accounting for normal variability (Le Goualher et al., 1998). First they used automatic methods to extract the cortical topography of 51 brains registered to the Talairach atlas and manually labelled 16 sulci on those brains. Then by averaging the 51 labelled graphs, they produced a 3D probabilistic map for each sulcus, i.e. the probability that a certain voxel belongs to a sulcus.

Perrot et al. used the probabilistic Statistical Parametric Anatomy Map (SPAM) model (Le Goualher et al., 1998) as the prior information about sulci locations. The SPAM model returns the probability of presence of each sulcus at a given 3D location. They used the SPAM model within a Bayesian framework (http://plato.stanford.edu/entries/bayes-theorem/) for sulci labelling. For each brain registered to the Talairach atlas, the SPAM model returns the probability of finding a given sulcal label, L_i, at the location D, which can be expressed as $P(D|L_i)$. Then for each fold of the graph, the probability that it can be labelled as L, or $P(L_i|D)$, can be obtained according to Bayes theorem using posterior probability:

$$P(L_i|D) = \frac{P(D|L_i)P(L_i)}{P(D)} \qquad \textbf{1-3}$$

Where $P(L_i)$, the probability of finding a sulcus somewhere in the whole brain, is obtained from the prior knowledge for that sulcus, and P(D) is the probability of finding any sulcus at that location which is obtained by summing over the probabilities of all sulcal labels:

$$P(D) = \sum_{L_i} P(D|L_i)$$

1-4

Hence, the sulci labelling was carried out by maximizing $P(L_i|D)$ or finding the most probable L_i at the given location. The Maximum A Posteriori (MAP) estimator, $\hat{L}_{MAP}$, was therefore calculated by:

$$\hat{L}_{MAP} = \arg\max_{L} P(L|D)$$

1-5

This Talairach-based method is easy to implement, however registration of different brains to the Talairach atlas does not reliably result in the alignment of their sulci (see chapter two for a detailed discussion). For this reason, Perrot et al. examined several other methods to obtain more reliable co-registration between the same sulci of different individuals and hence more accurate SPAM models (Perrot et al., 2009). This involved re-estimation of the registration parameters as well as redefining the SPAM model for each sulcus. It should be noted that sulci alignment and sulci labelling are two inter-related procedures. On one hand, an alignment method which aims to align the same sulci to a model requires that sulci be labelled, whilst on the other hand when the sulcal location changes as a result of the alignment process, its label can also change to match the SPAM model for this new location. Therefore, an iterative approach of joint registration and labelling was adopted which was based on consecutive optimisation of the registration parameters and sulci labelling. As before, the optimisations were carried out using MAP estimation within the Bayesian framework.

The SPAM model was estimated through joint registration and model selection using a training database. Once the model is known using the training database, sulci identification for any other brain can be achieved through joint registration and labelling while maximizing the posterior probability as explained before.

Perrot et al. applied two different techniques for registration, namely “global” and “local”. The global method consists of a rigid body registration with the same registration parameters (rotation, R_g, and translation, t_g) for all sulci. The local

method uses a sulcus-wise non-linear registration, trying to find registration parameters for each label separately. For applying the local method, the brain is first (jointly) registered and labelled using the global method. Then each sulcus undergoes a rigid body registration with its own specific registration parameters so as to optimize the registration on a sulcus-by-sulcus basis.

They also added another option, the “Markovian” algorithm, which similarly to the local method follows the global registration, but uses the information about the relations and distances between neighbouring sulcal segments for labelling the sulci.

To estimate the recognition rate, they used the leave-one-out method for a database of 62 subjects. This involves using all brains but one to estimate the SPAM model. The remaining one was then labelled according to the obtained model and the error rate of labelling was computed. For each sulcus, the estimation of the error rates was performed by calculating the false positives (voxels erroneously labelled as belonging to that sulcus) and false negatives (voxels erroneously excluded from that label) in comparison with the manually labelled brain. They showed that with their sulci recognition algorithm a global recognition rate of 86% (14% error rate) was obtained.

1.4 Using Brainvisa for identification of eloquent cortical areas

The complexity of associating function with anatomy arises from between-individual difference in the activation pattern leading to uncertainty about the appropriate anatomical label that can best be associated with activation (Brett et al., 2002; Delvin et al., 2007).

A widely used anatomical label is the 3D coordinates of the activation foci with reference to an atlas. This often requires normalization of each individual brain to a template. Therefore each point in the brain is assigned a unique set of coordinates and the activated regions can be specified by spatial coordinates. Group studies can be performed by averaging all individuals’ activation maps since all activation maps are in the same space. The advantage of between-individual averaging is the potential increase of the statistical power. Two well-

known 3D atlases used for this purpose are the Talairach and MNI (Evans et al., 1993, 1994) atlases.

Talairach and Tournoux used a single post-mortem brain as the template and created an atlas that has been widely used since then by defining a coordinate system to identify each point in the brain. In this coordinate system, the Anterior Commissure (AC) was regarded as the origin and the brain was rotated so that the line connecting AC and the posterior Commissure (PC) was in the horizontal direction describing the y-axis with the inter-hemispheric fissure in the vertical plane. The z-axis was defined as the line in the vertical plane that passes through AC and is perpendicular to the y-axis. Therefore the x-coordinate indicates whether a point is in the left or right hemisphere. Only one hemisphere was presented in any detail, assuming symmetry between the two hemispheres.

To align a brain with the Talairach and Tournoux atlas, AC and PC are found in the brain and the brain is aligned with the Talairach axes first. Then the AC-PC distance is altered so that PC coincides with the PC in the atlas. The distances between the AC and the top, bottom and sides of the brain and between the PC and the back of the brain are also rescaled to match the atlas. This transformation is termed the Talairach proportional grid normalization. Therefore each point in the brain is identified using the reference from the atlas.

The main drawback with the atlas of Talairach and Tournoux is that it has been constructed from a single brain whereas the brain shape varies considerably with race, age, sex, etc. Therefore, the Talairach and Tournoux atlas may not be a precise representative of all brains.

In addition, the areas of activation expressed in the coordinate system of Talairach and Tournoux, are extensively related to the Brodmann's areas (Brodmann, 1909). However, cytoarchitectonic area extent and location could be inaccurate on the Talairach brain (Brett et al., 2002). Furthermore the variability in location and extent of cytoarchitectonic areas means that Brodmann area assignment on the basis of spatial location is prone to error (Uylings et al., 2005; Amunts et al., 1999).

To address the inaccuracy of the Talairach and Tournoux atlas, the Montreal Neurological Institute (MNI: http://www.mni.mcgill.ca/) created the MNI atlas which

was also adopted by the International Consortium of Brain Imaging (ICBM: http://www.loni.ucla.edu/ICBM/) as an international standard atlas. The first MNI template, MNI305, was created using a two-stage process (Evans et al., 1993). First, 250 brains were oriented and scaled to the Talairach brain manually. The next 55 images were then registered to the average of the 250 first-pass images using automatic linear registration and averaged to obtain the MNI305. The MNI 305 brain was made up of all right handed subjects (239 M, 66 F, age 23.4 +/- 4.1). The current standard MNI template, known as the ICBM152, is the average of 152 brains that were registered to MNI305 using a 9 parameter affine transform (Evans et al., 1994). The MNI also created a high quality image of a single individual, known as colin27, which was an average of 27 co-registered scans of the same person, normalized to MNI305.

Macro-anatomical features (specific cortical area or deep brain structure) can also be used for activation attribution. These features are especially popular for parts of the brain which are known to be involved in certain types of cognitive tasks. For example, the Heschl's gyrus is known to be associated with the primary auditory cortex even though the number and size of these gyri is variable among individuals (Penhune et al., 1996; Rademacher et al., 2001). Other examples include pre- and post-central gyrus which is involved in sensorimotor activation (Sunaert, 2006) and the role of the occipital lobe in visual activation (Goebel et al., 1998; Sereno et al. 1995).

It has been shown that due to the normal variability in cortical patterns, the same sulci can be found at different location on different brains (Szikla, 1977). It has been suggested that 3D normalization may not necessarily align the cortical regions accurately (Anticevic et al., 2008) resulting in erroneous localization of activation (given the established relationship between cortical regions and activation). Furthermore fMRI group studies can suffer from such misalignment and the statistical power can be reduced.

As mentioned earlier, Brainvisa produces the sulcal labels in the native space (although a virtual transformation to a common space is used for sulci recognition, the final results are obtained in the native space). By identification of cortical sulci, the activation foci can be attributed to cortical regions, obviating the need for normalization.

1.5 Discussion

Brainvisa provides a wide range of possibilities for MRI studies. These include automatic labelling of the cortex, brain morphometry (such as brain tissue volumes), and cortical morphometry (for example gyrification of the cortex as well as sulcal attributes such as volume, length, depth, etc.).

The automatic sulci recognition is promising given the fact that manual identification of the sulci is usually challenging even for experienced neuro-radiologists. The sulcal attributes can then be automatically computed using the package. The automatic sulci identification can also be helpful in finding the eloquent cortical regions in fMRI studies avoiding the problems with normalization to an atlas.

Due to the complexity of most neurological diseases and psychiatric disorders, there is still an ongoing attempt to find new possibilities for cortical analysis. A considerable number of studies have focused on finding new biomarkers for abnormal brain in cross-sectional studies. Morphometry has been shown to be successful in finding biomarkers of neurological diseases or psychiatric disorders (Thompson et al., 2003; Garcia-Marti et al., 2008; Shenton et al., 2001; Bigler et al., 2010; Kim et al., 2008; Moorhead et al., 2007). However, as the abnormality related difference is usually small and can be overshadowed by subtle inaccuracies and remain undetected, it is important to assess the robustness of this software package and the reliability and reproducibility of the morphometry results. The factors which can impact the accuracy need to be identified and taken into account or controlled where possible.

Chapter 2. Literature review

2.1 Overview

This chapter includes a detailed review of the most widely used cortical surface-based methods and what has been achieved by these methods. Some studies on possible benefits of these methods in between-individual alignment of the cortex and how fMRI studies can benefit from these approaches have also been reviewed. The chapter ends by a discussion on how the findings of the reviewed studies can be used in this thesis.

2.2 Background

The rationale of surface-based approaches for cortical analysis is due to the fact that cortex is essentially a folded sheet. Thus, firstly because of its sheet-like structure and topology, the cortex may not be best characterized using the 3D space and secondly, the folds bring the distant cortical regions closer making the 3D, Euclidean distances ineffective. In other words, the neighbouring voxels on cortex do not necessarily correspond to the neighbouring regions on the cortical sheet. This is illustrated by figure 2-1 for the two points shown by the arrows. This can also be problematic in fMRI studies which aim to identify the eloquent cortical areas near deep sulci. In such cases, even a small error in the localization of brain activity can become more pronounced by attributing the activation to the opposite bank of a sulcus or the opposite gyrus (Brett et al., 2002). Consequently cortical studies can benefit from approaches that take its specific structure and topology into account.

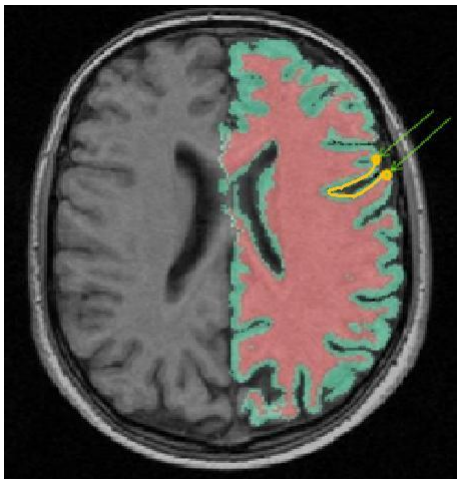

Figure 2-1 The effect of cortical folds on reducing the 3D distance between different cortical regions

Another aspect of the inaccuracy of the 3D space for cortical analysis is the between-subject brain alignment. Due to the between-subject variability in cortical folding pattern, the same sulcus (or gyrus) can be found in different locations among individuals (Szikla, 1977). As a result, 3D-based methods of brain registration may be inaccurate for aligning the cortical sulci (Fischl et al., 1999b; Anticevic et al., 2008). The accurate alignment of cortical regions can improve the statistical power in fMRI group studies where the same cortical region is expected to be activated in all subjects.

Cortical surface-based registration methods, which aim at registering cortical features e.g. sulci, have been considered to achieve more robust between-subject registration. Many of these methods use a two-dimensional (2D) coordinate system and atlas. This is discussed in more detail in the following sections.

2.3 Cortical surface reconstruction

High resolution, 3D T1- weighted images are often used for cortical-based analysis. Several approaches have been suggested for automatic detection of the complex pattern of the cortex whilst reducing the probability of errors arising from limitations such as magnetic field non-uniformity, spatial resolution, noise, etc.

Cortical surface reconstruction algorithms are divided into two categories: bottom-up methods (e.g. Dale et al., 1999) which segment the cortex on a structural MRI volume and create a mesh from the cortex boundaries, and top-down methods

(e.g. Kim et al., 2005) that start with a polygonal mesh and use deformation-based algorithms to deform it until the cortical mesh is obtained (figure 2-2).

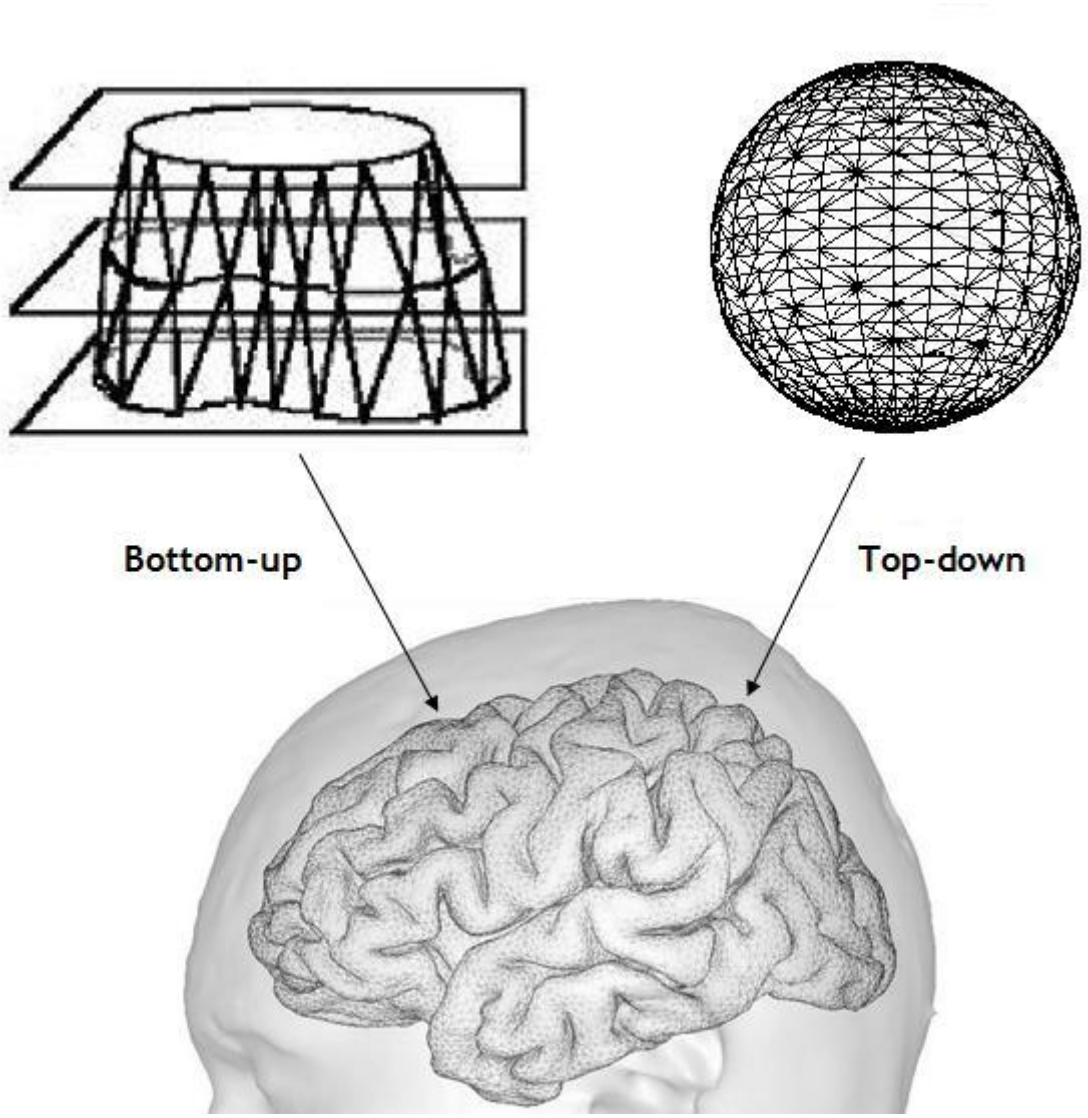

Figure 2-2 Bottom-up and top-down methods of cortical surface reconstruction

The top-down methods are based on the fact that in each hemisphere, the borders of the cortex (borders with the white matter or the pial surface) have the topology of a sphere, i.e. they can transform into a sphere under deformations such as stretching or bending. Thus, the original polygonal mesh (with a spherical topology) can be deformed to the cortical surface.

Cortical surfaces can be reconstructed to represent the boundary between the GM and WM, commonly called WM mesh, or the pial surface. Pial surface reconstruction however, is susceptible to errors arising from the partial volume effect. The partial volume effect refers to situations where some voxels at the

boundary between two different tissue types contain both tissue types. Even in high resolution images, some voxels in the sulci can contain both CSF and GM. As a result, for tight sulci where the distance between the opposite banks of a sulcus is smaller than the resolution of the MR image, the CSF inside that sulcus may remain undetected and the reconstructed surface fails to go deep down the sulcus causing the sulcal wall to appear fused. Figure 2-3 shows an example of WM mesh and pial surface.

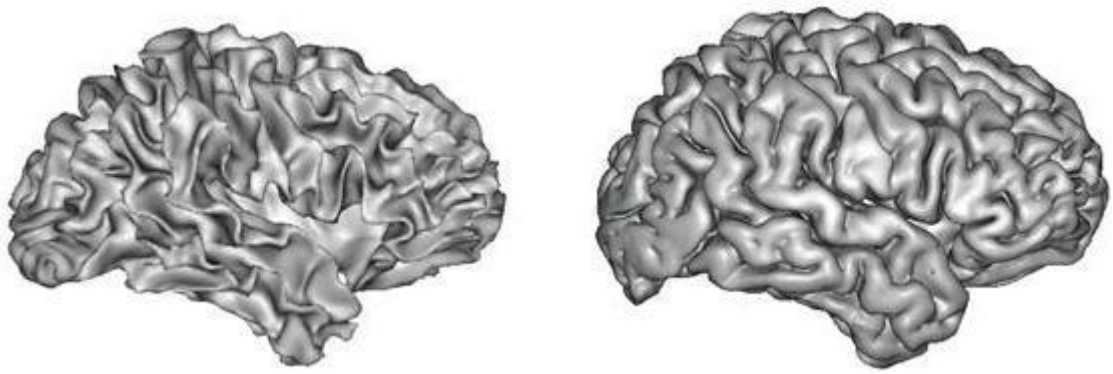

Figure 2-3 Reconstructed cortical surfaces
(left) WM mesh, and (right) pial surface

Dale et al. introduced an automated method of cortical reconstruction (Dale et al., 1999). Their method included several steps for bias field correction, brain extraction, brain segmentation, hemisphere separation and cortical surface reconstruction.

To find the bias field at each point on the image, they first smoothed the histogram of each axial slice to reduce the noise and then found the WM peak (the rightmost peak) in the histogram. After removing the outliers, they defined a coefficient for each point in the z direction (long axis of the bore) by interpolating the WM peaks for different slices. These coefficients were then used to adjust the intensities of the x-y plane. The remaining bias field was then iteratively estimated and corrected by automatically detecting a set of control points which, from the information about their intensity and neighbourhood, were determined to represent WM. They used the intensity of the control points as an estimate of the remaining bias field. Other points were assigned the bias field value of their closest control point (Voronoi partitioning: Aurenhammer et al., 2000). Finally the estimated values were used to scale each point's intensity to correct for the bias field.

The next step included skull-stripping the image using a tessellated ellipsoid positioned inside the brain which was iteratively deformed to match the brain. Two forces were used to drive this deformation process: an MRI-based force which pushed the ellipsoid outward from the brain towards the CSF surrounding the brain, and a curvature reducing force acting as a smoothing constraint on the deformation.

For brain segmentation, they first performed a preliminary tissue classification based on the voxel's neighbourhood and the bias corrected intensities by applying predefined upper and lower thresholds for WM as well as the upper threshold for GM. For voxels which could not be clearly labelled as either of the two tissue types from the intensity and neighbourhood information, a plane-of-least-variance was determined by calculating the intensity variance within slabs of voxels with different orientations, distributed uniformly over the unit hemisphere. The preliminary classification of the ambiguous voxel was then reversed if a significant number of voxels within this slab-of -least-variance were labelled as a different class.

Then two cutting planes, an axial plane through the pons and a sagittal plane running through the corpus callosum were used to exclude subcortical structures and separate the two hemispheres. Using connected-component analysis regions with no connectivity to WM were removed and the regions with no connectivity to the WM complement were filled and added to it. Lastly, a triangular tessellation was used to reconstruct the meshes for WM and the pial surface.

MacDonald et al. used a top-down approach by simultaneous deformation of multiple surfaces whilst avoiding inter-surface constraint and self-intersection by using the expected cortical thickness as a constraint for the deformation process (MacDonald et al., 2000). Their algorithm which they called Anatomic Segmentation using Proximity (ASP), used a function to push each vertex on the deforming surface which consisted of six terms: a) an image term corresponding to the distance from a vertex on the deforming surface to the nearest image boundary in the direction of the local surface normal, b) a stretch term which controlled each edge length (for any two neighbouring vertices) by making it as close as possible to a predefined value, c) a bending term that tends to change the surface so that its shape matches a model, d) a self-proximity term to prevent the

non-adjacent polygons in a polyhedral mesh from getting closer than a set threshold and hence avoid self-intersection, e) an inter-surface proximity term to prevent the pial and WM surfaces from coming within a certain distance to each other, and f) a term enforcing vertex-vertex proximity constraint, taking into account the fact that the distance between corresponding vertices on the pial and WM surfaces (vertices with the same index i on the two surfaces) need to be as close as possible to a set value (the expected cortical thickness).

To avoid using a predefined cortical thickness which often is not a valid assumption throughout the cortex, Kim et al. proposed a modification to the ASP algorithm mentioned above which they called Constrained Laplacian Anatomic Segmentation using Proximity (CLASP). Instead of using any assumptions about a cortical thickness value, they used an estimation of the partial-volumed voxels for reconstructing the pial surface (Kim et al., 2005). Following signal inhomogeneity correction and brain extraction, they used a k-nearest neighbour algorithm (Lemm et al., 2011) to classify each voxel as GM, WM, or CSF based on the grey level values and spatial priors about the probability of each voxel belonging to a given tissue type. A statistical map for partial volume effects was then used to label the voxels as mixed (containing more than one tissue type) or pure. The fractions of each tissue type within mixed voxels were calculated using maximum likelihood estimation (Harris et al., 1998). The partial volume CSF (including all voxels with some CSF content) was binarized (corresponding voxels were set to 1 and the remaining voxels that did not contain CSF were set to 0) and then skeletonised (figure 2-4).

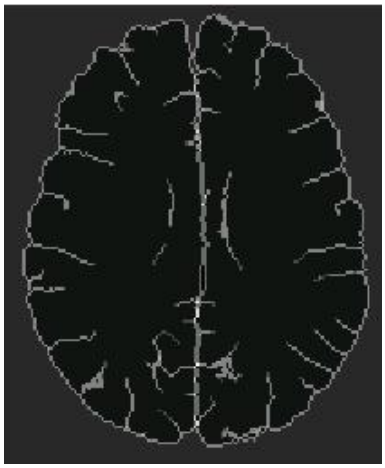

Figure 2-4 The skeletonised CSF
For illustration purposes only

The surface reconstruction was based on finding the GM-WM interface for each hemisphere separately and expanding the GM-WM surface to reach to the skeletonised CSF in such a way that was also controlled by the Laplacian field between the two surfaces. This can be thought of as assigning a low value to one surface and a high value to the other. As the values are constant throughout each surface, the Laplacian will have smaller values in thicker and larger values in thinner parts of the cortex. Thus, the expansion driven by the Laplacian would result in a coherent expansion to the pial surface. In other words, the pial surface is expanded slowly in regions of thinner cortex and expanded faster in the thicker parts of the cortex. This was done to ensure that every vertex on the surface moves to the outer boundary of GM at a uniform rate, proportional to the local thickness, and hence the local variations in cortical thickness are preserved.

2.4 Surface-based coordinate system

Starting from the cortical surface reconstructed by Dale et al., Fischl et al. continued by further processing of the cortical surface through unfolding the cortical mesh and established a surface-based coordinate system (Fischl et al., 1999a).

To unfold and inflate the cortical mesh, they defined an energy function, which when minimized, would unfold the mesh while keeping metric distortion to a minimum. The term included in the energy function for minimization of the metric distortion was obtained from the difference in the geodesic distance between vertices (the distance between vertices along the cortical mesh) in the deformed surface from those in the original (folded) surface. Inflating the cortical surface was achieved by defining an energy function which contained two terms: a spring force to smooth the surface and a metric preservation term. The inflation process was driven by the average convexity of the region. In other words, points lying on the concave regions moved outward during the inflation process while the convex regions moved inward. By integrating normal movement, average convexity at each vertex was calculated with either a positive or negative value representing sulcal or gyral regions, respectively. They showed that average convexity could capture the major sulci, while being relatively insensitive to the small folds that typically occur on the banks of the sulci. Mean curvature, on the other hand, attains equally high values for small secondary and tertiary folds in a surface as for

the primary folds. An example of maps of the mean curvature and the average convexity on the inflated cortical surface is shown in figure 2-5.

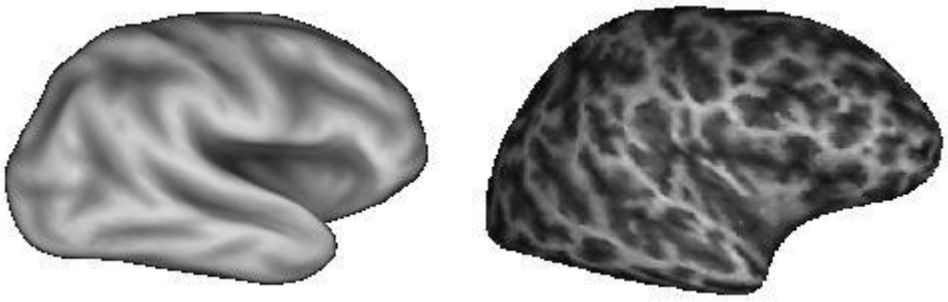

Figure 2-5 The folding pattern on the inflated cortical surface
Map of (left) average convexity, and (right) mean curvature

By projecting the inflated cortical surface onto the unit sphere such that each vertex was projected to the closest point on the unit sphere, and then unfolding the surface to minimize the geometric distortions introduced during inflating and projection steps, a spherical representation of the cortical surface was obtained. To ensure that the surface is completely unfolded, an oriented area was defined for each triangle in the tessellation such that it could take negative or positive values if the triangle was on a folded or unfolded area, respectively. Minimization of the energy function would then avoid negative oriented areas. This is illustrated in figure 2-5 for three neighbouring vertices of the triangular mesh i, j, and k. The vector A is defined so as to have a magnitude equal to the area of the triangle defined by the three vertices and a direction normal to the triangle. By defining n as the unit vector normal to and pointing outwards from the sphere, an oriented area, A_n, can be defined (as shown by figure 2-5) such that it can take both positive and negative values.

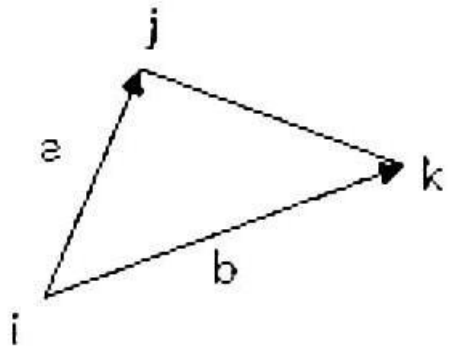

$$A = \frac{a \times b}{2}$$

$$A_n = A.n$$

Figure 2-6 Definition of areal term for the energy function using oriented area

The software package “FreeSurfer” which is based on the algorithm discussed above is extensively used in cortical morphometry.

2.5 Between-subject alignment

Using the spherical representation of the cortical surface of 40 subjects, each with its own convexity pattern, Fischl et al. computed the average spherical atlas of cortical pattern (Fischl et al., 1999b). Each point on this spherical atlas was then indexed using its longitude and latitude. Each individual brain could then be registered to this atlas by first creating a spherical representation of the cortical surface and then aligning its folding pattern (convexity map) to the atlas while keeping metric distortion to a minimum and avoiding addition of the fold as explained in section 2.4.

They showed that the alignment of major sulci is considerably improved with their method compared to the Talairach method. They also used a retinotopic mapping experiment (De Yoe et al., 1996; Engel et al., 1997; Sereno et al., 1995) to compare the spread of the average map obtained by the two methods and showed both visually and quantitatively that their method of between-subject alignment resulted in less blurred functional maps. However it should be noted that the Talairach atlas may not be an accurate representative of other brains as stated before and therefore registration to other atlases such as MNI might result in better sulci alignment.

Saad et al. proposed to use a standardized cortical mesh for each individual to facilitate between-subject averaging (Saad et al., 2004). To create a standard mesh, they started by inflating the cortical mesh to a sphere and warping it to match the template sphere according to its sulcal patterns according to the method described above (Fischl et al., 1999a). Then a standard triangulated icosahedron with a certain number of nodes, whose co-centered sphere has a radius equal to that of the warped sphere, was projected onto the warped sphere. The projection entailed finding the coordinates of each node of the icosahedron by interpolation from its neighbouring nodes on the warped sphere. This approach results in having the same number of nodes in each individual cortical mesh where each node’s index would define a specific anatomical location in every individual’s cortex. Thus, the between-subject averaging could be facilitated using a node-

based analysis. They presented a software package based on their method which they called SUMA.

Van Essen et al. created a Population Average, Landmark and Surface based (PALS-B12) atlas of human cortical surface, which was derived from the structural MRI volumes of 12 normal subjects (Van Essen et al., 2005). For this purpose, they first registered 12 structural images to the Washington University stereotaxic atlas, 711-2C, which is the average of 12 subjects (Buckner et al., 2004) followed by non-uniformity correction, segmentation, and cortical surface reconstruction. The reconstructed mesh ran half way through the cortex (the midline between GM-WM interface and the pial surface). Cerebral hull, which can be thought of as the layer covering the outer surface of the cortical mesh, was produced by applying a series of dilation and subsequent erosions to the initially segmented surface. When the original cortical surface is overlaid on the cerebral hull, the regions corresponding to gyri fall outside the cerebral hull while the sulcal regions fall inside. They created a map of sulcal depth which was defined as the 3D distance from each vertex of the surface to the nearest point on the cerebral hull. The sulcal depth was used as an alternative to the average convexity used by Fischl et al., to capture both coarse and fine shape attributes. They also produced the map of cortical geography defining the sulcal and gyral areas (figure 2-7).

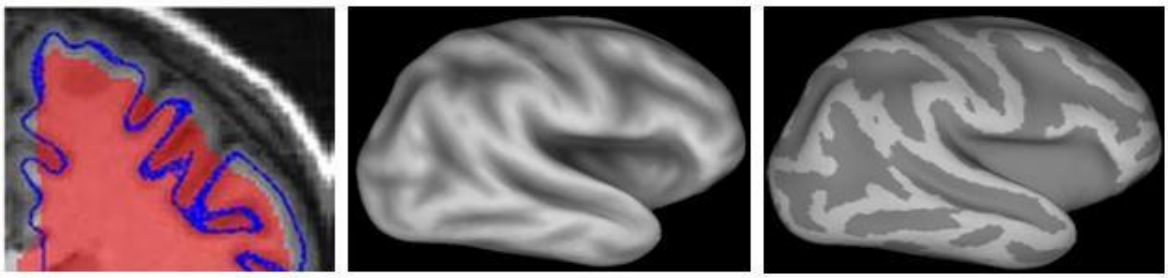

Figure 2-7 Using the brain hull to produce sulcal depth and geography maps
(left) brain hull (red area) and cortical surface (blue line) are shown on T1 image, (middle) map of sulcal depth, and (right) cortical geography on the inflated cortex.

For each subject, they delineated six well-defined and consistent landmarks and projected them to a standard spherical mesh to obtain the average landmark contours for left and right hemispheres. The right and mirror-flipped version of the left landmark contours were averaged to obtain the PALS-B12 atlas to represent each hemisphere.

Van Essen et al. assembled the whole algorithm in the software package Caret (http://brainvis.wustl.edu/caret).

2.6 Application of the surface-based approach in fMRI

Owing to successful cortical surface reconstruction and between-subject registration, researchers have been interested to explore whether this technique provides more accuracy in fMRI analysis. This requires mapping the functional data (either the functional images or the activation map, both of which have volumetric format) to the cortical surface. In other words, each vertex on the cortical surface is assigned a corresponding value from the functional data. In practice various possibilities exist for mapping. Bearing in mind that activation occurs across the whole thickness of the cortex whereas the cortical surface only represents a thin layer of cortex (chosen as GM-WM interface, pial surface, or between these two boundaries), the precise method of mapping can have a great influence on the final results. The simplest and possibly easiest to implement method is using the intersection of the functional data and surface and assign to each vertex the value of the voxel in which it resides. However, if the GM-WM boundary or pial surface is used to represent the cortical surface, with an intersection-based algorithm, a major part of activation (activated voxels inside the GM) may not be mapped onto the cortical surface. To address this problem two methods have been suggested (Desai et al., 2005): the Centre-of-Normal (CN) method which aims at finding the normal to the GM-WM surface at each vertex and sampling the voxel that is closest to centre of GM on this normal, and the Two-Surface (TS) method which maps the maximum activation across the cortical thickness to the surface. The TS method uses the pairs of corresponding vertices on GM-WM and pial surfaces to find the maximum activation along this segment.

Desai et al. compared the effect of surface-based and Talairach registration in auditory activation localization as well as the precision of between-individual alignment (Desai et al., 2005). For surface-based alignment, they tried two approaches: Landmark Based Warping (LBW), which aligns the brains according to landmarks using a flattened representation of the cortical sheet (e.g. Van Essen et al., 1998) and Automated Spherical Warping (ASW), which involves registration to the spherical atlas of the cortical surface (Fischl et al. 1999b). They also added smoothing for registration to the Talairach atlas to account for between-individual

differences ad examined its effect (blurred Talairach or TLB). Individual brains and statistical maps were smoothed and projected to the Talairach space. Cortical surface was reconstructed using FreeSurfer and a flat map of a region containing the areas involved in an auditory task was created. For displaying group data, they used the Colin anatomy, or N27, (Holmes et al., 1998) and created the same flat map on it as described above. For the LBW method, they chose five gyri (or parts of them) as landmarks and registered individual cortical surfaces to the flat map of N27 brain. For the ASW method, spherical surfaces were created and registered to the canonical spherical surface, using FreeSurfer. Using SUMA, standard meshes were created for each subject as well as the template brain to assign a one-to-one correspondence between nodes of different standard meshes. Maps of functional activity were first obtained in the 3D space and then mapped to the cortical surface. For mapping the functional data, they used both CN and TS methods. The TS method was shown to capture more activation for their experiment.

Using each of the four methods: Talairach (TL), blurred Talairach (TLB), LBW, and ASW, the functional data for each subject were mapped onto the template N27 brain. With the exception of TLB, a small amount of smoothing was applied on the template surface by averaging the activation of each node with that of its neighbours and the group analysis was then performed. For each subject they calculated mean activation with all the four methods (TL, TLB, ASW, and LBW) using ROI-based analysis of functionally active regions and showed that with both ASW and LBW methods only one activation patch was observed on the superior temporal gyrus while TL and TLB methods also resulted in another patch on medial temporal gyrus. Since the individual maps did not include activation on medial temporal gyrus, they concluded this was due to better registration of these two gyri with ASW and LBW compared to TL. Moreover, due to between-individual differences in the precise location of Heschl's gyrus along the ventral–dorsal axis as well as along the anterior–posterior axis and consequently less group overlap on the Heschl's gyrus, this gyrus was less activated with TL and TLB methods than ASW and LBW. The results showed that the TLB method does not show superiority over TL, suggesting that smoothing did not compensate for anatomical variability.

To compare the anatomical accuracy of the alignment obtained by each method, certain points were selected on the flat map for each subject and the surface coordinates of each point were computed. For each point, they calculated the group mean coordinates and the average of the distance from this mean, which they defined as the Dispersion Radius (RD). They showed that while the LBW method shows considerable superiority over the Talairach method with respect to the alignment (smaller values of RD for all points), the ASW method only slightly improves the alignment with RD values slightly smaller than those with the Talairach method. They hence concluded that firstly, cortical surface-based methods were more successful in alignment of cortical regions compared to Talairach-based approaches and secondly among surface-based methods, landmark-based methods resulted in even more accurate alignment than methods based on spherical warping.

Argall et al. compared the result of registration to the Talairach atlas and surface-based registration on the average functional map for motor, visual, and auditory activations (Argall et al., 2006). They first reconstructed cortical surfaces and their spherical representation using FreeSurfer. Each brain volume was aligned to the Talairach atlas. Then using the method proposed by Saad et al., they standardized each cortical mesh such that each node index would roughly correspond to the same location in all brains. Therefore, inter-subject averaging could be performed by averaging the values of interest across subjects at each node index. To obtain the average structural image, the coordinates of each node index were averaged among subjects. For each subject, the functional map was obtained in the 3D space and mapped to the cortical surface using an intersection algorithm. Then the t-values associated with each node were averaged among subjects to obtain the average activation map. For volumetric analysis, brains were first normalized to Talairach space and the average anatomical data was obtained. Then similar to surface-based analysis, the average functional map was obtained by averaging the t-values at each point. Using Regions of Interest (ROIs) selected within the areas of visual, auditory, and motor activation, they calculated mean, maximum and median t-values and showed that all of these three statistics of the t-values had significantly larger values with the surface-based method compared to the volume-based method. Their ROI-based analysis involved an additional step (compared to the approach of Desai et al.) to take into account the effect of different thresholding in the ROI selection. More (or less) conservative thresholds

were chosen by applying thresholds which included voxels (or vertices) in the ROI that were activated in a larger (or fewer) number of subjects. The most conservative threshold limited the ROI to voxels or vertices activated for all subjects and the most liberal threshold included all the voxels or vertices that were activated in at least one subject.

To evaluate the alignment of functional data with the two methods, they measured the maximum value within the ROI of each subject and averaged the maximum values among individuals and compared it to the maximum value in the ROI from the average functional data. If inter-subject alignment were perfect and activation patterns were identical across subjects, these two values would be equal. They showed that with surface-based averaging these two values were closer, and hence better alignment of functionally similar regions across subjects was achieved. Similar analyses were repeated for the other two parameters: mean and median and similar results confirmed the superiority of the surface-based approach versus the volume-based method in aligning the functional maps.

There are two points to consider about the studies mentioned above. Firstly in both studies, the activation detection did not directly follow a surface-based approach. Instead, the activation maps were first obtained in the 3D space (similar to previous methods) and then mapped to the cortical surface. Thus, the problem of expansion of the activation across the opposite sides of sulci may not necessarily be addressed by these approaches. Moreover, mapping the activation to the cortical surface entails assumptions which may not be accurate. Secondly, in both studies the performance of the cortical surface-based method is compared to volume-based methods which involve registration to the Talairach atlas. However, as stated in chapter one, the Talairach atlas was developed from a single brain and does not account for normal variations of brain. Hence, registration to the Talairach atlas may not be as accurate in aligning different brains as can be achieved by other volume-based atlases such as MNI. A comparison between a surface-based method and a volume-based method with a more representative atlas may therefore produce different results from the findings of these studies.

To avoid the problem of spreading the activation map across a sulcus, surface-based smoothing methods were developed. Smoothing is usually performed on

functional images to increase the signal to noise ratio (SNR) and results in spreading the activation map. However, this can result in the activation map being extended to the opposite side of a sulcus, and hence to a different cortical region. In a number of studies, Jo et al. used a surface-based smoothing filter: heat kernel (Chung et al., 2005), and compared the activation maps resulting from heat kernel and 3D Gaussian smoothing filters for simulated (Jo et al., 2007a,b) and real data (Jo et al., 2008). Heat kernel smoothing will be described in detail in chapter eight. In practical terms, it involves an iterative procedure where at each iteration, the value at each vertex of the cortical surface is replaced by the weighted average of its neighbouring vertices values. They showed that for simulated data, while there was no benefit of applying heat kernel smoothing in the absence of noise, when noise was added to the data the heat kernel smoothing method showed superiority over the Gaussian method. In another study (Jo et al., 2008), they examined the effect of the kernel smoothing on real data involving activation in the hand area of the primary motor area and primary somatosensory cortex and showed that although the heat kernel smoothing increased the sensitivity, both methods cause a shift in the activation centre with reference to the unsmoothed data. However, analyzing the change in the whole activation map (rather than only the activation centre) may provide more useful information about how the activation pattern changes with each smoothing method.

Anticevic et al. evaluated surface- and volume-based methods for the analysis of functional activation during a memory task using the n-back paradigm for healthy subjects and schizophrenic patients (Anticevic et al., 2008). In the n-back task, the subject is presented with a sequence of stimuli and is asked to respond whenever a stimulus is a repetition of its n-th previous stimulus. They examined the 2-back task consisting of verbal and face stimuli. They first registered structural data to the 711-2B stereotaxic atlas using a 12-parameter affine transformation and registered the fMRI data to structural data. Cortical surfaces whose boundaries ran midway through the cortical thickness were created using Caret and registered to the PALS-B12 left-right composite atlas followed by standardization of the cortical meshes so that averaging could be performed. They chose five sulci from regions involved in memory processing and projected them back to the volumetric presentation by assigning 3 and 5 mm cortical thicknesses. Then for each sulcus of each subject, they calculated the ratio between the number of vertices (or voxels) that reside in the region of 50% overlap across subjects to the total

number of vertices (or voxels) that belong to that sulcus. They then averaged the ratios for all subjects to compute the alignment precision for both surface- and volume-based registration methods. To analyze the effect of size of the overlap region, 40% and 30% overlaps were also studied. They showed that for all five sulci, the chosen sulci were better aligned with surface-based registration compared to the volume-based method, with the best results for the central sulcus. This was shown to be the case for all overlap thresholds and different cortical thickness values. The superiority of surface-based registration over volume-based registration was slightly greater for patients with schizophrenia than for controls which they concluded to be due to subtle abnormality. However, they did not further investigate if such increased benefit for patients with schizophrenia was significant.

They also mapped the functional activation patterns from both the unsmoothed and the data smoothed using a volumetric Gaussian filter with the Full Width at Half Maximum (FWHM) of 9 mm to the cortical surface prior to registering the cortical surfaces. 2D smoothing was also applied to the non-smoothed data by iterative weighted averaging of each vertex value with its neighbours' values similar to heat kernel smoothing. In total, they compared three groups of processed datasets for each subject: 1) Non-smoothed, 2) 2D-smoothed (approximately equivalent to a 12 mm Gaussian kernel) and 3) 3D-smoothed with a 9 mm Gaussian kernel. It should be noted, however, that even for the non-smoothed data, their method of mapping included some degree of smoothing by trilinear interpolation between neighbouring voxels in the activation map.

They then compared the statistical power (t-values) by surface and volume registration methods using ROI-based analysis similar to the approach of Argall et al. however they tailored their method to remove bias towards either of the methods. For this purpose, they used the intersection of ROIs extracted from volumetric and from surface-based data to create surface ROIs. The volume ROIs, were then obtained by applying a 3mm thickness to the surface-based ROI to restrict it to cortical GM. They showed that for unsmoothed data with surface-based registration, stronger activation (higher t-values) were produced compared to volume-based registration particularly for the schizophrenia group. This was in agreement with their finding about improvement in between-subject registration with more emphasis for the schizophrenia group. However, smoothing with a 9

mm Gaussian filter seemed to have overcome the problem with statistical power and resulted in comparable t-values for the surface- and volume-based registration methods.

2.7 Discussion

Cortical surface-based methods have been developed to accommodate the convoluted shape of the cortex and to perform analyses and measurements of cortical parameters such as thickness, depth and folding pattern. Such measurements have gained considerable interest in cross-sectional studies. In contrast to these algorithms, however, the estimation of cortical properties with Brainvisa is mainly carried out by automatically detecting the cortical folds and labelling them as sulcal pieces with an acceptable recognition rate (see section 1.3.8). This is promising given the fact that unlike the above-mentioned algorithms, even small folds can be identified. In addition, compared to these methods, a wider range of properties such as length, geodesic depth, surface, coordinates, orientation and so on can be calculated for each sulcal piece. For these reasons, Brainvisa (version 4.0) was chosen in this project to investigate the cortical properties of abnormal brains.

The complete analysis of a T1-weighted image using a Windows XP (32-bit)-based PC with 3 GB RAM took between two to three hours. However, in cases where manual corrections were necessary the processing time could take up to an hour longer (three to four hours in total).

The manual corrections (where necessary) could involve tuning the parameters (for example in bias correction, histogram analysis, or brain extraction) or manually editing the extracted mask (for example in hemispheres separation or brain extraction).

However, the cortical thickness was not included as a morphometric measure in this project as the reproducibility of its estimation was found to be very poor (around 10%). This was mainly due to the fact that Brainvisa does not allow for manual correction of errors (for example when some pieces of the folds fail to be detected leading to overestimation of the cortical thickness).

Most of the reviewed studies have shown that sulci of different subjects are better aligned using cortical surface-based registration than Talairach-based registration. A comparison between surface-based registration and registration to the 711-2B stereotaxic atlas (Anticevic et al., 2008) also confirmed the superiority of surface-based registration to volume-based methods in terms of sulcal aligning. This finding can be promising for fMRI group studies where improved alignment of cortical regions can result in better registration of activation maps and hence increased statistical power. Nonetheless, the mapping of fMRI data from the 3D space to the cortical surface adopted in the above studies entails approximations and may not be very accurate. Likewise, mapping from 3D space to the cortical surface may not necessarily address the problem of spreading the activation between different cortical regions if the original activation detection is performed using the 3D Gaussian smoothing. In other words, Gaussian smoothing could have already mixed the values of the voxel at the opposite sides of a sulcus prior to mapping. Another limitation of the above ROI-based approaches is that the choice of ROI can be subjective and the results may vary for different ROIs.

Although the findings of Jo et al. did not confirm the superiority of surface-based smoothing over Gaussian smoothing, their study only focused on the t-values and lacked a comprehensive comparison between the final activation maps obtained by the two methods. A more informative comparison should include different aspects such as the degree of smoothing, the spread, as well as the statistical power.

Despite being successful in the alignment of different individuals' sulci, the cortical surface-based methods have not shown to be beneficial to fMRI analysis. In fact these approaches introduce an additional limitation due to the difficulty of correspondence between the 3D and 2D spaces.

It should be noted however that the main limitation of fMRI analysis in the 3D space does not arise from the volume-based approach per se, but from the fact that smoothing can mix the voxels at the opposite sides of a sulcus. Therefore, any 3D space-based fMRI analysis that avoids the extension of activation to other cortical areas, would address the problem whilst also allowing for a direct comparison between different smoothing filters. For this purpose, two alternative smoothing filters are presented in chapter eight of this thesis. These filters are

applied to the volumetric functional images such that they prevent mixing voxel values across the sulci. The activation maps obtained by smoothing with these filters are compared to those obtained from Gaussian smoothing by considering smoothness, spread and shift of the activation map, and t-values.

Chapter 3. Assessment of the impact of the scanner-related factors on brain morphometry analysis with Brainvisa

3.1 Overview

This chapter reviews the repeatability and reproducibility of the morphometry analysis using Brainvisa. The morphometric measures studied include some brain attributes such as volumes of the brain as well as its different tissue types and sulcal attributes such as depth and surface (as a proxy for its volume). Despite being used in several morphometry studies, Brainvisa has not yet been assessed against scan-related factors.

In order to investigate possible reasons for low reliabilities and estimate how the results can be improved, a comparison with FSL (http://www.fmrib.ox.ac.uk/fsl) in brain segmentation is also carried out.

The chapter starts with a background of the study and a review of related studies using methods and packages other than Brainvisa. Then, the morphometric measures considered in this study are described and followed by the evaluation of the repeatability and reproducibility of the results.

All data analyses in this chapter were solely performed by the author. The results of this study have been presented as oral presentation in the British Institute of Radiology meeting 2011 and have also been submitted for publication in BMC Medical Imaging which has been accepted subject to revision.

3.2 Background

Brain morphometry has proven to be a powerful tool in identifying biomarkers of many neurological and psychiatric disorders. Several studies have investigated the link between the changes in the brain morphology and certain diseases such as Alzheimer's disease (Thompson et al., 2003), schizophrenia (Garcia-Marti et al., 2008; Shenton et al., 2001), autism (Bigler et al., 2010), epilepsy (Kim et al., 2008), and Bipolar disorder (Moorhead et al., 2007).

Brainvisa has been used for cortical morphometry and the pathology related changes in the sulcal mean depth and surface for patients with cerebral autosomal dominant arteriolopathy with subcortical infarcts and leukoencephalopathy (CADASIL) (Jouvent et al., 2008). It has also been used to show the changes in the average cortical grey matter thickness and the sulcal span with normal aging (Kochunov et al., 2008). Moreover, the decreased global sulcal index (GSI), calculated by Brainvisa from the ratio between the folded and the unfolded surfaces of the cortex, has been reported for schizophrenic patients with auditory hallucinations (Cachia et al., 2008) as well as patients with bipolar disorder and unipolar depression (Penttila et al., 2009 a,b). Changes in cortical pattern has also been studied for patients with epilepsy (Kim et al., 2008).

Nonetheless, the reliability of the brain morphometry is a major issue in cross-sectional studies where the disease-related variation may be small and dominated by the low measurement reliabilities.

Scanner-related factors can complicate the cross-sectional studies where both between-group variability and within-group variability (due to inter-individual variability in brain anatomy) already exist. Scanner instability and variations over time may result in bias in the derived morphometric measures and should be taken into account especially in longitudinal studies such as normal brain aging. Furthermore, there has been a growing interest in multicentre studies (O'Sullivan et al., 2008; Friedman et al., 2006) as they provide the researchers with larger datasets by pooling data from different sites and hence improve the statistical power. Nevertheless, multicentre studies may introduce a between-centre variance component which can overshadow small between-group (patients vs.

normal subjects) variances. Consequently it is essential to verify the effect of scanner-related factors (either within-centre or between-centre) on the estimated values for the morphological parameters.

While a considerable amount of studies on the scanner-related variability have focused on functional MRI (Friedman et al., 2008; Yendiki et al., 2010; Gountouna et al. 2010), a number of similar studies concerning structural MRI have also been reported. Using their previously developed algorithm (Schnack et al., 2001), Schnack et al. studied the variability of brain tissue segmentation for data acquired from multiple centres, different manufacturers and under different acquisition protocols (Schnack et al., 2004). Han et al. looked into the effects of scanner-related factors such as field strength, scanner manufacturer, upgrade, and pulse sequence as well as data processing factors on the cortical thickness measurement (Han et al., 2006) using FreeSurfer (http://www.surfer.nmr.mgh.harvard.edu/). Moorhead et al. investigated both within-scanner and between-scanner variability in the segmentation of grey and white matters using SPM5 (http://www.fil.ion.ucl.ac.uk/spm/) (Moorhead et al., 2009). Suckling et al. studied both within-centre and between-centre variability in the distribution of grey matter using FSL (http://www.fmrib.ox.ac.uk/fsl) with the aim of power calculation for two-group, cross-sectional study designs (Suckling et al., 2010).

The above studies have considered some of the currently used morphometric measures, however there has been no similar reports for the automatically computed sulcal attributes despite being used in morphometry analysis. More research regarding such measures still needs to be carried out.

In addition the reliability not only depends on the scanner-related dissimilarities but also on the measurement method and the package used for the analysis. The measurement process introduces another source of variance which may vary among different packages. While variability may depend on the analysis method, a study on the assessment of morphometry with Brainvisa has not been reported yet.

3.3 Aims and objectives

This chapter presents an assessment of reliability and robustness of morphometry using Brainvisa against the scanner-related variability, whilst also investigating the possible causes which reduce the reliability. The aim in this chapter is twofold: 1) assessment of viability of multicentre and longitudinal studies using Brainvisa and 2) investigating the robustness and reproducibility of morphometry with Brainvisa using repeated scans (both between- and within-centre) of the same subjects.

To cover the most commonly used morphological parameters, the variability and reliability for all brain tissue volumes and GSI as well as the sulcal attributes have been evaluated. For sulcal attributes, the assessments were performed independently with each of the four recognition algorithms provided in Brainvisa, as they produce slightly different results. The above-mentioned choice of parameters is also useful in the assessment of the reliability associated with each particular pre-processing step within Brainvisa.

To further investigate the possible causes which could have an impact on the reliability, the brain segmentation was repeated using FSL and the results were compared to those obtained with Brainvisa segmentation.

Moreover, to verify the performance of Brainvisa in different field strengths and hence various degrees of signal to noise ratio, two separate groups of data acquired with 1.5 T and 3T scanners were used and the variability and the reliability within each group was investigated.

3.4 Methods

3.4.1 Data

The retrospective data used here included two sets of 3D T1-weighted MR scans, pooled from 1.5 T and 3T scanners of CaliBrain (funded by a Chief Scientist Office -Scotland Project Grant :CZB/4/427) and Psygrid (http://www.psygrid.org/) projects, respectively. Both datasets had been obtained from healthy individuals with no history of head injury, psychiatric or neurological disorder. The study

permission to use the retrospective data was granted by the West of Scotland Research Ethics Committee.

The CaliBrain project included MR scans from thirteen healthy participants (ten male, mean age 36.3, age range 22–51 years). The subjects had been scanned twice at three different sites: The Department of Radiology, University of Aberdeen; The Division of Psychiatry and The SFC Brain Imaging Research Centre within The Centre for Clinical Brain Sciences (CCBS) at The University of Edinburgh; and The Institute of Neurological Sciences, NHS Greater Glasgow South University Hospitals Division. The T1-weighted scans were acquired using a 3D inversion recovery-prepared fast gradient echo volume sequence. All three 1.5 T scanners were manufactured by General Electric (GE Healthcare, Milwaukee, Wisconsin).

For the Psygrid project, eleven male, healthy volunteers (mean age 25, range 20–35 years) were scanned twice at five centres: The Wolfson Brain Imaging Centre (University of Cambridge), Magnetic Resonance Imaging Facility (University of Manchester), the Institute of Psychiatry (Kings College, London), the Department of Clinical Neurosciences at the University of Edinburgh and the Institute of Neurological Sciences in Glasgow, and the Centre for Clinical Magnetic Resonance Research, (University of Oxford). Of all the MR scanners, two were manufactured by GE, two by Siemens, and one by Philips. The 3D T1-weighted images were acquired using the Magnetization Prepared Rapid Gradient Echo (MP-RAGE) sequence.

Briefly, the whole dataset consisted of two groups: the first group included thirteen subjects scanned twice at three centres with 1.5 T scanners (presented here as A, B, C) and the second group consisted of eleven subjects scanned twice at five centres using 3 T scanners (presented here as D, E, F, G, H). The scanner type and manufacturer as well as imaging parameters for the two groups of datasets are given in tables 3-1 and 3-2. In all cases, the first and second visits were performed using the same scanner. Figures 3-1 to 3-4 exemplify the variations of the T1-weighted images across of the same subject corresponding to different centres or different visits to a single centre.

Centre	A	B	C
MR Scanner	GE Signa NVi/CVi 1.5T	GE Signa LX 1.5 T	GE Signa 1.5 T
Head Coil	8-channel	8-channel	8-channel
Acceleration Factor	No	No	No
TR (ms)	5.9	8.9	5.9
TE (ms)	1.9	3.3	1.4
TI (ms)	600	600	600
Flip Angle (°)	15	15	15
Image Size (voxels)	256x256x124	256x256x124	256x256x125
Voxel Size (mm^3)	0.86 x0.86x1.7	0.86 x0.86x1.7	0.86 x0.86x1.8

Table 3-1 The scanners' specifications and imaging parameters for the 1.5 T group TR, TE, and TI represent Repetition Time, Echo Time, and Inversion Time, respectively.

Centre	D	E	F	G	H
MR Scanner	GE 3T HD	GE 3T HDx	Siemens 3T Tim Trio	Siemens 3T Tim Trio	Philips 3T Intera-Achieva
Head Coil	8-channel	8-channel	8-channel	12-channel	8-channel
Acceleration Factor	No	ASSETfactor 2	No	No	SENSE factor 2
TR (ms)	6.5	7.0	9.0	9.4	8.2
TE (ms)	1.5	2.85	2.98	4.66	3.8
TI (ms)	500	650	900	900	885
Flip Angle (°)	12	8	9	8	8
Image Size (voxels)	260x260x160	260x260x160	256x256x160	256x256x160	256x256x160
Voxel Size (mm^3)	1 .1x 1.1x 1	1.1 x 1x 1	1 x 1x 1	1 x 1x 1	1 x 1x 1

Table 3-2 The scanners' specifications and imaging parameters for the 3T group TR, TE, and TI represent Repetition Time, Echo Time, and Inversion Time, respectively.

Figure 3-1 compares the images of the same subject corresponding to the first visit to the three centres of the 1.5 T group.

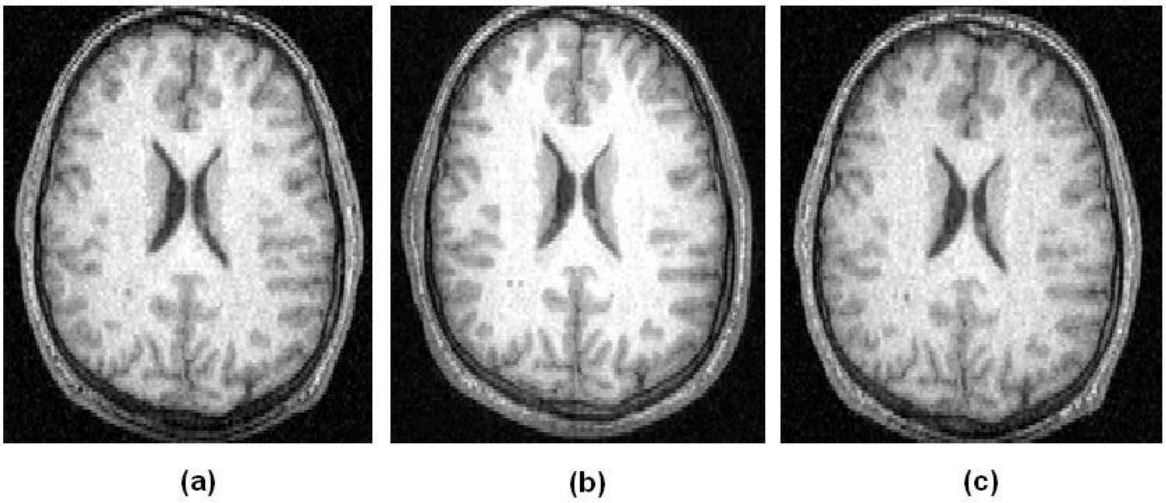

Figure 3-1 T1-weighted images acquired at different centres of the 1.5 T group Images correspond to the first visit of the same subject to a) centre A, b) centre B, and c) centre C.

Figure 3-2 displays the scans acquired at the two visits of the same subject to centre A (from 1.5 T group).

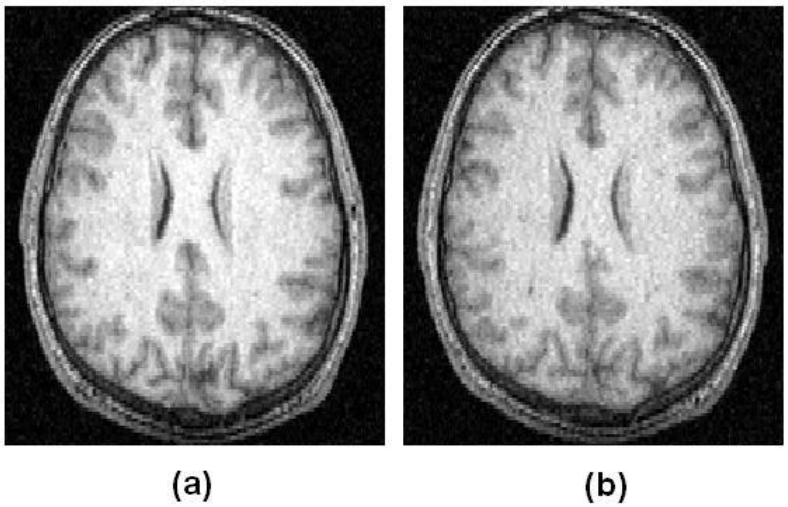

Figure 3-2 T1-weighted images acquired at the two visits to one centre from the 1.5 T group Images correspond to a) the first and b) second visits of the same subject to centre A.

Similarly figures 3-3 and 3-4 show images of the same subjects acquired at different centres and different visits to the same centre of the 3 T group, respectively.

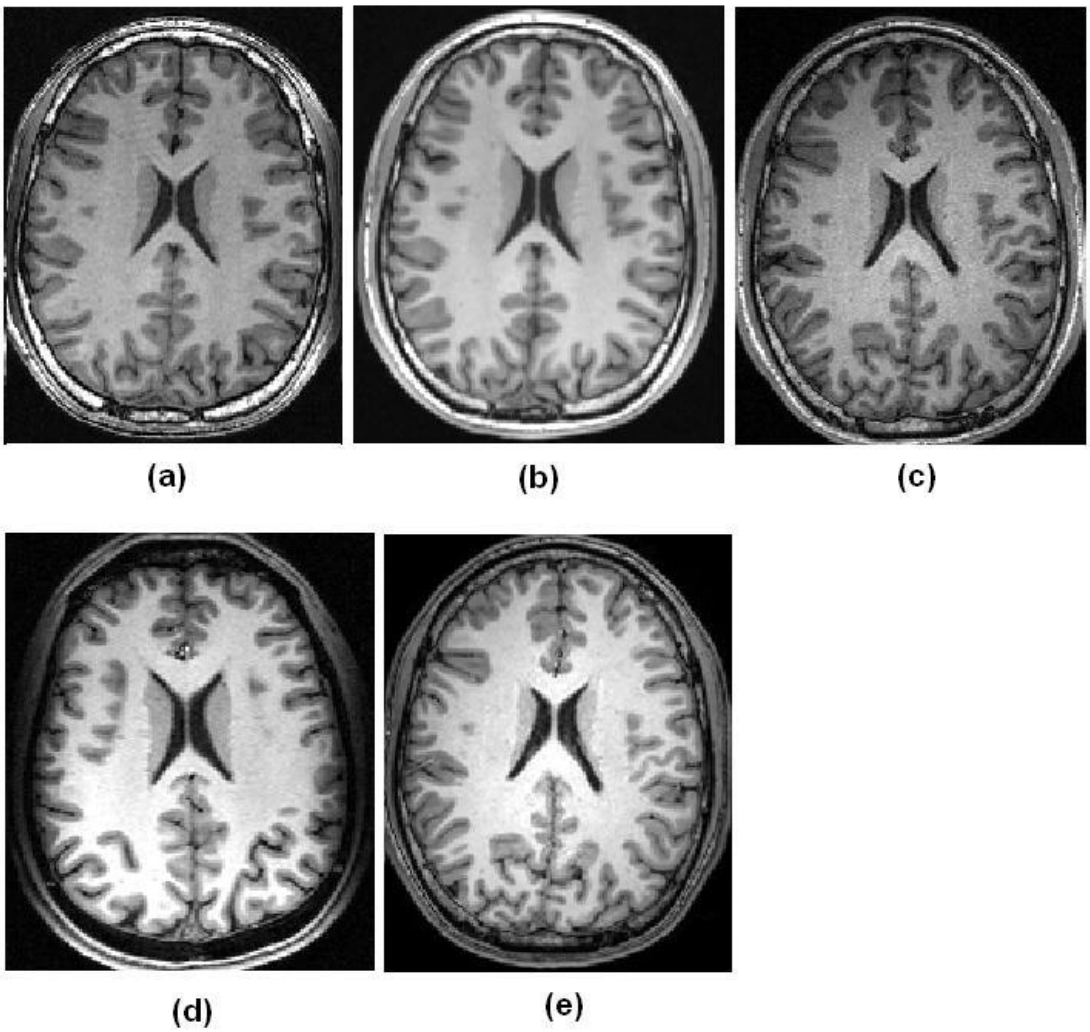

Figure 3-3 T1-weighted images acquired at different centres of the 3 T group
Images correspond to the first visit of the same subject to a) centre D, b) centre E, c) centre F, d) centre G, and e) centre H.

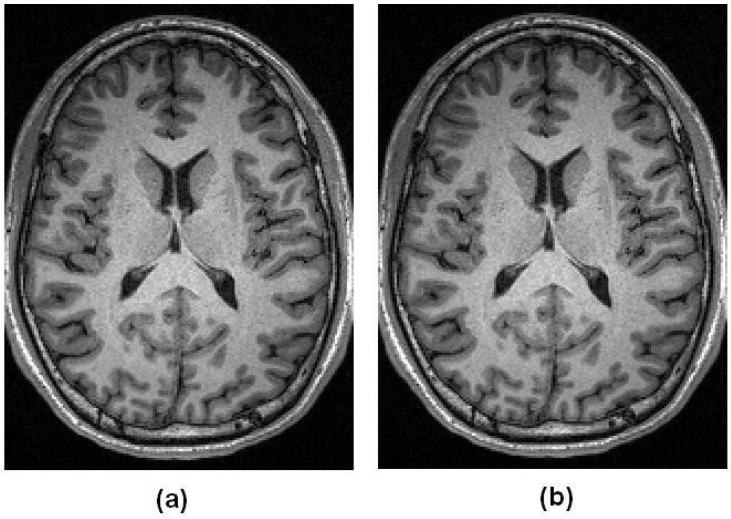

Figure 3-4 T1-weighted images acquired at the two visits to one centre from the 3 T group
Images correspond to a) the first and b) second visits of the same subject to centre F.

Due to routine quality assurance (QA) tests the geometrical distortion arising from gradient nonlinearity was estimated to cause less than 1% error in brain images and was therefore regarded as negligible.

3.4.2 Image pre-processing

Image pre-processing included bias field correction, histogram analysis, brain extraction, splitting the brain into two hemispheres and the cerebellum, segmentation, extraction of the cortical folds and sulci identification using all four SPAM algorithms: Global, Local, Markovian, and Talairach. A detailed explanation of all these steps is provided in chapter one.

3.4.3 Morphometry analysis

Using Brainvisa, all metrics were calculated for every scan of each subject and on each cerebral hemisphere independently. The metrics were either global (brain tissue volumes, and GSI) or sulcal (parameters that were calculated for each sulcus independently; i.e. sulcus surface and sulcus mean geodesic depth).

3.4.3.1 Global parameters

Brain tissues volumes: Brain segmentation is used to define for each hemisphere, the binary images corresponding to WM, GM, and CSF and the volumes of these binary masks were calculated.

GSI: This is an estimation of the cortex gyrification and is defined as the ratio between the total area of all the cortical folds and the area of the outer cortical surface or unfolded cortex (figure 3-5a).

3.4.3.2 Sulcal parameters

The following sulcal parameters were calculated for each of the four SPAM algorithms separately:

Sulcus surface: Since the sulci are formed from the skeleton surface which is only one voxel-thick, the volume of these skeleton segments depends on the voxel size

and orientation and is not a reliable estimate of the sulcal volume. Instead, the total surface area of the sulcus (figure 3-5b) which is not affected by voxel size gives a better estimation of voxel size. Therefore the sulcus surface was used as the proxy for its volume.

Sulcus mean geodesic depth: The geodesic depth of a sulcus is defined as the geodesic distance (along the cortical mesh) between the external line of the fold (on the brain hull), and the bottom line of the sulcus (figure 3-5c).

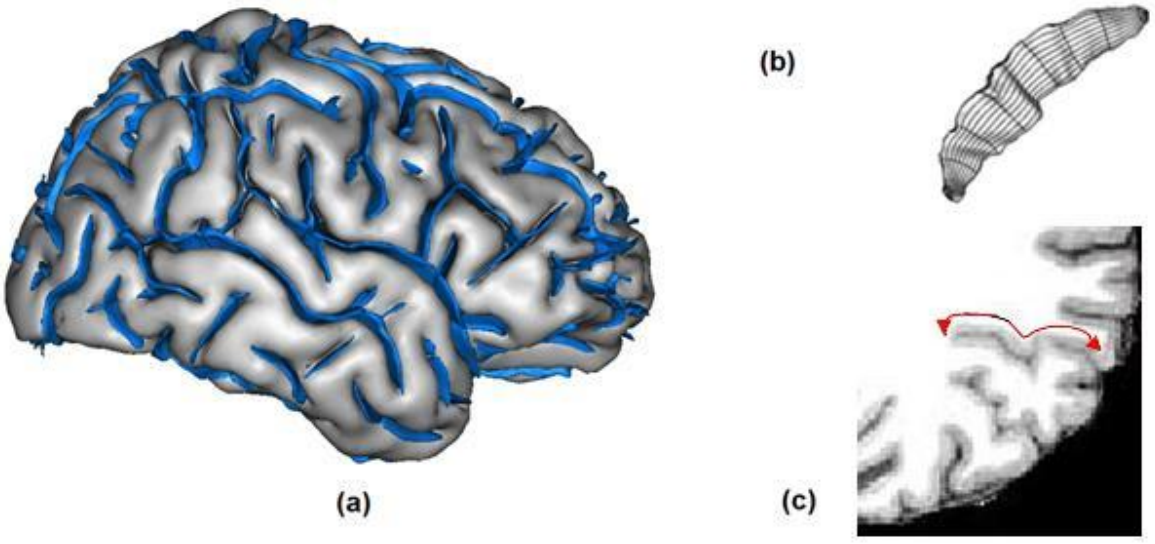

Figure 3-5 Illustration of the morphometrical parameters
a) GSI can be described as the ratio between the surface of the folded areas (blue) and unfolded areas (grey). It should be noted that the blue surface is the skeletonised version of the folded area. (b) The surface of a sulcus, the shaded area, is defined as its total surface area. (c) The geodesic depth of a sulcus shown by the red arrow. It should be noted that the geodesic depth of a given sulcus is not constant throughout its length. Therefore mean geodesic depth is considered as a morphometric parameter.

3.4.4 Statistical analysis

For each morphometric measure, the Analysis of Variance (ANOVA) was conducted using Minitab 16 at the significance level of 0.05 to investigate whether the values corresponding to different centres or different visits were significantly different. Thus an effect was considered significant if the observed p-value under the null hypothesis that the effect is non-significant was smaller than 0.05. P-values were not adjusted for multiple testing and therefore have to be considered as descriptive. In order to take the between-subject difference into account, a “subject” factor was included in the ANOVA model. For the analysis of GM, WM,

and CSF volumes as well as GSI, the brain volume was also included as a covariate. For sulcal parameters, both brain volume and GSI were included as covariates.

In addition to the significance of centre and visit factors, the scanner-related reliability was evaluated to assess the influence of the variability on the ability to distinguish between individuals. In other words, the reliability returns an estimate of how close the values calculated from different scans of the same subject are and whether the between-centre or between-visit variability is the dominant source of variation which overshadows other sources of variation. For this purpose a random effects ANOVA model was used to compute the variance components associated with all sources of variability present in each field strength group. Then the reliability for each factor was calculated as the ratio of the variance excluding the contribution from that factor to the total variance.

$$between - centre\ reliability = \frac{V_{total} - V_{centre}}{V_{total}}$$

$$between - visit\ reliability = \frac{V_{total} - V_{visit}}{V_{total}}$$

3-1

Where V_{total} is the total variance corresponding to all sources of variability and is obtained from the sum of all variance components, and V_{centre} (or V_{visit}) is the sum of the variances associated with the centre (or visit) factor and its interactions with other factors. The reliability ranges from zero to one, representing cases where the variance associated with the centre (or visit) factor is the only source of variance or is negligible, respectively.

3.4.5 Segmentation with FSL vs. Brainvisa

In order to further explore the factors limiting the reliability of Brainvisa morphometry, brain segmentation was repeated by FSL (version 4.1.4) and the results of the two packages were compared. Since the bias correction and histogram analysis are fundamental steps in Brainvisa with great influence on the

final results, a comparison between the two packages in brain segmentation (which is a direct result of these two steps) can be helpful in the assessment of robustness of each of these processes.

While it is usually suggested to use SIENA/SIENAX tools within FSL (http://www.fmrib.ox.ac.uk/fsl/siena/index.html) for longitudinal or cross-sectional studies, these tools may introduce bias since they involve a registration step. Consequently, segmentation was carried out using the FAST algorithm (version 4.1) of FSL which employs a Hidden Markovian Random Field model that for voxel classification, takes the tissue type of its neighbouring voxels into account (Zhang et al., 2001), whilst also correcting for the bias field. To ensure that the comparison between the two packages only concerns the segmentation process and not the brain extraction, the same skull-stripped brain created with Brainvisa was used for segmentation with FAST.

To compare the bias correction of FAST and Brainvisa, masks of all the three tissue types were applied to each bias corrected T1-weighted image (bias corrected with Brainvisa and FAST) and the coefficient of variation was calculated within each mask. More robust bias correction should result in narrower histogram peaks associated with each tissue type and hence smaller values for the coefficient of variation. Moreover, WM/GM contrast in each bias corrected image was calculated by dividing the WM peak value by the GM peak value. The peak values were directly calculated from the distribution of signal intensities within each tissue. To avoid bias towards either of the two programs, each mask was defined as the intersection between the masks obtained with FAST and Brainvisa.

3.5 Results

The distribution and mean values of the global parameters across all subjects, visits, and centres are displayed by figure 3-6. The volumes of GM, WM, and CSF calculated by Brainvisa and FAST have been shown. This figure also demonstrates the calculated GSI values. The values have been calculated for each hemisphere independently and thus each value corresponds to only one hemisphere and not the whole brain.

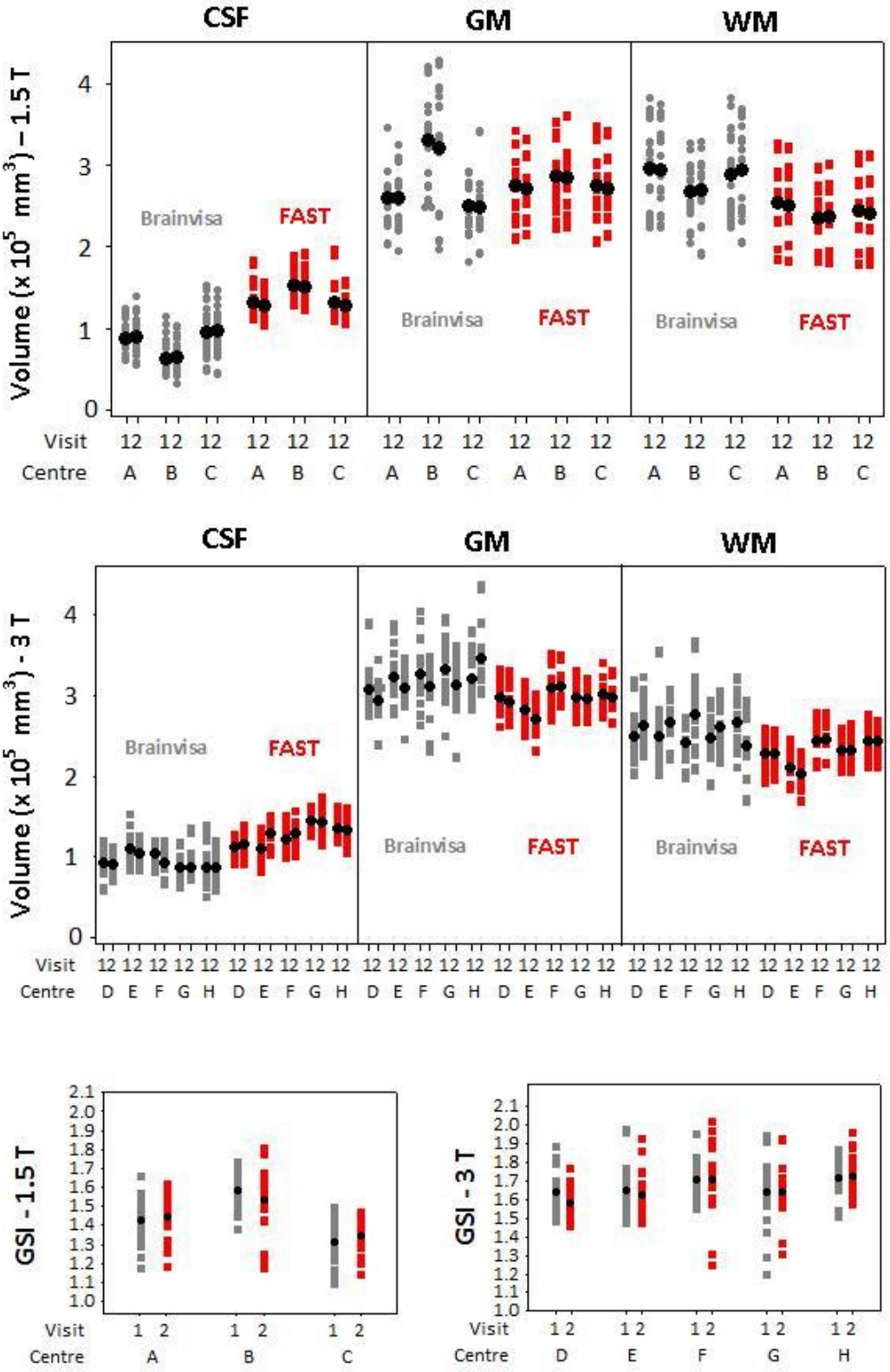

Figure 3-6 Plots of the distribution of global parameters across subjects
The plots of CSF, GM, and WM volumes in mm^3 calculated using FAST and Brainvisa for the two visits and all centres of the 1.5 T group (top) and the 3 T group (middle). The plots of GSI for the 1.5 T groups (bottom left) and the 3 T group (bottom right) are also shown. The mean values have also been shown in each individual plot. The volumes and GSI are calculated for each hemisphere separately and the values of both hemispheres are presented.

The numerical presentation of segmentation results with Brainvisa and FAST are also given in tables 3-3 and 3-4 for the 1.5 T and 3 T groups, respectively.

Centre /Visit	GM Volume ($x10^5$ mm^3)		WM Volume ($x10^5$ mm^3)		CSF Volume ($x10^4$ mm^3)	
	Brainvisa	FAST	Brainvisa	FAST	Brainvisa	FAST
A/1	2.59±0.35	2.75±0.36	2.96±0.45	2.53±0.44	8.71±1.79	13.23±2.05
A/2	2.59±0.34	2.70±0.32	2.93±0.47	2.49±0.39	8.91±2.02	12.68±1.56
B/1	3.22±0.65	2.86±0.34	2.74±0.29	2.34±0.33	6.22±2.06	15.29±1.80
B/2	3.21±0.68	2.85±0.35	2.74±0.24	2.36±0.34	6.38±1.89	15.14±2.07
C/1	2.49±0.31	2.74±0.38	2.88±0.48	2.43±0.41	9.61±2.85	13.08±2.28
C/2	2.47±0.34	2.70±0.32	2.93±0.51	2.39±0.38	9.64±2.62	12.84±1.50

Table 3-3 The mean and standard deviation of GM, WM, and CSF volumes across subjects for the 1.5 T group
The results of segmentation using Brainvisa and FAST are given (mean ± standard deviation) for each visit to each centre.

Centre /Visit	GM Volume ($x10^5$ mm^3)		WM Volume ($x10^5$ mm^3)		CSF Volume ($x10^4$ mm^3)	
	Brainvisa	FAST	Brainvisa	FAST	Brainvisa	FAST
D/1	3.08±0.31	2.98 ±0.20	2.49±0.29	2.28 ±0.20	9.26±1.73	1.12 ±0.12
D/2	2.94 ±0.25	2.93 ±0.19	2.64 ±0.28	2.27 ±0.18	9.09±1.38	1.16 ±0.15
E/1	3.24 ±0.28	2.82 ±0.17	2.50 ±0.42	2.11 ±0.19	11.12±2.13	1.11 ±0.15
E/2	3.10±0.27	2.71 ±0.20	2.68 ±0.31	2.02 ±0.17	10.50±1.06	1.30 ±0.16
F/1	3.28 ±0.36	3.09 ±0.22	2.41 ±0.23	2.45 ±0.21	10.49 ±1.06	1.22 ±0.15
F/2	3.11 ±0.32	3.12 ±0.21	2.78 ±0.43	2.46 ±0.22	9.36 ±1.26	1.29 ±0.14
G/1	3.32 ±0.39	2.98 ±0.18	2.47 ±0.28	2.32 ±0.16	8.75 ±1.77	1.44 ±0.13
G/2	3.14 ±0.37	2.95 ±0.19	2.61 ±0.28	2.32 ±0.18	8.78 ±1.76	1.43 ±0.18
H/1	3.21 ±0.30	3.01 ±0.17	2.67 ±0.34	2.45 ±0.20	8.72 ±2.63	1.36 ±0.13
H/2	3.46 ±0.38	2.99 ±0.18	2.37 ±0.34	2.44 ±0.19	8.71 ±1.68	1.33 ±0.14

Table 3-4 The mean and standard deviation of GM, WM, and CSF volumes across subjects for the 3 T group
The results of segmentation using Brainvisa and FAST are given (mean ± standard deviation) for each visit to each centre.

As figure 3-6 and table 3-3 suggest, for the 1.5 T group the distribution and the mean values are relatively consistent between the two visits with both Brainvisa and FAST. However, there is less consistency between centres and the inconsistency is more pronounced with Brainvisa. More specifically, the values estimated for centre B seem to considerably vary from those for the other two centres. For the 3 T group with both methods, the between-visit consistency is less compared to the 1.5T group.

Furthermore for both groups on average, Brainvisa seems to be classifying more voxels as WM compared to FAST. Figure 3-6 also shows that within the 1.5 T group, the between-visit consistency of GSI for centre B is lower compared to centres A and C. This observation can also be confirmed from table 3-5 which shows that the interaction term of centre and visit is significant ($p=0.024$), indicating that the between-visit variability for centre B is significantly different for those for centres A and C.

The mean GSI was equal to 1.44 for the 1.5 T group and equal to 1.66 for the 3 T group. As GSI presents the ratio of the buried to unburied cortex, the fraction of the whole cortex that is buried in sulci will be equal to GSI/(1+GSI). Thus on average, it has been estimated that for the 1.5 T group 59% and for the 3T group 62% of the cortex is buried in sulci.

Figure 3-7 gives an overview of the mean and 95% interval of the sulcal surface and the mean geodesic depth with all four sulci recognition algorithms. This figure shows qualitatively that all algorithms are very consistent in predicting the mean and the 95% confidence interval for the sulcus surface at each centre. However, the mean geodesic depth is estimated differently and on average, Local and Markovian algorithms estimate higher values for the mean geodesic depths compared to Global and Talairach algorithms.

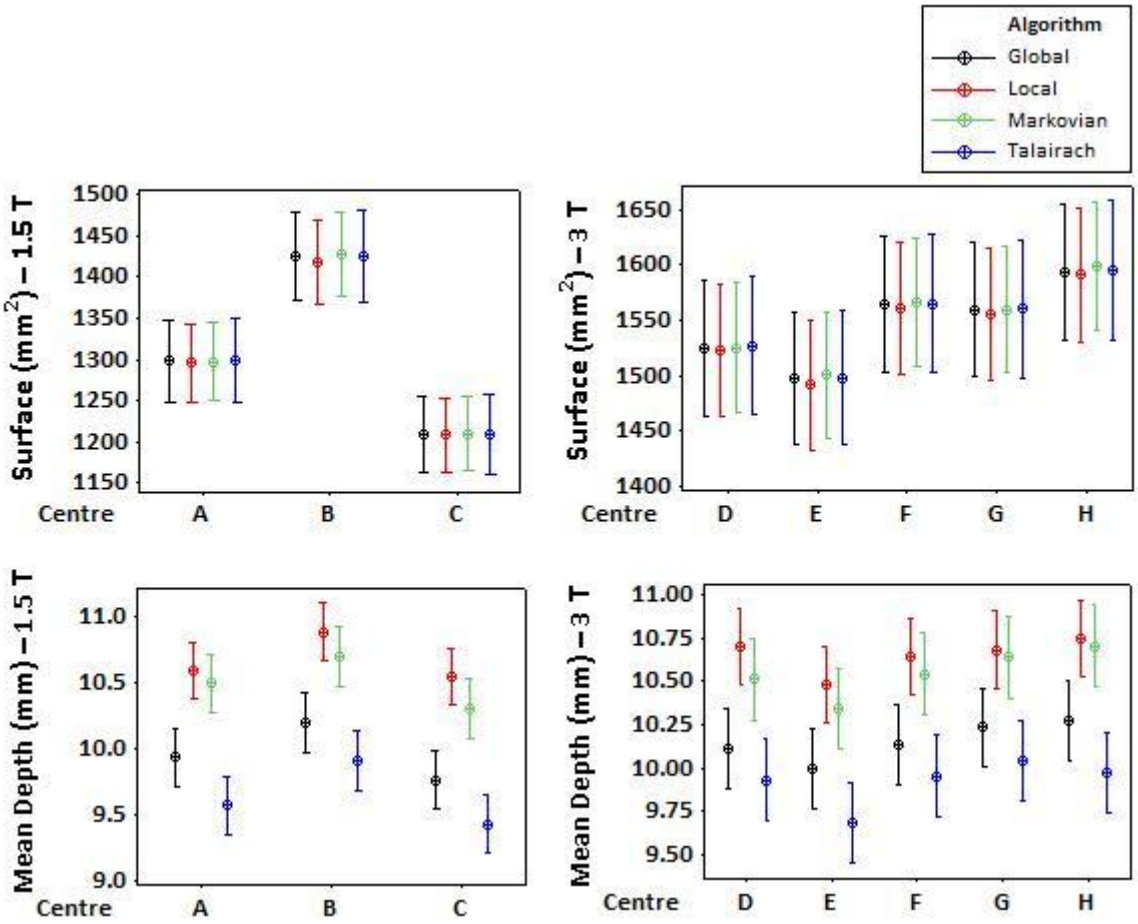

Figure 3-7 The mean and 95% confidence interval of the sulcal parameters across subjects The mean (the average of all subjects, visits, and sulci) and the 95% confidence interval of the sulcal surface (top) and mean geodesic depth (bottom), calculated for each of the four sulci recognition algorithms for the 1.5 T group (left) and the 3 T group (right). Mean geodesic depth refers to the average geodesic depth across a given sulcal label (note that the depth of a sulcus is usually not uniform throughout its length). The values are calculated for each hemisphere independently and are presented for both hemispheres.

3.5.1 Visit and Centre effects

P-values of the main and interaction effects for centre and visit are given in table 3-5 for all parameters. For sulcal parameters the p-values were computed for all recognition algorithms.

The volume of cerebral hemisphere was calculated from the sum of GM, WM, and CSF for each hemisphere of each subject's brain. The comparison between values for the volumes of a hemisphere and the segmented hemisphere into GM, WM, and CSF provides an estimation of the performance of the segmentation process.

Parameter	1.5 T Group			3 T Group		
	Centre	Visit	Centre*Visit	Centre	Visit	Centre*Visit
GM volume	<0.001	0.272	0.875	<0.001	0.015	<0.001
WM volume	<0.001	0.624	0.642	0.036	<0.001	<0.001
CSF volume	0.013	0.311	0.993	<0.001	0.003	0.535
Hemisphere volume	<0.001	0.739	0.285	<0.001	0.599	0.109
GSI	0.017	0.011	0.024	0.203	0.088	0.094
Sulcus surface						
Global	0.827	0.895	0.885	<0.001	0.777	0.843
Local	0.821	0.909	0.808	<0.001	0.673	0.807
Markovian	0.778	0.855	0.944	<0.001	0.486	0.865
Talairach	0.847	0.792	0.925	<0.001	0.847	0.863
Mean geodesic depth						
Global	0.887	0.754	0.547	0.028	0.937	0.649
Local	0.573	0.820	0.574	0.002	0.121	0.943
Markovian	0.742	0.422	0.603	0.001	0.182	0.381
Talairach	0.574	0.427	0.857	0.006	0.956	0.711

Table 3-5 The p-values for Centre and Visit effects
P-values for the main effect of Centre and Visit as well as their interaction for all Brainvisa metrics are given for the 1.5 T and 3 T groups. For sulcal parameters, p-values are given for all sulci recognition algorithms.

As shown in table 3-5, with the exception of GSI for the 1.5 T group and GM and WM volumes for the 3T group, for all other parameters the interaction between the visit and centre factors was non-significant. The significance of the interaction between these two factors is indicative of the inconsistency of all the scanners in the variability between the two visits. This inconsistency can be interpreted in two ways: 1) some scanners result in increased and others decreased values from the first to the second visit, or 2) for some scanners, there's no significant variability between the two visits, while for other scanners this variability is significant. As visits don't follow any logical order, the interaction term can only be considered important for cases where the second interpretation applies. As stated earlier, for GSI of the 1.5 T the second case applies. Whereas, as can be inferred from figure

3-6, for GM/WM volumes of the 3 T group the significance of the interaction term seems to be mainly arising from the first reason (difference in the direction of change from first to second visit).

Table 3-5 also indicates that for the 1.5 T group, the two visits to the same centre did not produce significantly different values for GM, WM, CSF, and hemisphere volumes, however these values were significantly different across centres. For the 3 T group the two visits produced similar results for hemisphere volumes. Nevertheless, for all other volumes the results vary significantly between the two visits as well as between scanners. In addition, the values of GSI for the two visits and across all scanners of the 3 T group were not significantly different.

For sulcal parameters both centre and visit as well as their interaction are non-significant for the 1.5 T group, however for the 3 T group, the centre factor is significant for both surface and depth and with all four algorithms.

3.5.2 Between-visit and between-centre reliabilities

The between-visit and between-centre reliabilities were computed for all parameters according to the equation 3-1. As a rule of thumb, the reliability values smaller than 0.50, between 0.50 and 0.70, between 0.70 and 0.90, and greater than 0.90 were considered poor, moderate, good, and excellent, respectively.

Table 3-6 shows the results for the global parameters. For the 1.5 T group, the between-visit reliability is excellent for the volumes of GM, WM, CSF and hemisphere. Between-centre reliabilities are excellent for hemisphere volume, moderate for WM and CSF volumes, and poor for GM volume. For GSI, the between-visit reliability is good whereas between-centre reliability is poor. For the 3 T group, the between-centre and between-visit reliabilities of the hemisphere volume are almost excellent. However following segmentation, the reliabilities of the resulting segmented volumes are mostly poor. Hence, it can be concluded that the segmentation has led to a significant reduction in the reliability. The between-visit and between-centre reliabilities of GSI for the 3 T group are moderate and poor, respectively.

Parameter	1.5 T Group		3 T Group	
	Between-visit	Between-centre	Between-visit	Between-centre
GM volume	0.92	0.36	0.29	0.25
WM volume	0.95	0.67	0.13	0.15
CSF volume	0.90	0.50	0.55	0.34
Hemisphere volume	0.99	0.97	0.96	0.88
GSI	0.75	0.13	0.62	0.43

Table 3-6 The between-visit and between-centre reliabilities for global parameters The global parameters calculated using Brainvisa are given for both 1.5 T and 3 T groups.

The reliabilities for sulcal parameters were calculated for each sulcal piece independently due to huge variability in sulcal parameters for different sulci (especially for sulcal surface). Figure 3-8 depicts the distribution of reliabilities across 59 sulcal pieces using all sulci recognition algorithms implying that the reliabilities range from poor to excellent. The figure suggests that in all cases the average between-visit reliability is greater than the average between-centre reliability. Moreover, among the four algorithms Markovian and Global resulted in highest reliabilities, whereas Talairach resulted in lowest reliabilities.

For a quantitative comparison between the four algorithms, the average reliabilities (across all sulci) are presented in table 3-7 for both 1.5 T and 3 T groups.

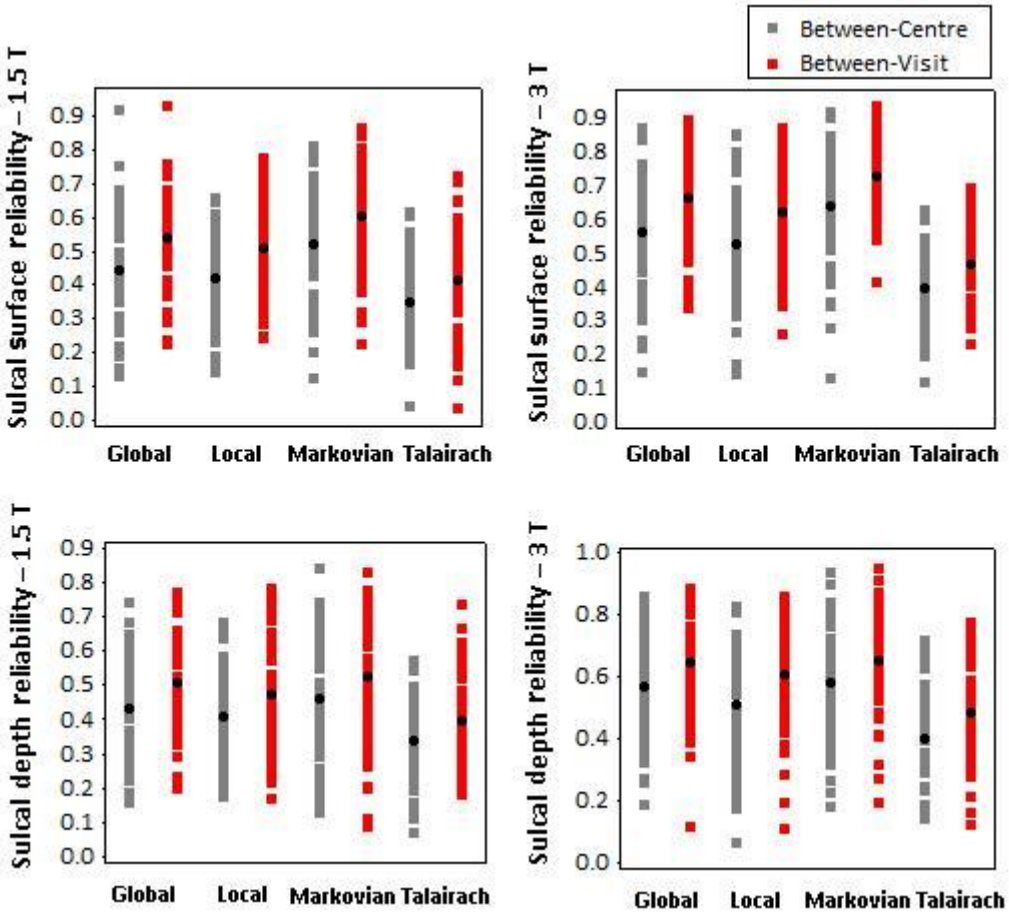

Figure 3-8 Distribution of between-centre and between-visit reliabilities for sulcal parameters
The distribution of the reliability of sulcal surface (top) and depth (bottom) is displayed for different sulci using all four sulci recognition algorithms. The results correspond to the 1.5 T group (left) and the 3 T group (right).

		1.5 T		3T	
		Between-visit	Between-centre	Between-visit	Between-centre
Surface	Global	0.54	0.44	0.66	0.56
	Local	0.51	0.42	0.62	0.52
	Markovian	0.60	0.52	0.73	0.64
	Talairach	0.41	0.35	0.47	0.39
Mean geodesic depth	Global	0.51	0.43	0.65	0.57
	Local	0.47	0.41	0.61	0.51
	Markovian	0.52	0.46	0.66	0.58
	Talairach	0.40	0.34	0.48	0.40

Table 3-7 The average between-visit and between-centre reliabilities of sulcal parameters
The results are given as the average across all sulci and are computed for the 1.5 T and 3 T groups using all four algorithms.

3.5.3 Segmentation with FSL vs. Brainvisa

The p-values of the centre and visit effects as well as their interaction for GM, WM, and CSF volumes estimated using FAST are given in table 3-8. For the 1.5 T group, each segmented volume is significantly different across centres but similar for the two visits to the same scanner. The interaction term is now significant for WM volume, nonetheless as figure 3-6 is indicative of relative consistency between the two visits, the significance of the interaction term can mainly be due to small changes but with various directions from first to second visit.

Parameter	1.5 T Group			3 T Group		
	Centre	Visit	Centre*Visit	Centre	Visit	Centre*Visit
GM volume	0.054	0.868	0.651	<0.001	<0.001	<0.001
WM volume	<0.001	0.230	0.028	<0.001	<0.001	<0.001
CSF volume	0.018	0.312	0.311	<0.001	<0.001	<0.001

Table 3-8 The p-values for segmentation results with FAST
P-values for the main effect of Centre and Visit as well as their interaction are given for the 1.5 T and 3 T groups.

For the 3 T group, both centre and visit factors as well as their interaction are significant for all volumes which, as can be inferred from figure 3-6, indicates that some scanners produce less consistent results between the two visits. As figure 3-6 suggests this inconsistency mainly arises from centre E.

Table 3-9 summarizes the between-visit and between-centre reliabilities of brain segmentation using FAST. The table suggests that except for CSF, the reliabilities of GM and WM volumes have significantly improved with FAST.

Parameter	1.5 T Group		3 T Group	
	Between-visit	Between-centre	Between-visit	Between-centre
GM volume	0.88	0.84	0.72	0.47
WM volume	0.93	0.89	0.77	0.41
CSF volume	0.78	0.49	0.65	0.22

Table 3-9 The between-visit and between-centre reliabilities for segmentation results with FAST
The results are given for both 1.5 T and 3 T groups.

Figure 3-9 demonstrates the effect of bias correction with Brainvisa and FAST in terms of the coefficient of variation within each tissue type as well as WM/GM contrast for the 1.5 T and 3 T groups. As can be seen, the calculated coefficients of variation with FAST and Brainvisa are very similar. According to the figure, the coefficient of variation is lowest within WM and slightly higher within GM which is mainly due to the partial volume effect (Mangin, 2000) and considerably higher for CSF. To examine the WM/GM contrast achieved by each method, the histogram peaks associated with GM and WM were computed within the tissue masks for each method and the WM/GM contrast was calculated as the ratio between WM and GM peaks values. (It should be noted that this method of peak detection is different and independent from peak detection in the histogram analysis with Brainvisa). Figure 3-9 suggests that with FAST there is a significant increase in WM/GM contrast compared to Brainvisa (p-value of smaller than 0.001 for 1.5 T group and 0.032 for 3 T group).

Figure 3-10 shows the plot of main effects for method (Brainvisa vs. FAST) and centre for the WM/GM contrast. The figure shows that for the 1.5 T group, centre B has significantly higher WM/GM contrasts compared to centres A and C with both Brainvisa and FAST. For the 3T group, centres F and G have the highest and centre H has the lowest values.

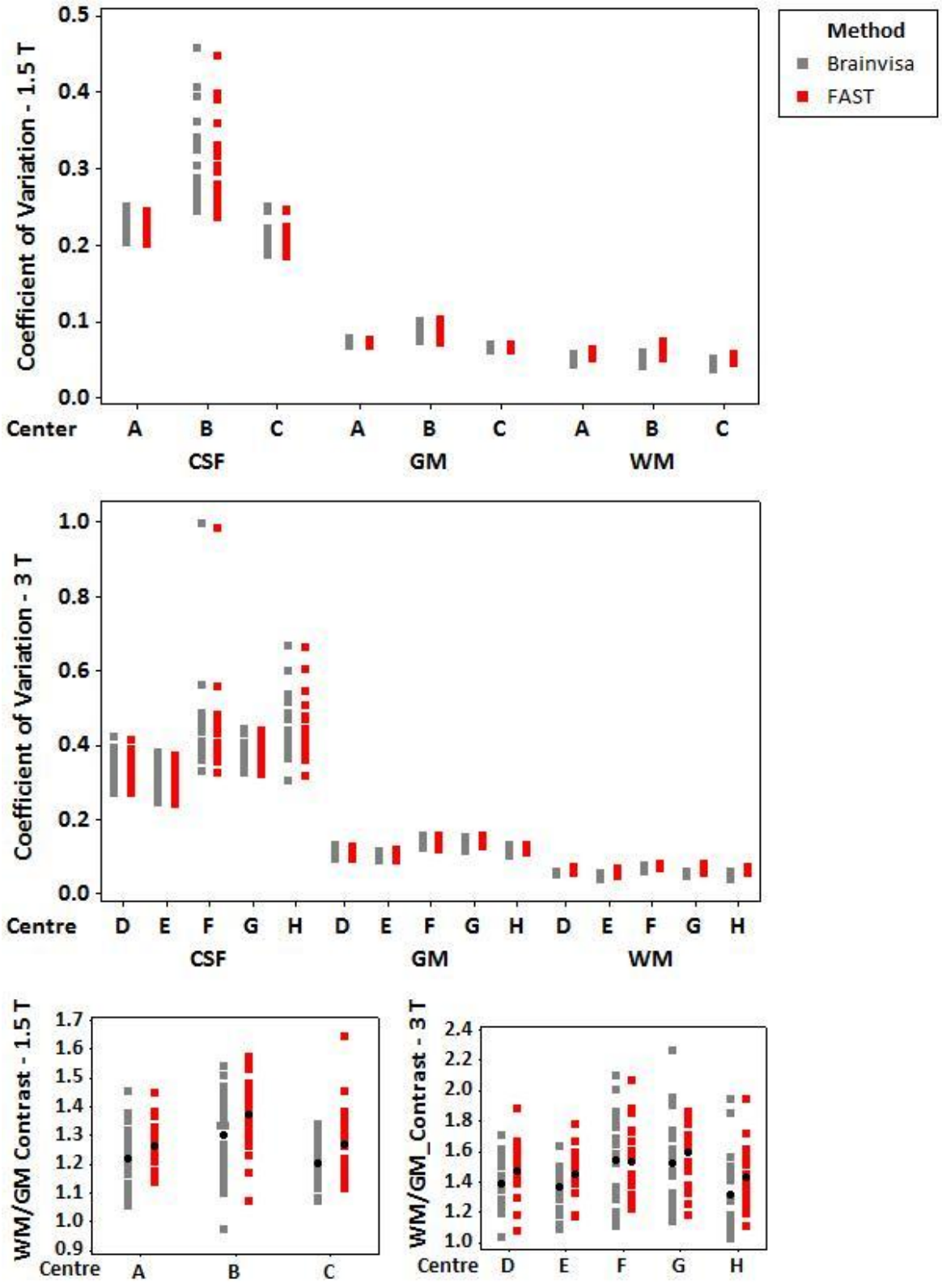

Figure 3-9 Coefficient of variation within each tissue type and WM/GM contrast following bias correction using Brainvisa and FAST
The coefficient of variation within the CSF GM, and WM masks of the bias corrected T1 images are presented for the 1.5 T (top) and 3 T (middle) groups. The WM/GM contrasts are shown for the 1.5 T (bottom left) and 3 T (bottom right) groups. Since the FAST algorithm does not split the cerebrum into two hemispheres, the values are calculated within both hemispheres (and not individual hemispheres) for both Brainvisa and FAST algorithms.

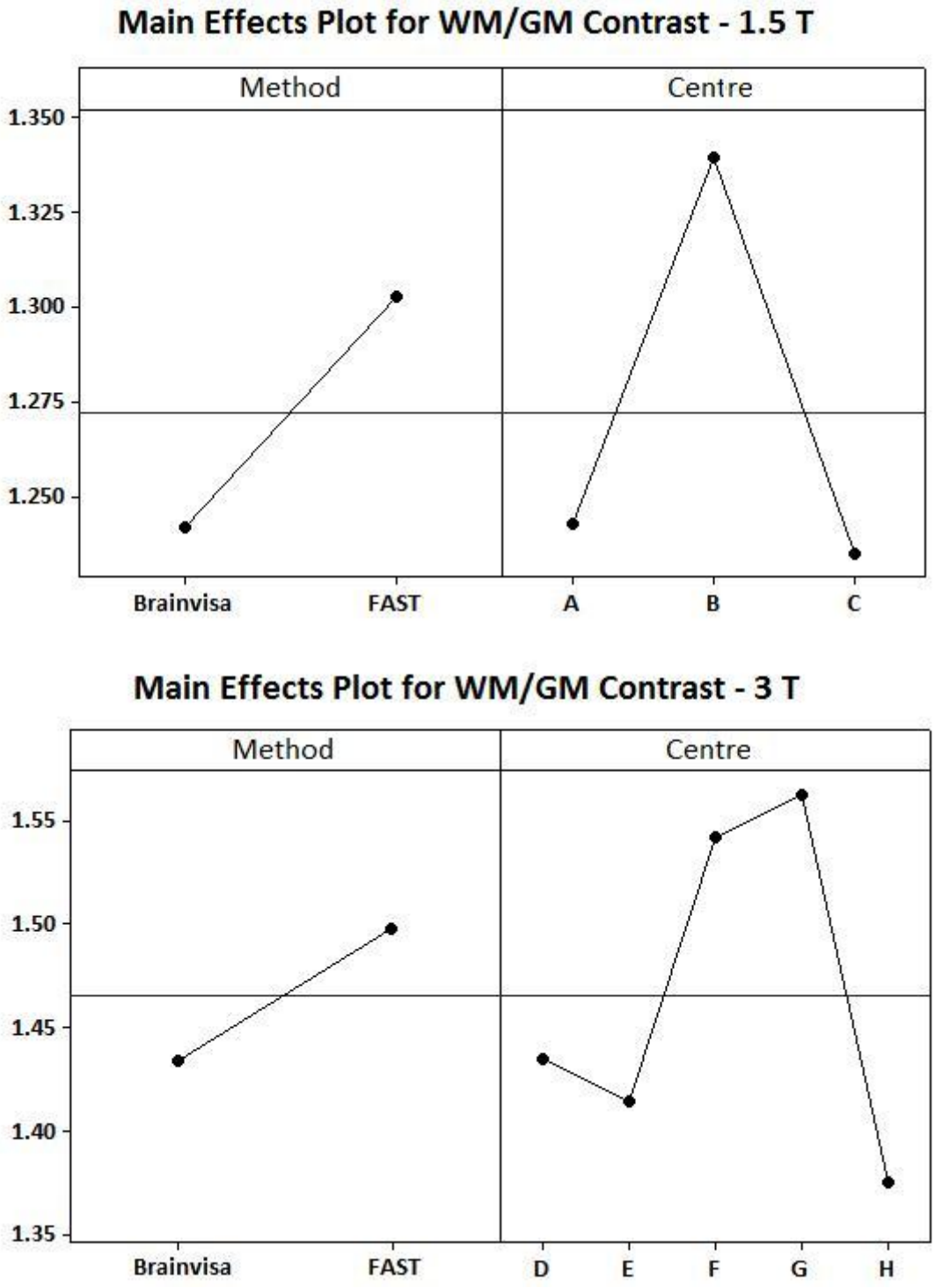

Figure 3-10 Plots of main effect of Centre and Method for the WM/GM contrast
The main effect plots are shown for the 1.5 T (top) and 3 T (bottom) groups.

As can be seen from tables 2 and 3, compared to the 1.5 T group, there are more variations in image acquisition parameters across scanners of the 3 T group. This is mainly due to the fact that unlike the 1.5 T group, various manufacturers and coils have been used in the 3 T group. However, as figures 3-6 and 3-9 (bottom

right) suggest, such disparities might not have necessarily caused a bias in the morphometry results. For example, larger TIs for scanners F, G, and H compared to those for scanners D and E have not resulted in a consistent change in the brain tissue volumes or GSI calculated using scanners D and E and those for scanners F, G, and H. Moreover, as the figure 3-10 suggests, the WM/GM contrasts are most similar for the same scanner types. This suggests that WM/GM contrasts estimated in this study has mainly been affected by scanner type and acquisition parameters have had less impact.

Nonetheless, a comparison between the T1-weighted images of the same subject acquired at 5 centres (figure 3-3), suggests that between the two GE scanners, scanner E (figure 3-3b) shows higher SNR compared to centre D (figure 3-3a). This might have been resulted from lower flip angle and higher TI used for scanner E compared to centre D (and hence better recovery of longitudinal magnetization) which leads to higher signal magnitudes.

3.6 Discussion

Brain morphometry is extensively used in cross-sectional and longitudinal studies. Combining data from multiple scanners has been a popular approach for increasing the statistical power in cross-sectional studies, enabling the researchers to detect small between-group differences. However, the scanner-related sources of variability such as scanner manufacturer and hardware, field strength, pulse sequence, scanner upgrade, and image acquisition parameters may overshadow the small between-group differences. Moreover, longitudinal studies may suffer from changes in the scanner over time. Therefore, it is necessary to assess the scanner-related variability and reliability.

Here the robustness of Brainvisa in brain morphometry and estimation of the most widely used morphometric measures have been assessed in terms of scanner-related variability and reliability. For this purpose two groups of retrospective datasets from two multi-centre studies were used. Both groups of datasets included repeated scans acquired at 1.5 T and 3 T from healthy subjects using the MP-RAGE pulse sequence.

In some cases the morphometry results were significantly different across different scanners or across the two sessions of the same scanner. It should be noted however, that the results of this study correspond to small groups of subjects and therefore for a larger dataset, even the non-significant cases may become significant. In addition, both between-centre and within-centre reliabilities ranged from poor to excellent for most parameters which also emphasizes the impact of scanner-related factors. However the within-centre reliability was found to be better than the between-centre reliability for almost all morphometric measures.

A comparison between the reliability values for the cerebral hemisphere volume and the segmented tissues (GM, WM, and CSF) revealed that while hemisphere volumes were very consistent both between- and within-scanners, the segmented volumes showed considerably different result in most cases. This implied that the inconsistency between the brain tissue volumes had arisen from the segmentation process. When the segmentation was carried out using the FAST algorithm within FSL, the reliabilities were mostly improved. Further investigation indicated that even though the coefficients of variation within each tissue (following bias correction) were similar for Brainvisa and FAST compared to Brainvisa, FAST resulted in significantly higher WM/GM contrasts. A comparison between WM/GM contrast obtained for different scanners, revealed that scanner B of the 1.5 T group had significantly higher values compared to the other two scanners of the same group (A and C). This might be one reason for the disparity between the estimated volumes and GSI for centre B and those for centres A and C. However for the 3T group, significantly higher GM/WM contrasts of centres F and G did not produce a similar result in terms of between-scanner variability in volumes or GSI. Nonetheless, as the average WM/GM contrasts were higher in the 3 T group, the above observation raises the possibility of the existence of a threshold for WM/GM contrast in order to achieve better reliabilities with Brainvisa.

In addition image acquisition parameters were slightly different across scanners within each group. Such disparities may affect and complicate the interpretation of the effect of WM/GM contrast on the estimated reliabilities.

As the bias correction with FAST is more robust compared to Brainvisa, it is suggested to perform the bias correction using FAST and repeat all the following

steps to assess the reliabilities. This would allow the evaluation of the robustness of the following analysis steps using Brainvisa. The histogram-based approach of Brainvisa can then be compared to the Hidden Markovian Random Field model-based approach of FAST. Such a step-by-step comparison can in turn help in identifying the ways in which the program can become more robust. Currently, it is not possible to skip the bias correction step and import a bias corrected image. Instead, all the steps need to be performed subsequently within the program.

Using both Brainvisa and FAST, the between-visit and between-centre reliabilities for GM and WM volumes were mostly smaller compared to the calibration study of Schnack et al. which confirms the effectiveness of using a calibration factor for brain segmentation in multi-centre studies.

For sulcus-specific attributes, the evaluation was performed with each of the four sulci identification algorithms so that the different algorithms could be compared. On average, Local and Markovian algorithms predicted higher values for mean geodesic depths compared to Global and Talairach algorithms, suggesting that Local and Markovian tend to group deeper folds within the same sulcus. In terms of reliability, for all sulcal parameters, Talairach showed lowest reliabilities whereas Markovian and Global achieved highest reliabilities. This confirms the fact that registration of different brains to Talairach atlas entails poor sulci alignment between individuals and that the other three algorithms are more successful in sulci alignment.

Nevertheless, the average reliabilities with all algorithms were mostly moderate. This clearly limits the suitability of sulcal surface and mean geodesic depth for cross-sectional studies. Further improvement may be achieved by improving the primary steps (bias correction and possibly histogram analysis) so as to obtain more reproducible estimations.

Although a direct comparison between the 1.5 T and 3 T groups is not possible due to different sources of variability (e.g. subjects, age, gender, field strength, number and types of scanners, and image acquisition parameters), a qualitative comparison suggests that while reliabilities of segmented brain volumes are higher for the 1.5 T group compared to the 3 T group (with both Brainvisa and FAST), for

sulcal parameters the reliabilities are higher for the 3 T group. This suggests that fold detection and volume calculations are not similarly affected by factors such as slice thickness, signal to noise ratio, and diversity in the scanner type. For a more accurate verification of the main causes, a prospective study with various field strengths, slice thicknesses, and scanner types on the same subjects would be useful in independently investigating the effect of each of the above-mentioned factors on the reliability of the results. Further investigation of the contribution of each factor, may also be useful in correcting for scanner-related sources of variability as well as providing information about the required criteria (image resolution, for example) for achieving more robust morphometry results and higher reliabilities with Brainvisa.

3.7 Conclusion

In this chapter the consistency of brain morphometry results using Brainvisa among different scanners and different sessions of the same scanner has been explored. The results indicate that there is occasionally considerable disparity between the values estimated for different centres and different sessions. However, the different sessions of the same scanners were more consistent compared to the different scanners. These findings emphasize that for any kind of morphometry analysis with Brainvisa using data from multi-centre or longitudinal studies, the scanner-related variability must be taken into account and where possible the resultant inconsistency should be corrected for. Furthermore, these findings provide a first step for further investigation of the possibilities for improvement of Brainvisa.

Chapter 4. Investigation of the effect of the MR image acquisition parameters and image artifacts on brain morphometry using Brainvisa

4.1 Overview

In this chapter the robustness of Brainvisa against the main factors limiting the image quality is assessed and the variations of the brain morphometry results with these factors are estimated. Since manipulation of these factors may not directly be achieved by real data, simulated data are used for this purpose. The estimation of the factors which can have an impact on the results is useful for determining optimal image acquisition parameters, field strength, and so on. Nevertheless, such estimation has not been previously reported.

This chapter starts by discussing the possible factors affecting the image quality and continues by examining how the morphometry results change with these factors.

All data analyses in this chapter were solely performed by the author. This study has been presented as a poster at the SINAPSE 2011 annual meeting.

4.2 Background

Automated image processing methods offer a wide range of possibilities which with manual methods are either impossible or time-consuming and prone to human errors. However, automated methods can also be sensitive to the factors limiting the image quality. The robustness of such methods against variations in

the image quality arising from the image acquisition therefore needs to be assessed.

In chapter three, the effect of scanner variability (either between- or within-scanner component) on brain and sulcal morphometry with Brainvisa was evaluated. Although, data from 3T and 1.5T scanners were used, a direct comparison between the two field strengths was not possible due to study design. Nevertheless, the results suggested that fold detection and brain segmentation might be differently affected by field strength and hence the SNR. Another distinguishing factor between the two groups of datasets was that slice thickness was larger in the 1.5T group compared to the 3T group. It is therefore unclear how much of the variation in results was due to these factors.

In order to estimate the effect of each factor determining the image quality, one possibility is to use simulated images (Simmons et al., 1996; Kwan wt al., 1996, 1999; Collins et al., 1998) at varying levels of the above factors and examine how the morphometry results change at different levels of the factors. The advantage of simulated over real images is that with real images factors such as noise and bias field may not be directly controlled whereas simulated images make it possible to estimate the contribution of each factor in the final result independently.

In the following section factors determining the quality of MR images are reviewed.

4.2.1 Image quality in MRI

In general, MR imaging is a trade off between several factors which describe the image quality. These factors are discussed in the following paragraph.

4.2.1.1 SNR

A high SNR, defined as the ratio between the tissue signal intensity and the noise, is desirable in every MR image. Noise can arise from thermal or physiological sources as well as temporal artefacts. Thermal noise is caused by thermal motion of electrons inside the subject’s body or the electronic circuits of the MR scanner. Thermal noise has the same magnitude at all frequencies (white noise) and is

increased when using smaller voxel sizes. Physiological noise is the signal produced by cardiac and respiratory pulsations and can be reduced by filtering out the associated frequencies. Cardiac gating, which limits acquisition to a specific phase of the cardiac cycle, is also another solution. Temporal artefacts mostly result from scanner instabilities and subject motion which often contribute to low frequency components in the signal and can therefore be overcome by removing low frequency components. SNR depends on the following factors:

Static (main) field strength: SNR increases with increasing main field intensity. This is due to the increase in the number of excited protons, and therefore the signal intensity, with increasing magnetic field.

RF coil: Reducing the sensitive volume of the RF coil will improve the SNR by reducing the noise from the adjacent structures of the selected slice plane. However, larger RF coils produce more uniform signal response across the volume.

Pulse sequence and imaging parameters: The selected pulse sequence and imaging parameters such as Repetition Time (TR), Echo Time (TE) and flip angle can affect the signal intensity and hence the SNR. The SNR increases with increasing TR or decreasing TE.

Voxel size: Increasing the voxel size will result in an increase in the number of excited spins in each voxel which in turn will result in larger signal intensity and therefore larger SNR.

Number of excitations: The number of excitations (NEX) is defined as the number of times the signal from each slice is measured. Signal intensity depends on the tissues' properties and is therefore identical for each excitation whereas the noise is random and varies for each excitation. Thus by averaging the values of all excitations, the signal sum increases linearly with the number of excitations but the noise only increases proportionally to the square root of the number of excitations. Thus, the SNR (which is proportional to the square root of the number of excitations) increases by increasing the NEX.

Receiver bandwidth: The receiver bandwidth refers to the range of frequencies collected during frequency encoding. The wider the receiver bandwidth, the faster the MR signal is sampled. However, a wider receiver bandwidth also means recording more background noise (white noise) and therefore lower SNR.

4.2.1.2 Spatial resolution

Spatial resolution, or the power to discriminate small features, is determined by the voxel size, in terms of the both in-plane resolution and slice thickness. Partial volume effect is a major limiting factor in spatial resolution and occurs when a voxel is large enough to contain more than one tissue type and consequently the signals from more than one tissue contribute to the voxel intensity. Decreasing the voxel size can provide higher spatial resolution however, as mentioned before, at the expense of reducing the SNR.

4.3 Aims and Objectives

The objective of this study is to evaluate the changes in morphometry results using Brainvisa with intensity non-uniformity (bias field), noise, and voxel size (by varying the slice thickness). The morphometric measures included in this study are the brain tissue volumes and cortical gyrification (GSI).

4.4 Methods

4.4.1 Simulated images

Simulated 3D T1-weighted images at different levels of noise, slice thickness, and bias field were obtained from Brainweb (http://www.bic.mni.mcgill.ca/brainweb). Simulated images are produced by using the anatomical model for the distribution of different tissue types and modelling the Bloch equation (McRobbie et al., 2007) in order to obtain the signal intensity at each voxel. The anatomical model used for simulations is based on the high resolution (1mm isotropic voxel) N27atlas (Holmes et al., 1998). Automated classification followed by manual correction of the image was then used to obtain a digital brain phantom (Collins et al., 1998). This digital brain phantom is then used to calculate the MR signal intensity at each

voxel of the brain phantom according to the pulse sequence and the magnetic properties of each tissue type in terms of their relaxation times (Kwan et al., 1999). Table 4-1 shows the tissue MR parameters used for the simulation.

Tissue	T1 (ms)	T2 (ms)	T2* (ms)	PD
Background	0	0	0	0
CSF	2569	329	58	1
GM	833	83	69	0.86
WM	500	70	61	0.77
FAT	350	70	58	1
Muscle / Skin	900	47	30	1.0
Skin	2569	329	58	1
Skull	0	0	0	0
Glial Matter	833	83	69	0.86

Table 4-1 MR parameters for different brain tissue types used for simulation

3D T1-weighted images were produced using Spoiled Fast Low Angel Shot (SFLASH) sequence with TR=18 ms, TE= 10ms, Flip angle=30 degrees, and in-plane pixel size=1x1 mm^2.

To estimate the effect of slice thickness, noise, and RF inhomogeneity, varying level of these parameters were chosen. Noise was simulated by a pseudorandom Gaussian field whose standard deviation defined the noise level and by using the WM signal intensity as the reference. Intensity non-uniformity (INU) was simulated using a multiplicative bias field with a range of values given by the chosen INU level. For example a 20% level, correspond to bias field values of 0.90 to 1.10 over the brain area. For other INU levels, the field is linearly scaled accordingly (for example, to a range of 0.80 ... 1.20 for a 40% level). The INU fields which had been estimated from real MRI scans are non-linear, slowly-varying fields of a complex shape.

The whole simulated dataset consisted of almost all combinations of different levels of the three factors with 0%, 3%, 5%, and 9% levels for noise, 0%, 20%, and 40% levels for INU arising from the RF coil, and slice thicknesses of 1, 1.3, 1.6, and 1.9 mm. However in practice, Brainvisa failed to produce reasonable

results for combinations of higher values of noise when slice thickness was larger than 1 mm. Consequently, the reported results include only noise levels of 0%, 3%, and 5% for slice thicknesses larger than 1 mm. For slice thickness of 1 mm, all noise levels (0% to 9%) were included. Figure 4-1 shows two examples of simulated T1-weighted images corresponding to the slice thickness of 1 mm, INU of 40%, and noise levels of 3% and 7%. An example of the real data (acquired using scanner F of the 3 T group studied in chapter three) is also shown in this figure for comparison.

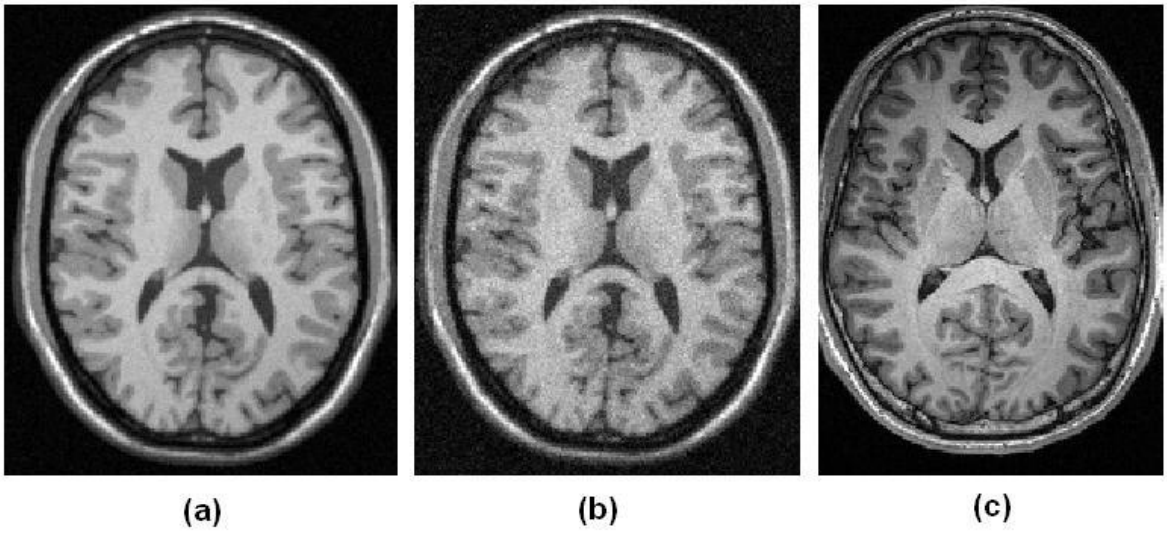

Figure 4-1 Comparison between simulated and real T1-weighted images
Simulated images correspond to the slice thickness of 1 mm, INU of 40% and noise level of a) 3% and b) 7%. c) For comparison, a real T1-weighted image acquired with scanner F of the 3 T group studied in chapter three is also shown.

4.4.2 Image analysis

Image analysis was performed using Brainvisa 4.0 and included image pre-processing followed by calculation of GM, WM, and CSF volumes as well as GSI. Image pre-processing included bias field correction, histogram analysis, brain extraction, splitting the brain into two hemispheres and the cerebellum, segmentation, extraction of the cortical folds as explained in chapter one.

4.4.3 Statistical analysis

Using Minitab16, the regression analysis was conducted to estimate the contribution of slice thickness, noise, and magnetic field non-uniformity in

variations in changes in brain segmentation and fold detection. For each parameter, the linear regression estimated the coefficient associated with each factor (β) as shown by equation 4-1.

$$Parameter = C + \beta(ST) \times SliceThickness + \beta(Noise) \times Noise + \beta(INU) \times INU$$

4-1

Where C is the constant term and β(ST), β(Noise), and β(INU) represents the coefficient for the factors: Slice thickness, Noise, and the Intensity non-uniformity. The relationship between the estimated parameter and each of the above factors was then considered to be statistically significant if the p-value corresponding to its coefficient (β) was smaller than0.05.

4.5 Results

The results of the regression analysis for brain tissue volumes are shown in table 4-2. These tables show the coefficients for each factor and their corresponding t- and p-values.

	Slice Thickness			Noise			Intensity Non-uniformity			R^2
	β (mm^2)	t	p	β	t	p	β	t	p	
GM volume	-20242	-5.96	<0.001	-8124	-18.50	<0.001	-64	-0.93	0.357	0.80
WM volume	23173	7.54	<0.001	5924	14.91	<0.001	70	1.12	0.266	0.73
CSF volume	-4547	-1.72	0.089	2494	7.27	<0.001	-22	-0.41	0.681	0.45

Table 4-2 Regression analysis for GM, WM, and CSF volumes
The table shows the coefficients as well as t- and p-values for each factor in additions to the R^2 value of the regression model

As can be seen from the table, while the GM and WM volumes significantly change with varying the slice thickness (p<0.001), the CSF volume is not significantly affected by changes in the slice thickness (p=0.089). The estimated values for β show that by increasing the slice thickness, the GM volume decreases

whereas the WM volume increases. It can be inferred therefore that the increase in slice thickness lead to some GM voxels being labelled as WM voxels.

Table 4-2 also suggests that all brain tissue volumes are significantly affected by noise ($p<0.001$). In other words with increasing the noise level, the GM volume decreases whereas both WM, and CSF volumes increase, suggesting that GM segmentation can suffer from noise. None of the brain tissue volumes significantly vary with intensity non-uniformity.

Figures 4-2 to 4-4 show the plots of the interaction between the slice thickness and noise for each brain tissue volume. The volumes are shown as the average across different levels of intensity non-uniformity.

Figure 4-2 confirms that for all slice thicknesses, the GM volume decreases with noise. The GM volume also decreases with increasing the slice thickness however on average, an increase in slice thickness from 1 mm to 1.9 mm leads to approximately 6% reduction of the GM volume.

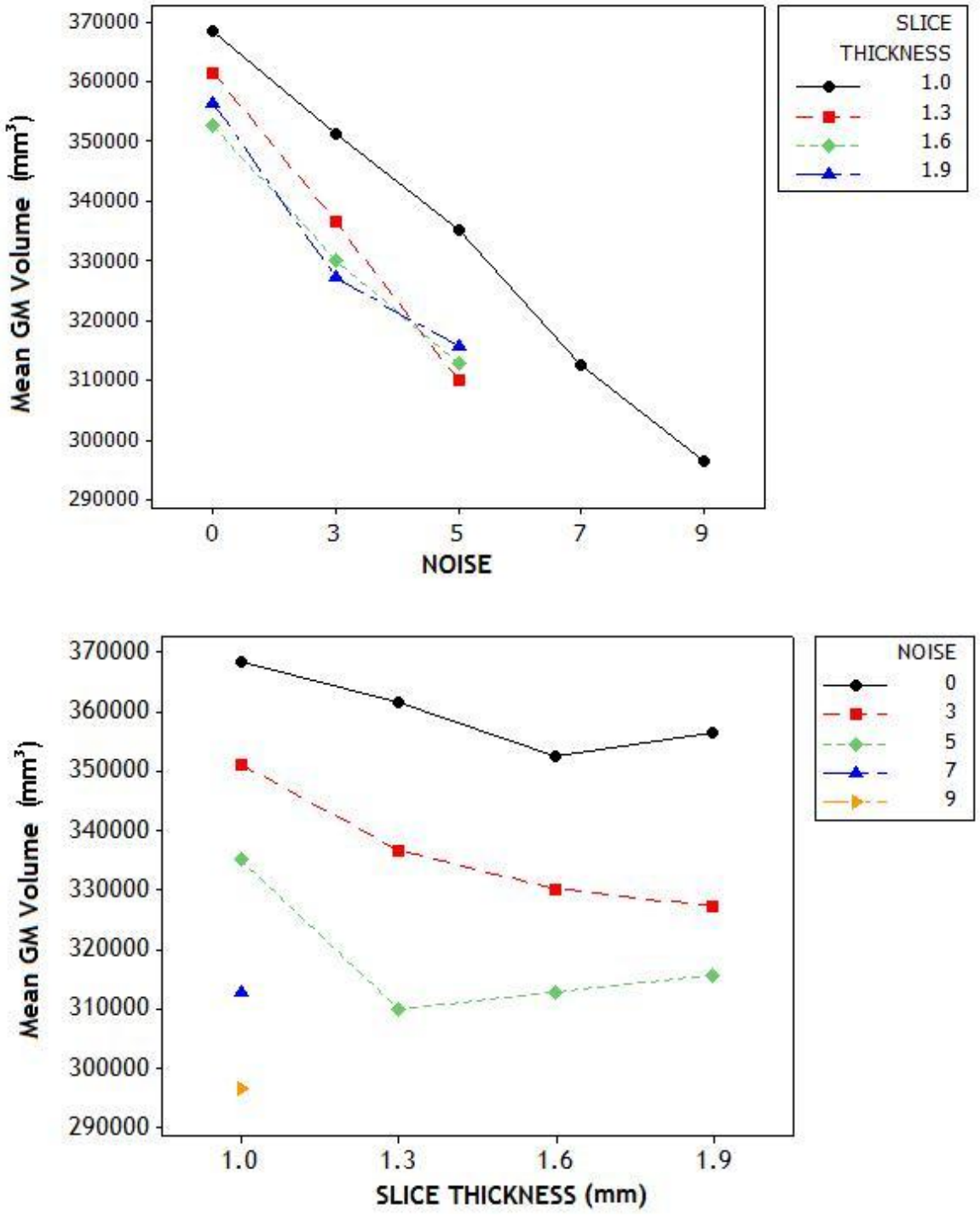

Figure 4-2 The plots of interaction between slice thickness and noise for GM volume
The plots show the variations in the average GM volume across different levels of intensity non-uniformity (top) with noise at different levels of slice thickness and (bottom) with slice thickness at different levels of noise.

Figure 4-3 shows that the WM volume increases with an increase in slice thickness or noise however, the increase in the WM volume with noise is even more pronounced with slice thicknesses larger than 1mm.

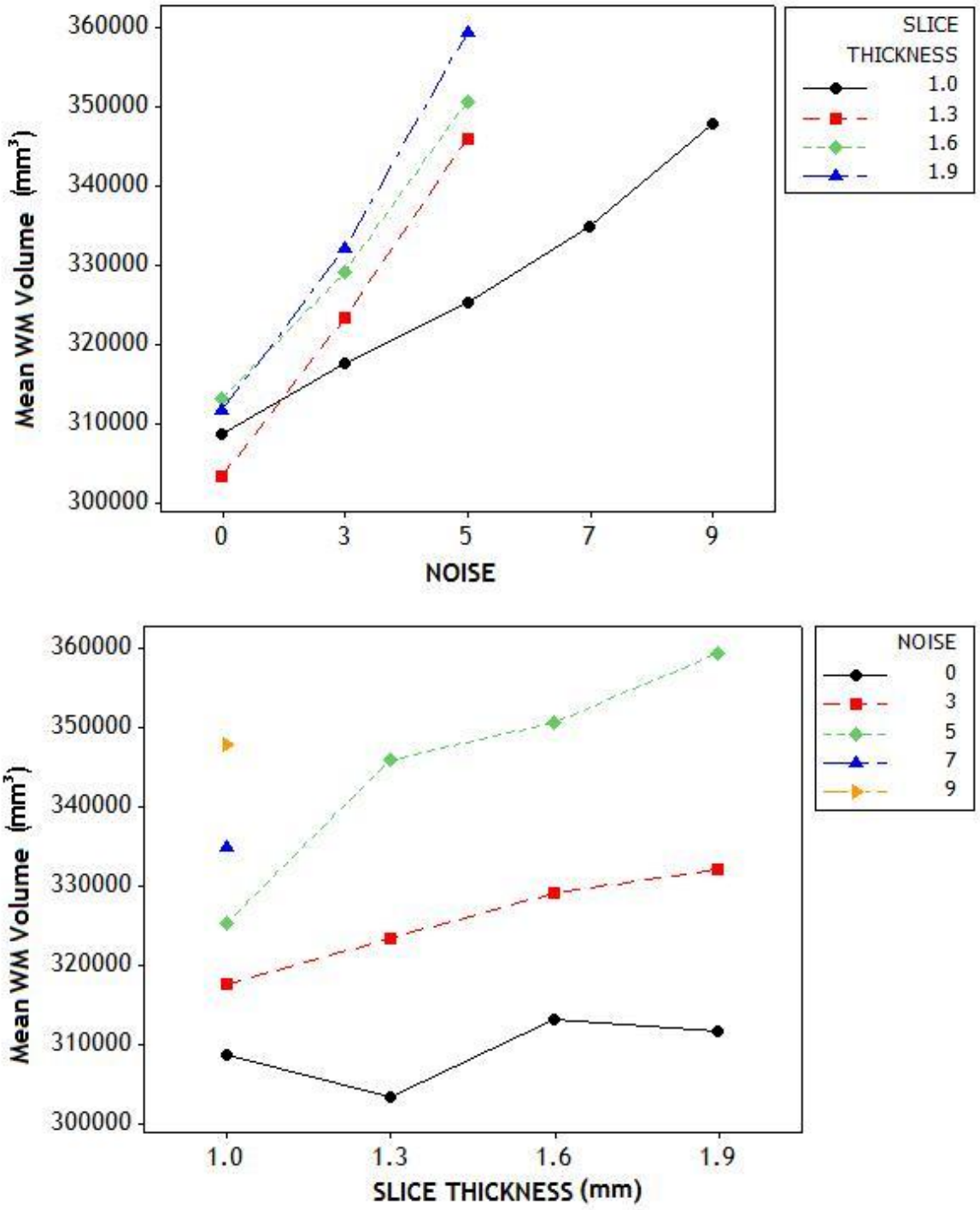

Figure 4-3 The plots of interaction between slice thickness and noise for WM volume
The plots show the variations in the average WM volume across different levels of intensity non-uniformity (top) with noise at different levels of slice thickness and (bottom) with slice thickness at different levels of noise.

Figure 4-4 shows the CSF volume mostly increases with increasing the noise. However, increasing the slice thickness does not have a significant effect on CSF volume. The figure also suggests that for all noise levels, the maximum CSF volume was estimated at the slice thickness of 1.3 mm.

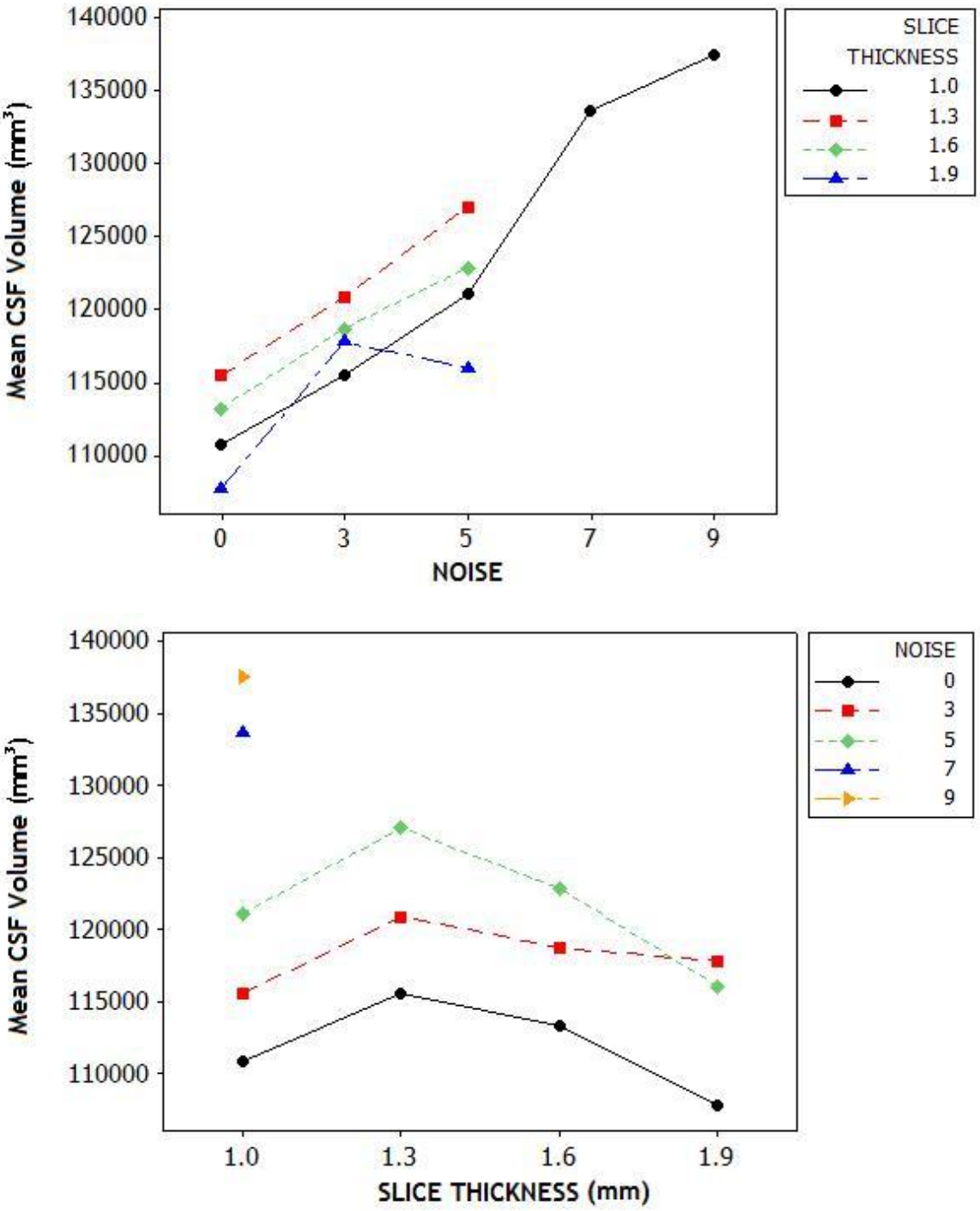

Figure 4-4 The plots of interaction between slice thickness and noise for CSF volume
The plots show the variations in the average CSF volume across different levels of intensity non-uniformity (top) with noise at different levels of slice thickness and (bottom) with slice thickness at different levels of noise.

The result of the regression analysis for GSI is given in table 4-3. As indicated by this table, noise does not have a significant impact on GSI. However, GSI decreases by increasing the slice thickness. In addition, the effect of variations in intensity non-uniformity on GSI is only slightly above the significance level.

Figure 4-5 shows the plots of interaction between the slice thickness and intensity non-uniformity for GSI. This figure suggests that except for the slice thickness of 1.9 mm, for all other slice thicknesses, GSI is not significantly affected by intensity non-uniformity. In other words, intensity non-uniformity can lead to reduced GSI only at high slice thicknesses (at least 1.9 mm). Nevertheless, for all levels of intensity non-uniformity, GSI decreases by increasing the slice thickness and on average, an increase in the slice thickness from 1 mm to 1.9 mm, results in around 10% reduction in the GSI value.

Slice Thickness			Noise			Intensity Non-uniformity			R^2
$\beta(mm^{-1})$	t	p	β	t	p	β	t	p	
-0.164	-10.57	<0.001	-0.002	-1.26	0.211	-0.001	-1.93	0.057	0.59

Table 4-3 Regression analysis for GSI
The table shows the coefficients as well as t- and p-values for each factor in additions to the R^2 value of the regression model

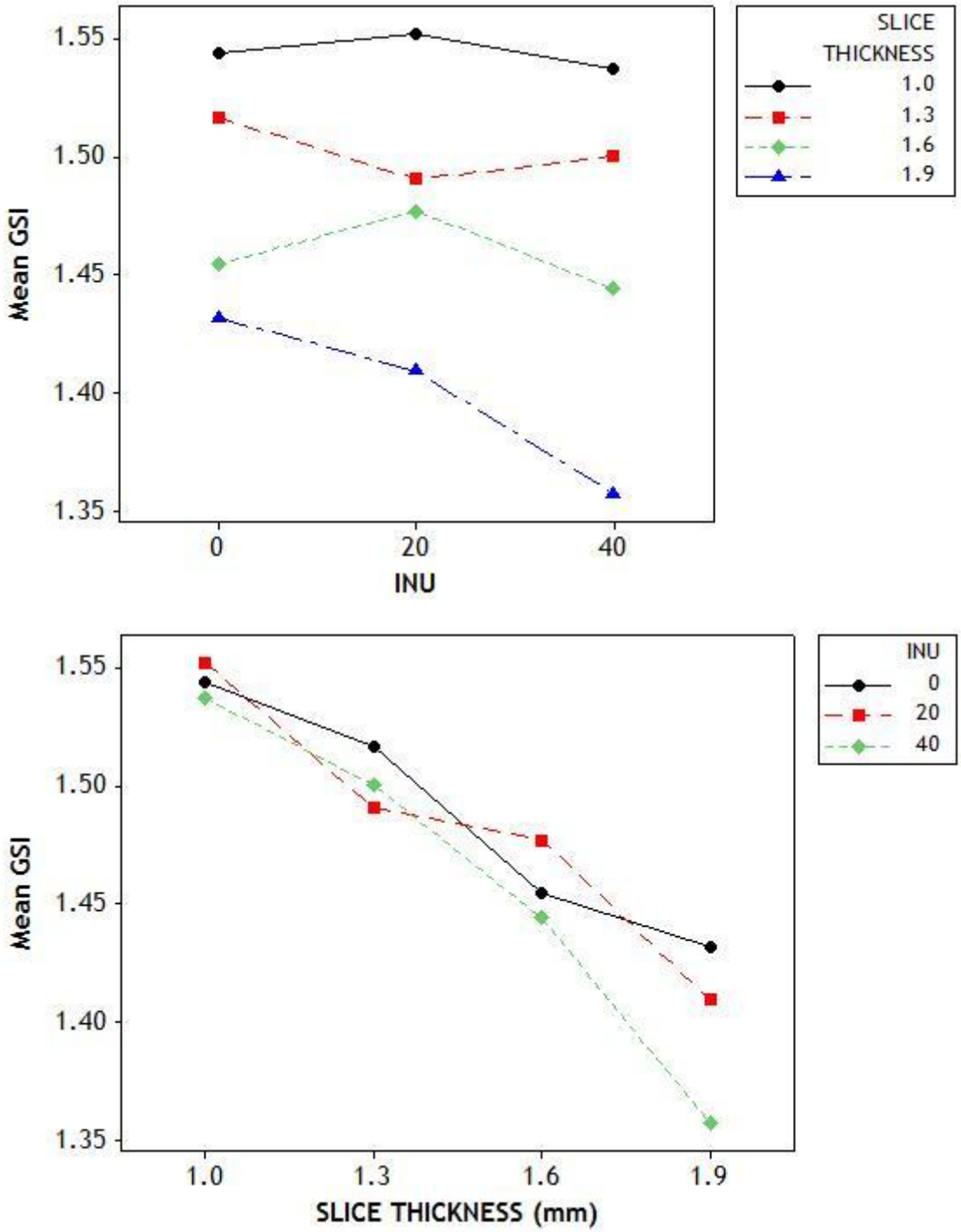

Figure 4-5 The plots of interaction between slice thickness and intensity non-uniformity for GSI
The plots show the variations in the average GSI across different levels of noise (top) with intensity non-uniformity at different levels of slice thickness and (bottom) with slice thickness at different levels of intensity non-uniformity.

4.6 Discussion

In chapter three the reproducibility of brain morphometry with Brainvisa was assessed using two separate datasets acquired at 1.5T and 3T field strengths. In

general, it was observed that the reproducibility of brain segmentation was relatively higher for the 1.5T group compared to the 3T group. Conversely, GSI estimation was more reproducible for the 3T group relative to the 1.5T group. In order to find the image acquisition parameters which can generate highly reproducible morphometry results it is desirable to estimate the contribution of each parameter on the reproducibility of the results. However due to a variety of difference between the two datasets including different field strengths, scanners, image acquisition parameters, and subject groups (also different age range, gender, etc.), an investigation of the contribution of each factor (regardless of the scanner-related variations) on the reproducibility of the results was not possible. For example, values for both slice thickness and noise (lower SNR due to lower field strength) were higher in the 1.5T and it was not clear which mostly affects the brain segmentation and which has the strongest effect on GSI. Here the impact of several factors with potential impact on brain morphometry with Brainvisa is assessed by making use of simulated data.

Brain segmentation was shown to be susceptible to noise. More precisely, by an increase in noise, more GM voxels are labelled as WM or CSF suggesting that the GM segmentation can be significantly improved by scanning at higher field strengths. Conversely, bias field appears not to have a significant impact on the brain segmentation, at least up to a 40% INU level. An increase in slice thickness was shown to result in GM voxels to be labelled as WM however the variation in CSF volume with slice thickness did not reach the significance level. Nevertheless, the relatively low value of R^2 for linear regression of the CSF volume suggests that the variations in the CSF volume may not be best modelled by linear relationship with the above factors. Interestingly, while increasing the slice thickness from 1 mm to 1.3 mm led to the increase in the CSF volume, further increase of the slice thickness (from 1.3 mm) reduced the CSF volume. This suggests that the initial increase in the CSF volume (corresponding to varying the slice thickness from 1 mm to 1.3 mm) resulted from the partial volume effect leading to classifying voxels at the GM/CSF boundary as CSF instead of GM. At slice thickness of 1.6 mm already all partial volume voxels at the GM/CSF boundary have been classified as CSF. Increasing the slice thickness from 1.3 mm has probably therefore only led to the reduction in the CSF volume possibly by classifying the CSF voxels at WM/CSF boundary as WM.

The results show that noise does not have a significant impact on GSI. Bearing in mind that folds are detected through skeletonising the union of GM and CSF, this can be due to the fact that changes in the GM and CSF volumes with noise can cancel out each other, making the GM/CSF union less susceptible to noise. However, GSI decreases by increasing the slice thickness. This can result from the overall reduction in the volume of GM/CSF union with increasing slice thickness (note the negative coefficient for slice thickness in linear regression for GM and CSF volumes on table 4-2). Image non-uniformity has been shown to have a significant effect on GSI only at 1.9 mm slice thickness. This might arise from limitations of bias correction for higher slice thicknesses.

4.7 Conclusion

The variations in morphometry results using Brainvisa with noise, slice thickness, and magnetic field non-uniformity was assessed using simulated T1-weighted images. GM segmentation was shown to suffer from both noise and slice thickness suggesting that with higher field strengths and smaller slice thicknesses, the GM segmentation would be more accurate. Detection of the cortical folds was found to be relatively robust against the noise while shown to suffer from large slice thicknesses. Compared to noise and slice thickness, both brain segmentation and fold detection were relatively robust against magnetic field non-uniformity suggesting that noise and slice thickness can have the main impact on the results.

Chapter 5. The estimation of changes in the sulcal size associated with autism spectrum disorder by sulcal morphometry using Brainvisa

5.1 Overview

This chapter assess the use of sulcal morphometry in the analysis of the abnormality-related, structural changes in cortex. Several structural changes in cortex have already been suggested for subjects with Autism including the local increase in cortical gyrification. This raises the possibility that some sulci might have increased size in subjects with Autism. Nevertheless, an investigation of changes in sulcal size has not previously been reported.

In this chapter changes in sulcal size are assessed. The chapter begins with a review of studies which have analysed the structural changes in brain associated with Autism and identified several biomarkers of the disorder. For each automatically labelled sulcus, the sulcal size is estimated in a groups of adolescents with Autism and a group of age-, sex-, IQ-matched control adolescents and the results are compared between the two groups.

All data analyses in this chapter were solely performed by the author. The results of this study have been presented as oral presentation in the ESMRMB 2011 congress and have also been submitted for publication in Neuroimage.

5.2 Background

Finding biomarkers for Autism Spectrum Disorder (ASD) is challenging due to the diversity in the age group, gender, IQ, the inherent heterogeneity of the disorder, and the wide range of type and severity of the symptoms (Rojas et al., 2006). To date several biomarkers including cortical thickness (Hardan et al., 2006; Hadjikhani et al., 2006), regional and total grey matter volume (McAlonan et al., 2002; Waiter et al., 2004), and regional white matter volume (Waiter et al., 2005; Radua et al. 2011) have been investigated. In addition, abnormality of the cortical shape in terms of the sulcal depth pattern (Nordahl et al., 2007), folding and gyrification (Kates et al., 2009), mean convexity, mean curvature and metric distortion (Ecker et al. 2010) has been investigated. To avoid the above-mentioned complexity, studies are usually focused on specific sub-groups of the ASD patients including high functioning (Hadjikhani et al. 2005, Waiter et al. 2004, 2005; Nordahl et al. 2007), low- functioning (Nordahl et al. 2007), and Asperger's syndrome (McAlonan et al., 2002; Nordahl et al. 2007). Different age groups are also considered usually categorized as children (Hardan et al., 2006; Nordahl et al. 2007; Kates et al. 2009; McAlonnan et al., 2005), adolescents (Waiter et al. 2004, 2005; Nordahl et al., 2007), and adults (Hadjikhani et al., 2005; McAlonan et al., 2002; Ecker et al., 2010).

Several studies have suggested cortical abnormalities in ASD patients and there has been a growing interest in the pathology-related changes in cortical pattern (Levitt et al., 2003; Nordahl et al. 2007; Ecker et al., 2010). Levitt et al. investigated the changes in the sulcal maps of a group of children and adolescents with ASD (Levitt et al., 2003) by manually tracing 11 major sulci and confirmed the displacement of the superior frontal sulcus (in both hemispheres), the right Sylvian fissure, the superior temporal sulcus (in both hemispheres), and the left inferior frontal sulcus, relative to the control group. Nordahl et al., compared the sulcal depth maps of three different groups of the ASD patients: low-functioning, high-functioning, and Asperger's syndrome (Nordahl et al. 2007) and showed variations in the anterior insula and the frontal operculum in the low-functioning group, the parietal operculum and ventral postcentral gyrus in the high-functioning group, and the intraparietal sulcus of the group with Asperger's syndrome, relative to the control group. Ecker et al. introduced the idea of multi-parameter analysis and

suggested using five morphological parameters including both geometric and volumetric features of the cortical surface simultaneously (Ecker et al., 2010). Using these parameters and a method based on Support Vector Machine (SVM: (Muller et al., 2001), they showed the ASD and healthy groups could successfully be discriminated. These findings indicate that cortical parameters may constitute suitable biomarkers of Autism.

Most of the above-mentioned abnormalities in the cortical pattern are not based on the properties of the macro-anatomical cortical features (sulci/gyri) but rather properties of the cortical surface. However, the cortical surface has been variably defined as the GM/WM interface (Fischl et al., 1999a) as was used in the study by Ecker et al., pial surface (Fischl et al., 1999a), or an intermediate surface running halfway through the cortical thickness (Van Essen et al., 2005), as was used by Nordahl et al. Thus, the measures are sensitive to the algorithm used to define them which impedes their replicability. Conversely, sulcal attributes such as size (volume, length, etc.) offer a direct measure of cortical properties and so can be independent of defined cortical surface.

In addition the previous finding about altered cortical folding and gyrification (Kates et al., 2009) raises the question as to whether some sulci have altered size in ASD, bearing in mind that cortical gyrification is expected to correlate with sulci dimensions. Changes in sulcal size can reflect long-standing developmental influences on the folding process. For example correlates of handedness on the size of the sulci located in motor areas have previously been confirmed (Mangin et al. 2004). Despite the demonstrated change in the cortical pattern in ASD, to date similar investigation of sulcal size has not been verified.

5.3 Aims and Objectives

In this chapter the changes in the sulcal size and depth are examined using Brainvisa 4.0 for a group of adolescents with ASD and the results are compared to a group of age-, sex-, and IQ-matched control adolescents. Moreover, the correlation of the sulcal changes with other structural and functional abnormalities previously identified in the same group of subjects with ASD was assessed. A previous structural study on the same subjects revealed significant increase in the

local GM volume of the ASD group in several cortical regions including the right fusiform gyrus, the right temporo-occipital region and the left frontal pole (Waiter et al., 2004), relative to the control group. A functional study on the same subjects verifying the between-group difference in the activation pattern during very simple imitation confirmed the reduced activity in the right parietal lobe and left insula, left amygdala, and right parietal lobe for the ASD group compared to the control group (Williams et al., 2006).

5.4 Methods

5.4.1 Participants

The participants included 15 adolescents with ASD and 14 healthy controls. The ASD participants were recruited through clinic attendance and contact with local voluntary societies and the control participants were recruited through local youth groups. All participants were right-handed males and aged between 12 and 20.

The ethical approval for the study was obtained from the local medical ethics committee and all participants gave informed, signed consents. Participants were assessed on the Autism Diagnostic Observation Schedule-Generic (ADOS-G) (Lord et al., 2000) and the Autism Diagnostic Interview (Lord et al. 1994). IQ assessments were carried out using the WISC-III R (Wechsler, 1982) for participants under 16 years and WAIS-IV (Wechsler, 1981) for those over 16 years. The handedness inventory (Oldfield, 1971) was also administered. Participants were excluded if they had any known neurological disability, full scale IQ <70, or had any contraindications to MRI. Participant details are shown in Table 5-1.

	ASD group (N=15)	Control group (N=14)
Age (years)	15.4 (2.2)	15.5 (1.6)
Verbal IQ	100.9 (23.4)	101.3 (21.1)
Performance IQ	98.4 (19.0)	97.6 (13.9)
Full scale IQ	100.4 (21.7)	99.7 (18.3)

Table 5-1 Participant information: mean (standard deviation)

All ASD participants had an unambiguous clinical diagnosis of Autistic Disorder or Asperger's syndrome according to DSM-IV criteria. All scored above the diagnostic threshold on the algorithm associated with the ADI-R (2000) and all but one scored above the diagnostic threshold for Autistic Spectrum Disorder on the ADOS-G diagnostic algorithm.

5.4.2 Image acquisition

High resolution, 3D T1-weighted images were acquired using a 1.5 T GE scanner, a quadrature head coil and the following image acquisition parameters: TR of 20 msec, TE of 6 msec, NEX of 1, flip angle of 35 degrees, image resolution of 1*1*1.6 mm^3, and matrix size of 256*256*124 voxels (124 contiguous and1.6 mm thick axial slices). Figure 5-1 shows an example of the acquired T1-weighted images from each group.

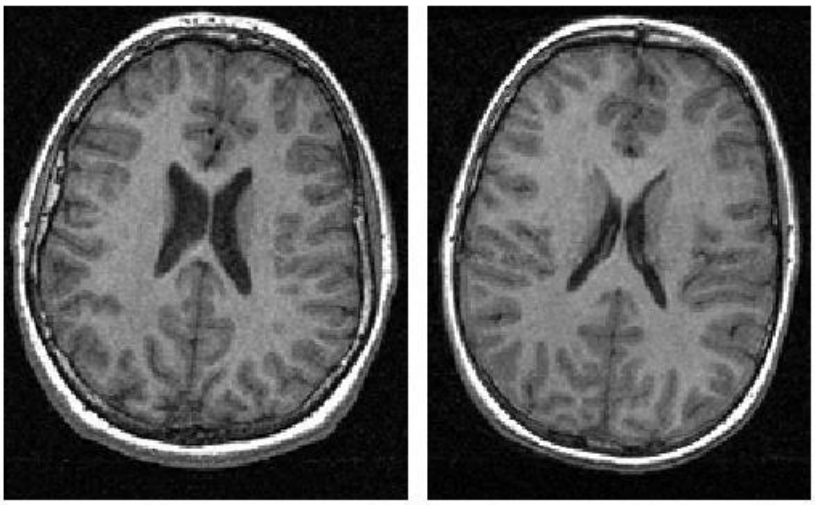

Figure 5-1 Examples of T1-weighted images acquired for this study
The images correspond to a subject from a) the ASD and (b) control groups.

5.4.3 Image pre-processing

Data pre-processing included bias field correction, histogram analysis, brain extraction, splitting the brain into two hemispheres and the cerebellum, segmentation, extraction of the cortical folds and sulci identification using the Global algorithm (as explained in chapter one). Since Local and Markovian

algorithms include an additional sulcus-wise registration step (see chapter one), using assumptions which may not be valid for abnormal brains due to the possibility of local changes in the cortical pattern, these algorithms were not examined. Furthermore, the Talairach algorithm was avoided as this had been shown (in chapter three) to result in low reliabilities.

5.4.4 Morphometry analysis

As mentioned earlier the analysis with Brainvisa is carried out on each hemisphere separately and therefore morphometric measures correspond to each individual hemisphere.

To estimate the abnormalities associated with brain sulcation and gyration as well as sulcal parameters the following parameters were computed using morphometry analysis within Brainvisa:

Global Sulcal Index (GSI): GSI is an estimation of the cortex gyrification and is defined as the ratio between the total area of all the cortical folds and the area of the outer cortical surface (unfolded cortex). GSI is calculated for each hemisphere separately and provides a comparison between brain sulcation of the two groups and is useful as a change in brain sulcation with ASD has already been reported (Kates et al. 2009).

Sulcal surface: Since the sulci are formed from the skeleton surface which is only one voxel-thick, the volume of these skeleton segments depends on the voxel size and orientation and is not a reliable estimate of the sulcal volume. Instead, the total surface area of the sulcus which is not affected by voxel size gives a better estimation of sulcus size. Therefore the sulcus surface was used as the proxy for its volume.

Sulcal length: sulcal length is measured as the size of voxels on the junctions between a sulcus and the brain hull and is used as another estimate of the size of the sulci.

Sulcus mean geodesic depth: The geodesic depth of a sulcus is defined as the geodesic distance (along the cortical mesh) between the external line of the fold (on the brain hull), and the bottom line of the sulcus.

Independent estimation of the length and surface is necessary as the altered sulcal size can be reflected in either of these parameters. For example, an increase in sulcal surface may not necessarily result from an increase in its length but its depth. Likewise, increased length may not have a correlation with increased surface if cancelled out by the decrease in depth.

5.4.5 Statistical analysis

For each morphometric parameter, the General Linear Model (GLM) within Minitab16 was used to examine whether the estimated values for the ASD and control groups were significantly different at the significance level of 0.05. As the morphometry results may vary with the hemisphere size and age of the subjects, these two parameters were used as covariates in the GLM model. Briefly, the model included “group” (ASD vs. Control) as a factor, “hemisphere volume” and “age” as covariates.

For sulcal parameters (surface, length, and mean geodesic depth), the analysis was followed by multiple comparisons test using Tukey’s method at the 0.95 confidence interval to compare the values estimated for each sulcus of the ASD and control groups.

5.5 Results

Though GSI was higher for ASD compared to control, this difference did not reach significance (p=0.183 for left hemisphere, and p=0.153 for right hemisphere).

The statistical analysis for the surface of all sulci, revealed increased surface of insula only in the left hemisphere of the ASD group (p=0.016). The box plots for the surface of the left insula for both ASD and control groups are shown on figure 5-2.

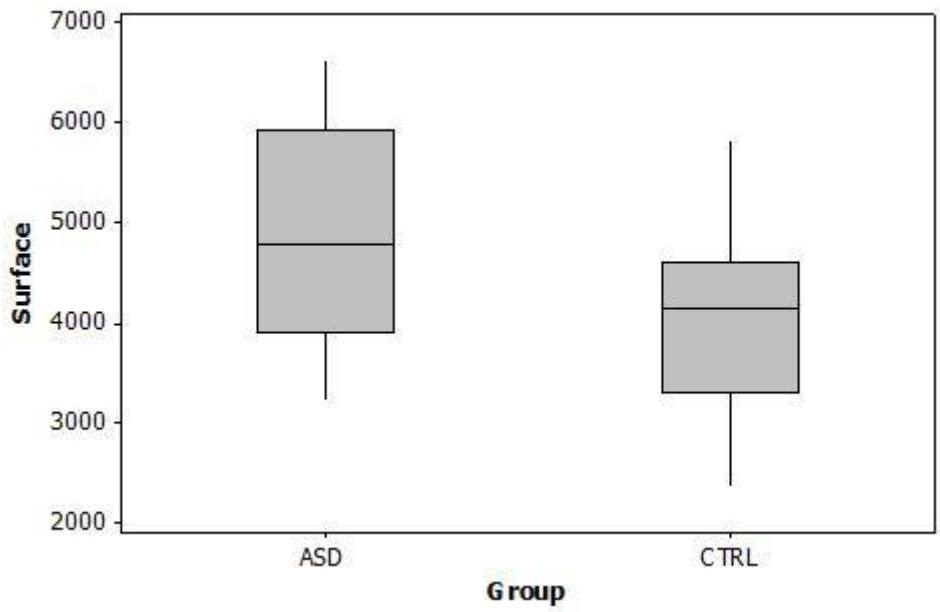

Figure 5-2 The box plots of left insula surface for the Autism and control groups
The medians and inter-quartile ranges are shown in mm^2 for the Autism group (ASD) and controls (CTRL).

A similar analysis for the sulcal length was indicative of increased length of the right intraparietal sulcus in the ASD group compared to controls (p=0.015) as can also be verified from figure 5-3.

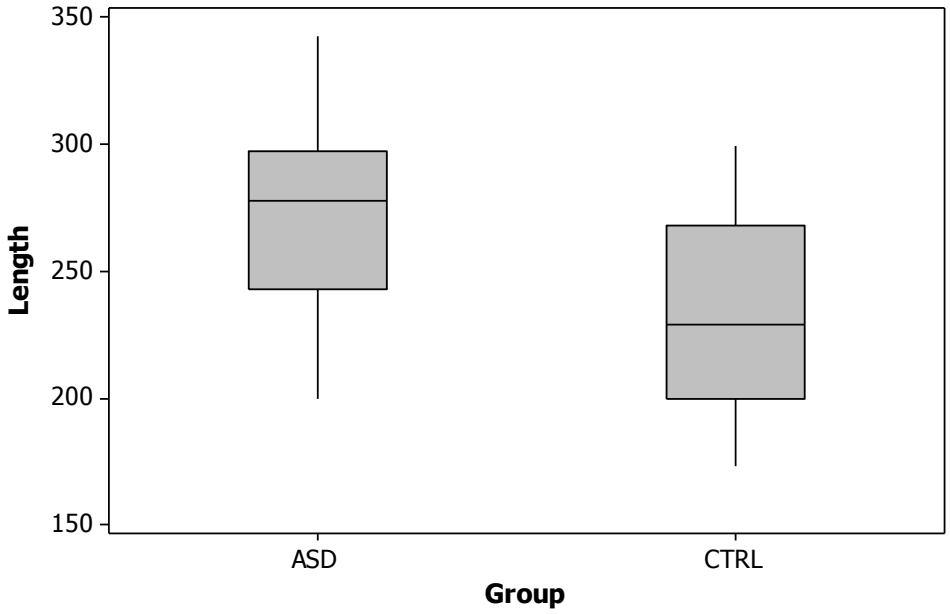

Figure 5-3 The box plots of the length of the right intraparietal sulcus for the Autism and control groups
The medians and inter-quartile ranges for the length of the right intraparietal sulcus are shown in mm for the Autism group (ASD) and controls (CTRL).

However no significant between-group difference were detected for mean geodesic depth for any of the sulcal pieces.

5.6 Discussion

The first question was whether people with autism showed greater or lesser amounts of folding overall, and to this end the GSI was compared between groups. Although GSI was higher in the ASD group, the difference was non-significant. This confirms findings by Kates et al. who also found no significant difference in the global gyrification index between the ASD and healthy groups (Kates et al., 2009).

However, Kates et al. did find that the right parietal lobe gyrification index was significantly higher in both Autistic children and their co-twins compared to controls. As GSI is defined as the ratio between folded and unfolded areas of the cortex, the increased GSI may stem from increased size of some sulci. Therefore, this is in accord with this study which showed significant increase in the length of the right intraparietal sulcus (rIPS). The rIPS has previously been shown to have decreased thickness of cortical grey matter in autism (Hadjikhani et al.,2006) and Nordahl et al. reported increased depth of the rIPS in Asperger's syndrome with the depth correlating with severity of symptomatology on the social reciprocity domain of the ADI-R (Nordahl et al., 2007). The rIPS has been implicated in social cognitive function through its role in imitation and the mirror neuron system (Williams et al., 2006; Williams 2008).

Moreover, the surface of the insula in the left hemisphere was found to be increased in the ASD group, which also replicates Nordahl et al., (2007) who found the insula to have an increased depth in a low-functioning group of children and adolescents with autism.

Interestingly, the functional study by Williams et al. on the same subjects as those in this study revealed that while in the control group left insula was activated during imitation-observation paradigm a similar activation was missing in the ASD group. Although the association between functional deficiency and altered sulcal surface requires further investigation, the convergent findings of both structural

and functional abnormalities in the same group of patients points to a key role for the left insula in the studied group of ASD patients. This is of particular interest given the possibility that, like the rIPS, the insula also serves an important 'mirror neuron' function (Gallese 2004), and given more recent evidence for the important role of insula in autism and social cognitive function (Uddin and Menon, 2009).

However, the results of this study failed to replicate the finding of altered sulcal depth of any area of cortex in autism reported by Nordahl., et al. This may be because of differences in the way that sulcal depth was measured. Nordahl et al., measured sulcal depth as the nearest distance between the brain hull and bottom of the cortical fold, whereas the geodesic depth in the current study refers to the distance between the bottom of the fold and the external line of the sulcus along the cortical surface. Also, the mean values (mean geodesic depth) used here may be less sensitive to subtle abnormalities compared to the local variations in depth along each sulcus.

Nevertheless, the degree that this study has been able to replicate the findings of Nordahl et al. (regardless of using different patients groups) suggests that sulcal parameters can be appropriate biomarkers of ASD.

It is therefore, a challenging question to ask why greater folding should result in impaired social development and function. Comparing the results of this study with the voxel-based analysis of the GM distribution on the same groups of subjects (Waiter et al., 2004) no correlation was found between changes in sulcal surface or length and the local variations in the GM volume. For one thing, this may reflect the different ways in which cortical abnormalities reflect neurodevelopment and brain function. Whilst folding patterns and sulcal parameters are likely to reflect long-standing neurodevelopmental influences (Van Essen, 2006), GM volumes are more likely to reflect patterns of learning (Driemeyer et al., 2008).

One limitation of this study is that the morphometry results might have been affected by the scanner variability over time. As shown in chapter three, the within-scanner variability for sulcal morphometry could be problematic especially for data acquired using 1.5 T scanners. This results in increased variance which may impede the detection of small between-group differences.

5.7 Conclusion

In this chapter group differences in sulcal measurement parameters has been identified in brain areas previously implicated in the aetiology of autism. The results of this study suggest that automated measures of sulcal surface and length can successfully reflect cortical abnormality in autism.

Chapter 6. Assessment of cerebral plasticity for pre-surgical planning in patients with brain tumours and vascular malformations using Brainvisa

6.1 Overview

This chapter is an attempt to explore the performance of Brainvisa for patients with brain tumours, cysts, or vascular malformations. These pathologies represent space occupying lesions which may also be expected to displace or damage the adjacent eloquent tissue and which may therefore serve as a confound in identifying eloquent areas.

Here the sulci recognition feature of Brainvisa is used to identify the eloquent areas using fMRI for patients with the above-mentioned pathologies. Since using Brainvisa for such abnormalities has not been previously reported, this chapter presents a pilot study to assess the suitability of Brainvisa for the estimation of the cerebral plasticity in these patients.

The patients had previously undergone fMRI for the purpose of pre-surgical planning. Depending on the location of the lesion, the fMRI of each patient included mapping of the motor function, the language function, or both.

All data analyses in this chapter were solely performed by the author.

6.2 Background

Surgical removal of the tumours and vascular malformations in the brain incurs the risk of functional deficit. To minimize such a risk therefore, pre-surgical assessment needs to be carried out in order to decide whether or not surgery is an appropriate choice. fMRI provides a non-invasive method for pre-surgical planning through mapping of the brain activation and estimating how far from the margins of the lesion have the functionally activate regions been located. This allows for the assessment of whether the removal of the lesion can safely preserve the eloquent brain areas (Fandino et al., 1999; Baciu et al., 2003; Krings et al. 2001; Sunaert, 2006; Bookheimer, 2007).

The importance of activation mapping for pre-surgical assessment is due to the fact that the activated areas may be different from those that are normally expected. The pattern of activation is quite often altered in pathological brains through cortical reorganization or plasticity (the relocation of function from damaged to healthy areas as a result of the pathology). For example, Alkadhi et al. have suggested that for patients with arteriovenous malformation (AVM) situated in the motor areas, function can be relocated within the same hemisphere, or to the opposite hemisphere, or to non-primary motor areas (Alkadhi et al., 2000). Carpentier et al. proposed a grading scheme for classification of plasticity (Carpentier et al. 2001) which covered the normal activation pattern (grade 1), reflecting the mass effect (grade 2), altered activation pattern without any evidence of plasticity (grade 3), possible local plasticity (grade 4), definite ipsilateral (within the same hemisphere) plasticity (grade 5), and definite contralateral plasticity (grade 6). Furthermore, it has been shown that there is no correlation between the cerebral reorganization and the type or location of the lesion (Baciu et al., 2003). In other words, the same type of tumour located in the same area of different patients' brains can result in various pattern of reorganization in those patients. Therefore, due to the possibility of cortical reorganization in pathologic brains, the activation pattern should independently be verified for each patient.

Motor and language function mappings are among the most widely used experiments in pre-surgical planning as damage to these areas during surgery can cause significant disability. In healthy brains, the anterior and posterior banks of

the central sulcus contain the primary motor and sensory cortex, respectively. The somatotopic organization of the primary motor cortex is such that feet correspond to the medial surface and the vertex of the hemisphere, hands are associated with the superior part of the hemisphere , and lips with the inferior portion of the lateral hemisphere, for example (Sunaert, 2006). In pre-surgical fMRI mapping this somatotopy can be mapped using several tasks such as finger-tapping, hand-grasping, lip-puckering, and movement of the toes (Fandino et al., 1999; Roux et al., 2000; Lehericy et al. 2000). However, language mapping is usually more challenging due to the variability in the location of the activation foci even across healthy individuals (Bookheimer, 2002). It has been suggested that several functional subdivisions including syntax, phonology, and even higher order semantic operation do exist in the inferior frontal gyrus. Likewise, Wernicke's area covers a number of regions in the temporal and parietal lobes contributing to the sound recognition, word recognition, symbolic analysis, sequencing, and in the inferior temporal region, recognition of words, objects and object naming (Bookheimer, 2007; Wise et al., 2001). Despite its complexity however, it has been shown that language mapping using fMRI can be a valuable preoperative tool which can successfully identify the language-sensitive areas (Pouratian et al., 2002; Cannestra et al. 2004; Benson et al.'s 1999; Fitzgerald et al. 1997; Ulmer et al. 2004; Ruge et al. 1999).

The studies regarding cortical reorganization for pre-surgical planning usually involve overlaying the activation map on the high-resolution T1-weighted image and visually identifying the activated area. Manual identification however, can be challenging due to the distortion resulting from the mass effect of the lesions (Sunaert, 2006) or when the lesion has pushed some parts of the brain.

An automatic method of identification of the brain regions could address such difficulties and provide a useful tool in the analysis of the cerebral plasticity. Using sulcal labels also enables a more precise identification of the activated regions. By identifying the sulci in the neighbourhood of the activated region, the activation patterns of different individuals can be compared.

The different types of the pathologies considered in this study include: AVM, cavernous angioma, oligodendroglioma, glioblastoma and cyst. AVM and

cavernous angioma are two groups of vascular malformations. AVM refers to a congenital anomaly of blood vessel development which results in a direct communication between the arterial and venous channels without an intervening capillary network. Cavernous angioma occurs less frequently compared to AVM and appears a compact honeycomb-like mass of capillaries (Atlas, 1996). Primary brain tumours (initiated within the brain) on the other hand, are usually categorized according to their degree of malignancy, growth rate and pattern, and the anatomical compartment in which they are located. Tumour grade refers to the degree of malignancy and is based on its tendency to spread and grow into the surrounding tissues (infiltrate), the growth rate, whether or not it contains dead cells (necrosis), the blood supply (vascularity), and similarity to normal cells. It ranges from grade I (least malignant tumours) to grade IV (most malignant tumours). Oligodendrogliomas which are mostly found in the cerebral hemisphere originate from oligodendrocytes and can be low-grade (grade II) or high-grade (grade III). Glioblastoma Multiform (GBM) is mostly found in cerebral hemispheres and can grow very rapidly and can mix with normal brain tissue. Cysts are tumour-like spheres which can contain fluid, blood, tissue or tumour cells (American Brain Tumour Association, 2004).

6.3 Aims and objectives

The aim of this chapter is to assess the suitability of Brainvisa for cortical plasticity studies of patients with brain lesions. Using Brainvisa, the eloquent areas of the cortex are estimated in a group of 12 patients with brain tumours, cysts, or vascular malformations, previously scanned for pre-surgical planning. For this purpose, activation detection is first carried out using SPM8, and then Brainvisa is used to locate the activation with reference to the automatically identified sulci.

6.4 Methods

6.4.1 Patients

This study was approved by the West of Scotland Research Ethics Committee. The patients included in this study had been previously scanned at the Institute of

Neurological Sciences (INS), Southern General Hospital, Glasgow, for pre-surgical evaluations. The MR scans were acquired using one of the two scanners: GE 3T HD and GE Signa 1.5 T. The functional scans and the 3D T1-weighted scans were used for this study to map the brain activation (using fMRI) and find the activated anatomical feature using the 3D T1-weighted images with the cortical labelling facility of Brainvisa.

6.4.2 fMRI experiments

Depending on the location of the tumour or the vascular malformation, the fMRI experiments were chosen from among various motor and language mapping paradigms. The motor mapping experiment included paradigms such as finger tapping, hand grasping, and feet movement. These paradigms a block design with 20 alternating blocks of activation and rest, each with a duration of 30 seconds. The patients had been told to perform the tasks at their own pace.

The language mapping experiments consisted of word generation and noun-to-verb conversion paradigms, both with the same block design as the motor mapping experiment. During the word generation task, a single letter was visually presented at the beginning of each active block and the patient was asked to think of the words starting with that letter. Within the rest blocks only a cross sign was displayed to exclude visual activations in the final map. In the noun-to-verb conversion task a noun appeared on the screen every 2 seconds within the active block (15 stimuli in each active block) and the patient was asked to think of a verb that could be associated with that noun. Again within the rest blocks only a cross sign was displayed. However, due to the repetition of the visual stimuli during active blocks, the noun-to-verb paradigm is also expected to activate the visual cortex.

6.4.3 Image acquisition

The details of patients' pathologies, and the acquisition parameters for the 3D T1-weighted images are given in table 6-1.

Patient	Pathology	Scanner	Sequence	TR (ms)	TE (ms)	TI (ms)	Flip angle (°)	Image size Voxelsize (mm^3)
P01	AVM	1.5 T	IRFSPGR	11	2.3	400	20	256x256x124 1x1x1.4
P02	Right lateral temporal cyst	3 T	IRFSPGR	7.2	1.6	500	12	512x512x160 0.5x0.5x1
P03	Cavernous angioma	1.5 T	IRFSPGR	9.3	2	450	10	256x256x124 1x1x1.4
P04	Right oligodendroglioma grade II	1.5 T	IRFSPGR	11	2.3	400	20	256x256x168 1x1x1
P05	Right frontal oligodendroglioma grade II	1.5 T	IRFSPGR	8.7	1.9	450	10	256x256x124 1x1x1.4
P06	Left grade II posterior frontal oligodendroglioma	3 T	IRFSPGR	6.9	1.6	500	12	512x512x160 0.5x0.5x1
P07	Cavernous angioma	3 T	IRFSPGR	6.5	1.5	500	12	512x512x160 0.5x0.5x1
P08	Unknown	1.5 T	IRFSPGR	8.7	1.9	450	10	256x256x124 1x1x1.4
P09	AVM	3 T	IRFSPGR	6.5	1.6	500	12	512x512x160 0.5x0.5x1
P10	Left parafalcine low grade lesion	3 T	IRFSPGR	7.8	1.7	500	12	512x512x124 0.5x0.5x1.4
P11	AVM	1.5 T	IRFSPGR	8.7	1.9	450	10	256x256x124 1x1x1.4
P12	Left temporo-parietal glioblastoma	3 T	SPGR	30	6	----	45	512x512x160 0.5x0.5x1

Table 6-1 The types of pathology and acquistion parameters for the T1 images of the patients

Functional images were acquired using the Gradient Echo (GRE)- Echo Planar Imaging (EPI) sequence with TR=3 secs, TE=40 msec on 1.5 T scanner and 30 msec on the 3 T scanner. The image size was 128x128x25 (voxels) for patients scanned with the 3 T scanner, and 64x64x25 (voxels) for patients scanned with the 1.5 T scanner. The voxel size was 1.88x1.88x4.5 mm^3 for patients scanned with the 3 T scanner, and 64x64x25 (voxels) for patients scanned with the 1.5 T scanner. An exception to this was that for patient P08 the image and voxel size were 64x64x30 (voxels) and 3.75x3.75x4 mm^3, respectively.

6.4.4 Image analysis

Activation detection was carried out using SPM8 and included the following steps:

Head movement correction: The subject's head movement during the scan will result in each voxel's time-series corresponding to different points in the brain

instead of a single point. Therefore head movement correction is performed to align all the volumes through a rigid-body registration (Ashburner et al., 2004). At this step, a mean image is also produced which is the average of all the realigned functional volumes.

Smoothing: Smoothing is performed to increase the SNR and to meet the assumptions of the statistical analysis (Ashburner et al., 2004). Smoothing was carried out using a Gaussian filter with 5 mm FWHM.

Activation detection: The statistical analysis on time-series was performed using GLM which tries to find the best linear fit between the signal intensity and the stimulation for each voxel (Ashburner et al., 2004). Then the t-test was employed to find the voxels with p-values corresponding to the null hypothesis of no correlation between signal intensity and activity smaller than a predefined significance level. For multiple comparisons correction, the family-wise error (FWE) was applied with the significance level of 0.05. At this stage the final activation map will be obtained.

Co-registration: The activation map is co-registered to the 3D T1-weighted image. This was done, by first registering the mean image produced in the head movement correction step, and then applying the same registration parameters to the activation map. The co-registration between the EPI and T1-weighted images was performed using the normalized mutual information method (Studholme et al., 1999) within SPM8. The result of co-registration was visually checked and where necessary, both EPI and T1-weighted images were skull-stripped. The registration was then performed on the extracted brains to achieve better results.

It should be noted, however, that due to the distortion of EPI images arising from the susceptibility artifact, the accuracy of the registration can be prone to error. This can be more severe in regions with higher susceptibility artifact (for example close to sinuses). Field mapping methods are useful for reducing such distortions (Andersson et al., 2001). It is therefore suggested that in prospective studies field maps are acquired during data collection and the distortion be corrected.

For structural analysis, the 3D T1-weighted image was analyzed using Brainvisa 4.0 and the extracted cortical folds were automatically labelled using the Global algorithm for sulci recognition within Brainvisa (see chapter one). Using Anatomist, a visualization facility within Brainvisa, the activation map of each paradigm was then overlaid on the cortical mesh (reconstructed using Brainvisa) and the location of activation was estimated with reference to the sulcal labels.

Prior to fold detection, the lesion was excluded from the brain mask to prevent its internal space from being labelled as GM or CSF, resulting in folds inside the lesion.

6.5 Results

6.5.1 Motor mapping

The location of the main activation centres (with strongest activation) with various motor mapping experiments, with reference to their proximity to the cortical sulci are summarized in table 6-2.

The overlay of the activation patterns of patients who performed the motor mapping task on their cortical meshes are presented in figures 6-1 to 6-10. For each case the hemispheres without activation is not displayed. The activation maps are displayed using a colour-coded scale from blue (minimum activation) to red (maximum activation) where regions with red and blue represent the highest and lowest activation. In these figures the locations with highest activity are shown by red arrows. It should be noted that the activation maps present regions with higher signal intensities during activation blocks compared to rest blocks. Out of phase activation was therefore not included as the purpose of the fMRI mapping in this study was to identify regions involved in performing the motor/language tasks.

In most patients, a region above the posterior part of the anterior cingulate sulcus (where the anterior and posterior parts of the sulcus join together) is shown to be activated. Nevertheless, this area is not considered a primary region for motor activation and is therefore not included in table 6-2.

Patient	Activation centres- motor task	Reorganization
P01	❖ Right hand: around central sulcus of the left hemisphere	No
P03	• Left finger: around central sulcus of right hemisphere • Left foot: around pre-central sulcus of right hemisphere	No
P04	❖ Left finger: around pre-central sulcus of right hemisphere ❖ Right finger: around pre-central sulcus of left hemisphere ❖ Left foot: around pre-central sulcus of right hemisphere	No
P05	• Left hand: around the central sulcus of right hemisphere • Left foot: around central and post-central sulci of right hemisphere	No
P06	❖ Right hand: around central sulcus of left hemisphere ❖ Left hand: around pre-central sulcus of right hemisphere	No
P07	• Right hand: around post-central sulcus of left hemisphere • Left hand: around post-central sulcus of right hemisphere	Shift towards the posterior parts of both hemispheres
P08	❖ Right hand: around central sulcus of left hemisphere ❖ Left hand: around central sulcus of right hemisphere	No
P09	• Right hand: around post-central sulcus of left hemisphere • Left hand: around post-central sulcus of right hemisphere	Shift towards the posterior parts of both hemispheres
P10	❖ Right hand: around post-central sulcus of left hemisphere ❖ Left hand: around post-central sulcus of right hemisphere ❖ Right foot: around post-central sulcus of left hemisphere	Shift towards the posterior parts of both hemispheres
P11	• Right finger: around post-central sulcus of right hemisphere	Ipsilateral (right hemisphere) activation

Table 6-2 Location of the activation centres of the motor task with respect to the sulci

As can be seen from table 6-2 and figures 6-1 to 6-10 in patients P07, P08, P09, and P10, the motor activation is shifted posteriorly although still in the same hemisphere. For patient P11, the activation was relocated in the opposite hemisphere. For all other patients, no reorganization was observed.

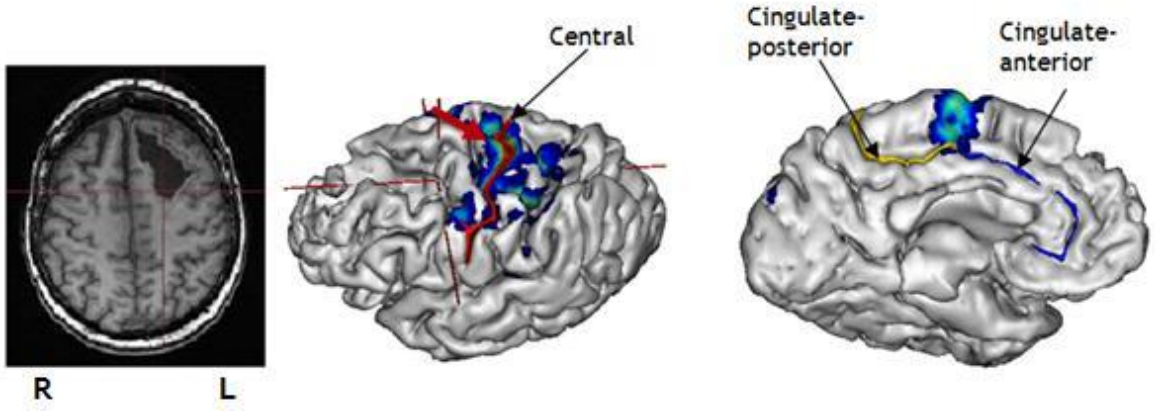

Figure 6-1 The activation map for the right hand grasping of patient P01
(left) T1-weighted image (shown in radiological orientation), (middle) lateral, and (right) medial views of the cortical mesh of the left hemisphere are displayed. Location of the AVM is shown by the red crosshair in both T1-weighted image and the cortical mesh. Activation centre is pointed by the red arrow. Also the region above the cingulate sulcus has been activated in this patient.

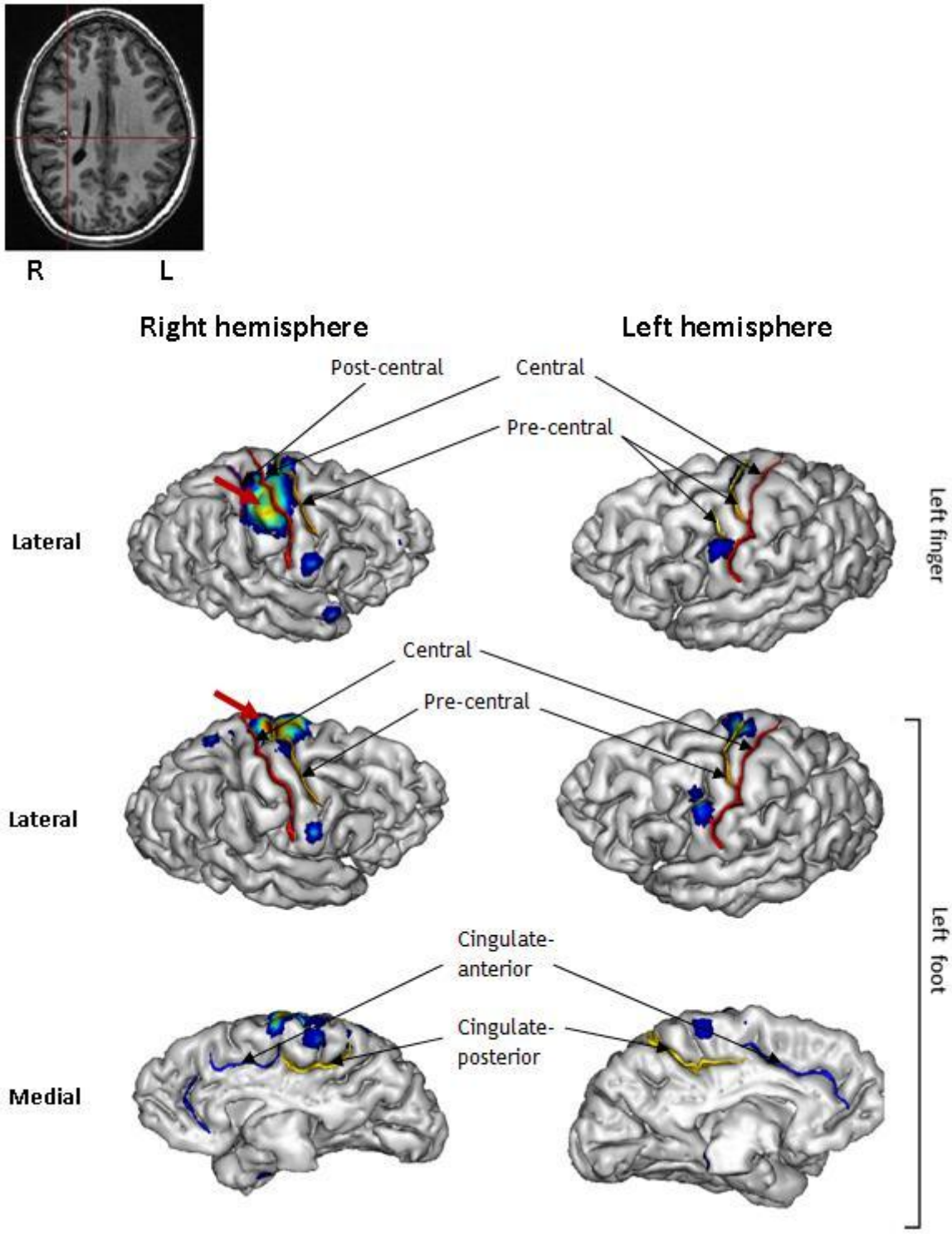

Figure 6-2 The activation map for motor tasks of patient P03
Location of the cavernous angioma is shown by the red crosshair in the T1-weighted image (shown in radiological orientation). Activation centres are pointed by the red arrow in the lateral view of the right hemisphere.

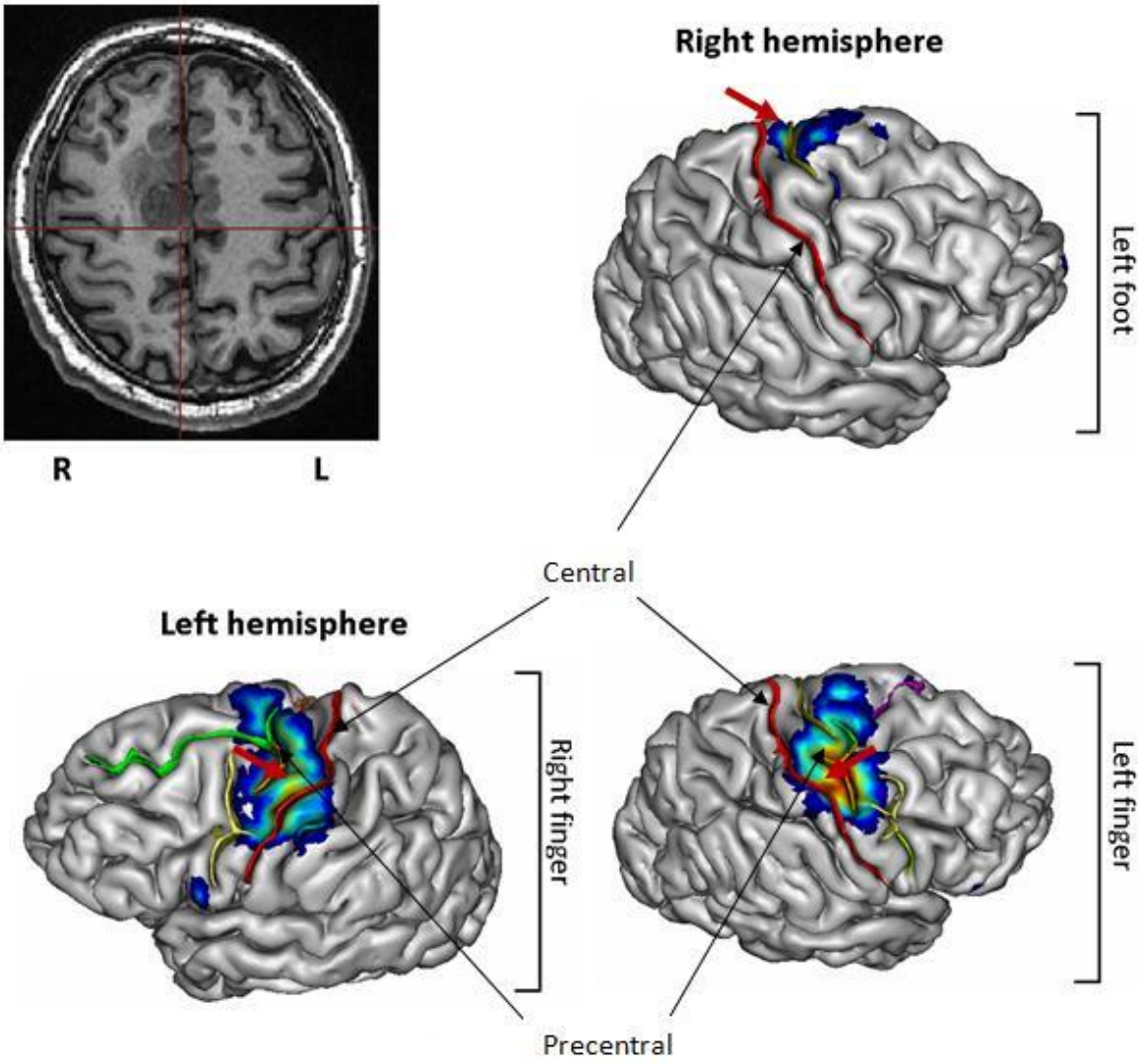

Figure 6-3 The activation map for motor tasks of patient P04
Location of the tumour is shown by the red crosshair in the T1-weighted image (shown in radiological orientation). Activation centres are pointed by the red arrow in the lateral views of both hemispheres.

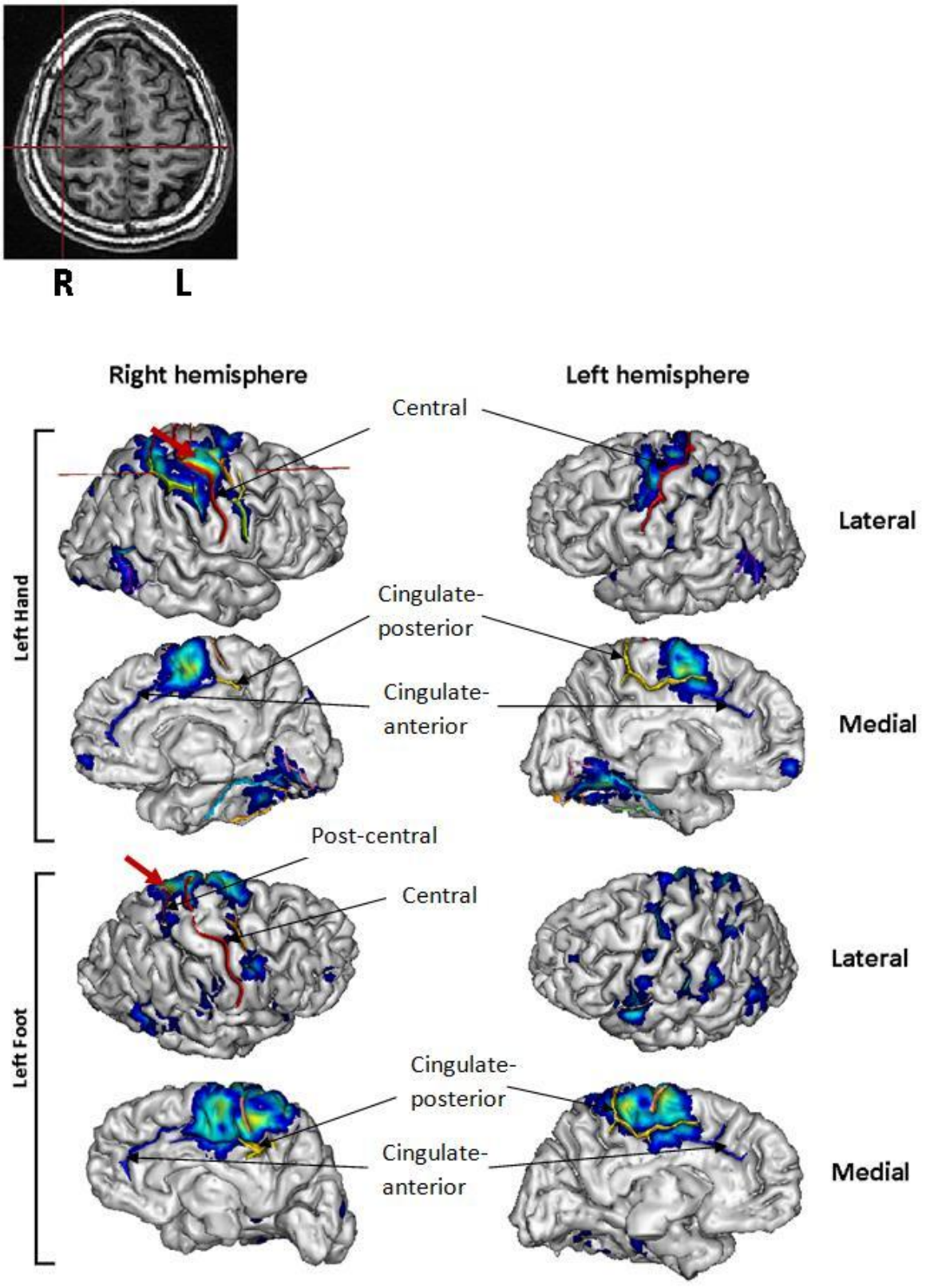

Figure 6-4 The activation map for motor tasks of patient P05
Location of the tumour is shown by the red crosshair in the T1-weighted image (shown in radiological orientation) and the cortical mesh. Activation centres are pointed by the red arrow in the lateral view of the right hemisphere. Also the region above the cingulate sulcus has been activated in this patient.

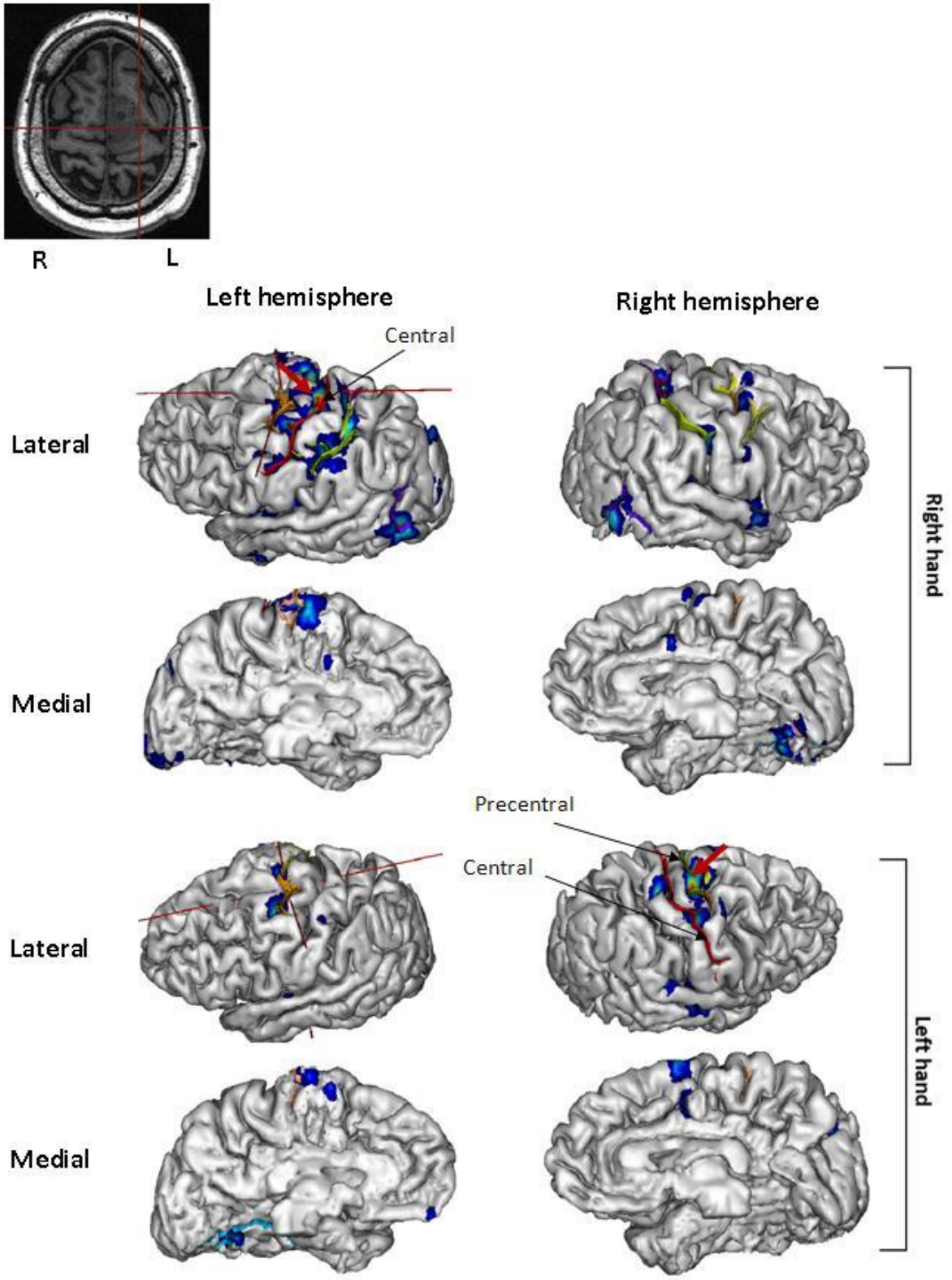

Figure 6-5 The activation map for motor tasks of patient P06
Location of the tumour is shown by the red crosshair in the T1-weighted image (shown in radiological orientation) and the cortical mesh. Activation centres are pointed by the red arrow in the lateral views of both hemispheres.

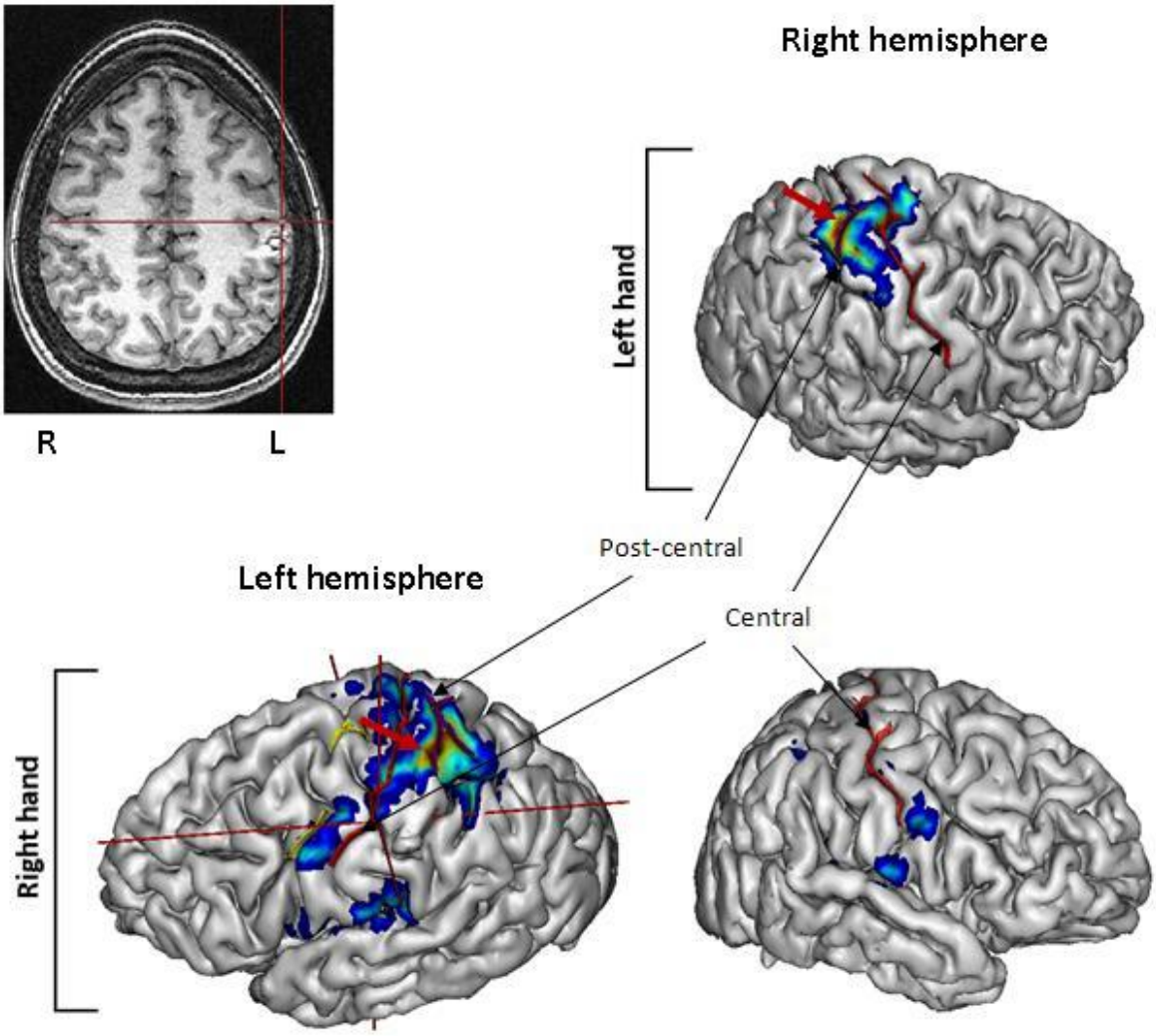

Figure 6-6 The activation map for motor tasks of patient P07
Location of the cavernous angioma is shown by the red crosshair in the T1-weighted image (shown in radiological orientation) and the cortical mesh. Activation centres are pointed by the red arrow in the lateral views of both hemispheres.

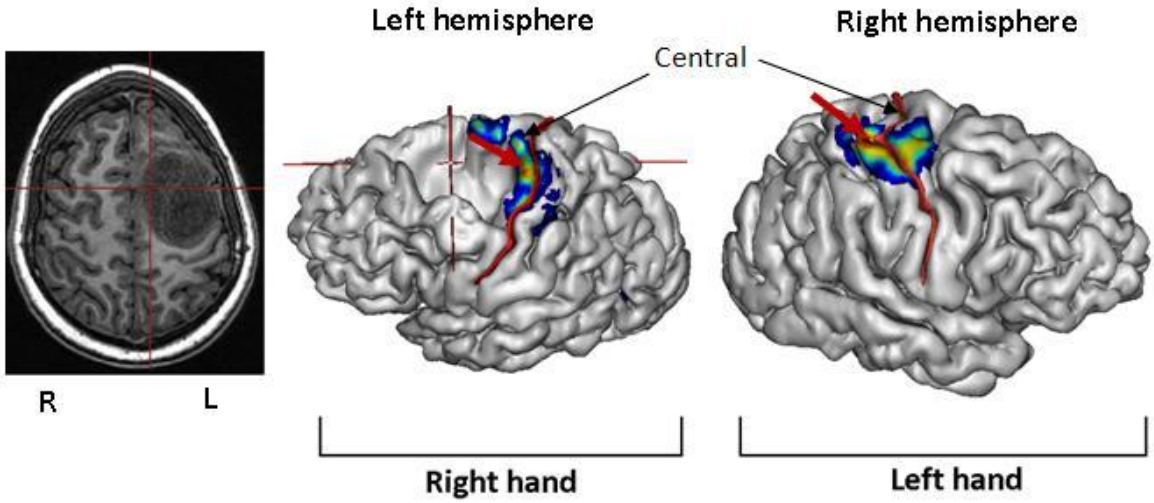

Figure 6-7 The activation map for hand grasping tasks of patient P08
Location of the lesion is shown by the red crosshair in the T1-weighted image (shown in radiological orientation) and the cortical mesh. Activation centres are pointed by the red arrow in the lateral views of both hemispheres.

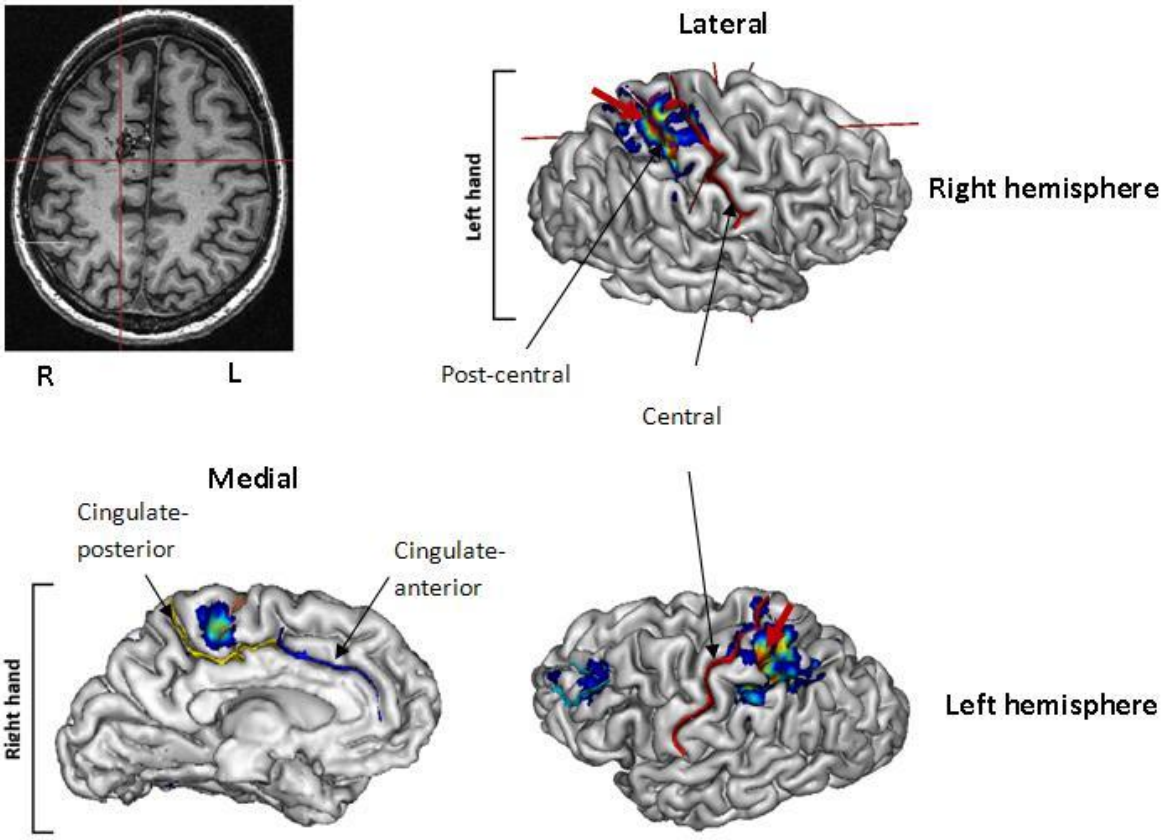

Figure 6-8 The activation map for hand grasping task of patient P09
Location of the AVM is shown by the red crosshair in the T1-weighted image (shown in radiological orientation) and the cortical mesh. Activation centres are pointed by the red arrow in the lateral views of both hemispheres. Also the region above the cingulate sulcus has been activated in this patient.

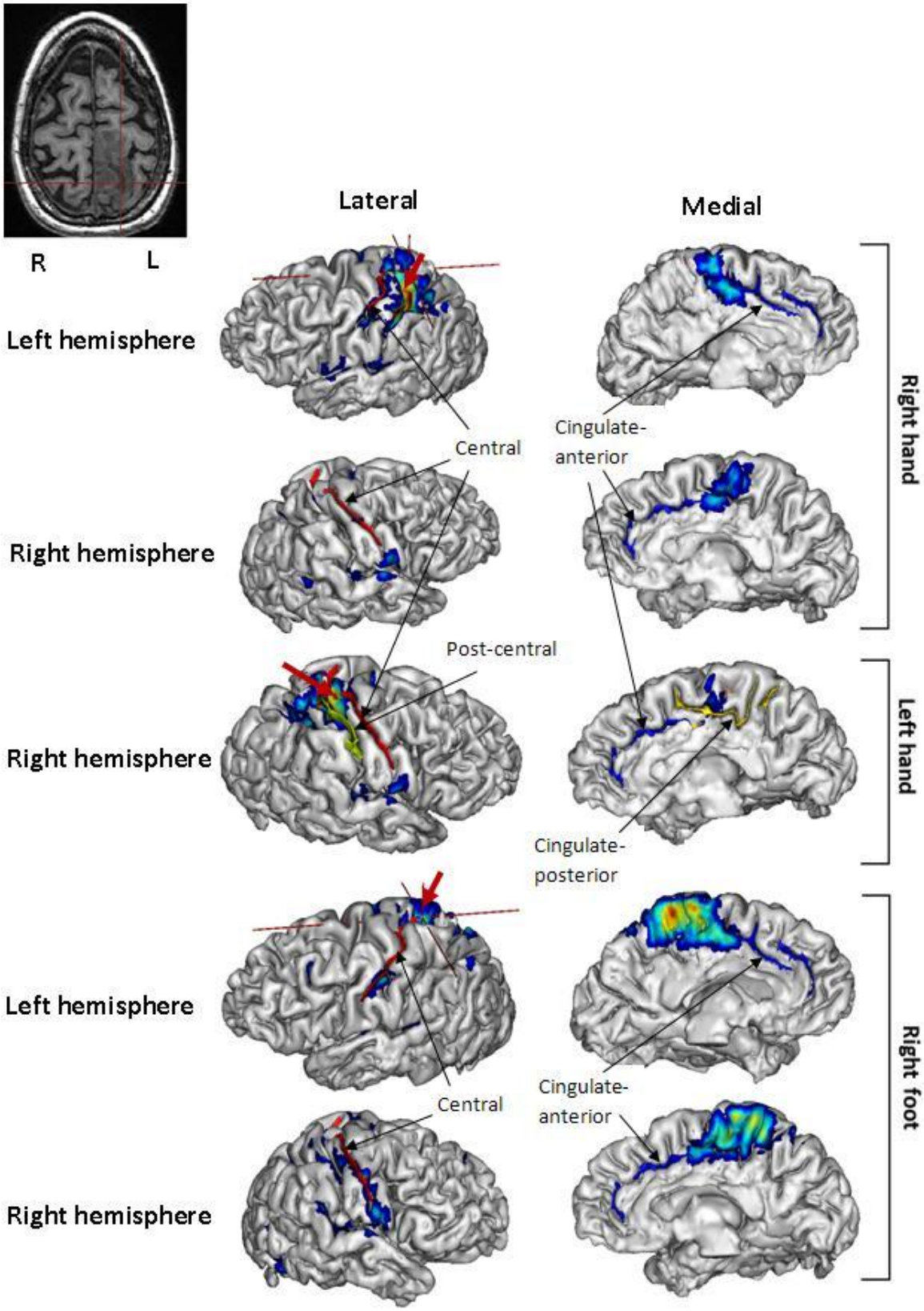

Figure 6-9 The activation map for motor tasks of patient P10
Location of the lesion is shown by the red crosshair in the T1-weighted image (shown in radiological orientation) and the cortical mesh. Activation centres are pointed by the red arrow in the lateral views of both hemispheres. Also the region above the cingulate sulcus has been activated in this patient.

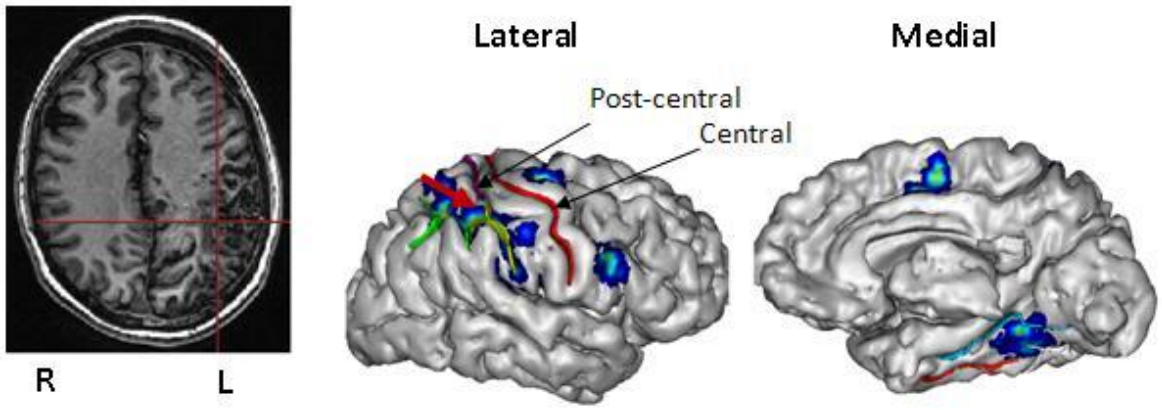

Figure 6-10 The activation map for right fingers tapping of patient P11
Location of the AVM is shown by the red crosshair in the T1-weighted image (shown in radiological orientation). Activation centre is pointed by the red arrow in the lateral view of the right hemisphere. Also the region above the cingulate sulcus in the right hemisphere has been activated in this patient.

6.5.2 Language mapping

The results of language mapping for patients P01, P02, P11, and P12 are presented in table 6-3 and figures 6-11 to 6-14. As before the colour-coded representation of the activation map is used to identify the main activation centres.

It can be seen from table 6-3 and figures 6-11 to 6-14 that while for patients P01, P02, and P12 no reorganization of the language function can be observed in patient P11, the language activation in the temporal lobe is shifted to the right hemisphere.

With the exception of patient P11, the sulci involved in the activation pattern are consistent between the other three patients.

Patient	Activation centres- language task	Reorganization
P01	❖ Noun-to-verb Around left inferior frontal sulcus Around left pre-central sulcus Around posterior parts of left inferior temporal sulcus Around left intraparietal sulcus ❖ Word generation Around left inferior frontal sulcus Around left pre-central sulcus Around intraparietal sulcus	No
P02	• Noun-to-verb Below left inferior frontal sulcus Around left pre-central sulcus Around posterior parts of left superior temporal sulcus Around left intraparietal sulcus • Word generation Around left inferior frontal sulcus	No
P11	❖ Noun-to-verb Around left inferior frontal sulcus ❖ Word generation Around left inferior frontal sulcus Around right superior temporal sulcus Parietal lobe	Only in right temporal area (no reorganization for frontal lobe activity)
P12	• Noun-to-verb Below left inferior frontal sulcus Around left pre-central sulcus Around posterior parts of left inferior temporal sulcus Around intraparietal sulcus • Word generation Below left inferior frontal sulcus Around left pre-central sulcus Around posterior parts of left inferior temporal sulcus Around left intraparietal sulcus	No

Table 6-3 Location of the activation centres of the language task with respect to the sulci

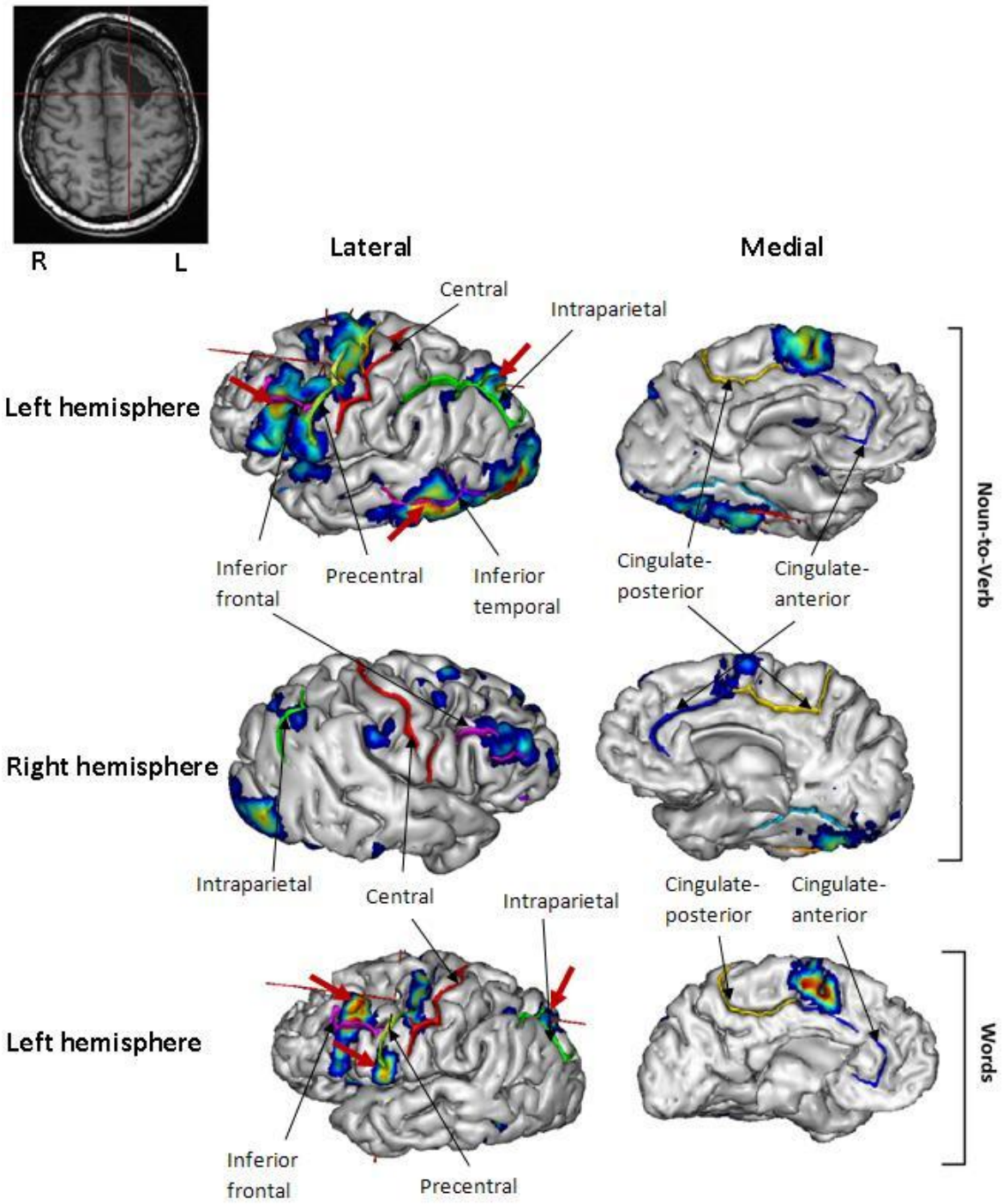

Figure 6-11 The activation map for language tasks of patient P01
Location of the AVM is shown by the red crosshair in the T1-weighted image (shown in radiological orientation) and the cortical mesh. Activation centres are pointed by the red arrow in the lateral view of left hemisphere. Also the region above the cingulate sulcus has mainly been activated in the left hemisphere.

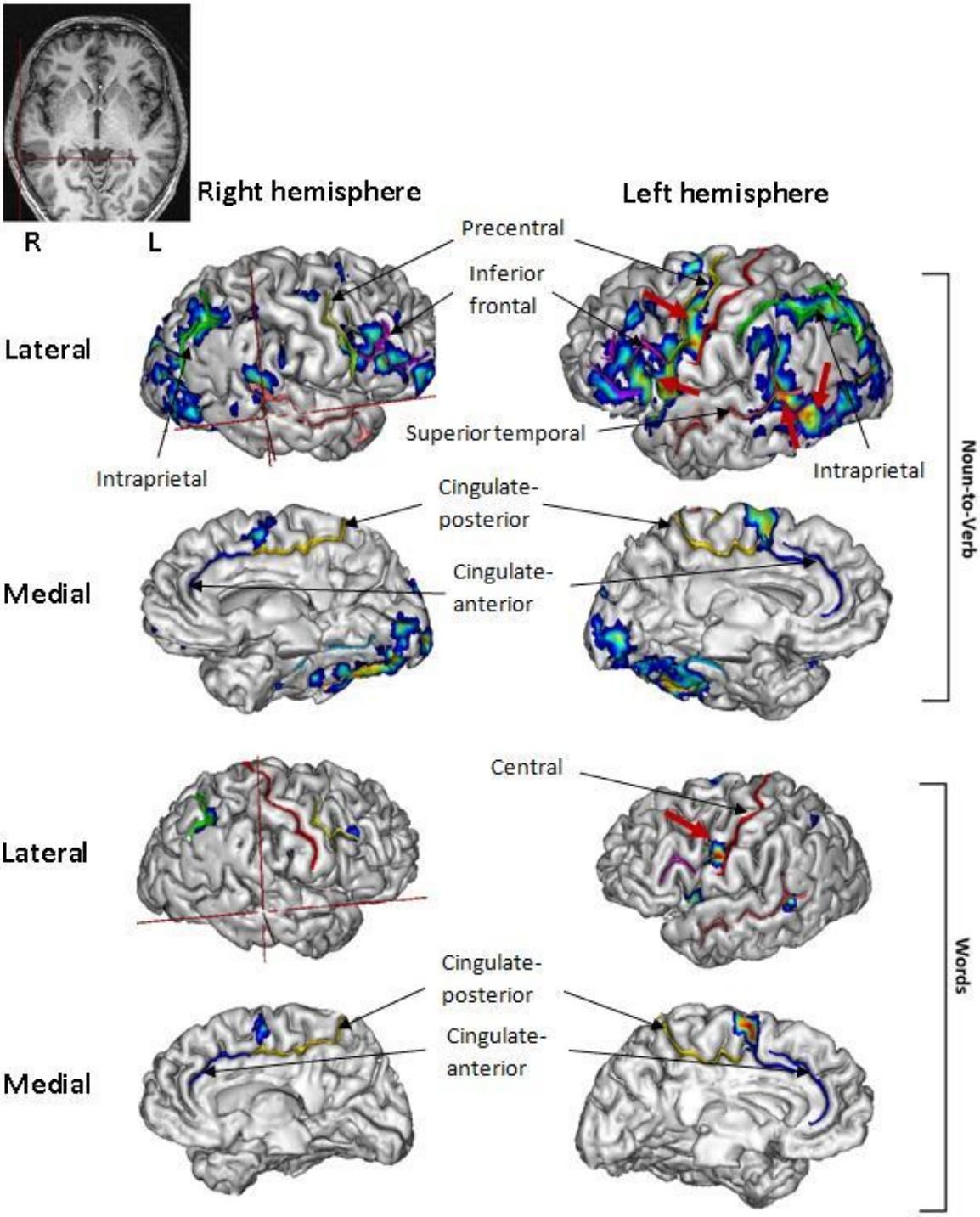

Figure 6-12 The activation map for language mapping of patient P02
Location of the cyst is shown by the red crosshair in the T1-weighted image (shown in radiological orientation) and the cortical mesh. Activation centres are pointed by the red arrow in the lateral view of left hemisphere. Also the region above the cingulate sulcus has mainly been activated in the left hemisphere.

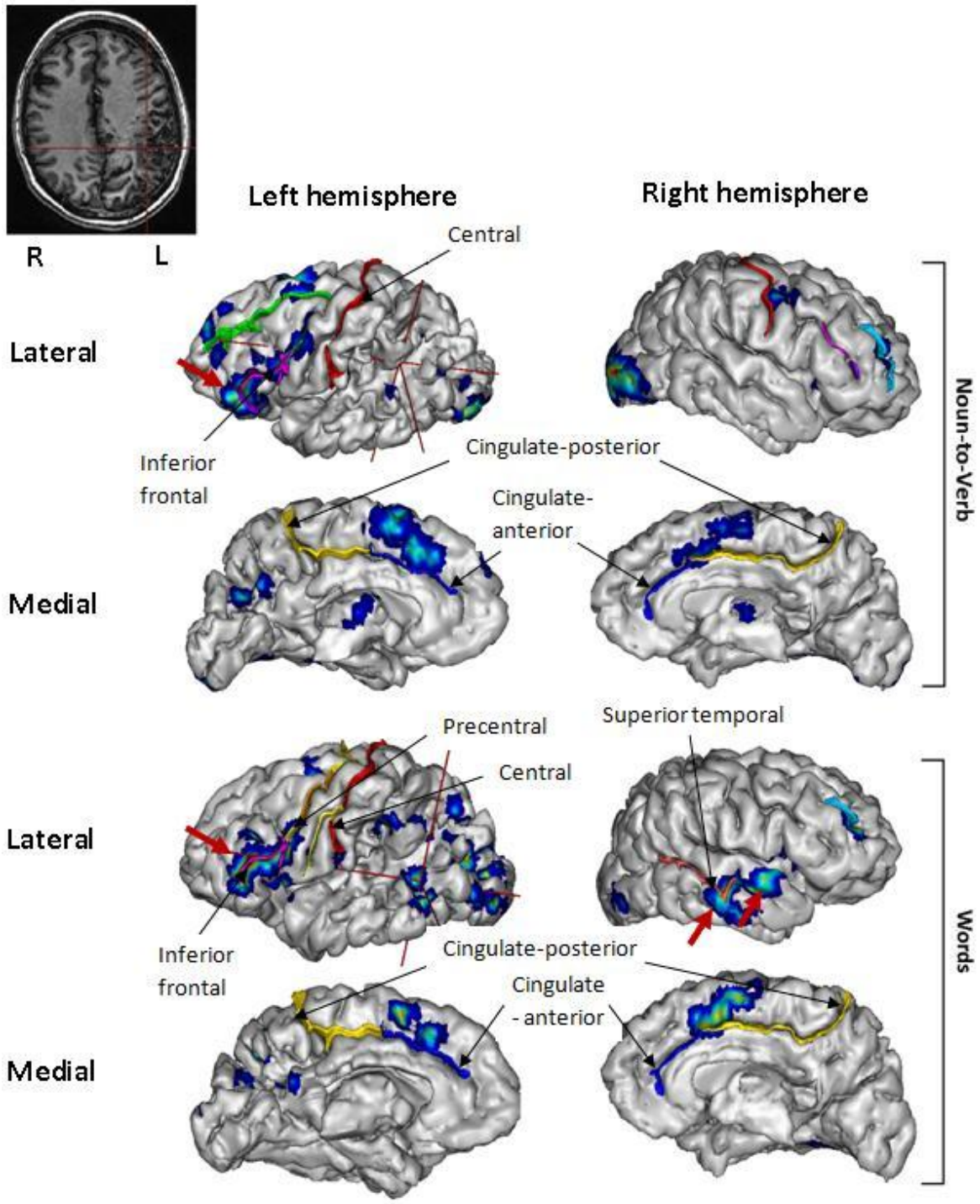

Figure 6-13 The activation map for language mapping of patient P11
Location of the AVM is shown by the red crosshair in the T1-weighted image (shown in radiological orientation) and the cortical mesh. Activation centres are pointed by the red arrow on lateral views of both hemispheres. Also in both hemispheres, the regions above the cingulate sulcus have been activated.

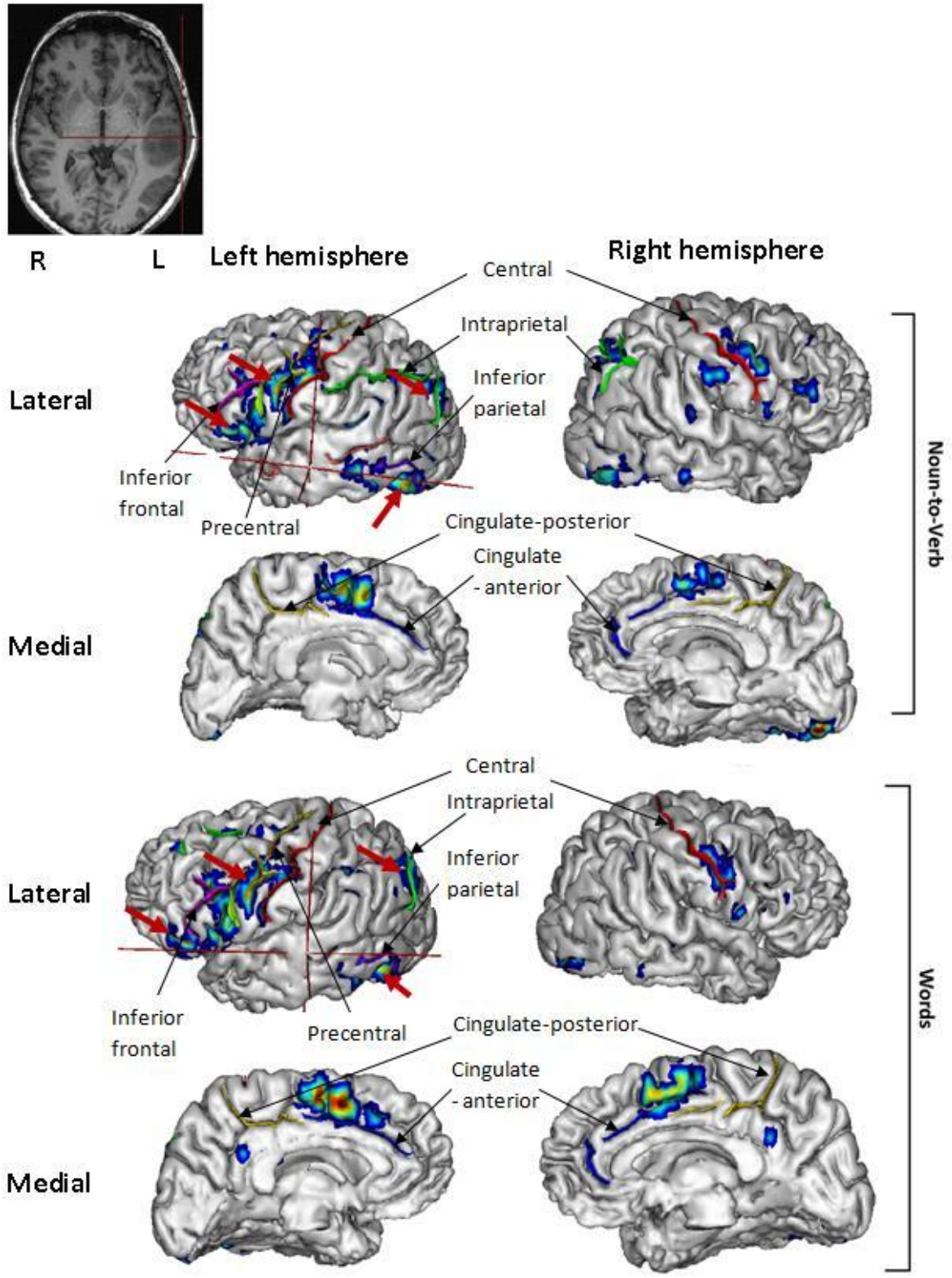

Figure 6-14 The activation map for language mapping of patient P12
Location of the tumour is shown by the red crosshair in the T1-weighted image (shown in radiological orientation) and the cortical mesh. Activation centres are pointed by the red arrow in the lateral view of left hemisphere. Also the region above the cingulate sulcus has mainly been activated in the left hemisphere.

6.6 Discussion

Brainvisa facilitates the identification of the eloquent areas and the evaluation of cerebral plasticity for pre-surgical planning of patients with brain lesions. It also addresses the difficulty of manual identification of regions arising from the mass effect of the lesions. However, the erroneous detection of false folds inside the lesions poses a limitation on its utility for these pathologies.

A major difficulty in fMRI analysis arises from the between-subjects variability in the activation pattern even for healthy brains. This lack of a gold standard causes ambiguity in distinguishing between the normal and pathology-related variations in the activation pattern. Nevertheless, the results of this study indicate that in most cases, sulcal labels of the activated areas were relatively consistent among different patients, qualitatively suggesting that Brainvisa can be a useful tool for these studies.

In three of the ten patients who had undergone motor mapping the activation was shifted posteriorly although still in the same hemisphere and in one patient, the motor function was relocated to the opposite hemisphere.

Language mapping was performed in the four of the patients. For Three patients no reorganization of language function was observed. However, for the same patient who had shown reorganization of the motor activation to the opposite hemisphere, the language area in the temporal lobe was relocated to the right hemisphere. More precisely, right finger tapping and the language task (which are both expected to activate their corresponding regions in the left hemisphere) activated the right hemisphere due to the presence of AVM in the left hemisphere. However, such pattern of reorganization was not observed in all patients with AVM. Thus these results are in agreement with previous findings regarding no correlation between the type or location of tumour and pattern of cortical reorganization (Baciu et al. 2003).

Although as discussed before, language mapping can be less straightforward compared to motor mapping, the activated regions were relatively consistent among different patients.

One difficulty of interpreting the activation pattern in pathologic brains is that it is not clear whether extra activation (usually less strong compared to the main activation) arises from the abnormality or not. Moreover, head movement that is correlated with performing the task especially in the motor mapping experiments can also produce false positives. Nevertheless, for some patients some sort of reorganization was unquestionably detected.

It should be noted however, that using fMRI mapping in the assessment of brain plasticity and pre-surgical planning can sometimes be inaccurate due to some limitations. Firstly as have been suggested by several studies, the activation in the vicinity of lesions may erroneously remain undetected due to the neurovascular decoupling or abnormal blood flow even though those areas are functionally active (Schreiber et al., 2000; Bookheimer, 2007). This can happen as a result of the mass effect of the tumour which disrupts the normal blood flow response and inhibits the detection of the Blood Oxygenation Level Dependant (BOLD) signal. Also it has been suggested that the magnetic susceptibility can change in areas close to AVM, cavernous hemangioma, and necrotic tumours with intra-tumoural bleeding for example, causing image distortion and hence a false presentation of the activation centre (Sunaert, 2006). Secondly, fMRI mapping does not enable to distinguish between the essential and non-essential areas for performing a given task. Removing the non-essential areas may not result in functional deficit even though they show activation during task performance (Sunaert, 2006). Thirdly, smoothing which is often used to increase the SNR in functional images can shift the activation map and result in false presentation of the activation centre (Geissler et al. 2005). This is further discussed in chapter eight of the thesis where new smoothing filters are developed in order to address this issue.

Despite all the above-mentioned limitations, as has been shown in this chapter, fMRI can successfully be used in both motor and language mapping. In addition, Brainvisa facilitates these assessments by automatically identifying the eloquent cortical areas. It should be noted however, that sulci identification is obtained from a probabilistic model which is based on healthy brains and hence in cases where a brain lesion pushes its surrounding areas and displaces some sulci, the sulcal labels may not be valid. Nevertheless, for other regions it can provide a helpful means of identifying the brain regions.

Another limitation of this study is that since susceptibility-related distortion was not corrected for the EPI data (due to the fact that the field maps had not been acquired during data collection), such distortions could have reduced the accuracy of registration between EPI and T1-weighted images. This could have introduced some error to the estimation of activated labels especially at regions with higher susceptibility artifact such as those in proximity to sinuses or even some types of tumours.

6.7 Conclusion

Brainvisa is a promising tool for the assessment of the cerebral reorganization in patients with brain lesions despite the potential problems with sulci identification in these abnormalities. It would also be useful to improve the algorithm to avoid the detection of false folds inside the lesions.

It is therefore suggested to extend this study to a larger group of patients with brain lesions and verify the consistency of activation centres in a larger population. Likewise, a similar evaluation for other patient groups undergoing fMRI mapping for pre-surgical planning would be another interesting extension of this study. In the next chapter, a similar methodology is followed for patients with epilepsy.

Chapter 7. Assessment of cerebral plasticity for pre-surgical planning in patients with epilepsy using Brainvisa

7.1 Overview

In this chapter the cerebral plasticity is assessed for a group of patients with epilepsy using language mapping. Similar to the approach in chapter six, Brainvisa is used to find the anatomical location of activation. The activated areas and the hemisphere which is dominantly activated are estimated for each patient and the results for different patients are qualitatively compared. In addition, the results are compared with those for patients with brain tumour or vascular malformation studied in chapter six.

The novelty in this automated approach is that unlike previous methods of the evaluation of the language mapping for epilepsy patients, sulcal labels are used which can potentially offer more precision in identification of the activated regions. All data analyses in this chapter were solely performed by the author.

7.2 Background

In chapter six the brain plasticity due to the presence of brain lesions was assessed for a group of patients with brain tumours or vascular malformation. It was discussed that the major difficulty in fMRI mapping for such patients is due to firstly to the mass effect or artefacts associated with the tumour or vascular malformation which impede the detection of the BOLD signal and secondly, the possibility of the cortical folds being mislabelled due to the mass effect of the

lesion, for example arising from a gyrus being displaced by the lesion. The activation mapping for epilepsy patient however differs from that for patients with brain lesions in that there is no lesion-related artefact or mass effect inhibiting the activation detection or causing mislabelling of the sulci. In fact in epilepsy, the abnormality is usually more subtle compared to brain tumour or vascular malformations. Hence, automated sulci identification should be less problematic. Another differentiating feature in fMRI experiments and pre-surgical planning for patients with epilepsy from similar studies for patients with brain tumour or vascular malformation is that the reorganization of the language function can be observed more frequently (Bookheimer 2007). The typical language activation is characterized by left hemisphere dominance which is estimated to be the case for around 98% of right handed and the majority of left handed normal subjects (Bookheimer 2007). However, this can be replaced by right-hemisphere or bilateral dominance especially in patients with epilepsy (Woermann et al., 2003; Bookheimer 2007; Gaillard et al., 2002). For this reason, pre-surgical planning for epilepsy often involves language mapping.

This study includes fMRI mapping of the language function for a group of patients with epilepsy previously scanned at the Institute of Neurological Sciences, Southern General Hospital in Glasgow. The types of epilepsy were not known for all patients and included uncertainty for some others. However, several types such as cortical dysplasia (failure in proper migration of neurons resulting in the malformation of the cortex), occipital, and temporal epilepsy (referring to where in the brain the abnormal neuronal discharges associated with epilepsy start) had been identified in a number of patients.

7.3 Methods

7.3.1 fMRI experiments

fMRI experiment consisted of the “noun-to-verb conversion” and “word generation” paradigms explained in chapter six. All timings are the same as those described in chapter six.

7.3.2 Image acquisition

This study was approved by west of Scotland research ethics committee. Similar to the subject group studied in chapter six, both 3D T1-weighted and fMRI scans had been acquired for these patients with epilepsy using either 1.5T or 3T GE scanners. The details of patients as well as the acquisition parameters for the 3D T1-weighted images are given in table 7-1. Unfortunately information about the handedness of these patients was not available.

Functional images were acquired using the GRE-EPI sequence with TR=3 sec, TE=40 msec on the 1.5T scanner and 30 msec on the 3T scanner. The image size was 128x128x25 (voxels) for patients scanned with the 3 T scanner, and 64x64x25 (voxels) for patients scanned with the 1.5T scanner. The voxel size was 1.88x1.88x4.5 mm^3 for patients scanned with the 3T scanner, and 64x64x25 (voxels) for patients scanned with the 1.5T scanner.

7.3.3 Image analysis

Data analysis included sulci labelling using the T1-weighted images with Brainvisa4.0 and activation detection using SPM8 using the procedure mentioned in chapter six. Activation localization was performed by overlaying the activation map on the labelled cortex.

The decision regarding the language dominance and laterality was made using an approach similar to that of Woermann et al (2003) by visual inspection of the activation pattern and verifying the locations with the strongest activation.

Patient	Pathology	Scanner	Sequence	TR (ms)	TE (ms)	TI (ms)	Flip angle (°)	Image size Voxel size(mm^3)
P01	disorder of probable left temporal origin	3T	IRFSPGR	7.2	1.6	500	12	512x512x160 0.5x0.5x1
P02	Unknown	3T	IRFSPGR	7.6	1.5	500	12	512x512x160 0.5x0.5x1
P03	dysplasia	1.5T	IRFSPGR	8.7	1.9	450	20	256x256x124 0.94x0.94x1.4
P04	Left occipital epilepsy	3T	IRFSPGR	7.6	1.5	500	12	512x512x124 0.5x0.5x1.4
P05	Left inferior frontal cortical dysplasia	3T	IRFSPGR	6.5	1.5	500	12	512x512x160 0.5x0.5x1
P06	Unknown	1.5T	IRFSPGR	11	2.3	400	20	256x256x124 0.94x0.94x1.4
P07	Left temporal epilepsy	3T	IRFSPGR	7.2	1.5	500	12	512x512x196 0.5x0.5x1
P08	Left temporal lesion	3T	IRFSPGR	7.6	1.5	500	12	512x512x124 0.5x0.5x1.4
P09	Extensive lesion	3T	IRFSPGR	7.2	1.6	500	12	512x512x160 0.5x0.5x1
P10	probably temporal epilepsy-left side	3T	IRFSPGR	7.2	1.6	500	12	512x512x160 0.5x0.5x1
P11	Unknown	3T	IRFSPGR	7.2	1.6	500	14	512x512x160 0.5x0.5x1
P12	Left medial temporal epilepsy	3T	IRFSPGR	7.2	1.6	500	15	512x512x160 0.5x0.5x1

Table 7-1 The types of pathology and acquistion parameters for the T1-weighted images of the patients

7.4 Results

For patients P04 and P10 no activation was detected. For the rest of the patients, the main activation centres (with strongest activation) with each paradigm are summarized in table 7-2. In this table, the activation centres are localized by their proximity to the cortical sulci.

The activation was observed to be much stronger in some patients than the rest. However, such disparity between the activation patterns of different individuals can be observed even in healthy groups.

Figures 7-1 to 7-10 show the activation maps overlaid on the reconstructed cortical meshes of the patients. As before the colour-coded representation of the activation map is used to describe the strength of the activity in terms of the t-values where red and blue refer to the highest and lowest t-values, respectively. In these figures the locations with highest activity are shown by red arrows. In most patients, a region above the posterior part of the anterior cingulate sulcus (where the anterior and posterior parts of the sulcus join together) is shown to be activated. Nevertheless, this area is not considered a primary region for language activation and is therefore not included in table 7-2.

Table 7-2 and figures 7-1 to 7-10 show that several areas in the frontal, temporal and parietal cortex are activated during the language mapping experiment. However in general, with the “noun-to- verb conversion” paradigm stronger and more extensive activation is obtained relative to the “word generation” paradigm.

Patient	Language dominance	Activation centres "noun-to-verb"	Activation centres "word generation"
P01	Left	❖ Around left inferior frontal sulcus ❖ Around posterior part of left superior temporal sulcus	❖ Around left inferior frontal sulcus ❖ Around posterior part of left superior temporal sulcus
P02	Bilateral	• Above left/right inferior frontal sulcus • Around left pre-central sulcus • Around left intraparietal sulcus • Around posterior part of left/ right inferior temporal sulcus	• Around left intermediate frontal sulcus • Around left intraparietal sulcus • Around posterior part of left/ right inferior temporal sulcus
P03	Left	❖ Around left inferior frontal sulcus ❖ Around left pre-central sulcus ❖ Around left intraparietal sulcus ❖ Around posterior part of left inferior temporal sulcus	❖ Around left inferior frontal sulcus ❖ Around left pre-central sulcus ❖ Around left intraparietal sulcus ❖ Around posterior part of left inferior temporal sulcus
P05	Left	• Around left inferior frontal sulcus • Around left pre-central sulcus	• Around left inferior frontal sulcus
P06	Left	❖ Around left pre-central sulcus	❖ no activation
P07	bilateral	• Below left/right inferior frontal sulcus • Around of left/right pre-central sulcus • Around posterior part of left superior temporal sulcus	• Around left/right pre-central sulcus • Around posterior part of left superior temporal sulcus
P08	Bilateral	❖ Below left inferior frontal sulcus ❖ Around left/right pre-central sulcus	_____
P09	Left	• Above left inferior frontal sulcus • Around posterior part of left superior temporal sulcus • Around left intraparietal sulcus	• Above left inferior frontal sulcus • Around posterior part of left superior temporal sulcus
P11		❖ Around left inferior frontal sulcus ❖ Around left intraparietal sulcus	❖ Around left inferior frontal sulcus ❖ Around left pre-central sulcus ❖ Around left intraparietal sulcus
P12	Bilateral only for Wernicke's area	• Above left inferior frontal sulcus • Around left intraparietal • Around posterior part of left superior temporal sulcus	• Above left inferior frontal sulcus • Above posterior part of left/ right superior temporal sulcus

Table 7-2 Location of the activation centres with respect to the sulci

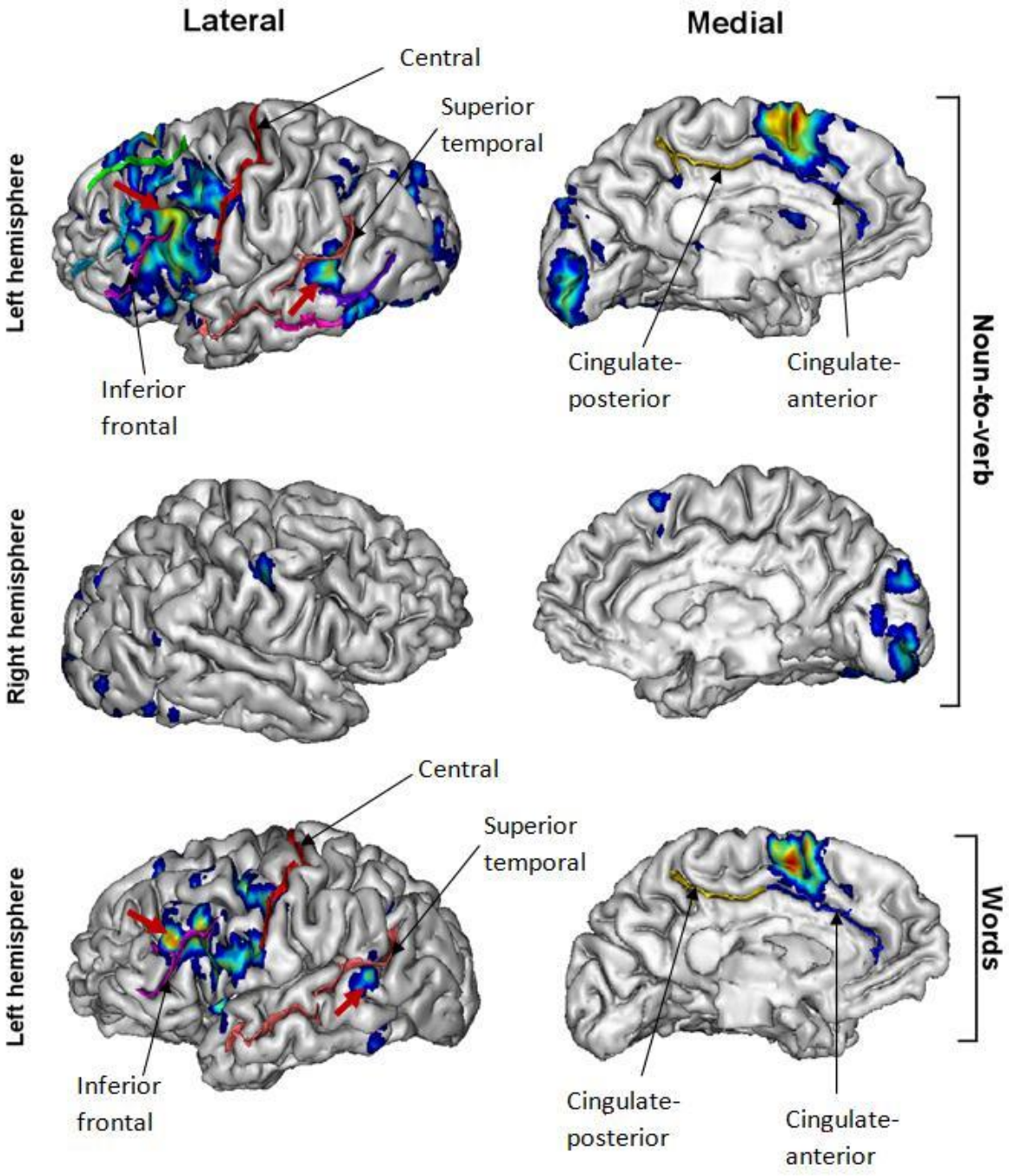

Figure 7-1 Language mapping for patient P01
The activation maps corresponding to "noun-to-verb conversion" and "word generation" paradigms are shown on the medial and lateral views of both hemispheres. Only views/hemispheres included in the activation pattern are shown. Red arrows point to the foci with strongest activations. In addition, the area above the cingulate sulcus is shown to be activated in left hemisphere.

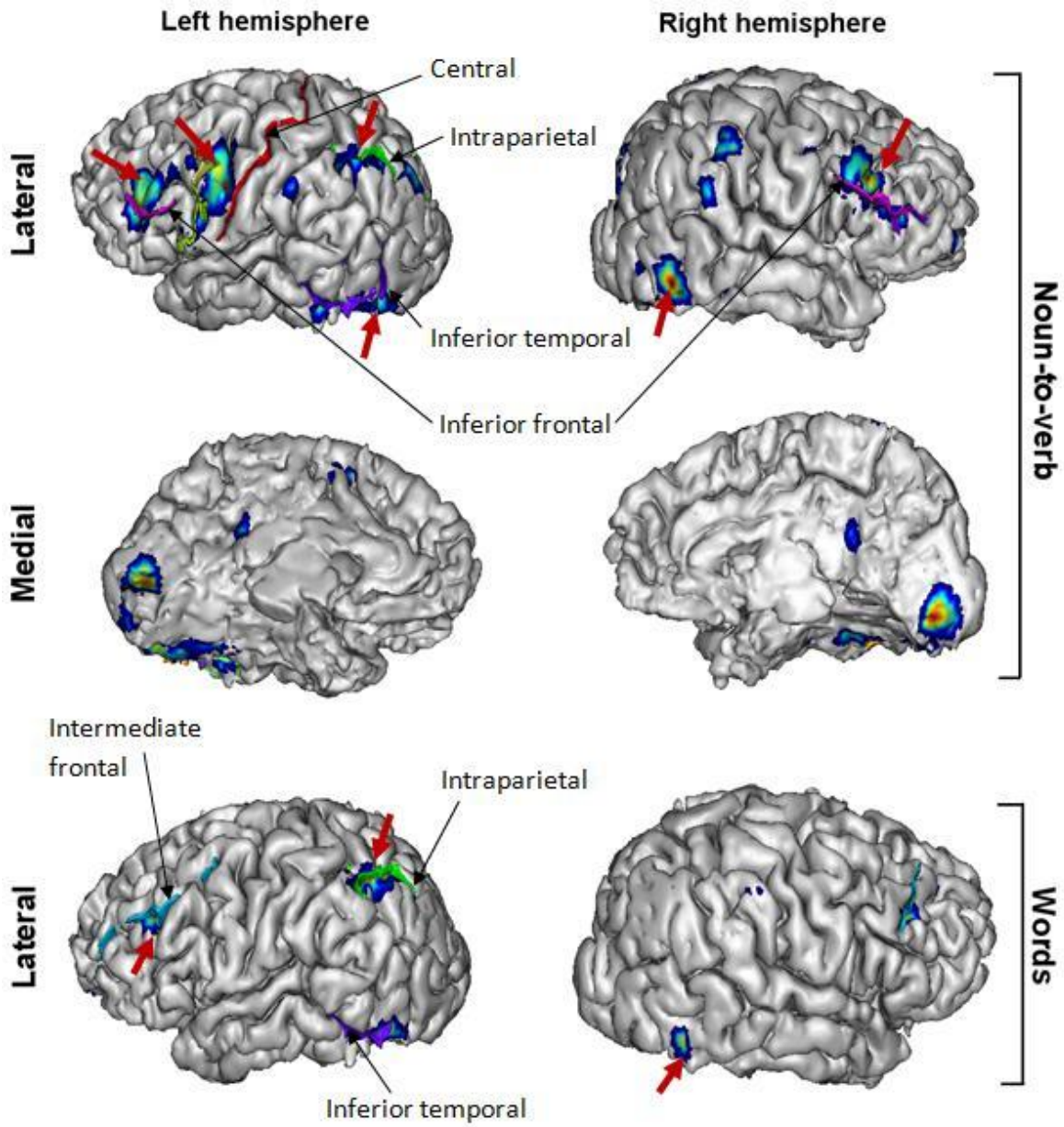

Figure 7-2 Language mapping for patient P02
The activation maps corresponding to "noun-to-verb conversion" and "word generation" paradigms are shown on the medial and lateral views of both hemispheres. Only views/hemispheres included in the activation pattern are shown. Red arrows point to the foci with strongest activations.

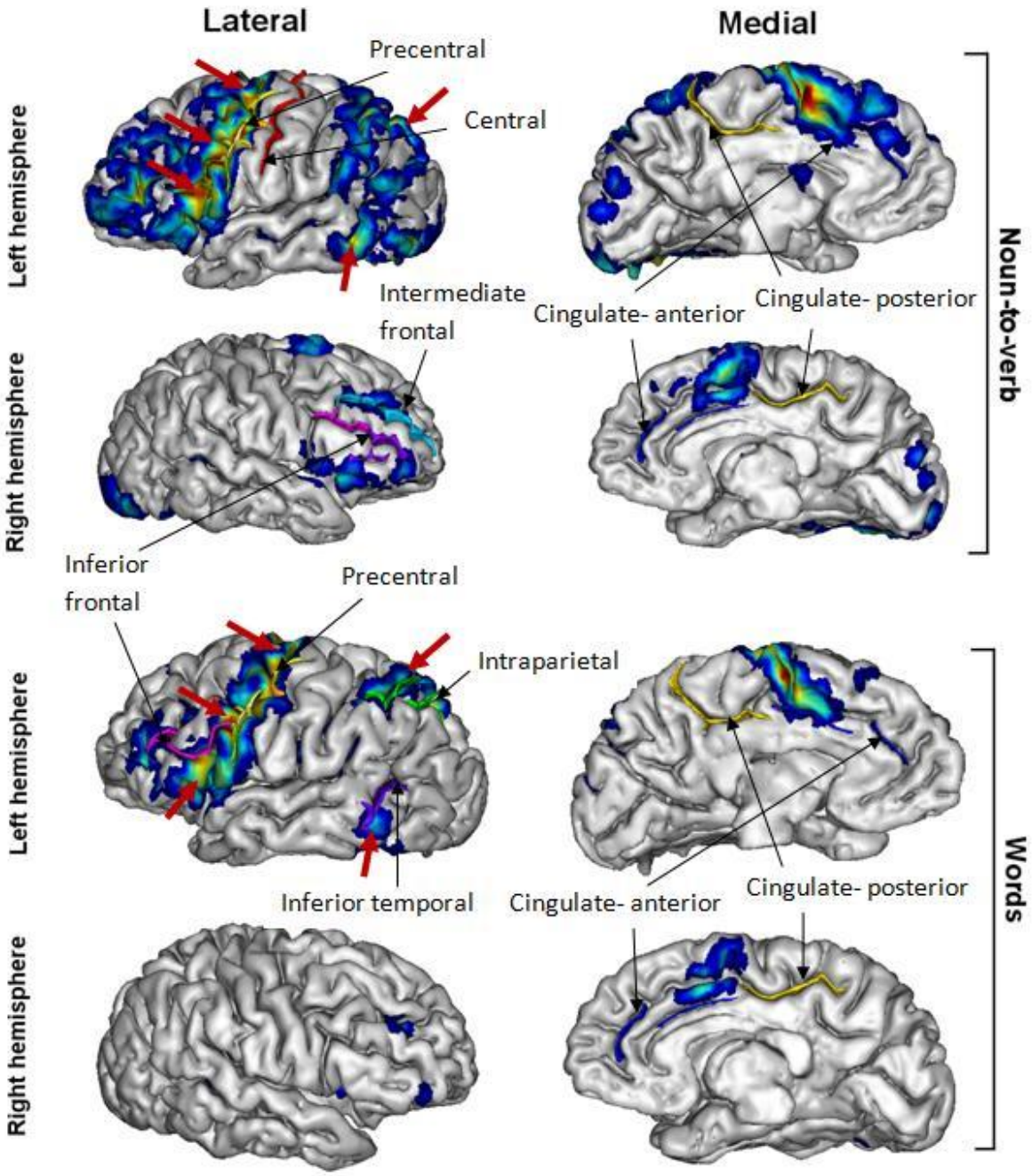

Figure 7-3 Language mapping for patient P03
The activation maps corresponding to "noun-to-verb conversion" and "word generation" paradigms are shown on the medial and lateral views of both hemispheres. Red arrows point to the foci with strongest activations. In addition, the area above the cingulate sulcus is shown to be activated mainly in the left hemisphere.

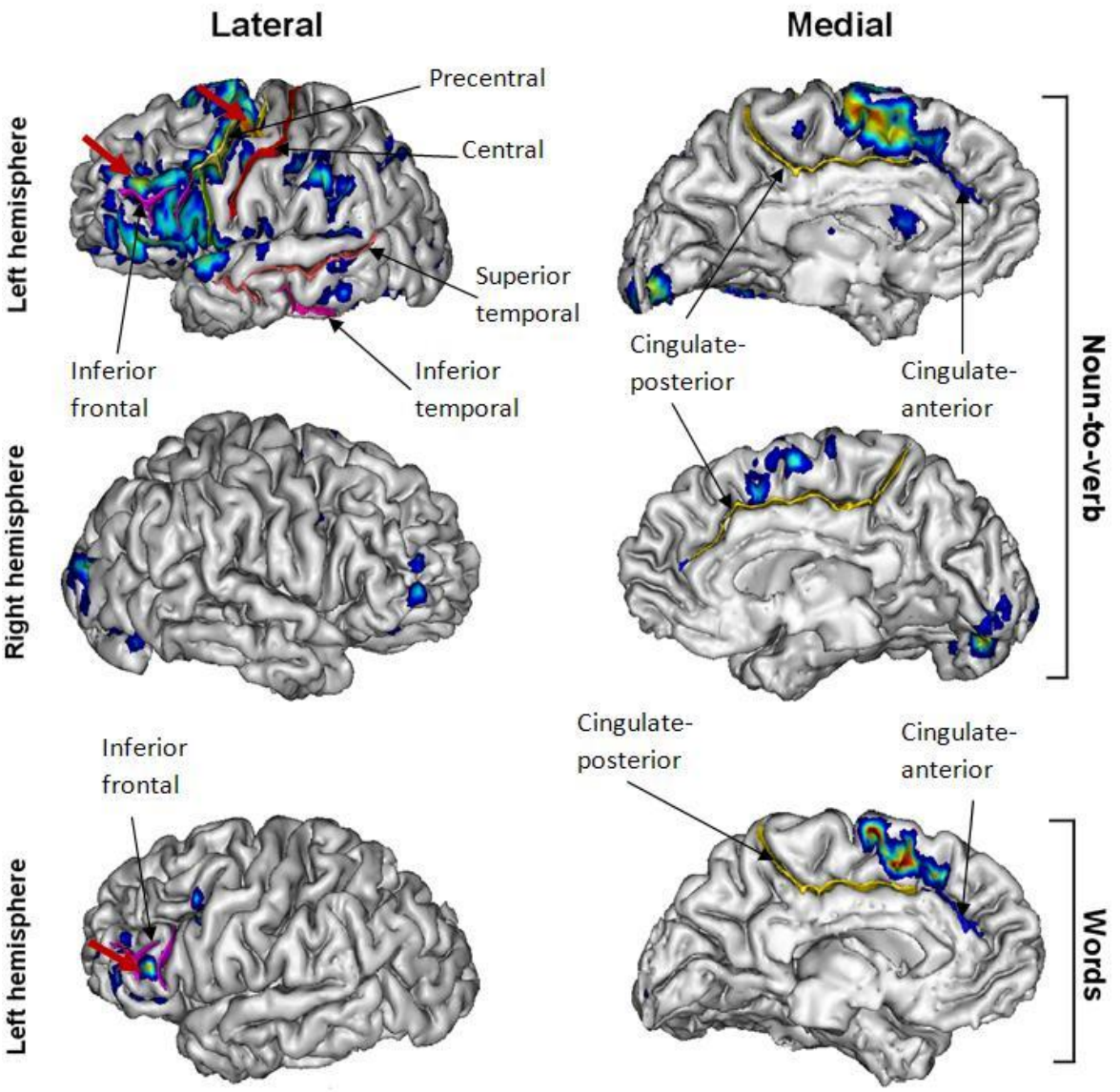

Figure 7-4 Language mapping for patient P05
The activation maps corresponding to "noun-to-verb conversion" and "word generation" paradigms are shown on the medial and lateral views of both hemispheres. Only views/hemispheres included in the activation pattern are shown. Red arrows point to the foci with strongest activations. In addition, the area above the left cingulate sulcus is shown to be activated.

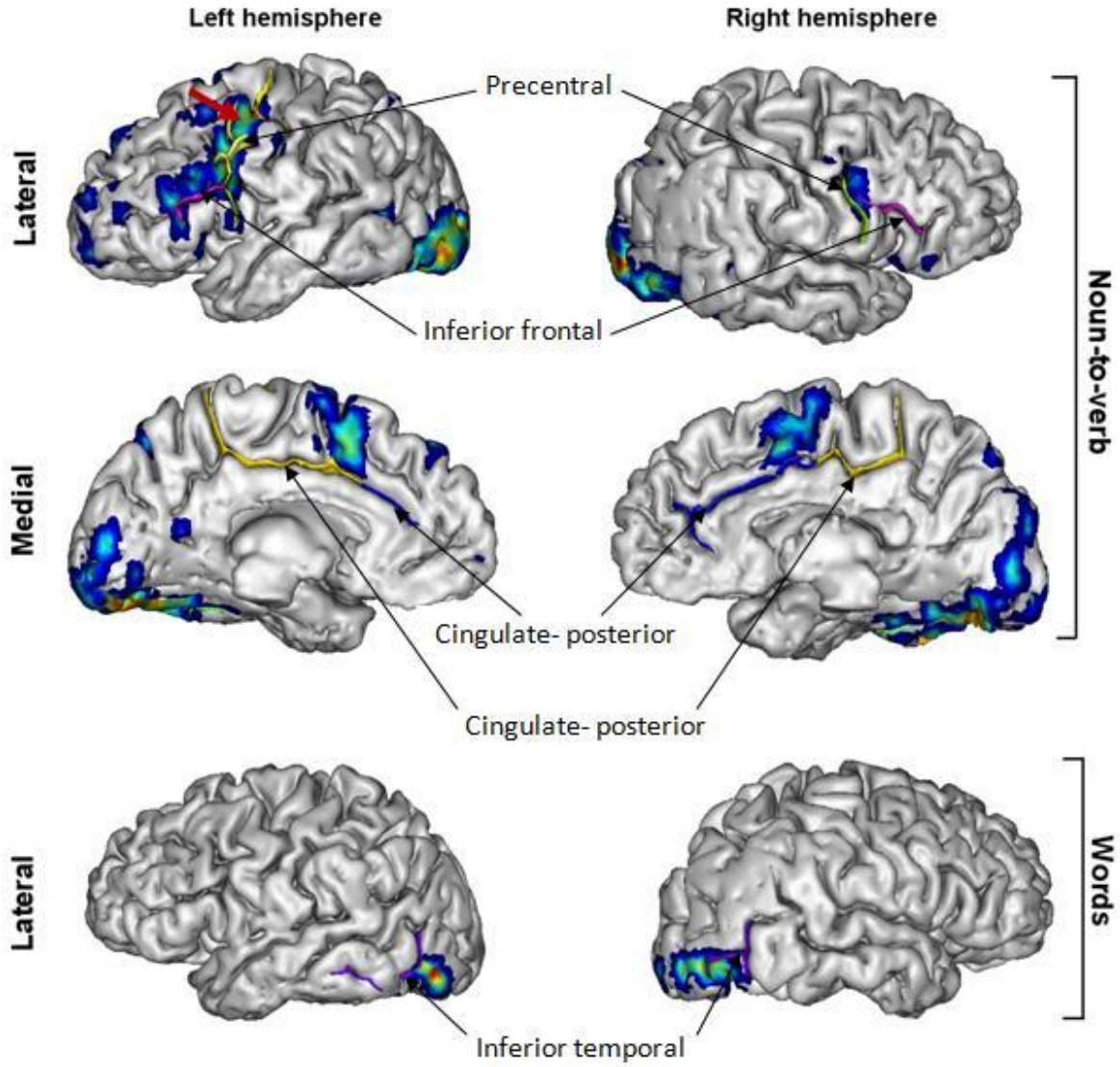

Figure 7-5 Language mapping for patient P06
The activation maps corresponding to "noun-to-verb conversion" and "word generation" paradigms are shown on the medial and lateral views of both hemispheres. Only views/hemispheres included in the activation pattern are shown. Red arrows point to the foci with strongest activations. In addition, the area above the both left and right cingulate sulcus is shown to be activated for this patient.

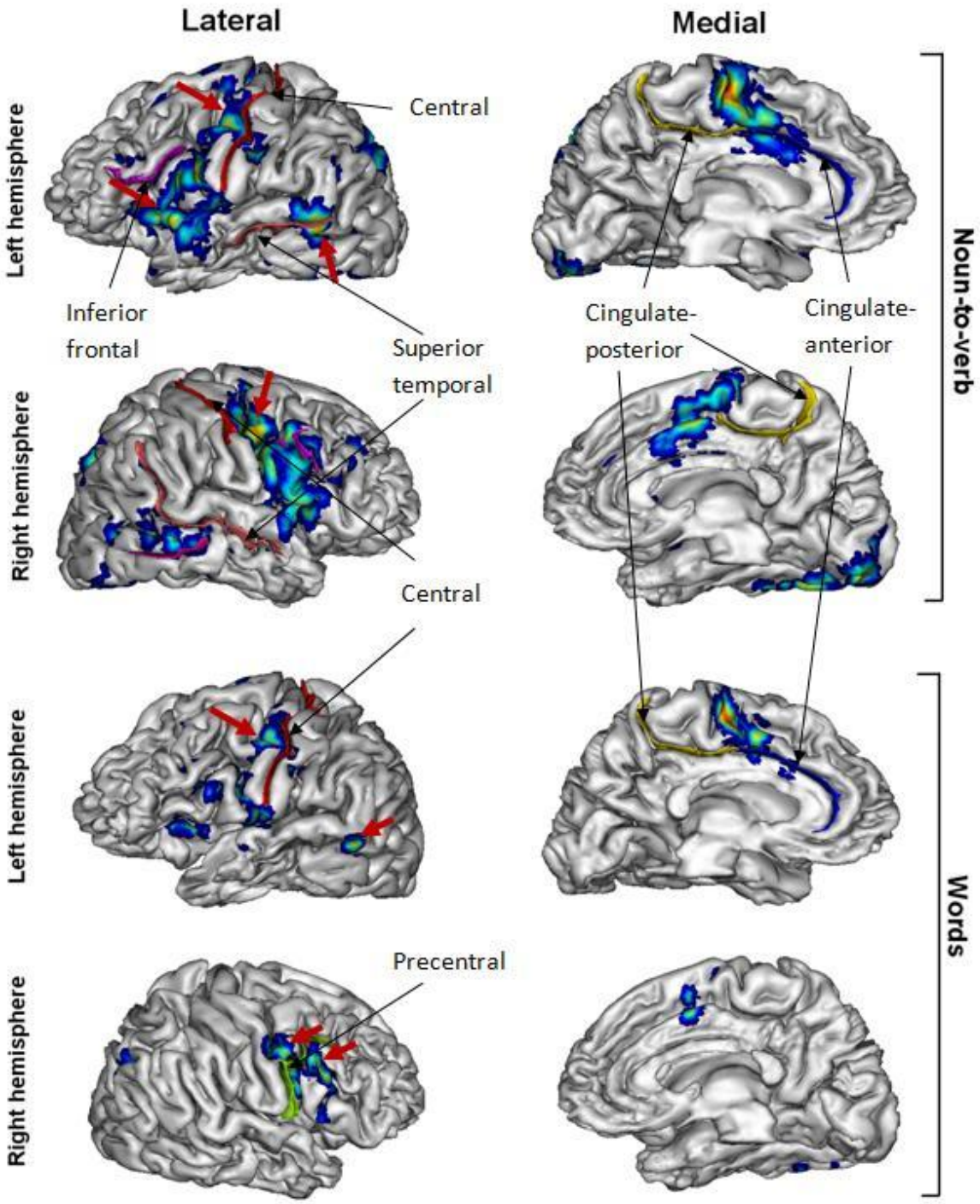

Figure 7-6 Language mapping for patient P07
The activation maps corresponding to "noun-to-verb conversion" and "word generation" paradigms are shown on the medial and lateral views of both hemispheres. Red arrows point to the foci with strongest activations. In addition, the area above the cingulate sulcus is shown t o be activated mostly in the left hemisphere.

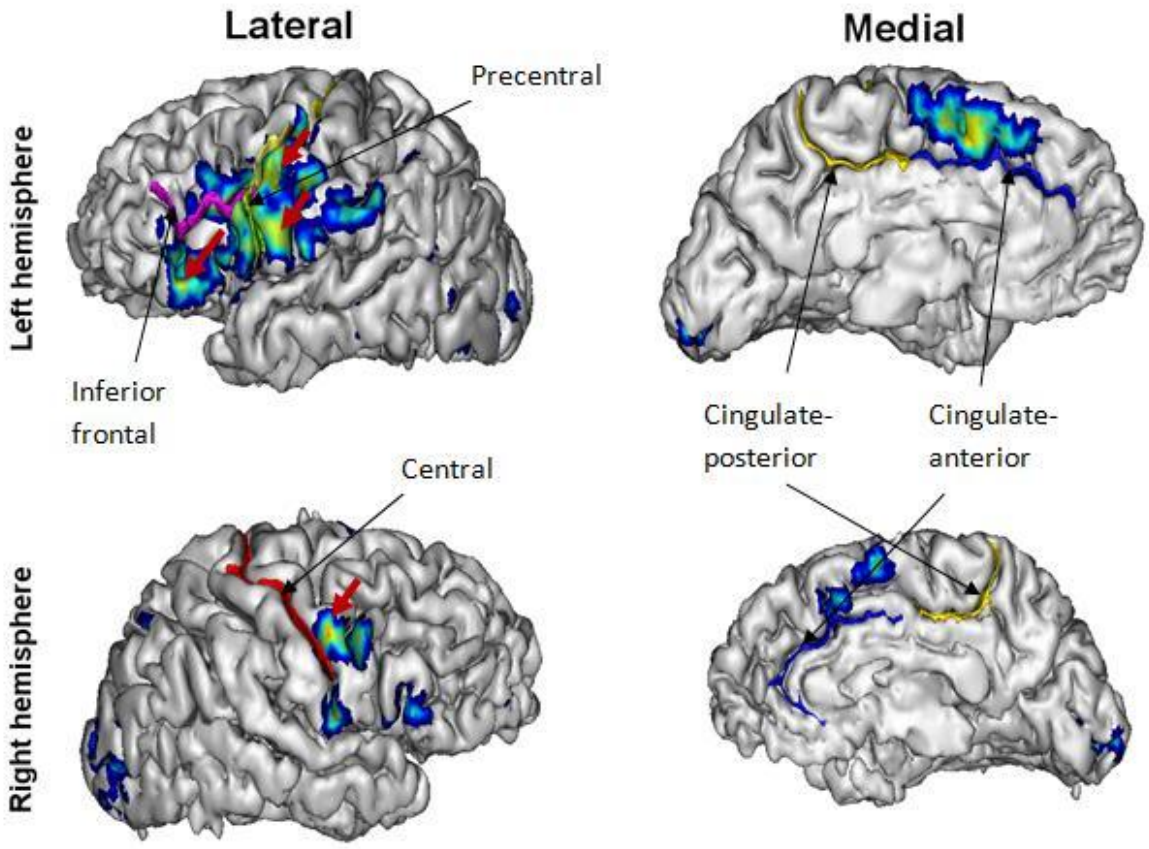

Figure 7-7 Language mapping for patient P08
The activation map corresponding to "noun-to-verb conversion" is shown on the medial and lateral views of both hemispheres. Red arrows point to the foci with strongest activations. In addition, the area above the left cingulate sulcus is shown to be activated.

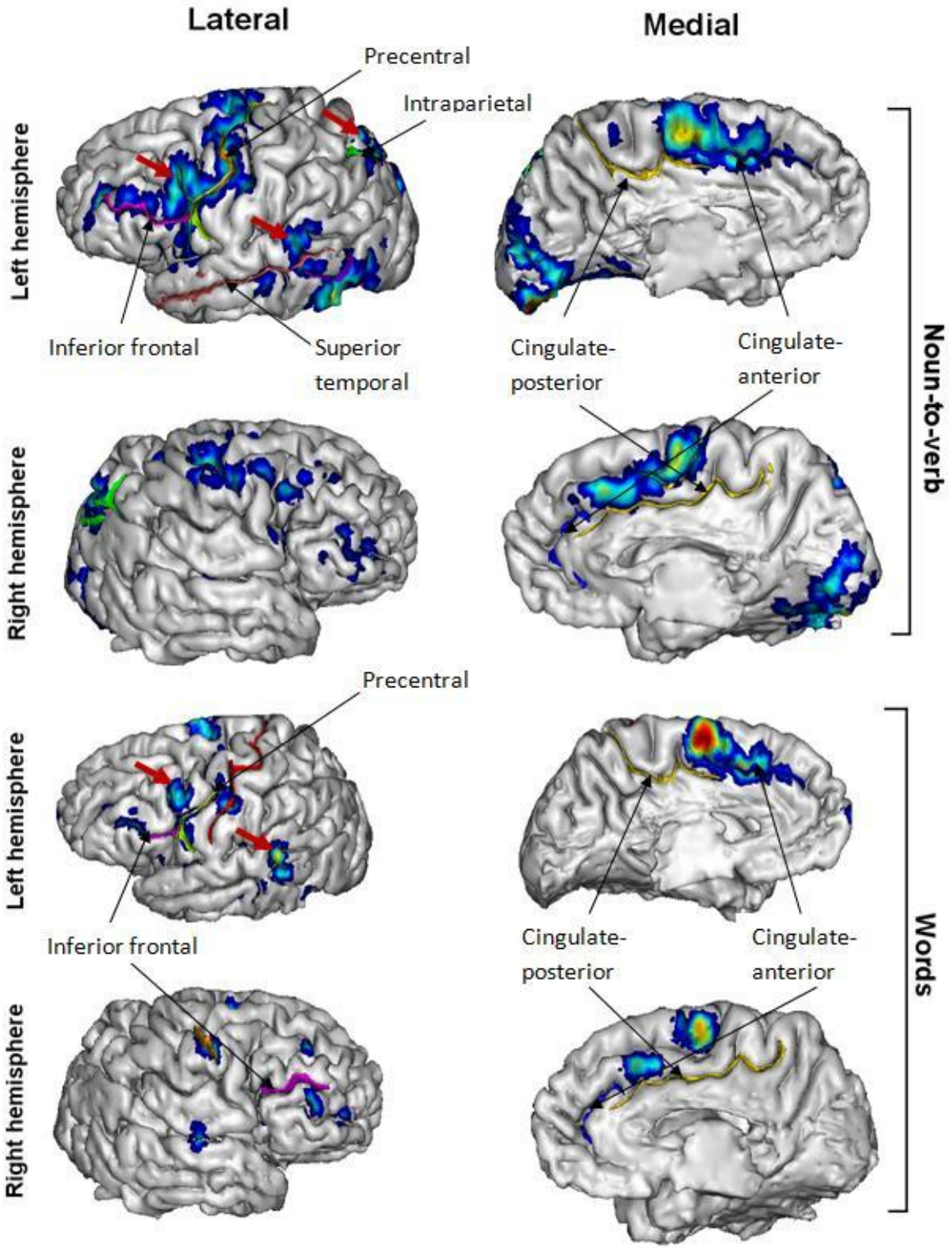

Figure 7-8 Language mapping for patient P09
The activation maps corresponding to "noun-to-verb conversion" and "word generation" paradigms are shown on the medial and lateral views of both hemispheres. Red arrows point to the foci with strongest activations. In addition, the area above the cingulate sulcus is shown to be activated.

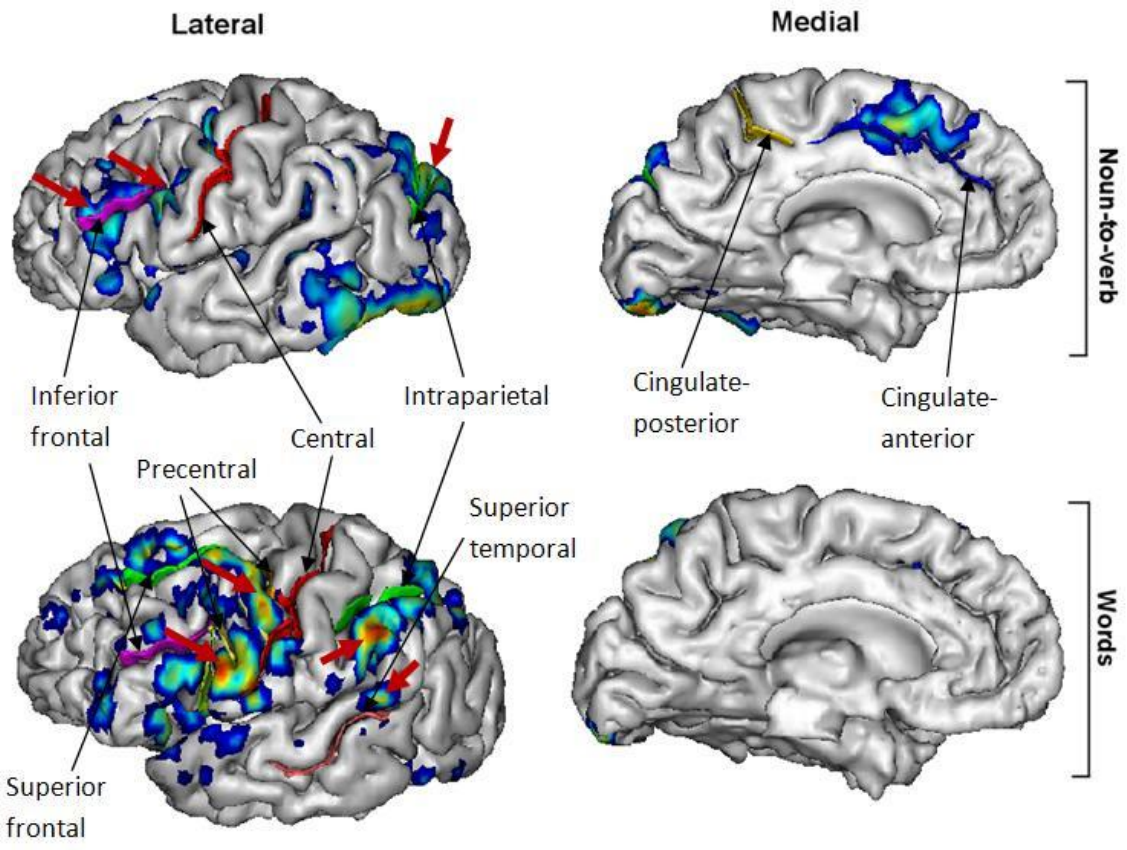

Figure 7-9 Language mapping for patient P11
The activation maps corresponding to "noun-to-verb conversion" and "word generation" paradigms are shown on the medial and lateral views of the left hemisphere only. No activation was detected on the right hemisphere. Red arrows point to the foci with strongest activations. In addition, the area above the left cingulate sulcus is shown to be activated only with "noun-to-verb conversion" paradigm.

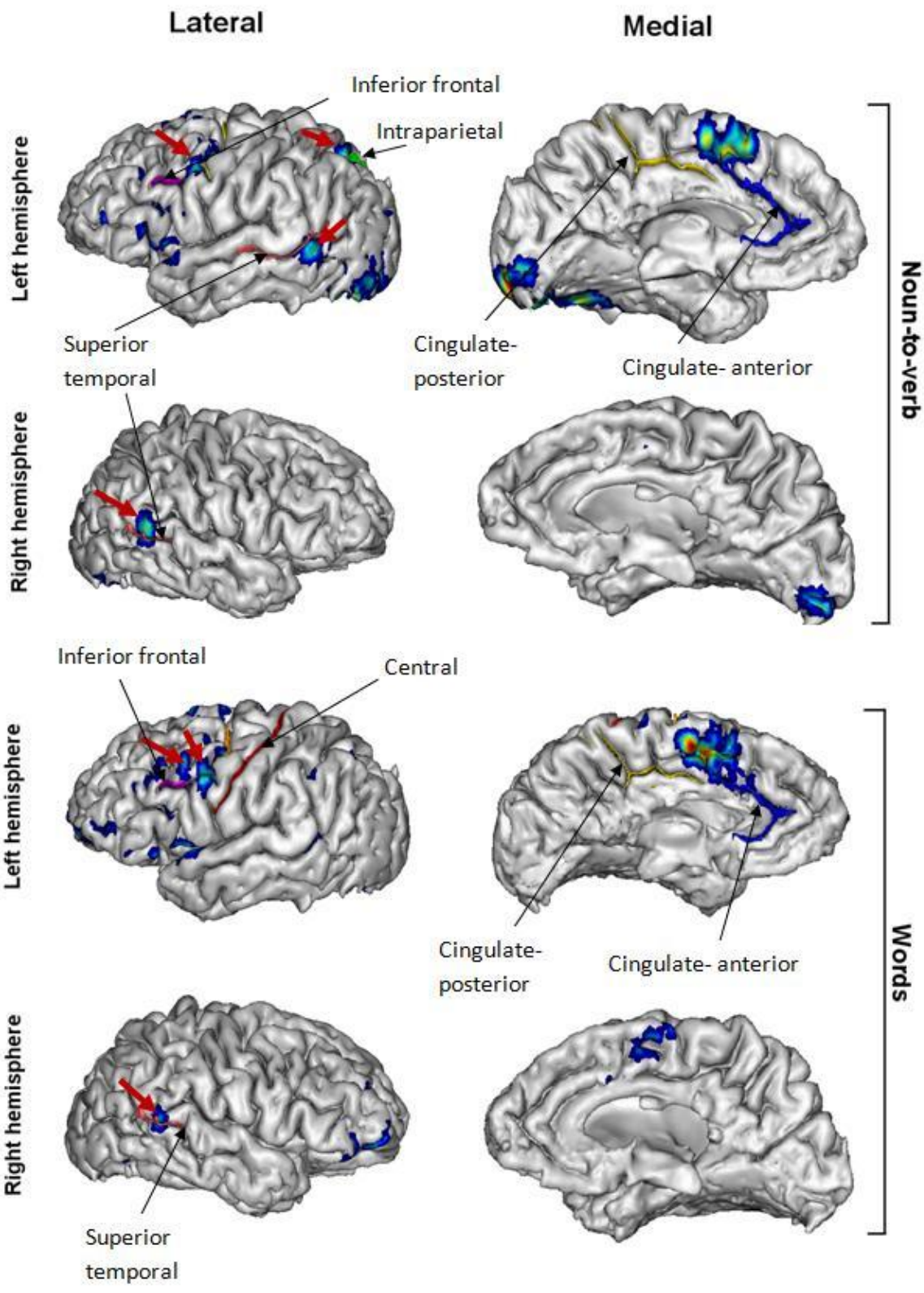

Figure 7-10 Language mapping for patient P12
The activation maps corresponding to "noun-to-verb conversion" and "word generation" paradigms are shown on the medial and lateral views of both hemispheres. Red arrows point to the foci with strongest activations. In addition, the area above the left cingulate sulcus is shown to be activated.

7.5 Discussion

In this study the functional maps associated with two language mapping tasks for a group of twelve patients with epilepsy were analyzed. Among the two studied paradigms, the “noun-to-verb conversion” paradigm was found to be more successful in detection of the language activation compared to the “word generation” task in almost all cases.

In two out of the twelve patients, the language mapping experiment failed to detect the functional activation. Among the remaining ten patients, four were found to have bilateral activation. In one of these four patients only the Wernicke’s activation was shifted to the contra-lateral hemisphere whereas the frontal lobe activation was preserved to the left hemisphere. The possibility of such mixed reorganization patterns has previously been discussed (Bookheimer 2007).

One problem in language mapping is that due to between-individual differences in the activation pattern it may be difficult to distinguish between the primary and non-primary activated areas. In other words, it is not clear if all the activated regions directly relate to language function. Cingulate sulcus is an example for such non-primary areas which has also previously been shown to be activated during language activation tasks (Crosson et al., 1999; Binder et al., 1997). As mentioned in chapter six, the normal variations between different subjects and the ambiguity concerning the essential regions in language function also adds to the difficulty of pre-surgical planning using fMRI experiments. Nonetheless, in most cases the major activation foci seemed to be centred on the inferior frontal sulcus, the pre-central sulcus, the intraparietal sulcus and the posterior parts of the inferior/superior temporal sulci.

Compared to the patients with brain tumours or vascular malformations studied in chapter six who had undergone the language mapping experiment, a very similar pattern of activation has been observed for patients with epilepsy. However as expected the left-hemisphere-dominance is violated in a larger fraction (40%) of the epilepsy patients compared to those studied in chapter six (25%). Nonetheless, the small number of patients included in both studies should be taken into account. A similar study on larger groups of patients with epilepsy would

provide a more accurate estimate of the occurrence of atypical language dominance.

One point to take into account is the question of the accuracy of sulci identification. As mentioned before, the degree of structural changes in epilepsy may not reach those for patients with brain tumour or vascular malformation which makes the sulci identification less questionable. Nevertheless, changes in cortical pattern associated with epilepsy have already been verified (Kim et al., 2008) which may make the localization approach based on the sulci labelling prone to error. It would therefore be useful to validate the sulcal labels through judgment by several neuro-radiologists and probably using inter-rater agreement, though even this highly trained group find sulcal identification challenging.

In addition, as mentioned in chapter six, the estimation of the activated labels could be prone to errors resulting from misalignment between EPI and T1-weighted images due to the susceptibility-related distortion in EPI.

In chapter two it was discussed that the 3D Gaussian smoothing may cause the extension of activation to other cortical areas and can therefore be problematic. Given the importance of activation localization for pre-surgical assessment, it would be helpful to examine the possibility of obtaining more localized activation centres by novel smoothing methods. For example, for some of the patients studied in this chapter, the region around the cingulate sulcus was activated on both hemispheres. It is not always clear whether this activation pattern arises from the extension of activation from one hemisphere to the other (as a result of smoothing) or it represents a genuine activation of both hemispheres. Hence, it is worthwhile to examine alternative approaches for smoothing the functional images in order to avoid such errors.

7.6 Conclusion

Given the fact that the morphological abnormality in epilepsy is subtle compared to brain tumour or vascular malformation, the automatic sulci identification can be less problematic. Moreover, the activated cortical areas were relatively consistent

across different patients with epilepsy suggesting that cortical labels can successfully be used in pre-surgical planning in epilepsy.

Chapter 8. Optimization of image smoothing for more accurate activation localization in fMRI

8.1 Overview

As discussed in chapter two, cortical surface-based smoothing methods have not yet been shown to improve activation localization with fMRI. It was also argued that fMRI data analysis could potentially benefit from smoothing filters which prevent the voxel values from the opposite sides of a sulcus to be combined. Moreover, a comparison between various smoothing filters should take different aspects such as the degree of smoothness, the shift and spread of the activation map, as well as the statistical power, which is missing in the previous studies.

This chapter includes an investigation on the possibility of improvement in activation localization using two novel smoothing filters. Unlike cortical surface-based approaches, these filters work in the 3D voxel-based space, allowing for a direct comparison with the conventional smoothing filter. Furthermore, the comparison with the conventional Gaussian smoothing filter includes an estimation of the smoothness, the shift in the activation pattern and the t-values.

The chapter starts by a discussion on the basics and the theoretical aspects of image smoothing, its implementation, and the role of smoothing in the analysis of functional images. The drawbacks of 3D-smoothing Gaussian methods are then discussed and two algorithms are presented in order to address the above issue. The performance of the new smoothing filters will then be compared to the 3D Gaussian filter.

All data analyses in this chapter were solely performed by the author. This study has been presented as a poster at the SINAPSE 2010 annual meeting and the BCISMRM 2011 meeting.

8.2 Aims and objectives

The purpose of this chapter is to examine the effects of two connectivity-based smoothing filters: “voxel-based diffusion smoothing” and “voxel-based averaging”. The activation maps are then compared with those obtained from the 3D Gaussian filter. Both of these methods use voxel connectivity to limit the spread of smoothing to close cortical regions. These voxel-wise approaches hence, allow direct comparison between different smoothing filters and provide more comparable results.

As discussed in chapter two, smoothing usually has multiple effects on the image such as increasing the SNR, lowering the spatial resolution as well as altering t-values. In fact, smoothing is a trade-off between factors such as the degree of smoothness, the displacement of the activation map, and the distribution of t-values. In other words, smoothing reduces the noise in an image by mixing each voxel value with the values of its neighbouring voxels and hence reducing the variations in the signal intensities of the image. Therefore the smoother the image (for example by increasing the smoothing filter width) the higher the SNR. The smoothness can be estimated from the variations in signal intensities (see the definition on smoothness on page 180). However as discussed in chapter two, smoothing can also reduce the spatial resolution and lead to a shift in the activation map. The ideal smoothing filter should thus return smoothest images (hence higher SNRs) whilst also maximizing the t-values and minimizing the shift in the activation map. Thus for the assessment of each smoothing filter, these factors were simultaneously estimated. In addition, since the equivalence between the filter widths of different methods is unknown, a range of filter widths for each method were used.

The choice of the paradigm can also be important for the assessment of the smoothing filter in functional studies. A paradigm with a well defined activation pattern can best approximate a gold standard and provide a powerful means for evaluation and comparison of different smoothing kernels. For this reason, the

motor mapping paradigm (which is well-established task for activating the motor cortex) was used.

8.3 Background

Smoothing is commonly used in image processing, mainly to improve the quality of noisy functional images and to increase the SNR. The role of smoothing in noise reduction can be understood by considering the fact that the values of neighbouring voxels are usually expected to be similar unless at the edges and sharp borders. Noise can manifest itself as an abrupt change in a voxel value. Thus smoothing can recover the image from noise by replacing each voxel value with a combination of those of its neighbours.

In mathematical terms, the smoothing procedure involves convolving the image with a smoothing filter. Figure 8-1 shows the result of convolving a matrix with two mean filters of different sizes. The mean filter simply replaces each voxel value by the average of values of its neighbouring voxels. As shown by figure 8-1, the degree of blurring is increased by increasing the filter size. For example by applying the mean filter of size 5 by 5 to the raw image in figure 8-1, the image is more blurred compared to when smoothed by a 3 by 3 filter.

Smoothing filters can be categorized in two main groups: linear and nonlinear filters. Linear filters perform a linear operation on the voxels. Examples of linear filters are mean filter and Gaussian filter. Smoothing by linear filters may result in disappearance of small details on the image such as sharp edges, while maintaining more prominent features. In other words, smoothing acts as capturing the main features of an image while removing the less important ones. Therefore smoothing an image by a linear filter often entails a trade off between preserving small details and noise reduction. Conversely, nonlinear filters can offer more flexibility in dealing with borders and special forms of noise such as salt and pepper noise. For such cases, the median filter may be a suitable choice. Figure 8-2 shows the effect of the median filter on the same raw image as figure 8-1.

$$\frac{1}{9}\begin{bmatrix}1 & 1 & 1\\ 1 & 1 & 1\\ 1 & 1 & 1\end{bmatrix}$$

$$\frac{1}{9}\times(8\times1+2\times1+17\times1+43\times1+61\times1+84\times1+15\times1+68\times1+91\times1)=43$$

4	8	2	17	9	15	78	23	164	44	7	3
9	43	61	84	52	98	32	20	56	122	4	1
6	15	68	91	53	147	31	45	79	103	34	2
10	37	22	144	85	39	74	38	66	51	27	9
16	85	32	77	93	176	88	46	97	22	10	15

(a)

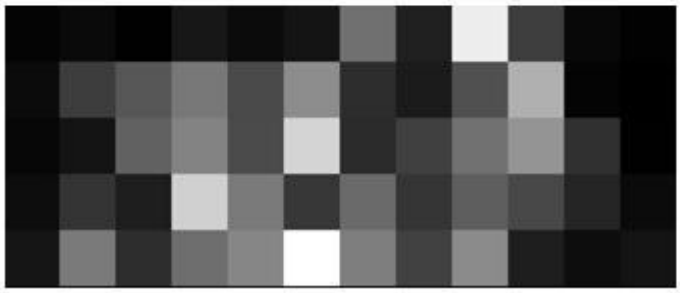

(b)

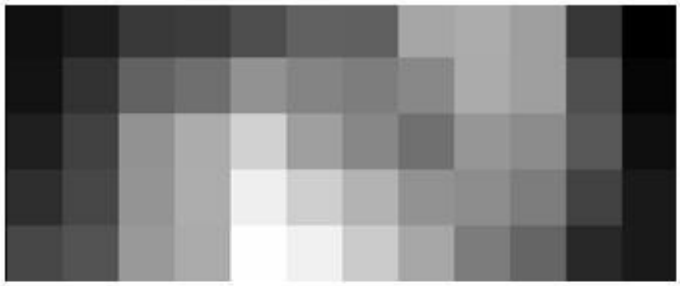

(c)

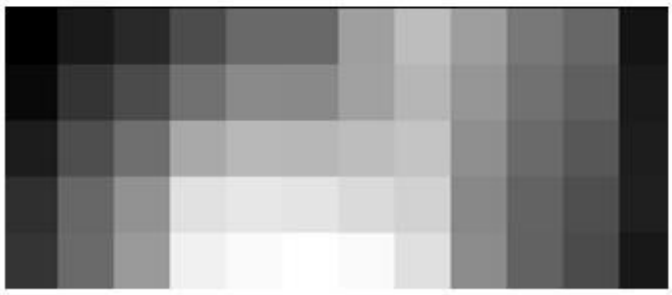

(d)

Figure 8-1 Convolution with different sizes of the mean filter
(a) The original matrix and (b) its corresponding image convolved with (c) 3 by 3 mean filter and (d) 5 by 5 mean filter

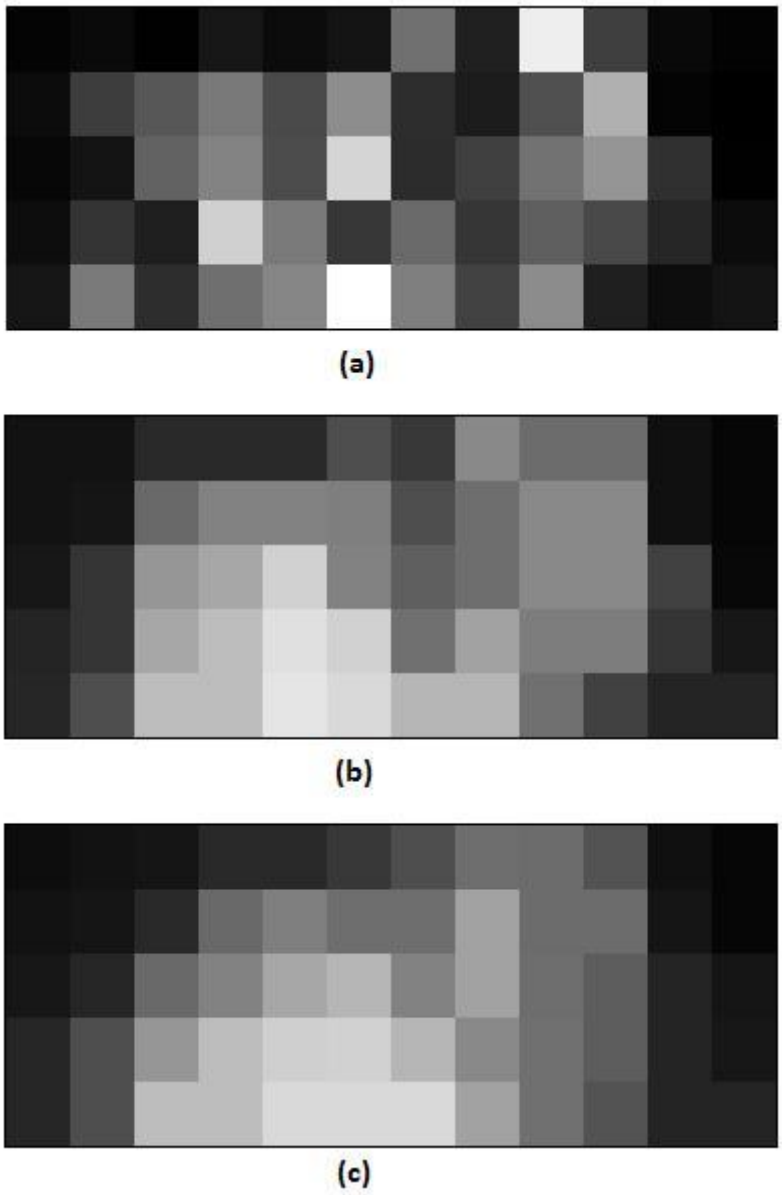

Figure 8-2 Schematic illustration of the effect of the median smoothing filters
(a) Raw image, (b) smoothed by 3 by 3 median filter, (c) smoothed by 5 by 5 median filter

8.3.1 Gaussian smoothing

Functional images are usually smoothed by convolution with the Gaussian function. Figure 8-3 shows how an EPI image which is blurred (shown in sagittal , coronal and axial cross sections) by applying a 3D, Gaussian function. The one dimensional Gaussian function with the mean equal to zero and σ is defined as:

$$G(x) = \frac{1}{\sqrt{2\pi\sigma^2}}\, e^{-\frac{x^2}{2\sigma^2}}$$

Where σ is the standard deviation of the Gaussian function and the FWHM is given by:

$$FWHM = \sigma\left(\sqrt{8ln2}\right) \approx 2.3548\,\sigma$$

8-2

Where "ln" refers to the natural logarithm (to the base "e"). Figure 8-4 shows a one-dimensional Gaussian function with mean=0 and σ=1.

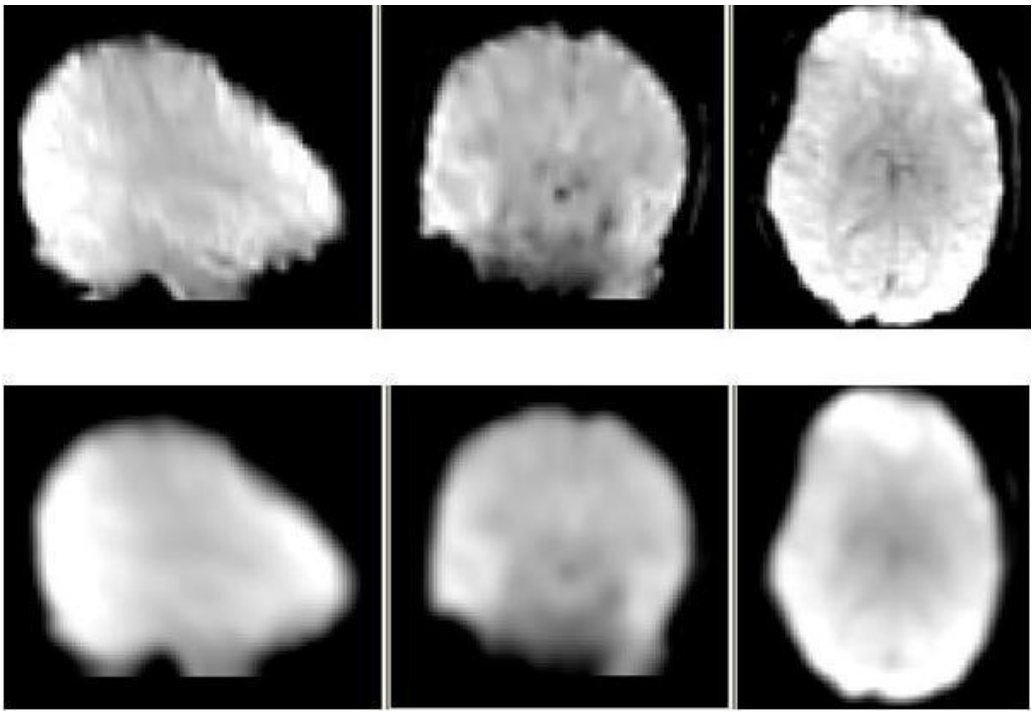

Figure 8-3 Effect of Gaussian smoothing
(top) Raw functional volume and (bottom) smoothed with Gaussian filter (FWHM=8)

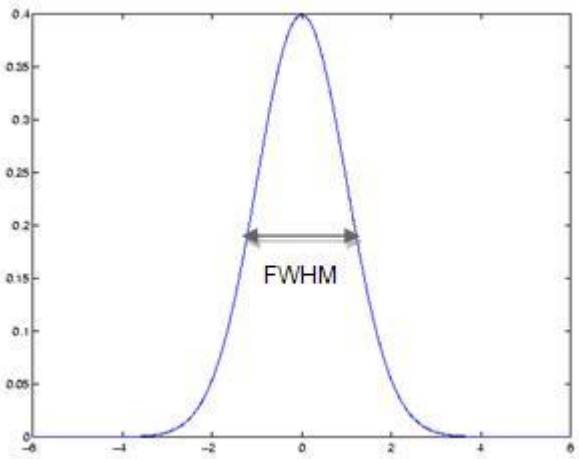

Figure 8-4 One-dimensional Gaussian function with mean=0 and σ=1

The two-dimensional Gaussian function is the product of two such Gaussians, one for each direction:

$$G(x,y) = \frac{1}{2\pi\sigma^2}\, e^{-\frac{x^2+y^2}{2\sigma^2}}$$

8-3

Similarly, the three dimensional function is defined as:

$$G(x,y,z) = \frac{1}{(2\pi\sigma^2)^{3/2}}\, e^{-\frac{x^2+y^2+z^2}{2\sigma^2}}$$

8-4

8.3.2 Smoothing in fMRI

There are several reasons for smoothing functional images. The first reason is to increase SNR, as mentioned before. Noise in functional images stems from physiological, thermal and scanner-related sources and is the major obstacle to activation detection. Moreover the hemodynamic response (the signal resulting from a single neuronal activation) is typically 2-5 mm wide (Ashburner et al., 2004). Consequently some degree of similarity between neighbouring voxels is expected. Also due to inter-subject differences, the precise location of the activation varies from subject to subject. The inter-subject variability arises from the anatomical and functional variability as well as the inter-subject registration error, and causes the location of activation of each subject to deviate from the common and expected location. These deviations can be modelled as a 3D Gaussian random variable with standard deviation σ_A. If the activation signal is modelled as a Gaussian function with standard deviation σ_S, then the smoothing process, or convolution of the signal plus noise with a Gaussian function with standard deviation σ_R , can lead to the maximum of SNR if the smoothing filter width matches the deviated signal width (Mikl et al., 2008) or:

$$\sigma_R = \sqrt{{\sigma_A}^2 + {\sigma_S}^2}$$

8-5

This is called the “matched filter theorem”. It can be inferred from this theorem that smoothing can increase the probability that a group study detects an activation which shows variability in the exact location across individuals. With smoother data and more similarity between voxel values, it is more likely that a supra-threshold voxel will have neighbours that are also supra-threshold; hence forming a cluster.

Another reason for spatial smoothing of functional images is because the subsequent statistical analysis for detection of activated voxels, is based on the Gaussian random field theory. This requires that the image smoothness be greater than the voxel size to ensure that the data more closely approximates a continuous field of random values.

Nonetheless, smoothing often entails additional voxels contributing to the activation map, leading to false positive (FP) voxels and hence decreasing the specificity of the activation localization.

Moreover, when the activation pattern includes several activation blobs, varying the smoothing kernel may result in either disappearance of a blob or merging two activation blobs. Therefore, the activation pattern is largely influenced by the smoothing kernel size, as shown by figure 8-5. Some examples of merging (shown by the blue arrows) and disappearing (shown by red arrows) blobs are shown on this figure.

However, the main drawback of smoothing with 3D Gaussian filter is that all voxels are treated similarly, regardless of their tissue types (GM, WM, and CSF) and whether they belong to cortical or sub-cortical regions. GM voxels can therefore be combined with those from WM and CSF, which clearly deteriorates the spatial resolution and specificity. The problem becomes even more complicated by considering the convoluted structure of the cortex, where the voxels that belong to different cortical regions (for example the opposite sides of a deep sulcus) can be mixed together. This is shown in figure 8-6 which also illustrates the desirable distribution of the activation.

In addition, it has been argued that smoothing often changes the location of activation centre. Geissler et al. conducted an experiment consisting of motor

activation and showed that smoothing causes a shift in the activation centre (the location of the local maxima) in the raw data (Geissler et al. 2005).

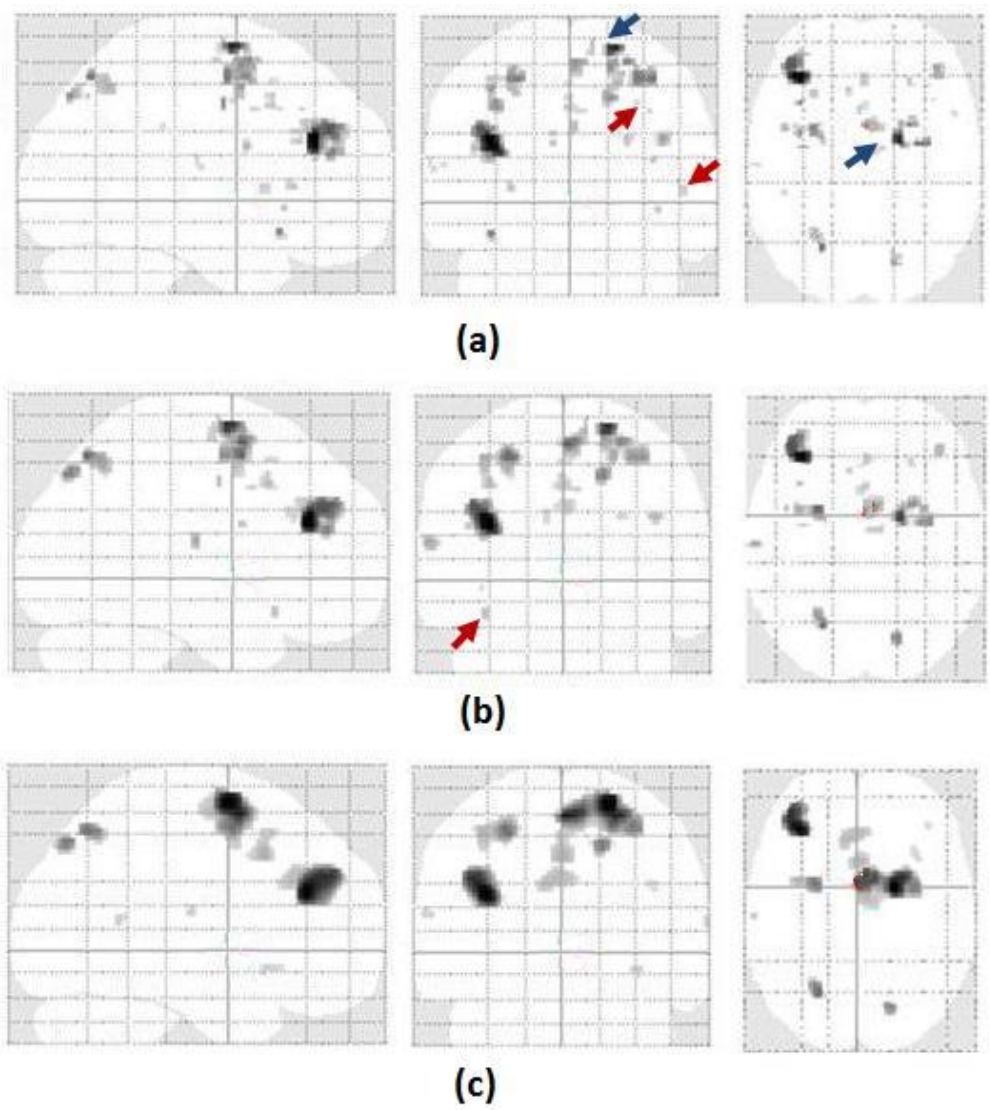

Figure 8-5 Effect of smoothing filter size on the activation map
The activation maps are displayed by Maximum intensity Projection on a glass brain for the n-Back task, contrast: 1Back-0Back, FWE (thresholded at 0.05). (a) raw data (b) smoothed with Gaussian filter with FWHM=4, (c) smoothed with Gaussian filter with FWHM=8.

Figure 8-6 Schematic comparison of the result of 3D and ideal smoothing filters
The activated voxels are shown in yellow on the raw image, (left) the image smoothed by the 3D Gaussian filter (middle), and the image smoothed by an ideal smoothing filter (right).

8.3.3 Cortical surface-based smoothing

To overcome the shortcomings of the 3D Gaussian smoothing, cortical surface-based smoothing filters have been proposed so as to smooth the data along the cortical sheet. In the following sections, these filters are discussed in more details.

8.3.3.1 Diffusion smoothing

The central idea with diffusion smoothing is a progressive propagation of each voxel's value. Figure 8-7 demonstrates the diffusion smoothing process on a one dimensional raw data and illustrates the propagation of the original non-zero voxel through an iterative process. At each iteration, the value of each voxel is replaced by the average of its two neighbours and its own value and the non-zero region grows owing to the iterative process. As the number of iterations increases, so does the range of the resulted non-zero (smoothed) voxels and hence the smoothing filter size.

Raw data	0	0	0	0	1	0	0	0	0	0
1st iteration	0	0	0	0.33	0.33	0.33	0	0	0	0
2nd iteration	0	0	0.11	0.22	0.33	0.22	0.11	0	0	0
3rd iteration	0	0.04	0.11	0.22	0.26	0.22	0.11	0.04	0	0

Figure 8-7 Diffusion of non-zero voxels through iterative process

The diffusion smoothing was first suggested by Andrade et al. (Andrade 2001) as an alternative to Gaussian smoothing, with reference to the theory established by Koenderink which stated that Gaussian convolution was equivalent to heat diffusion (Koenderink 1984).

The diffusion of heat with time (t), or the relationship between the temperature variations by time and location (r), is defined using the following equation:

$$\frac{\partial f(r,t)}{\partial t} = k\nabla^2 f(r,t)$$

Where K is a constant and ∇^2 is the Laplacian operator ($\nabla^2 f(x,y) = \frac{\partial^2 f}{\partial x^2} + \frac{\partial^2 f}{\partial y^2}$).

Now if t represents a smoothness parameter instead of time, then the solution of the equation 8-6 with k=0.5 is given by:

$$f(r, t = T) = f(r, t = 0) * (\frac{1}{2\pi T} e^{-\frac{x^2+y^2}{2T}})$$

8-7

The right hand side of the above equation is the convolution of the Gaussian filter (with $\sigma = \sqrt{T}$) with the unsmoothed function (t=0). In other words, applying a Gaussian spatial filter to an image is similar to smoothing the image with a diffusion process.

Andrade et al. applied this theory to implement their smoothing filter by creating the cortical mesh first and adopting a discrete diffusion function to represent iterative changes of the values assigned to each vertex on the cortical mesh. For this purpose, they defined the discrete version of the equation 8-6 at each iteration step Δt as:

$$\frac{f(r,t+\Delta t) - f(r,t)}{\Delta t} = k\nabla^2 \widetilde{f(r,t)}$$

8-8

Where $\nabla^2 \widetilde{f(r,t)}$ is the local estimation of the Laplacian at each vertex and needed to be calculated to extract the new value for the vertex at each iteration, f(r, t+Δt), from equation 8-8. To estimate ($\nabla^2 \widetilde{f(r,t)}$) at each vertex, they used the Taylor series expansion for each vertex and solved a linear system consisting of the relative positions of the vertex and its neighbours and the corresponding field value differences. To tailor the Laplacian for the curved surface of the cortical mesh, they applied a local transformation that mapped each surface element (a vertex and its first neighbours) into the plane, while keeping the edge distances and the angular proportions between the edges unchanged.

By comparison to the heat diffusion, for the case of smoothing, Δt should conceptually be equivalent to the inter-vertex distances. The closer a pair of

vertices is, the stronger their mutual influence and the faster the propagation. From equation 8-2, the effect of smoothing using the above approach after N iterations will be equivalent to a Gaussian smoothing filter with the FWHM equal to:

$$FWHM = \sqrt{8ln2}\sqrt{N\Delta t} \qquad \textbf{8-9}$$

For example for a Δt=0.1, the Gaussian kernel with FWHM=8 mm (σ = 3.397) requires 115 iterations ($N=T/\Delta t= \sigma^2/\Delta t$).

Andrade et al. then applied this method of smoothing to the EPI images involving motor activation (hand grasping) and estimated the sensitivity achieved by their cortical surface-based filter as well as the 3D Gaussian filter, in terms of successful detection of true positive voxels. For a range of thresholds, they measured the sensitivity of each method as the number of the resulting supra-threshold voxels at the local maxima obtained by the other method. They achieved higher sensitivity with their surface-based smoothing, however, the average t-values were not found to be significantly different for the two methods.

The difficulty of evaluating a smoothing filter for functional data is that there is usually no certainty about the precise location of activation. Consequently, in the absence of a gold standard to compare an activation map to, any comparison has to resort to indirect assessment of several parameters as proxies for the performance of the filter. However the assessment is more straightforward for structural analysis.

Chung et al. used the diffusion smoothing technique for increasing the SNR in structural analysis and measurement of metrics such as cortical surface area, thickness, curvature, and total volume of the GM (Chung et al. 2003).

To avoid the local flattening that Andrade et al. used for estimation of the Laplacian on the cortical surface, they used the Laplace-Beltrami operator (http://mathworld.wolfram.com/Laplace-BeltramiOperator.html) , Δf, as the extension of $\nabla^2 f$ to the cortical surface. To estimate the Δf at each vertex $p=p_0$ of

the cortical mesh, they used the Finite Element Method (FEM), which is used to obtain approximate solutions of the differential equations (such as the heat equation), and estimated the Δf at each vertex $p=p_0$ in terms of linear weights of the neighbouring vertices $p_1,...,p_m$:

$$\widehat{\Delta f(p)} = \sum_{i=1}^{m} w_i (f(p_i) - f(p))$$

8-10

Where the weights (w_i) are given by:

$$w_i = \frac{\cot\theta_i + \cot\varphi_i}{\sum_{i=1}^{m} \|T_i\|}$$

8-11

θ_i and φ_i in equation 8-11 are the two angles opposite to the edge connecting pi and p as demonstrated by figure 8-8, and $\|T_i\|$ is the area of the i-th triangle and were calculated according to:

$$\cot\theta_i = \frac{\langle p_{i+1} - p, p_{i+1} - p_i \rangle}{2\|T_i\|}, \quad \cot\varphi_i = \frac{\langle p_{i-1} - p, p_{i-1} - p_i \rangle}{2\|T_i\|}, \quad \|T_i\| = \frac{\|(p_{i+1} - p) \times (p_i - p)\|}{2}$$

8-12

In this equation, < > is the inner product sign and × is the cross product of the two vectors.

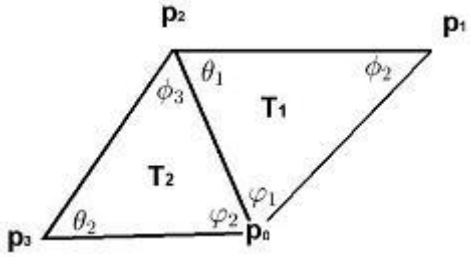

Figure 8-8 The angles and areas within the arrangement of vertices

They then used the finite difference scheme to iteratively solve the diffusion equation (equation 8-8) at each vertex p with the initial condition f(p, 0) = f(p) or:

$$f(p,t_{n+1}) = f(p,t_n) + (t_{n+1} - t_n)\widetilde{\Delta f(p)}$$

8-13

8.3.3.2 Heat kernel smoothing

To overcome the complexity of setting up the FEM, Chung et al. modified their first approach, described in the previous section, using what they called heat kernel smoothing (Chung et al. 2005). In this approach, the process of assigning value to each vertex was modified so that the weights for the neighbouring vertices were calculated based on their distance to the vertex.

A heat kernel, denoted by $K_\sigma(p,q)$, is the fundamental solution to the heat equation (equation 8-6), where p and q are two points on the manifold. They showed that if the band width (σ) is sufficiently small and p and q are close enough then the heat kernel is approximated by:

$$K_\sigma(p,q) \approx \frac{1}{\sqrt{2\pi\sigma}}\ exp\left(-\frac{d^2(p,q)}{2\sigma^2}\right)$$

8-14

Where d(p,q) is the geodesic distance between the two points. Heat kernel smoothing with large band width could be decomposed into iterated kernel smoothing with smaller band width via:

$$K_\sigma{}^{(k)} \times f = \underbrace{K_\sigma \times \ldots \times K_\sigma}_{k\ times} \times f = K_{\sqrt{k\sigma}} \times f$$

8-15

Now if Np = {q_0, q_1,. . .,q_m} is the set of nearest neighbouring vertices of vertex p, since the geodesic distance between neighbouring vertices is the same as the Euclidean distance (d(p, qi) = ||p_qi||), the term d(p,q) in equation 8-14 can be calculated as the Euclidean distance between p and q. They calculated the weighting factor for each neighbouring vertex, q_i, as the normalised kernel given by:

$$\widetilde{W_\sigma}(p,q_i) = \frac{exp\left(-\frac{d^2(p,q_i)}{2\sigma^2}\right)}{\sum_{j=0}^{m} exp\left(-\frac{d^2(p,q_j)}{2\sigma^2}\right)}$$

8-16

And computed the discrete convolution according to:

$$\widetilde{W_\sigma} \times f(p) = \sum_{i=1}^{m} \widetilde{W_\sigma}(p,q_i) f(q_i)$$

8-17

Hagler et al. argued that because of the discrete nature of the arrangements of the vertices in the cortical mesh, the assumption of continuous diffusion could not be valid and that the assumption becomes even less valid with increasing the distance between vertices (Hagler et al. 2006). Therefore the equivalence between FWHM of the Gaussian kernel and the value calculated from equation 8-9 for the heat kernel did not hold true.

They also suggested replacing the process of weighted average in heat kernel smoothing by simple average, where all the neighbouring vertices are assumed to have similar influence regardless of their distance to the main vertex. This simplified approach obviated the need for calculating the weighting factor for the neighbouring vertices which was computationally demanding. They showed that their technique provided a comparable smoothness to that of the heat kernel smoothing provided that the cortical mesh had high resolution so that the variance of inter-vertex distance was small.

8.3.4 Applying the heat kernel smoothing to functional data

Jo et al. implemented the heat kernel smoothing for simulated functional data, so as to set a gold standard for activated voxels. Using simulation they created T1-weighted and EPI images. The BOLD signal was chosen to originate from the motor cortex. They then compared the effect of the heat kernel smoothing with the 3D Gaussian smoothing on the simulated functional data (Jo et al., 2007 a,b). To examine the influence of noise, they added random noise and studied how closely the activation map approximated the gold standard in each case. To evaluate the performance of each smoothing technique, they calculated the sensitivity, False

Positive Fraction (FPF), Probabilistic Similarity Index (PSI), Probabilistic Overlap Fraction (POF), and Probabilistic Extra Fraction (PEF) which they defined as:

$$Sensitivity = \frac{TP}{TP+FN}$$

$$FPF = \frac{FP}{TN+FP}$$

$$PSI = \frac{\sum P_{x,gs=1}}{\sum l_{x,gs=1}+\sum P_x}$$

$$POF = \frac{\sum P_{x,gs=1}}{\sum l_{x,gs=1}}$$

$$PEF = \frac{\sum P_{x,gs=0}}{\sum l_{x,gs=1}}$$

8-18

Where TP, FP, TN and FN represent true positive, false positive, true negative and false negative, respectively. $\Sigma P_{x,gs=1}$ is the sum over the probability scores of all detected activation nodes for the gold standard, $\Sigma P_{x,gs=0}$ is the sum over the probability scores of all detected activation nodes outside of the gold standard, $\Sigma l_{x,gs=1}$ is the number of all nodes for the gold standard, and ΣP_x is the sum over the probabilities of all detected activation nodes. The PSI and POF have values ranging from 0 to 1, where higher PSI values indicate that the loci and extent of activation are closer to those of the gold standard with stronger probabilities.

Different smoothing kernel sizes equal to 6 mm, 8 mm, and 10 mm FWHM were examined. For heat kernel smoothing, the equivalent σ and number of iterations were calculated from equation 8-9. They showed that while there is no benefit of applying heat kernel smoothing in the absence of noise, for noisy data the heat kernel smoothing method increased the sensitivity and PSI. FPF, hence the specificity, was shown to be similar for both methods. However the heat kernel smoothing also leads to higher values for PEF.

Although, simulated data offers the possibility of defining a gold standard for activated voxels and direct comparison, they involve several presumptions about the extent and the exact location of BOLD signal, brain shape as well as noise distribution which may be different for real data and may thus provide an

unrealistic estimation of the accuracy of the smoothing kernel. In another study (Jo et al., 2008), they examined the effect of the kernel smoothing on real data involving activation in the hand area of the primary motor area and primary somatosensory cortex and calculated the shift in the activation centres resulting from each method of smoothing compared to the unsmoothed data (the risk map). They showed that although the heat kernel smoothing increased the sensitivity, both methods cause a shift in the activation centre with reference to the unsmoothed data.

The cortical surface-based smoothing methods discussed above require mapping of functional data to the cortical surface which entails approximations for projecting the 3D activation map to a 2D surface (for example using the intersection between the 3D map and 2D surface, or assigning the maximum value across the cortical thickness). Moreover, as a direct comparison between volume- and surface-based methods is not possible, the above-mentioned studies have used equivalent values for filter width to compare the two methods. However, as Hagler et al. showed, the equivalence between volume- and surface-based smoothing filters given by equation 8-9 is not a perfectly valid assumption (Hagler et al. 2006).

The main problem of the Gaussian method arises from the fact that the Euclidean distance between any two unrelated voxels can be so small that they can be combined during smoothing. Here two smoothing methods are examined which replace the Euclidean distance by a distance defined based on voxel connectivity in GM. This connected components-based distance can be thought of the equivalence of the Euclidian distance in the unfolded cortical sheet. This approach obviates the need for a cortical surface and node-wise statistical analysis. Instead, the statistical analysis can be performed on the voxel-based space similar to volume-based methods whilst also addressing the problems of the volume-based methods. Hence, the results can directly be compared between the two methods.

8.4 Methods

8.4.1 Subjects

The ethics approval for this study was obtained from West of Scotland Research Ethics Service. Three healthy volunteers with no history of brain injury,

neurological disease, or psychiatric disease were scanned using a GE 3T HD scanner.

8.4.2 fMRI experiments

In the absence of a clear-cut gold standard for functional activation, an optimum choice of a reference for comparison would resort to a paradigm which produce a well defined, localized and relatively strong activation map even without smoothing. Motor activation maps are among the paradigms that fulfil these requirements.

To cover different parts of the motor cortex, three separate tasks involving hands-grasping, lips-puckering and feet movement constituted the motor activation paradigm. For each of these three paradigms, a block design was used which comprised ten alternating active and rest blocks, each with duration of thirty seconds. The subjects were asked to perform the task during the active blocks at their own pace.

8.4.3 Image acquisition

The imaging parameters of the functional experiment (motor mapping) as well as the 3D T1-weighted scan are given in table 8-1.

Scan	Sequence	TR (msec)	TE (msec)	TI (msec)	Number of volumes	Flip angle(°)	Voxel size (mm^3)
Functional	GRE-EPI	3000	38	-------	100	90	1.88x1.88x4.5
3D T1	IR FSPGR	6	1	500	1	12	0.94x0.94x1

Table 8-1 Imaging parameters for acquisition of functional and structural data
TR, TE, and TI represent Repetition Time, Echo Time, and Inversion Time, respectively

8.4.4 Smoothing filter

Smoothing was performed using three different methods: 3D Gaussian, voxel-based diffusion, and voxel-based averaging. For each filter, different filter sizes were examined.

Voxel-based diffusion smoothing and voxel-based averaging filters only operate on GM voxels. For this purpose the GM mask was created using Brainvisa 4.0 (see chapter one), and was further refined by applying the skeleton mask (figure 1-10) to exclude the skeleton points (which correspond to CSF) from the GM mask. Figure 8-9 is a schematic description of the GM mask extracted from the 3D T1-weighted image and shows how a connectivity-based distance is defined for GM voxels.

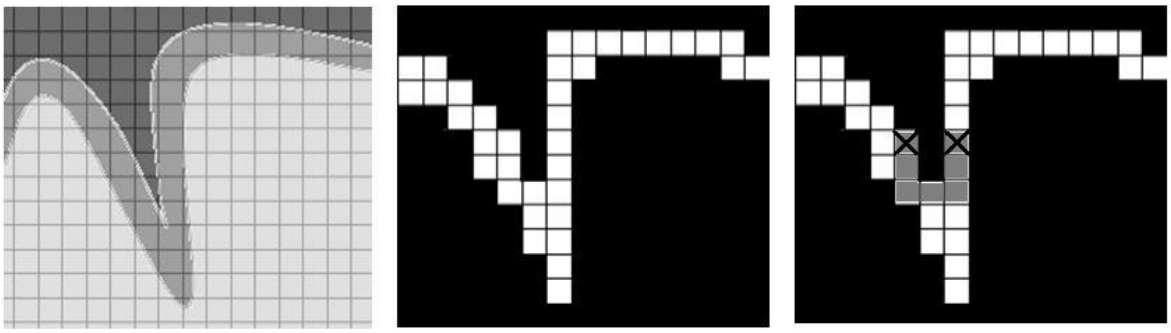

Figure 8-9 An illustration of the GM mask extraction and distance definition
(left) The T1-weighted image, (middle) the binary GM mask extracted from the T1-weighted image, and (right) the 4-connected component-based (in 2D space) distance between the two GM voxels marked by the cross signs

The programs corresponding to the developed filters were written by the author using Matlab 7.8.0 (http://www.mathworks.co.uk/products/matlab/index.html) and are given in the appendix.

In order to extract the GM voxels on the functional images, all the functional images were registered to the 3D T1-wighted image using SPM8. The registered functional images were then smoothed separately with each smoothing filter. The following sections describe the developed smoothing filters in more details.

8.4.4.1 Voxel-based diffusion smoothing

The main idea in this approach is to apply the diffusion smoothing on the GM voxels so that at each step of the iterative process, each GM voxel's value replaced the values of its immediate neighbours belonging to GM. This procedure was done in each direction (x, y, z) separately. In other words, each functional image was scanned along one direction and each GM voxel was smoothed by its two immediate neighbours along that direction. This procedure was then repeated

for the other two directions. At the end of this step the voxel value was replaced by all its neighbours (although each direction was processed separately).

The above procedure (smoothing along the three directions) was then repeated several times. The more repetition, the smoother the image and the wider the spread of the activation will be. An example of a GM-masked, smoothed image following 10 iterations is shown on figure 8-10. To clarify the changes associated with smoothing, the raw and smoothed images are masked by GM.

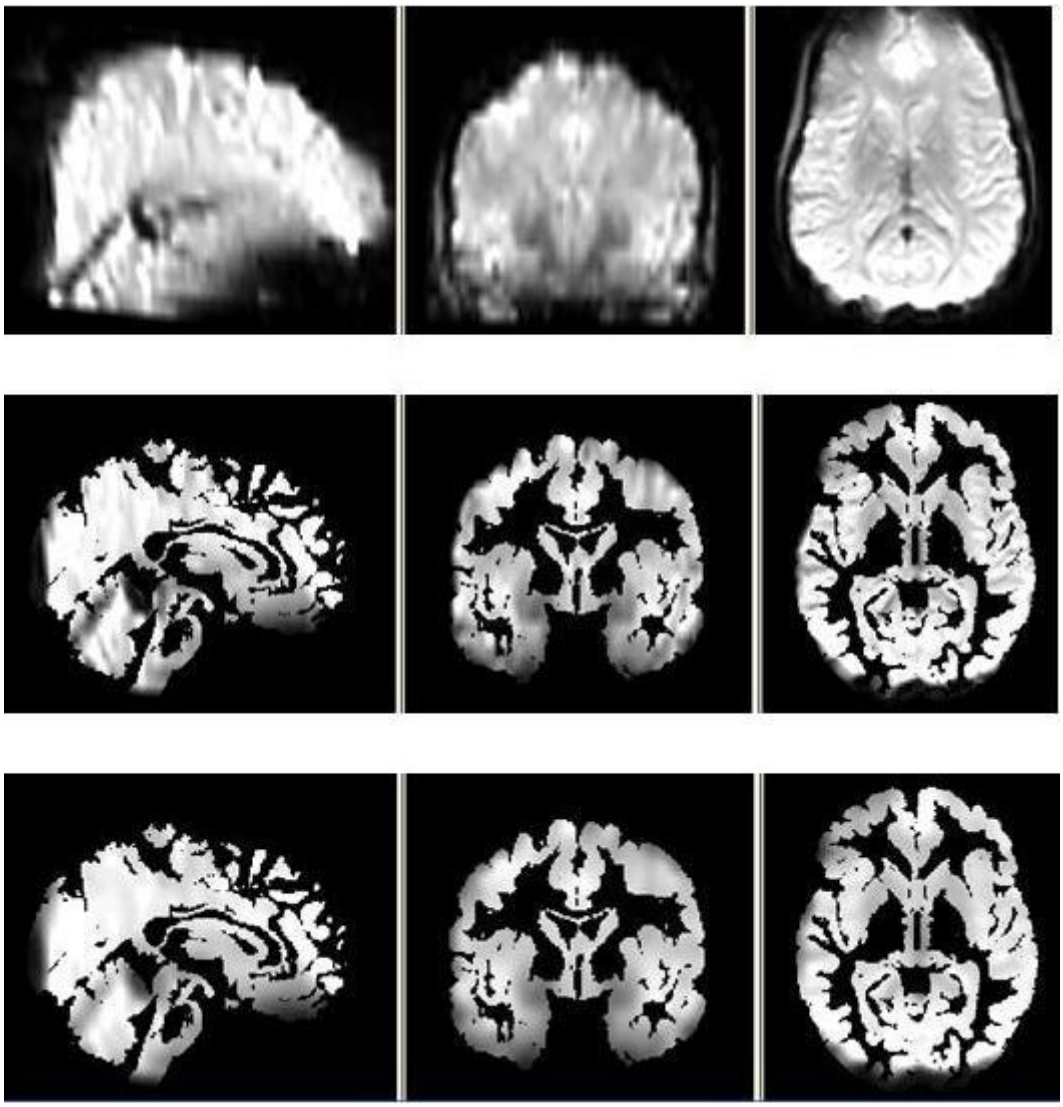

Figure 8-10 Voxel-based diffusion smoothing of a functional image (top) raw image (middle) masked with GM and (bottom) smoothed with 10 iterations

This algorithm was previously developed by Dr. Bill Moorhead from the University of Edinburgh and can be considered as an extension of the node wise diffusion smoothing filter to the voxel space. This has the benefit of being simple and easy to implement while avoiding the addition of the voxels that don't belong to the

cortex. In addition, since firstly the diffusion process stops at the GM/CSF border and secondly the smoothing is performed in an orderly manner in terms of neighbouring voxels, i.e., 1st order neighbours contribute in the first iteration, 2nd orders in the second iteration, and so on, the spread of activation to distant regions can be avoided. The smoothness is also controlled by choosing the number of iteration.

8.4.4.2 Voxel-based averaging

As mentioned earlier, simple averaging was suggested by Hagler et al. (Hagler et al. 2006) to substitute the iterative diffusion-based approach. Therefore, as an alternative for voxel-based diffusion filter, a voxel-based averaging filter was also tried.

The aim of the averaging method is to smooth the image through averaging each GM voxel by its neighbouring voxels within grey matter. The neighbourhood size, which determines how distant a voxel can be from the main voxel (to be smoothed) in order to contribute to the averaging process, is defined by the user. Obviously, the larger the neighbourhood size, the smoother the image will be. For each neighbourhood size, new neighbours are added by finding immediate neighbours of previously found neighbours. In other words finding the neighbours is done in an orderly manner: the first order neighbours are found first, the second order neighbours are then added by finding the immediate neighbours of the first order neighbours, and so on. This process is continued until the preset neighbourhood size is reached.

In the 2D space, the neighbouring pixels (for each neighbourhood order) can be found by using 4-connected pixels (figure 8-11a). Figure 8-11 shows 6th order neighbours of a given pixel (the central pixel shown in black) in the 2D space. A similar result can be obtained in the 3D space by replacing 4-connected pixels with 6-connected voxels as shown by figure 8-11b.

By limiting the above procedure to the GM voxels, new neighbours will be added only if they belong to the grey matter. If a newly found neighbour does not belong to the GM, it will not be included as a neighbour of the original voxel and the process of finding immediate neighbours for that specific voxel is terminated. This

is explained in figure 8-11d in which the pixels included as the neighbours of the main pixel have been delineated by the red contour. The GM pixels (highlighted in figure 8-11d) which have have not been included are also shown. Without the connectivity-based approach, these pixels would belong to the preset neighbourhood size (6^{th} order in this case) as shown by figure 8-11c. However with the connectivity-based distance, these pixels will fall outside the defined neighbourhood although their Euclidean distance to the main voxel may be even less than that for pixels included as neighbours.

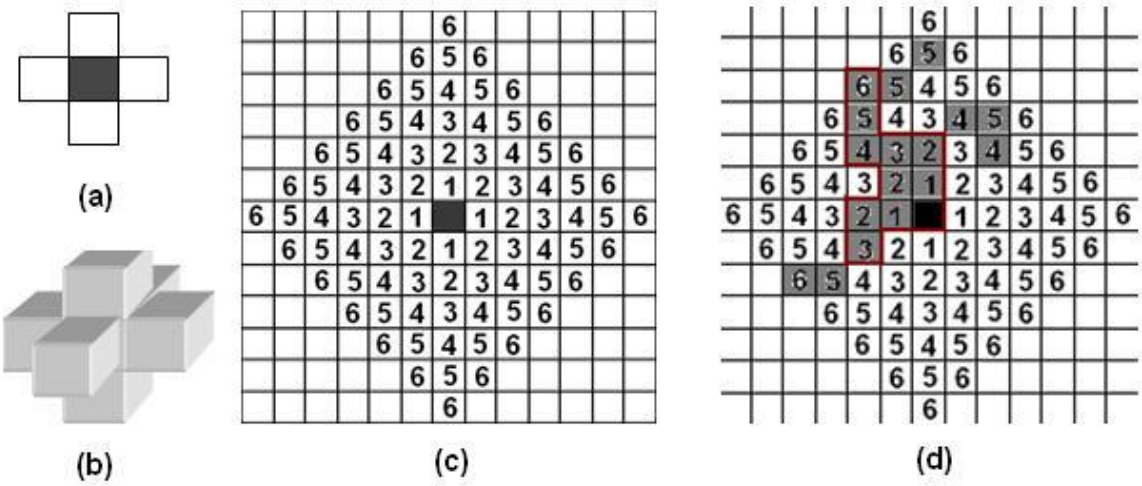

Figure 8-11 The neighbours definition based on the neighbourhood size
(a) The 4-connected pixels in 2D space and (b) its equivalent for the 3D space, 6-connected voxels. (c) 6^{th} order neighbours of the central pixel found by using 4-connected pixels, and (d) GM pixels included in the 6^{th} order neighbourhood (bounded by the red contour). As can be seen GM pixels (highlighted) outside the red contour have been excluded from neighbours of the main pixel as their connectivity-based distance exceeds the preset distance.

8.4.5 Image analysis

8.4.5.1 Image pre-processing

The 3D T1-weighted images were segmented using Brainvisa 4.0 into GM, WM, and CSF. The GM mask was further corrected by eliminating voxels belonging to the CSF skeleton.

The EPI images were corrected for head movement and were then co-registered to the 3D T1-weigthed image using SPM8. The functional images were then separately smoothed using three methods: 3D-Gaussian filter widths of 3,4, and 5 mm, voxel-based diffusion with 10, and 20 iterations, and voxel-based averaging

with 5,6, and 7 neighbourhood size. The statistical analysis using GLM, with FWE correction and the significance level 0f 0.05 was employed to identify the voxels with increased values in active periods.

8.4.5.2 Spread of the activation map

For each fMRI experiment of each subject, the extracted map resulting from the non-smoothed data defined the gold standard to which the maps of smoothed data could be compared. TP, FP, TN, and FN voxels were computed for smoothed maps with respect to the gold standard. It should be noted however, that the above definitions may be different from their conventional notions. For example FP refers to the expansion of activation map which is a direct result of smoothing and is not necessarily related to inaccuracy, however, FN is indicative of a shift in the activation map and means that some voxels originally included in the activation map of the non-smoothed data, have been excluded from the activation map as a result of the applied smoothing filter. In this context, Positive Predictive Value (PPV) was calculated as the proportion of activated voxels on the smoothed map which were also activated on the non-smoothed map (gold standard):

$$PPV = \frac{TP}{TP + FP} \qquad \textbf{8-19}$$

Larger values of PPV are desirable as PPV decreases with the spread of activation.

8.4.5.3 SNR and smoothness

As the main aim of smoothing is to reduce the SNR, it is necessary to compare the degree of smoothness achieved by each filter. For this purpose, smoothness was calculated from the distribution of signal intensities in the contrast image. The contrast image is produced following the statistical analysis and is a representation of “Active-Rest” image. In other words, the active voxels are brighter on the contrast image compared to the non-active voxels. The mean and standard deviation was calculated within each GM-masked contrast image and the

smoothness was calculated as the ratio between these two parameters (smoother images should correspond to higher values of “mean/standard deviation”):

$$Smoothness = \frac{mean\ sigal\ intensity\ within\ GM}{standard\ deviation\ of\ the\ sigal\ intensities\ within\ GM} \quad \textbf{8-20}$$

8.4.5.4 Maximum t-value

Smoothing in group studies results in greater overlap between activation maps of different individuals and hence the increase in the statistical power (and therefore t-values). However in each individual brain, the effect of smoothing is opposite and the t-values usually decrease as a result of the spread of the activation map.

To investigate how the t-values change with each smoothing method, the maximum t-value were calculated within all activation maps corresponding to different paradigms for different subjects.

8.5 Results

Figure 8-12, 8-13, and 8-14 show the plots of PPV vs. Smoothness for motor activations of the three studied subjects. These plots also show the filter size for each smoothing method. As can be seen from this plots, for a given degree of smoothness, the diffusion smoothing approach reaches higher PPV values compared to the Gaussian method which suggests the superiority of the diffusion smoothing method over the Gaussian method. However, the averaging method often does not provide the same degree of smoothness as the other two methods. The degree of smoothness for the averaging method can be increased by increasing the filter size, however this can be computationally intensive. In cases where the smoothness by averaging method is comparable to the other methods, the averaging method usually reaches lower PPV values for the same degree of smoothness relative to those methods. This suggests that averaging-based filters may not be a suitable substitute for the Gaussian filter.

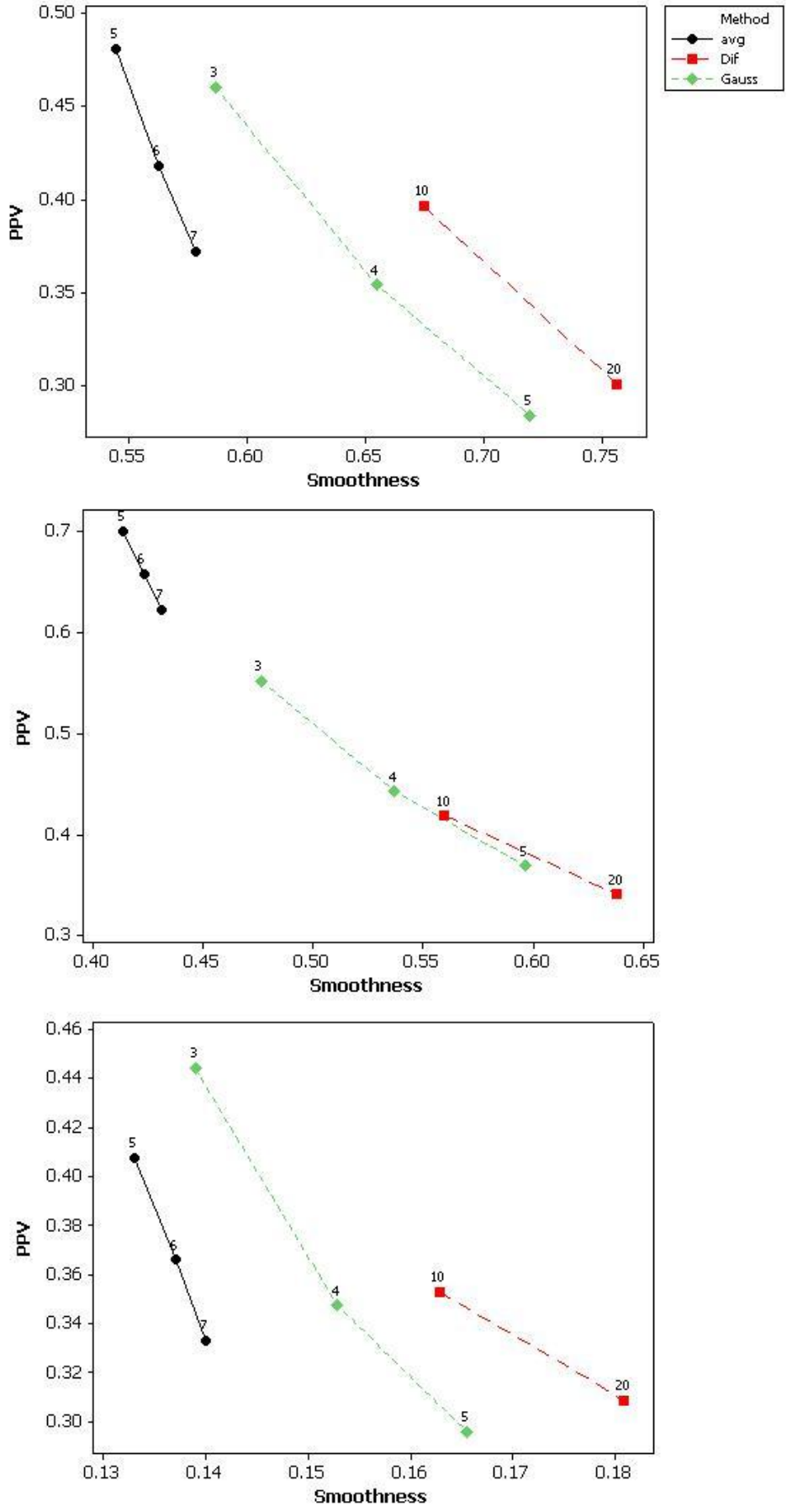

Figure 8-12 The plots of PPv vs. Smoothness for feet movement activation
The plots are shown for (top) subject S01, (middle) subject S02, and (bottom) subject S03.

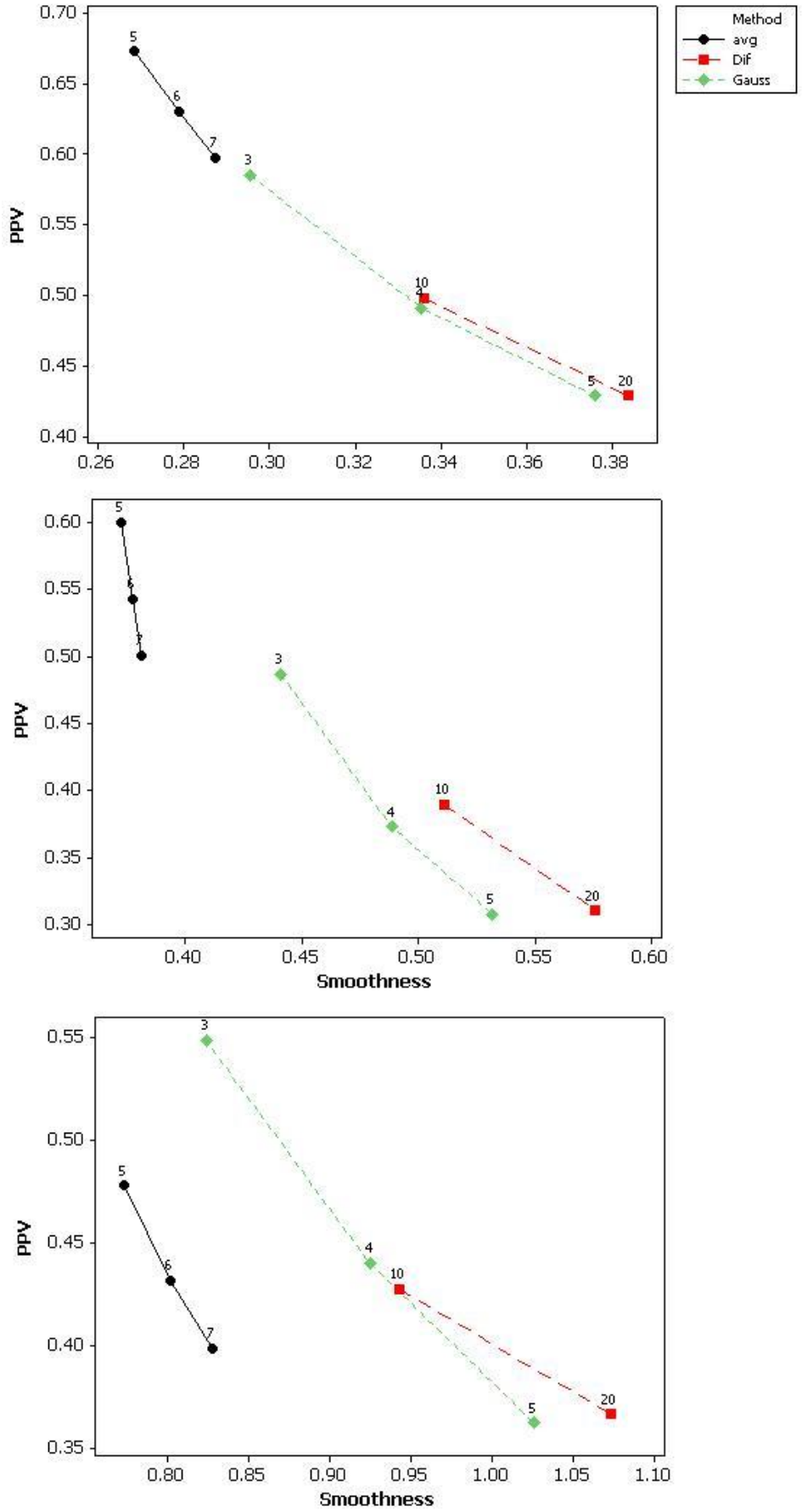

Figure 8-13 The plots of PPv vs. Smoothness for hands grasping activation
The plots are shown for (top) subject S01, (middle) subject S02, and (bottom) subject S03.

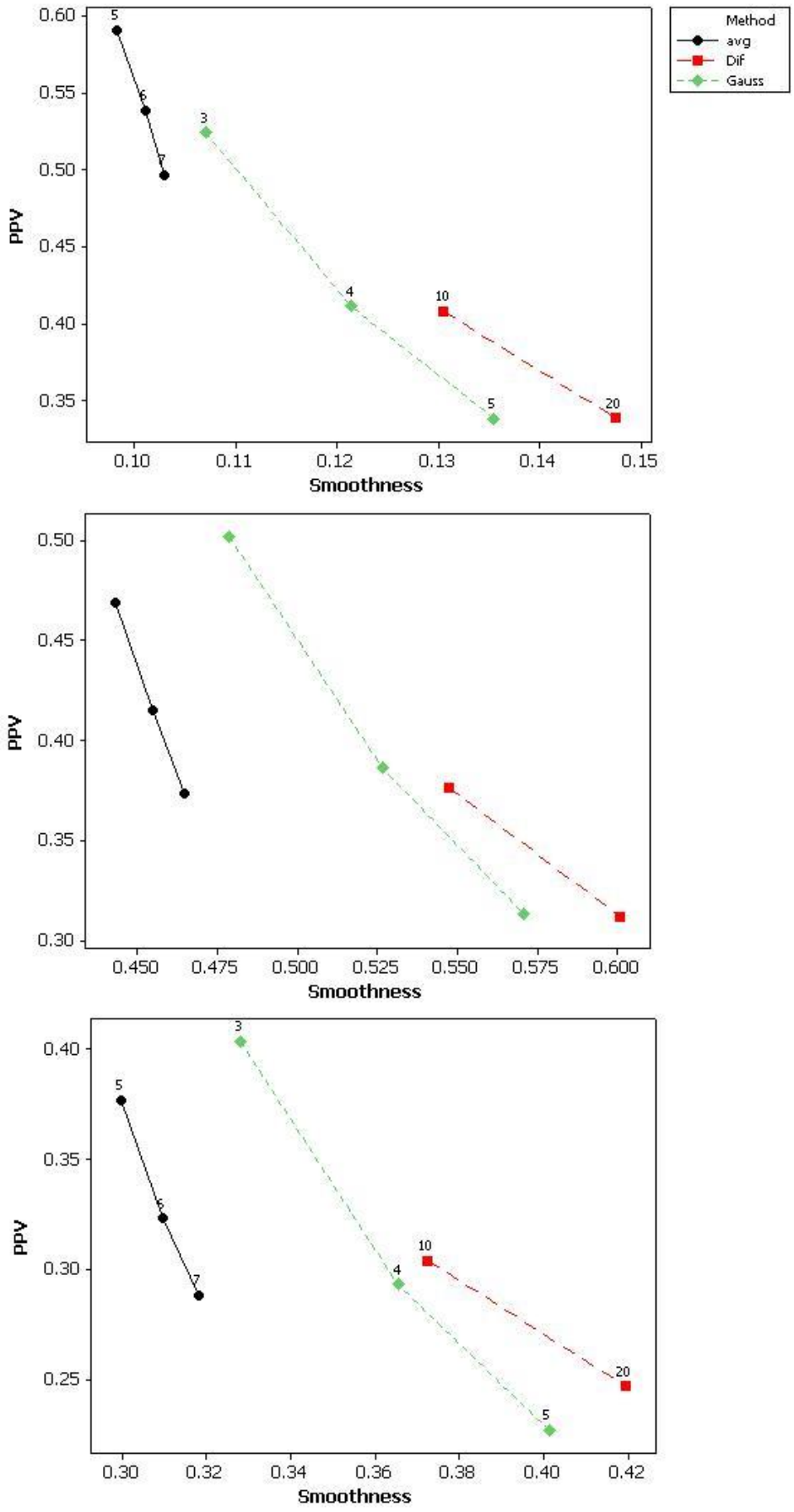

Figure 8-14 The plots of PPv vs. Smoothness for lip puckering activation
The plots are shown for (top) subject S01, (middle) subject S02, and (bottom) subject S03.

The maximum t-values with different smoothing filters, different filter size, and different paradigms of all subjects are shown by table 8-2. As expected, for each smoothing filter the maximum t-value is reduced by increasing the filter size. Again, for most cases the maximum t-values are slightly higher with diffusion smoothing compared to Gaussian smoothing.

	Feet			Hands			Lip		
	S01	S02	S03	S01	S02	S03	S01	S02	S03
Raw	11.302	18.784	13.445	23.068	15.943	15.632	16.0	19.647	15.064
Avg5	10.307	18.569	13.284	22.910	15.784	15.062	15.972	19.246	13.071
Avg6	10.296	18.514	13.252	22.869	15.751	14.965	15.955	19.153	13.040
Avg7	10.286	18.460	13.225	22.825	15.717	14.871	15.938	19.061	13.013
Dif10	10.300	18.244	13.202	21.501	15.554	14.738	16.310	18.927	12.926
Dif20	10.278	17.991	13.135	21.347	15.446	14.489	15.720	18.649	12.849
Gauss3	10.820	17.870	12.436	22.717	14.944	14.472	16.308	20.105	12.475
Gauss4	10.084	17.470	12.354	22.089	14.647	13.739	16.288	19.123	11.966
Gauss5	9.613	16.899	11.903	21.576	14.539	12.982	16.081	17.993	11.655

Table 8-2 The maximum t-values with different smoothing filters, different filter size, in addition to the raw (non-smoothed) data and different paradigms of all subjects

8.6 Discussion

A major limitation of the comparison between different smoothing filters is the absence of a gold standard or the ideal activation map mainly due to the between-individual differences in activation pattern. One possibility for such studies is therefore to use well-established functional paradigms with relatively well-defined activation patterns. This approach was adopted in this study to compare different smoothing filters in terms of PPV, smoothness, and the statistical power or the maximum t-value obtained by each method.

The results of this study suggest that diffusion smoothing can improve the specificity of activation mapping whilst also achieving the desired degree of smoothness.

It should be noted however, that the developed algorithms use information from structural images for the smoothing process. These methods are therefore very sensitive to the co-registration between the structural and functional images. For this reason, these methods can be more promising with higher resolution functional images. With higher magnetic field strengths, higher spatial resolution of the EPI images can be achieved which can improve the co-registration between the functional and structural image.

Another limiting factor for the success of the developed algorithms is their sensitivity to GM segmentation. More robust segmentation algorithms should provide a more accurate estimation of the cortical GM voxels which are included in the smoothing process.

In addition, since they require registering all functional images to the high resolution T1-weighted image, these approaches are computationally intensive compared to the Gaussian method.

8.7 Conclusion

In this chapter a comparison between several methods of smoothing the functional images is carried out in order to see if it is possible to improve the specificity of activation detection using fMRI. The diffusion smoothing method was found to be superior to Gaussian and averaging methods. This is promising given the importance of accurate activation localization especially in applications such as pre-surgical planning.

Chapter 9. Conclusion and future work

9.1 Summary and final conclusions

Brainvisa offers a wide range of possibilities for cortical analysis using the automatic sulci recognition feature of this package.

On one hand the automated sulci identification can be used in identifying the cortical areas. This can especially be of interest in fMRI studies of individual subjects as it obviates the need for normalization to an atlas. The normalization of abnormal brains may be problematic firstly because of abnormality-related changes, such as large tumours deforming some parts of the brain, can have an impact on the accuracy of normalization. Secondly, since atlases are usually based on healthy brains, even in the presence of subtle abnormalities normalization can be less accurate compared to healthy brains.

On the other hand, by automatically identifying the sulci and estimating a wide range of properties such as size, coordinates, direction, and pattern for each sulcus, sulcal morphometry studies can be hugely facilitated. Studies of abnormal brains have shown that morphometry analysis can provide valuable information regarding the structural changes associated with certain types of abnormalities. Nonetheless, most studies so far have focused on brain morphometry though some included a limited use of sulcal morphometry.

It should be noted however, that although automated methods are often a superior alternative to the manual methods by avoiding human errors, they can still be susceptible to limitations associated with image quality. Thus the robustness of these methods needs to be assessed. This can be done by estimating the

reliability and reproducibility of results as well as exploring the changes in results caused by such factors.

The reproducibility and repeatability of the morphometry analysis was estimated and discussed in chapter three of the thesis. The findings of this study indicate that the estimations can vary even between different scanning sessions of the same scanner. Such disparity is more pronounced across different scanners. It was also shown that the reliability of brain segmentation results were less compared to the FAST algorithm within the FSL package. It was found that the bias field correction with FAST resulted in higher WM/GM contrasts, relative to Brainvisa.

In addition, the variations in morphometry results using Brainvisa with noise, slice thickness, and magnetic field non-uniformity was assessed in chapter four using simulated T1-weighted images. Brain segmentation was shown to be susceptible to noise such that with increasing noise level, more GM voxels were classified as WM or CSF. Increasing the slice thickness usually led to a reduction in the GM volume and an increase in the WM volume. However, the variations in the CSF volume followed a more complex pattern in which increasing the slice thickness resulted in an initial increase but was followed by decrease in the CSF volume. Detection of the cortical folds was found to be relatively robust against the noise while shown to suffer from large slice thicknesses. Compared to noise and slice thickness, both brain segmentation and fold detection were relatively robust against signal intensity non-uniformity suggesting that noise and slice thickness can have the main impact on the results.

Changes in sulcal size (in terms of surface, length, and mean geodesic depth) with autism were evaluated using sulcal morphometry with Brainvisa for two groups of adolescents: those with autism and healthy subjects. The motivation for choosing the sulcal size, was due to the relatively increased (although non-significant) gyrification in the autism group. The altered size of the left insula (increased surface) and right intraparietal sulcus (increased length) was observed which suggests sulcal size can have some correlation with autism.

Localization of functional activity of the brain using cortical labels (obtained using Brainvisa) offers a direct method for identifying the eloquent areas of the cortex in fMRI studies. By using the cortical labels, the areas activated through performance

of a number of tasks were identified for a group of patients with brain tumour, vascular malformation, or epilepsy to evaluate the possibility of pathology-related reorganization of brain function. The locations of activation in terms of the sulci were relatively consistent among different patients suggesting that this method of identifying the activated regions can be useful. However, the possibility of false sulcal labelling due to the abnormality should also be considered.

The activation detection in the above-mentioned fMRI studies followed the conventional methods. However, the activation detection can also benefit by replacing the Gaussian smoothing of the functional volumes with alternative methods which prevent the extension of activation to other cortical areas. As was discussed in chapter two, cortical surface-based methods may not necessarily achieve this goal smoothing. To obtain more localized activation, two different smoothing filters were developed in chapter eight both of which reduced the mixing of the values of voxels across any sulcus. In practice however, only one method, voxel based diffusion smoothing, was shown to have superior performance over the Gaussian filter. This suggests that the Gaussian filter can be replace by voxel based diffusion smoothing filter in smoothing the functional images.

9.2 Suggestions for future work

Bias correction and histogram analysis steps of image analysis with Brainvisa have a key role in the results of morphometry analysis using this package. The findings in chapter three revealed that morphometry analysis could become more robust by improving the bias correction step. It would also be helpful to estimate the robustness of the histogram analysis in terms of brain segmentation. This can be done by comparing the segmentation results of Brainvisa and FAST. However given the current limitations of these packages which did not allow for segmentation of the same bias corrected image, no comparison could be made between these methods. It is therefore suggested that the analysis procedure become more flexible for example by allowing for importing a bias corrected image and skipping the bias correction step. This can be useful in estimating the ways of improving the robustness of Brainvisa.

The use of simulated T1-weighted images in chapter four provided useful means of evaluation of variations in morphometry results with image quality and image acquisition parameters. However, due to the approximations used for the simulation and given the fact that the effect of subject's movement in the scanner may not be taken into account, simulated data often differ from real data. Thus, it would be helpful if a similar analysis is performed using real data. For this purpose, an experiment including different values for image acquisition parameters, scanner type, field strength, and so on, using the same group of subjects can be carried out.

Estimation of the changes in sulcal size in adolescents with ASD studied in chapter five suggested that sulcal size can be used as a biomarker of this disorder. Given the heterogeneity of autism, it is suggested to carry out similar studies using different groups of subjects with this disorder, as this can provide a better insight into cortical changes associated with autism. In addition, optimization of image acquisition parameters (for example using smaller slice thicknesses) which have been shown to affect the fold detection is recommended for future studies.

Chapters six and seven suggest that using sulcal labels for the study of brain plasticity as well as pre-surgical assessment for patients with brain tumours, vascular malformations or those with epilepsy, can be an appropriate alternative to manual methods. Nevertheless, for a more comprehensive evaluation of the suitability of this method, it is suggested to continue this study for a larger group of patients. This can accompany the manual methods in routine clinical assessments. The consistency between the automatic (using Brainvisa) and manual methods can then be evaluated and the utility of Brainvisa for pre-surgical planning can thus be verified.

Further improvement in the activation localization can be achieved by correcting for the susceptibility-related warp in the EPI data which allows a more accurate registration between structural and functional images. In order to correct for such distortions, it is recommended to acquire the field maps during the scan so that the image distortions can be corrected.

One limitation of the application of Brainvisa for patients with brain tumour or vascular malformations is that the voxels inside the lesions can be regarded as normal brain tissues and hence be categorized as GM, WM, or CSF, according to their grey levels. This usually leads to extraction of folds inside lesions. Thus, it is suggested to modify the algorithm so as to prevent the fold detection inside the regions identified as the lesion mask by the user.

The results of chapter eight confirmed the superiority of voxel based diffusion smoothing method over the conventional Gaussian methods. Due to the importance of the accuracy of activation localization in pre-surgical assessments, it is suggested that in future the Gaussian filter be replaced with the diffusion smoothing filter for such patients' studies such as those mentioned in chapters six and seven. It should be noted that, as mentioned in chapter eight, the suggested method can be more successful for higher resolution of functional images. Thus, it would be useful to assess the performance of these methods in high resolution functional images.

Appendix: Source codes of the smoothing filters

1. Voxel-based diffusion smoothing

```
[s1,s2,s3]=size(GreyMask);

%Choose functional images

[filename,pathname,filterindex]=uigetfile({'*.hdr','analyze-files(*.hdr)'},...

   'Pick a file','MultiSelect', 'on');%write .hdr filenames in the array filename

for i=1:length(filename)

   image=analyze75read(filename{i});

   disp(['smoothing file: ' filename{i}])

   for j=1:Scope

      disp(['iteration ' num2str(j) ' of ' num2str(Scope)])

      temp=image;

      %iteration on 3rd dimension

      for m=2:s1-1

         for n=2:s2-1

            for k=2:s3-1

               if GreyMask(m,n,k)

                  IN=image(m,n,k);

                  for off=[-1,1]
```

```
                if GreyMask(m,n,k+off)
                    IN=horzcat(IN,image(m,n,k+off));
                end
            end
            temp(m,n,k)=mean(IN);
        end
    end
  end
end
image=temp;
%iteration on 2nd dimension
for m=2:s1-1
  for n=2:s2-1
    for k=2:s3-1
      if GreyMask(m,n,k)
        IN=image(m,n,k);
        for off=[-1,1]
          if GreyMask(m,n+off,k)
            IN=horzcat(IN,image(m,n+off,k));
```

```
            end
        end
        temp(m,n,k)=mean(IN);
    end
  end
 end
end
image=temp;
%iteration on 1st dimension
for m=2:s1-1
  for n=2:s2-1
    for k=2:s3-1
      if GreyMask(m,n,k)
        IN=image(m,n,k);
        for off=[-1,1]
          if GreyMask(m+off,n,k)
            IN=horzcat(IN,image(m+off,n,k));
          end
        end
```

```
                    temp(m,n,k)=mean(IN);
                end
            end
        end
    end
    image=temp;
end
image=permute(image,[2 1 3]);
fname=['dif' num2str(Scope) '_' filename{i}];
[p,f] = fileparts(fname);
fileprefix = fullfile(p, f);
copyfile(filename{i}, fname);%copy the original hdr file
fid = fopen(sprintf('%s.img',fileprefix),'w');
fwrite(fid,image,'int16');%write the smoothed image
fclose(fid);
end
disp('smoothing:done')
```

2. Voxel-based averaging

```
%For each voxel in the GM find its 6-connected neighbours within a given range.
List all GM voxels in the matrix V (each row of V refers to coordinates of a point)
and their corresponding neighbours in the matrix N
function [V,N] = neighbours (GM, range)
voxels = regionprops (GM,'Area');
n_voxels = sum ([voxels.Area]);
N = cell (n_voxels,1);
[s1,s2,s3] = size (GM);
V = [];
for i=range:s1-range
   for j=range:s2-range
      for k=range:s3-range
         if GM (i,j,k)
            V=vertcat(V,[i j k]);
            N{size(V,1),1}=findNb ([i,j,k], GM, range);
         end
      end
   end
end
end

function [M] = findNb(M,GM,range)
j=1;
while j<=size(M,1) && sum(abs(M(j,:)-M(1,:)))<range
   for p=[-1 1]
      x=M(j,1)+p; y=M(j,2); z=M(j,3);
      if GM(x,y,z) && newNeighbour(M,[x,y,z])
         M=vertcat(M,[x y z]);
      end
      x=M(j,1); y=M(j,2)+p; z=M(j,3);
      if GM(x,y,z) && newNeighbour(M,[x,y,z])
         M=vertcat(M,[x y z]);
      end
      x = M(j,1); y = M(j,2); z=M(j,3)+p;
```

```
        if GM (x,y,z) && newNeighbour (M,[x,y,z])
            M = vertcat (M,[x y z]);
        end
    end
    j=j+1;
end
end

function [new] = newNeighbour(A,X)
new=true;
for i=1:size(A,1)
    if A(i,:)==X
        new=false;
    end
end
end

% Apply smoothing to the functional images
[filename,pathname,filterindex]=uigetfile({'*.hdr','analyze-files(*.hdr)'},...
    'Pick a file','MultiSelect', 'on');%write .hdr filenames in the array filename
for m=1:length(filename)
    image=analyze75read(filename{m});
    disp(['smoothing file: ' filename{m}])
    temp=image;
    for k=1:length(N)
        im=[];
        for j=1:size(N{k,1},1)
            im=vertcat(im,image(N{k,1}(j,1),N{k,1}(j,2),N{k,1}(j,3)));
        end
        temp(V(k,1),V(k,2),V(k,3))=mean(im);
    end
    image=permute(temp,[2 1 3]);
    fname=['avg' filename{m}];
    [p,f] = fileparts(fname);
    fileprefix = fullfile(p, f);
    copyfile(filename{m}, fname);%copy the original hdr file
```

```
    fid = fopen(sprintf('%s.img',fileprefix),'w');
    fwrite(fid,image,'int16');%write the smoothed image
    fclose(fid);
end
disp('smoothing:done')
```

List of References

Alkadhi, H., Kollias, S. S., Crelier, G. R., Golay, X., Hepp-Reymond, M. C., & Valavanis, A. 2000, "Plasticity of the human motor cortex in patients with arteriovenous malformations: A functional MR imaging study", *American Journal of Neuroradiology*, vol. 21, no. 8, pp. 1423-1433.

American Brain Tumor Association 2004, *A Primer of Brain Tumors*, eigth edn.

Amunts, K., Schleicher, A., Burgel, U., Mohlberg, H., Uylings, H. B. M., & Zilles, K. 1999, "Broca's region revisited: Cytoarchitecture and intersubject variability", *Journal of Comparative Neurology*, vol. 412, no. 2, pp. 319-341.

Andersson, J. L. R., Hutton, C., Ashburner, J., Turner, R., & Friston, K. 2001, "Modeling Geometric Deformations in EPI Time Series", *Neuroimage*, vol. 13, no. 5, pp. 903-919.

Andrade, A., Kherif, F., Mangin, J. F., Worsley, K. J., Paradis, A. L., Simon, O., Dehaene, S., Le Bihan, D., & Poline, J. B. 2001, "Detection of fMRI activation using cortical surface mapping", *Human Brain Mapping*, vol. 12, no. 2, pp. 79-93.

Anticevic, A., Dierker, D. L., Gillespie, S. K., Repovs, G., Csernansky, J. G., Van Essen, D. C., & Barch, D. M. 2008, "Comparing surface-based and volume-based analyses of functional neuroimaging data in patients with schizophrenia", *Neuroimage.*, vol. 41, no. 3, pp. 835-848.

Argall, B. D., Saad, Z. S., & Beauchamp, M. S. 2006, "Simplified intersubject averaging on the cortical surface using SUMA", *Hum.Brain Mapp.*, vol. 27, no. 1, pp. 14-27.

Ashburner, J., Friston, K., & Penny, W. Human Brain Function. http://www.fil.ion.ucl.ac.uk/spm/doc/books/hbf2/ [2nd edition]. 2004.

Atlas, S. W. 1996, *Magnetic Resonance Imaging of the Brain and Spine*, 2nd edn, Lippincott-Ravon.

Aurenhammer, F. & Klein, R. 2000, "Voronoi Diagrams," in *Handbook of Computational Geometry*, J.-R.Sack & J.Urrutia, eds., North-Holland, Amsterdam, pp. 201-209.

Baciu, M., Le Bas, J. F., Segebarth, C., & Benabid, A. L. 2003, "Presurgical fMRI evaluation of cerebral reorganization and motor deficit in patients with tumors and vascular malformations", *European Journal of Radiology*, vol. 46, no. 2, pp. 139-146.

Benson, R. R., FitzGerald, D. B., LeSueur, L. L., Kennedy, D. N., Kwong, K. K., Buchbinder, B. R., Davis, T. L., Weisskoff, R. M., Talavage, T. M., Logan, W. J., Cosgrove, G. R., Belliveau, J. W., & Rosen, B. R. 1999, "Language dominance determined by whole brain functional MRI in patients with brain lesions", *Neurology*, vol. 52, no. 4, pp. 798-809.

Bigler, E. D., Abildskov, T. J., Petrie, J. A., Johnson, M., Lange, N., Chipman, J., Lu, J., McMahon, W., & Lainhart, J. E. 2010, "Volumetric and Voxel-Based Morphometry Findings in Autism Subjects With and Without Macrocephaly", *Developmental Neuropsychology*, vol. 35, no. 3, pp. 278-295.

Binder, J. R., Frost, J. A., Hammeke, T. A., Cox, R. W., Rao, S. M., & Prieto, T. 1997, "Human brain language areas identified by functional magnetic resonance imaging", *Journal of Neuroscience*, vol. 17, no. 1, pp. 353-362.

Bookheimer, S. 2002, "Functional MRI of language: New approaches to understanding the cortical organization of semantic processing", *Annual Review of Neuroscience*, vol. 25, pp. 151-188.

Bookheimer, S. 2007, "Pre-surgical language mapping with functional magnetic resonance imaging", *Neuropsychology Review*, vol. 17, no. 2, pp. 145-155.

Brett, M., Johnsrude, I. S., & Owen, A. M. 2002, "The problem of functional localization in the human brain", *Nat.Rev.Neurosci.* , vol. 3, no. 3, pp. 243-249.

Brodmann, K. 1909, *Vergleichende Lokalisationslehre der Grosshirnrinde in ihren Prinzipien dargestellt auf Grund des Zellenbaues* Barth, Leipzig.

Buckner, R. L., Head, D., Parker, J., Fotenos, A. F., Marcus, D., Morris, J. C., & Snyder, A. Z. 2004, "A unified approach for morphometric and functional data

analysis in young, old, and demented adults using automated atlas-based head size normalization: reliability and validation against manual measurement of total intracranial volume", *Neuroimage*, vol. 23, no. 2, pp. 724-738.

Cachia, A., Paillere-Martinot, M. L., Galinowski, A., Januel, D., de Beaurepaire, R., Bellivier, F., Artiges, E., Andoh, J., Bartres-Faz, D., Duchesnay, E., Riviere, D., Plaze, M., Mangin, J. F., & Martinot, J. L. 2008, "Cortical folding abnormalities in schizophrenia patients with resistant auditory hallucinations", *Neuroimage*, vol. 39, no. 3, pp. 927-935.

Cannestra, A. F., Pouratian, N., Forage, J., Bookheimer, S. Y., Martin, N. A., & Toga, A. W. 2004, "Functional magnetic resonance imaging and optical imaging for dominant-hemisphere perisylvian arteriovenous malformations", *Neurosurgery*, vol. 55, no. 4, pp. 804-812.

Carpentier, A. C., Constable, R. T., Schlosser, M. J., de Lotbiniere, A., Piepmeier, J. M., Spencer, D. D., & Awad, I. A. 2001, "Patterns of functional magnetic resonance imaging activation in association with structural lesions in the rolandic region: a classification system", *Journal of Neurosurgery*, vol. 94, no. 6, pp. 946-954.

Chung, M. K., Worsley, K. J., Robbins, S., Paus, T., Taylor, J., Giedd, J. N., Rapoport, J. L., & Evans, A. C. 2003, "Deformation-based surface morphometry applied to gray matter deformation", *Neuroimage*, vol. 18, no. 2, pp. 198-213.

Chung, M. K., Robbins, S. M., Dalton, K. M., Davidson, R. J., Alexander, A. L., & Evans, A. C. 2005, "Cortical thickness analysis in autism with heat kernel smoothing", *Neuroimage*, vol. 25, no. 4, pp. 1256-1265.

Collins, D. L., Zijdenbos, A. P., Kollokian, V., Sled, J. G., Kabani, N. J., Holmes, C. J., & Evans, A. C. 1998, "Design and construction of a realistic digital brain phantom", *Medical Imaging, IEEE Transactions on*, vol. 17, no. 3, pp. 463-468.

Condon, B. R., Patterson, J., Wyper, D., Jenkins, A., & Hadley, D. M. 1987, "Image non-uniformity in magnetic resonance imaging: its magnitude and methods for its correction", *The British Journal of Radiology*, vol. 60, no. 709, pp. 83-87.

Crosson, B., Sadek, J. R., Bobholz, J. A., Gokcay, D., Mohr, C. M., Leonard, C. M., Maron, L., Auerbach, E. J., Browd, S. R., Freeman, A. J., & Briggs, R. W.

1999, "Activity in the paracingulate and cingulate sulci during word generation: An fMRI study of functional anatomy", *Cerebral Cortex*, vol. 9, no. 4, pp. 307-316.

Dale, A. M., Fischl, B., & Sereno, M. I. 1999, "Cortical surface-based analysis. I. Segmentation and surface reconstruction", *Neuroimage.*, vol. 9, no. 2, pp. 179-194.

Desai, R., Liebenthal, E., Possing, E. T., Waldron, E., & Binder, J. R. 2005, "Volumetric vs. surface-based alignment for localization of auditory cortex activation", *Neuroimage.*, vol. 26, no. 4, pp. 1019-1029.

Devlin, J. T. & Poldrack, R. A. 2007, "In praise of tedious anatomy", *Neuroimage.*, vol. 37, no. 4, pp. 1033-1041.

DeYoe, E. A., Carman, G. J., Bandettini, P., Glickman, S., Wieser, J., Cox, R., Miller, D., & Neitz, J. 1996, "Mapping striate and extrastriate visual areas in human cerebral cortex", *Proceedings of the National Academy of Sciences*, vol. 93, no. 6, pp. 2382-2386.

Driemeyer, J., Boyke, J., Gaser, C., Buechel, C., & May, A. 2008, "Changes in Gray Matter Induced by Learning-Revisited", *Plos One*, vol. 3, no. 7.

Ecker, C., Marquand, A., Mourao-Miranda, J., Johnston, P., Daly, E. M., Brammer, M. J., Maltezos, S., Murphy, C. M., Robertson, D., Williams, S. C., & Murphy, D. G. 2010, "Describing the Brain in Autism in Five Dimensions-Magnetic Resonance Imaging-Assisted Diagnosis of Autism Spectrum Disorder Using a Multiparameter Classification Approach", *Journal of Neuroscience*, vol. 30, no. 32, pp. 10612-10623.

Engel, S. A., Glover, G. H., & Wandell, B. A. 1997, "Retinotopic organization in human visual cortex and the spatial precision of functional MRI", *Cerebral Cortex*, vol. 7, no. 2, pp. 181-192.

Evans, A. C., Collins, D. L., Mills, S. R., Brown, E. D., Kelly, R. L., & Peters, T. M. 1993, "3D Statistical Neuroanatomical Models from 305 Mri Volumes", *Nuclear Science Symposium & Medical Imaging Conference, Vols 1-3* pp. 1813-1817.

Evans, A. C., Collins, D. L., Neelin, P., MacDonald, D., Kamber, M., & Marret, T. S. 1994, "Three-dimensional correlative imaging: applications in human brain

mapping," in *Functional Neuroimaging: Technical Foundations*, R. W. Thatcher et al., eds., Academic Press, San Diego, pp. 145-162.

Fandino, J., Kollias, S. S., Wieser, H. G., Valavanis, A., & Yonekawa, Y. 1999, "Intraoperative validation of functional magnetic resonance imaging and cortical reorganization patterns in patients with brain tumors involving the primary motor cortex", *Journal of Neurosurgery*, vol. 91, no. 2, pp. 238-250.

Fischl, B., Sereno, M. I., & Dale, A. M. 1999 a, "Cortical surface-based analysis. II: Inflation, flattening, and a surface-based coordinate system", *Neuroimage.*, vol. 9, no. 2, pp. 195-207.

Fischl, B., Sereno, M. I., Tootell, R. B., & Dale, A. M. 1999 b, "High-resolution intersubject averaging and a coordinate system for the cortical surface", *Hum.Brain Mapp.*, vol. 8, no. 4, pp. 272-284.

FitzGerald, D. B., Cosgrove, G. R., Ronner, S., Jiang, H., Buchbinder, B. R., Belliveau, J. W., Rosen, B. R., & Benson, R. R. 1997, "Location of language in the cortex: A comparison between functional MR imaging and electrocortical stimulation", *American Journal of Neuroradiology*, vol. 18, no. 8, pp. 1529-1539.

Friedman, L., Glover, G. H., & FBIRN Consortium 2006, "Reducing interscanner variability of activation in a multicenter fMRI study: Controlling for signal-to-fluctuation-noise-ratio (SFNR) differences", *Neuroimage*, vol. 33, no. 2, pp. 471-481.

Friedman, L., Stern, H., Brown, G. G., Mathalon, D. H., Turner, J., Glover, G. H., Gollub, R. L., Lauriello, J., Lim, K. O., Cannon, T., Greve, D. N., Bockholt, H. J., Belger, A., Mueller, B., Doty, M. J., He, J. C., Wells, W., Smyth, P., Pieper, S., Kim, S. Y., Kubicki, M., Vangel, M., & Potkin, S. G. 2008, "Test-retest and between-site reliability in a multicenter fMRI study", *Human Brain Mapping*, vol. 29, no. 8, pp. 958-972.

Gaillard, W. D., Balsamo, L., Xu, B., Grandin, C. B., Braniecki, S. H., Papero, P. H., Weinstein, S., Conry, J., Pearl, P. L., Sachs, B., Sato, S., Jabbari, B., Vezina, L. G., Frattali, C., & Theodore, W. H. 2002, "Language dominance in partial epilepsy patients identified with an fMRI reading task", *Neurology*, vol. 59, no. 2, pp. 256-265.

Gallese, V., Keysers, C., & Rizzolatti, G. 2004, "A unifying view of the basis of social cognition", *Trends in Cognitive Sciences*, vol. 8, no. 9, pp. 396-403.

Garcia-Marti, G., Aguilar, E. J., Lull, J. J., Marti-Bonmati, L., Escarti, M. J., Manjon, J. V., Moratal, D., Robles, M., & Sanjuan, J. 2008, "Schizophrenia with auditory hallucinations: A voxel-based morphometry study", *Progress in Neuro-Psychopharmacology & Biological Psychiatry*, vol. 32, no. 1, pp. 72-80.

Geissler, A., Lanzenberger, R., Barth, M., Tahamtan, A. R., Milakara, D., Gartus, A., & Beisteiner, R. 2005, "Influence of fMRI smoothing procedures on replicability of fine scale motor localization", *Neuroimage*, vol. 24, no. 2, pp. 323-331.

Goebel, R., Khorram-Sefat, D., Muckli, L., Hacker, H., & Singer, W. 1998, "The constructive nature of vision: direct evidence from functional magnetic resonance imaging studies of apparent motion and motion imagery", *European Journal of Neuroscience*, vol. 10, no. 5, pp. 1563-1573.

Gountouna, V. E., Job, D. E., McIntosh, A. M., Moorhead, T. W. J., Lymer, G. K. L., Whalley, H. C., Hall, J., Waiter, G. D., Brennan, D., McGonigle, D. J., Ahearn, T. S., Cavanagh, J., Condon, B., Hadley, D. M., Marshall, I., Murray, A. D., Steele, J. D., Wardlaw, J. M., & Lawrie, S. M. 2010, "Functional Magnetic Resonance Imaging (fMRI) reproducibility and variance components across visits and scanning sites with a finger tapping task", *Neuroimage*, vol. 49, no. 1, pp. 552-560.

Hadjikhani, N., Joseph, R. M., Snyder, J., & Tager-Flusberg, H. 2006, "Anatomical differences in the mirror neuron system and social cognition network in autism", *Cerebral Cortex*, vol. 16, no. 9, pp. 1276-1282.

Hagler, D. J., Saygin, A. P., & Sereno, M. I. 2006, "Smoothing and cluster thresholding for cortical surface-based group analysis of fMRI data", *Neuroimage*, vol. 33, no. 4, pp. 1093-1103.

Han, X., Jovicich, J., Salat, D., van der Kouwe, A., Quinn, B., Czanner, S., Busa, E., Pacheco, J., Albert, M., Killiany, R., Maguire, P., Rosas, D., Makris, N., Dale, A., Dickerson, B., & Fischl, B. 2006, "Reliability of MRI-derived measurements of human cerebral cortical thickness: The effects of field strength, scanner upgrade and manufacturer", *Neuroimage*, vol. 32, no. 1, pp. 180-194.

Hardan, A. Y., Muddasani, S., Vemulapalli, M., Keshavan, M. S., & Minshew, N. J. 2006, "An MRI study of increased cortical thickness in autism", *American Journal of Psychiatry*, vol. 163, no. 7, pp. 1290-1292.

Harris, J. W. & Stocker, H. 1998, "Analysis by means of random sampling," in *Handbook of Mathematics and Computational Science*, Springer-Verlag, New York, pp. 820-844.

Holmes, C. J., Hoge, R., Collins, L., Woods, R., Toga, A. W., & Evans, A. C. 1998, "Enhancement of MR images using registration for signal averaging", *Journal of Computer Assisted Tomography*, vol. 22, no. 2, pp. 324-333.

Jo, H. J., Lee, J. M., Kim, J. H., Shin, Y. W., Kim, I. Y., Kwon, J. S., & Kim, S. I. 2007 a, "Spatial accuracy of fMRI activation influenced by volume- and surface-based spatial smoothing techniques", *Neuroimage.*, vol. 34, no. 2, pp. 550-564.

Jo, H. J., Lee, J. M., Chee, Y. J., Kim, I. Y., & Kim, S. I. 2007 b, "Volume- and surface-based fMRI analysis; Geometric influence of smoothing kernel", *2007 3rd International IEEE/EMBS Conference on Neural Engineering, Vols 1 and 2* pp. 261-264.

Jo, H. J., Lee, J. M., Kim, J. H., Choi, C. H., Gu, B. M., Kang, D. H., Ku, J., Kwon, J. S., & Kim, S. I. 2008, "Artificial shifting of fMRI activation localized by volume- and surface-based analyses", *Neuroimage*, vol. 40, no. 3, pp. 1077-1089.

Jouvent, E., Mangin, J. F., Porcher, R., Viswanathan, A., O'Sullivan, M., Guichard, J. P., Dichgans, M., Bousser, M. G., & Chabriat, H. 2008, "Cortical changes in cerebral small vessel diseases: a 3D MRI study of cortical morphology in CADASIL", *Brain*, vol. 131, no. Part 8.

Kates, W. R., Ikuta, I., & Burnette, C. 2009, "Gyrification Patterns in Monozygotic Twin Pairs Varying in Discordance for Autism", *Autism Research*, vol. 2, no. 5, pp. 267-278.

Kim, H., Bernasconi, N., Bernhardt, B., Colliot, O., & Bernasconi, A. 2008, "Basal temporal sulcal morphology in healthy controls and patients with temporal lobe epilepsy", *Neurology*, vol. 70, no. 22, pp. 2159-2165.

Kim, J. S., Singh, V., Lee, J. K., Lerch, J., Ad-Dab'bagh, Y., MacDonald, D., Lee, J. M., Kim, S. I., & Evans, A. C. 2005, "Automated 3-D extraction and evaluation of the inner and outer cortical surfaces using a Laplacian map and partial volume effect classification", *Neuroimage*, vol. 27, no. 1, pp. 210-221.

Kochunov, P., Thompson, P. M., Coyle, T. R., Lancaster, J. L., Kochunov, V., Royall, D., Mangin, J. F., Riviere, D., & Fox, P. T. 2008, "Relationship among neuroimaging indices of cerebral health during normal aging", *Human Brain Mapping*, vol. 29, no. 1, pp. 36-45.

Koenderink, J. 1984, "The structure of images", *Biological Cybernetics*, vol. 50, no. 5, pp. 363-370.

Krings, T., Reinges, M. H. T., Erberich, S., Kemeny, S., Rohde, V., Spetzger, U., Korinth, M., Willmes, K., Gilsbach, J. M., & Thron, A. 2001, "Functional MRI for presurgical planning: problems, artefacts, and solution strategies", *Journal of Neurology Neurosurgery and Psychiatry*, vol. 70, no. 6, pp. 749-760.

Kwan, R. K. S., Evans, A. C., & Pike, G. B. 1999, "MRI simulation-based evaluation of image-processing and classification methods", *Medical Imaging, IEEE Transactions on*, vol. 18, no. 11, pp. 1085-1097.

Kwan, R. K. S., Evans, A. C., & Pike, G. B. "An extensible MRI simulator for post-processing evaluation", 4th International Conference on Visualization in Biomedical Computing (VBC 96), pp. 135-140.

Kwan, R., Evans, A., & Pike, G. 1996, "An extensible MRI simulator for post-processing evaluation," pp. 135-140.

Le Goualher, G., Collins, D. L., Barillot, C., & Evans, A. C. 1998, *Automatic identificaiton of cortical sulci using a 3D probabilistic atlas*.

Lehericy, S., Duffau, H., Cornu, P., Capelle, L., Pidoux, B., Carpentier, A., Auliac, S., Clemenceau, S., Sichez, J. P., Bitar, A., Valery, C. A., Van Effenterre, R., Faillot, T., Srour, A., Fohanno, D., Philippon, J., Le Bihan, D., & Marsault, C. 2000, "Correspondence between functional magnetic resonance imaging somatotopy and individual brain anatomy of the central region: comparison with intraoperative stimulation in patients with brain tumors", *Journal of Neurosurgery*, vol. 92, no. 4, pp. 589-598.

Lemm, S., Blankertz, B., Dickhaus, T., & Mueller, K. R. 2011, "Introduction to machine learning for brain imaging", *Neuroimage*, vol. 56, no. 2, pp. 387-399.

Levitt, J. G., Blanton, R. E., Smalley, S., Thompson, P. M., Guthrie, D., McCracken, J. T., Sadoun, T., Heinichen, L., & Toga, A. W. 2003, "Cortical sulcal maps in autism", *Cerebral Cortex*, vol. 13, no. 7, pp. 728-735.

Lord, C., Rutter, M., & Lecouteur, A. 1994, "Autism Diagnostic Interview-Revised - A Revised Version of A Diagnostic Interview for Caregivers of Individuals with Possible Pervasive Developmental Disorders", *Journal of Autism and Developmental Disorders*, vol. 24, no. 5, pp. 659-685.

Lord, C., Risi, S., Lambrecht, L., Cook, E. H., Leventhal, B. L., DiLavore, P. C., Pickles, A., & Rutter, M. 2000, "The Autism Diagnostic Observation Schedule-Generic: A standard measure of social and communication deficits associated with the spectrum of autism", *Journal of Autism and Developmental Disorders*, vol. 30, no. 3, pp. 205-223.

MacDonald, D., Kabani, N., Avis, D., & Evans, A. C. 2000, "Automated 3-D Extraction of Inner and Outer Surfaces of Cerebral Cortex from MRI", *Neuroimage*, vol. 12, no. 3, pp. 340-356.

Mangin, J. F., Coulon, O., & Frouin, V. 1998, "Robust brain segmentation using histogram scale-space analysis and mathematical morphology", *Medical Image Computing and Computer-Assisted Intervention - Miccai'98*, vol. 1496, pp. 1230-1241.

Mangin, J. F. 2000, "Entropy minimization for automatic correction of intensity nonuniformity", *Ieee Workshop on Mathematical Methods in Biomedical Image Analysis, Proceedings* pp. 162-169.

Mangin, J. F., Riviere, D., Cachia, A., Duchesnay, E., Cointepas, Y., Papadopoulos-Orfanos, D., Collins, D. L., Evans, A. C., & Regis, J. 2004, "Object-based morphometry of the cerebral cortex", *Ieee Transactions on Medical Imaging*, vol. 23, no. 8, pp. 968-982.

Mangin, J. F., Frouin, V., Bloch, I., Regis, J., & Lopez-Krahe, J. 1995, "From 3D magnetic resonance images to structural representations of the cortex topography

using topology preserving deformations", *Journal of Mathematical Imaging and Vision*, vol. 5, no. 4, pp. 297-318.

McAlonan, G. M., Daly, E., Kumari, V., Critchley, H. D., van Amelsvoort, T., Suckling, J., Simmons, A., Sigmundsson, T., Greenwood, K., Russell, A., Schmitz, N., Happe, F., Howlin, P., & Murphy, D. G. M. 2002, "Brain anatomy and sensorimotor gating in Asperger's syndrome", *Brain*, vol. 125, pp. 1594-1606.

McAlonan, G. M., Cheung, V., Cheung, C., Suckling, J., Lam, G. Y., Tai, K. S., Yip, L., Murphy, D. G. M., & Chua, S. E. 2005, "Mapping the brain in autism. A voxel-based MRI study of volumetric differences and intercorrelations in autism", *Brain*, vol. 128, pp. 268-276.

McRobbie, D. W., Moore, E. A., .Graves, M. J., & Prince, M. R. 2007, *MRI From Picture to Proton*, 2nd Edition edn.

Mikl, M., Marecek, R., Hlustik, P., Pavlicova, M., Drastich, A., Chlebus, P., Brazdil, M., & Krupa, P. 2008, "Effects of spatial smoothing on fMRI group inferences", *Magnetic Resonance Imaging*, vol. 26, no. 4, pp. 490-503.

Moorhead, T. W., Gountouna, V. E., Job, D. E., McIntosh, A. M., Romaniuk, L., Lymer, G. K., Whalley, H. C., Waiter, G. D., Brennan, D., Ahearn, T. S., Cavanagh, J., Condon, B., Steele, J. D., Wardlaw, J. M., & Lawrie, S. M. 2009, "Prospective multi-centre Voxel Based Morphometry study employing scanner specific segmentations: procedure development using CaliBrain structural MRI data", *BMC.Med.Imaging*, vol. 9, p. 8.

Moorhead, T. W. J., McKirdy, J., Sussmann, J. E. D., Hall, J., Lawrie, S. M., Johnstone, E. C., & McIntosh, A. M. 2007, "Progressive gray matter loss in patients with bipolar disorder", *Biological Psychiatry* , vol. 62, no. 8, pp. 894-900.

Muller, K. R., Mika, S., Ratsch, G., Tsuda, K., & Scholkopf, B. 2001, "An introduction to kernel-based learning algorithms", *Ieee Transactions on Neural Networks*, vol. 12, no. 2, pp. 181-201.

Nordahl, C. W., Dierker, D., Mostafavi, I., Schumann, C. M., Rivera, S. M., Amaral, D. G., & Van Essen, D. C. 2007, "Cortical folding abnormalities in autism revealed by surface-based morphometry", *Journal of Neuroscience*, vol. 27, no. 43, pp. 11725-11735.

O'Sullivan, M., Jouvent, E., Saernann, P. G., Mangin, J. F., Viswanathan, A., Gschwendtner, A., Bracoud, L., Pachai, C., Chabriat, H., & Dichgans, M. 2008, "Measurement of brain atrophy in subcortical vascular disease: A comparison of different approaches and the impact of ischaemic lesions", *Neuroimage*, vol. 43, no. 2, pp. 312-320.

Oldfield, R. C. 1971, "Assessment and Analysis of Handedness - Edinburgh Inventory", *Neuropsychologia*, vol. 9, no. 1, p. 97-&.

Penhune, V. B., Zatorre, R. J., MacDonald, J. D., & Evans, A. C. 1996, "Interhemispheric anatomical differences in human primary auditory cortex: Probabilistic mapping and volume measurement from magnetic resonance scans", *Cerebral Cortex*, vol. 6, no. 5, pp. 661-672.

Penttila, J., Cachia, A., Martinot, J. L., Ringuenet, D., Wessa, M., Houenou, J., Galinowski, A., Bellivier, F., Gallarda, T., Duchesnay, E., Artiges, E., Leboyer, M., Olie, J. P., Mangin, J. F., & Paillere-Martinot, M. L. 2009 a, "Cortical folding difference between patients with early-onset and patients with intermediate-onset bipolar disorder", *Bipolar Disorders*, vol. 11, no. 4, pp. 361-370.

Penttila, J., Paillere-Martinot, M. L., Martinot, J. L., Ringuenet, D., Wessa, M., Houenou, J., Gallarda, T., Bellivier, F., Galinowski, A., Bruguiere, P., Pinabel, F., Leboyer, M., Olie, J. P., Duchesnay, E., Artiges, E., Mangin, J. F., & Cachia, A. 2009 b, "Cortical folding in patients with bipolar disorder or unipolar depression", *Journal of Psychiatry & Neuroscience*, vol. 34, no. 2, pp. 127-135.

Perrot, M., Riviere, D., & Mangin, J. F. 2008, "Identifying cortical sulci from localization, shape and local organization", *2008 Ieee International Symposium on Biomedical Imaging: from Nano to Macro, Vols 1-4* pp. 420-423.

Perrot, M., Riviere, D., Tucholka, A., & Mangin, J. F. 2009, "Joint Bayesian Cortical Sulci Recognition and Spatial Normalization", *Information Processing in Medical Imaging, Proceedings*, vol. 5636, pp. 176-187.

Pouratian, N., Bookheimer, S. Y., Rex, D. E., Martin, N. A., & Toga, A. W. 2002, "Utility of preoperative functional magnetic resonance imaging for identifying language cortices in patients with vascular malformations", *Journal of Neurosurgery*, vol. 97, no. 1, pp. 21-32.

Rademacher, J., Morosan, P., Schormann, T., Schleicher, A., Werner, C., Freund, H. J., & Zilles, K. 2001, "Probabilistic mapping and volume measurement of human primary auditory cortex", *Neuroimage*, vol. 13, no. 4, pp. 669-683.

Radua, J., Via, E., Catani, M., & Mataix-Cols, D. 2011, "Voxel-based meta-analysis of regional white-matter volume differences in autism spectrum disorder versus healthy controls", *Psychological Medicine*, vol. 41, no. 7, pp. 1539-1550.

Rojas, D. C., Peterson, E., Winterrowd, E., Reite, M. L., Rogers, S. J., & Tregellas, J. R. 2006, "Regional gray matter volumetric changes in autism associated with social and repetitive behavior symptoms", *Bmc Psychiatry*, vol. 6.

Roux, F. E., Boulanouar, K., Ibarrola, D., Tremoulet, M., Chollet, F., & Berry, I. 2000, "Functional MRI and intraoperative brain mapping to evaluate brain plasticity in patients with brain tumours and hemiparesis", *Journal of Neurology Neurosurgery and Psychiatry*, vol. 69, no. 4, pp. 453-463.

Ruge, M. I., Victor, J., Hosain, S., Corres, D. D., Relkin, N. R., Tabar, V., Brennan, C., Gutin, P. H., & Hirsch, J. 1999, "Concordance between functional magnetic resonance imaging and intraoperative language mapping", *Stereotactic and Functional Neurosurgery*, vol. 72, no. 2-4, pp. 95-102.

Saad, Z. S., Reynolds, R. C., Argall, B., Japee, S., & Cox, R. W. 2004, "Suma: An interface for surface-based intra- and inter-subject analysis with AFNI", *2004 2Nd Ieee International Symposium on Biomedical Imaging: Macro to Nano, Vols 1 and 2* pp. 1510-1513.

Schnack, H. G., Hulshoff Pol, H. E., Baarθ, W. F. C., Viergever, M. A., & Kahn, R. S. 2001, "Automatic Segmentation of the Ventricular System from MR Images of the Human Brain", *Neuroimage*, vol. 14, no. 1, pp. 95-104.

Schnack, H. G., van Haren, N. E. M., Pol, H. E. H., Picchioni, M., Weisbrod, M., Sauer, H., Cannon, T., Huttunen, M., Murray, R., & Kahn, R. S. 2004, "Reliability of brain volumes from multicenter MRI acquisition: A calibration study", *Human Brain Mapping*, vol. 22, no. 4, pp. 312-320.

Schreiber, A., Hubbe, U., Ziyeh, S., & Hennig, J. 2000, "The influence of gliomas and nonglial space-occupying lesions on blood-oxygen-level-dependent contrast enhancement", *American Journal of Neuroradiology*, vol. 21, no. 6, pp. 1055-1063.

Sereno, M. I., Dale, A. M., Reppas, J. B., Kwong, K. K., Belliveau, J. W., Brady, T. J., Rosen, B. R., & Tootell, R. B. H. 1995, "Borders of Multiple Visual Areas in Humans Revealed by Functional Magnetic-Resonance-Imaging", *Science*, vol. 268, no. 5212, pp. 889-893.

Shenton, M. E., Dickey, C. C., Frumin, M., & McCarley, R. W. 2001, "A review of MRI findings in schizophrenia", *Schizophr.Res.*, vol. 49, no. 1-2, pp. 1-52.

Simmons, A., Arridge, S. R., Barker, G. J., & Williams, S. C. R. 1996, "Simulation of MRI cluster plots and application to neurological segmentation", *Magnetic Resonance Imaging*, vol. 14, no. 1, pp. 73-92.

Simmons, A., Tofts, P. S., Barker, G. J., & Arridge, S. R. 1994, "Sources of Intensity Nonuniformity in Spin-Echo Images at 1.5-T", *Magnetic Resonance in Medicine*, vol. 32, no. 1, pp. 121-128.

Studholme, C., Hill, D. L. G., & Hawkes, D. J. 1999, "An overlap invariant entropy measure of 3D medical image alignment", *Pattern Recognition*, vol. 32, no. 1, pp. 71-86.

Suckling, J., Barnes, A., Job, D., Brenan, D., Lymer, K., Dazzan, P., Marques, T. R., MacKay, C., McKie, S., Williams, S. R., Williams, S. C. R., Lawrie, S., & Deakin, B. 2010, "Power Calculations for Multicenter Imaging Studies Controlled by the False Discovery Rate", *Human Brain Mapping*, vol. 31, no. 8, pp. 1183-1195.

Sunaert, S. 2006, "Presurgical planning for tumor resectioning", *Journal of Magnetic Resonance Imaging*, vol. 23, no. 6, pp. 887-905.

Szikla, G. 1977, *Angiography of the human brain cortex : atlas of vascular patterns and stereotactic cortical localization* Springer-Verlag, Berlin; New York.

Talairach, J. & Tournoux, P. 1988, *Co-planar Stereotaxic Atlas of the Human Brain* Thieme Medical, Newyork.

Thompson, P. M., Hayashi, K. M., de Zubicaray, G., Janke, A. L., Rose, S. E., Semple, J., Herman, D., Hong, M. S., Dittmer, S. S., Doddrell, D. M., & Toga, A. W. 2003, "Dynamics of gray matter loss in Alzheimer's disease", *Journal of Neuroscience*, vol. 23, no. 3, pp. 994-1005.

Uddin, L. Q. & Menon, V. 2009, "The anterior insula in autism: Under-connected and under-examined", *Neuroscience and Biobehavioral Reviews*, vol. 33, no. 8, pp. 1198-1203.

Ulmer, J. L., Hacein-Bey, L., Mathews, V. P., Mueller, W. M., DeYoe, E. A., Prost, R. W., Meyer, G. A., Krouwer, H. G., & Schmainda, K. M. 2004, "Lesion-induced pseudo-dominance at functional magnetic resonance imaging: Implications for preoperative assessments", *Neurosurgery*, vol. 55, no. 3, pp. 569-579.

Uylings, H. B. M., Rajkowska, G., Sanz-Arigita, E., Amunts, K., & Zilles, K. 2005, "Consequences of large interindividual variability for human brain atlases: converging macroscopical imaging and microscopical neuroanatomy", *Anatomy and Embryology*, vol. 210, no. 5-6, pp. 423-431.

Van Essen, D. C., Drury, H. A., Joshi, S., & Miller, M. I. 1998, "Functional and structural mapping of human cerebral cortex: solutions are in the surfaces", *Proc.Natl.Acad.Sci.U.S.A*, vol. 95, no. 3, pp. 788-795.

Van Essen, D. C. 2005, "A Population-Average, Landmark- and Surface-based (PALS) atlas of human cerebral cortex", *Neuroimage.*, vol. 28, no. 3, pp. 635-662.

Van Essen, D. C., Dierker, D., Snyder, A. Z., Raichle, M. E., Reiss, A. L., & Korenberg, J. 2006, "Symmetry of cortical folding abnormalities in Williams syndrome revealed by surface-based analyses", *Journal of Neuroscience*, vol. 26, no. 20, pp. 5470-5483.

Waiter, G. D., Williams, J. H. G., Murray, A. D., Gilchrist, A., Perrett, D. I., & Whiten, A. 2004, "A voxel-based investigation of brain structure in male adolescents with autistic spectrum disorder", *Neuroimage*, vol. 22, no. 2, pp. 619-625.

Waiter, G. D., Williams, J. H. G., Murray, A. D., Gilchrist, A., Perrett, D. I., & Whiten, A. 2005, "Structural white matter deficits in high-functioning individuals with autistic spectrum disorder: a voxel-based investigation", *Neuroimage*, vol. 24, no. 2, pp. 455-461.

Wechsler, D. 1981, "The Psychometric Tradition - Developing the Wechsler Adult Intelligence Scale", *Contemporary Educational Psychology*, vol. 6, no. 2, pp. 82-85.

Wechsler, D. 1982, "New Techniques - Wisc-R - Wechsler Intelligence-Test for Children (Revised Form)", *Revue de Psychologie Appliquee*, vol. 32, no. 1, pp. 63-64.

Williams, J. H. G., Waiter, G. D., Gilchrist, A., Perrett, D. I., Murray, A. D., & Whiten, A. 2006, "Neural mechanisms of imitation and 'mirror neuron' functioning in autistic spectrum disorder", *Neuropsychologia*, vol. 44, no. 4, pp. 610-621.

Williams, J. H. 2008, "Self-Other Relations in Social Development and Autism: Multiple Roles for Mirror Neurons and Other Brain Bases", *Autism Research*, vol. 1, no. 2, pp. 73-90.

Wise, R. J. S., Scott, S. K., Blank, S. C., Mummery, C. J., Murphy, K., & Warburton, E. A. 2001, "Separate neural subsystems within 'Wernicke's area'", *Brain*, vol. 124, pp. 83-95.

Woermann, F. G., Jokeit, H., Luerding, R., Freitag, H., Schulz, R., Guertler, S., Okujava, M., Wolf, P., Tuxhorn, I., & Ebner, A. 2003, "Language lateralization by Wada test and fMRI in 100 patients with epilepsy", *Neurology*, vol. 61, no. 5, pp. 699-701.

Yendiki, A., Greve, D. N., Wallace, S., Vangel, M., Bockholt, J., Mueller, B. A., Magnotta, V., Andreasen, N., Manoach, D. S., & Gollub, R. L. 2010, "Multi-site characterization of an fMRI working memory paradigm: Reliability of activation indices", *Neuroimage*, vol. 53, no. 1, pp. 119-131.

Zhang, Y. Y., Brady, M., & Smith, S. 2001, "Segmentation of brain MR images through a hidden Markov random field model and the expectation-maximization algorithm", *Ieee Transactions on Medical Imaging*, vol. 20, no. 1, pp. 45-57.